Title
Molecular Beam Photodissociation and Liquid Surface Scattering Dynamics

Author
Ramphal, Isaac Alexander

Publication Date
2021

Peer reviewed|Thesis/dissertation

Molecular Beam Photodissociation and Liquid Surface Scattering Dynamics

by

Isaac A. Ramphal

A dissertation submitted in partial satisfaction of the

requirements for the degree of

Doctor of Philosophy

in

Chemistry

in the

Graduate Division

of the

University of California, Berkeley

Committee in charge:

Professor Daniel M. Neumark, Chair
Professor Stephen R. Leone
Professor Michael Frenklach

Spring 2021

Molecular Beam Photodissociation and Liquid Surface Scattering Dynamics

Abstract

Molecular Beam Photodissociation and Liquid Surface Scattering Dynamics

by

Isaac A. Ramphal

Doctor of Philosophy in Chemistry

University of California, Berkeley

Professor Daniel M. Neumark, Chair

The photodissociation and liquid interfacial scattering dynamics of neutral species are described. Photofragment translational spectroscopy is used to determine active product channels and their relative importance, as well as providing insight into the detailed dissociation mechanisms leading to each channel. Modifications to the photodissociation apparatus enable experiments on evaporation and scattering from the surface of volatile liquid jets. These new experiments are capable of probing the detailed reactive and non-reactive interaction dynamics between atoms and molecules at the liquid-vacuum interface. Reactive free radicals are important species in fields such as terrestrial and non-terrestrial atmospheric chemistry, circumstellar and interstellar astrochemistry, and in combustion. For their widespread importance to these fields through their impact on interfacial chemistry and photochemistry, neutral free radicals are featured prominently in the enclosed studies.

Fulvenallene (C_7H_6) and the fulvenallenyl radical (C_7H_5) are important intermediates in the decomposition mechanism of toluene, a model system for aromatic combustion. Fulvenallene photodissociation was studied at 248 nm and 193 nm, in each case leading exclusively to H-loss. The data support a mechanism involving internal conversion to the ground state and subsequent energy randomization, leading to statistical production of H + fulvenallenyl. The absence of a proposed c-C_5H_4 + C_2H_2 channel indicated the necessary intersystem crossing to the triplet state must have a low transition probability. Fulvenallenyl radicals produced by fulvenallene dissociation absorbed a second photon and their photodissociation was thus determined. At both wavelengths, fulvenallenyl dissociation yielded n/i-C_5H_3 radical + acetylene (C_2H_2) and diacetylene (C_4H_2) + propargyl radical (C_3H_3). The translational energy distributions for these reactions were consistent with internal conversion of fulvenallenyl to its ground state, followed by statistical dissociation. The C_4H_2 + C_3H_3 channel accounted for 85 ± 10 % and 80 ± 15 % of fulvenallenyl dissociation at 248 nm and 193 nm respectively. The branching between these two channels agrees well with statistical Rice-Ramsperger-Kassel-Marcus (RRKM) calculations, supporting the proposed mechanism.

The methylsulfinyl radical (CH_3SO) is an important intermediate in the oxidation of biogenic sulfur-containing molecules in the terrestrial atmosphere, ultimately contributing to

acid-rain formation. The ultraviolet photochemistry of methylsulfinyl was assessed at 248 nm, finding evidence for CH_3S + O, CH_3 + SO, and CH_2SO + H channels. The existence of the very high energy O-atom loss channel relies on a dissociation mechanism mediated by a repulsive excited state of methylsulfinyl leading to ground state products, and this channel accounted for 77 ± 8 % of all methylsulfinaly photodissociation. The SO-loss channel had a bimodal translational energy distribution attributed to formation of SO in its X $^3\Sigma^-$ ground state and a $^1\Delta$ excited state, along with ground state CH_3 radical in each case. The SO-loss channels accounted for 22 ± 8 % of dissociation, approximately 12 % from the ground state and 10 % via the excited state channel. Finally, H-loss to form sulfine, CH_2SO, occurred on the ground state following internal conversion and energy randomization, and accounted for 1.5 ± 0.5 % of dissociation. For the ground-state CH_3 + SO and CH_2SO + H channels, their branching ratio agrees well with RRKM calculations.

The cyclohexyl radical (c-C_6H_{11}) is a cycloalkyl radical relevant in combustion and astrochemical environments. Cyclohexyl radicals were excited to their $3p_z$ Rydberg state using 248 nm photons, leading to three channels: C_6H_{10} + H, C_5H_3 + CH_3, and C_4H_7 + C_2H_4. The bimodal translational energy distribution for H-loss was attributed to 'slow' statistical ground state and 'fast' repulsive excited state channels for which cyclohexene is the major and exclusive C_6H_{10} isomer respectively. The initially prepared $3p_z$ state converts to the 3s state, which is separated from the ground state by a conical intersection that determines branching between impulsive H-loss and population of the ground state potential energy well, from which H-atom loss is a possible dissociation channel. The translational energy distributions for the C_5H_3 + CH_3 and C_4H_7 + C_2H_4 channels were both consistent with statistical ground state mechanisms initiating with ring-opening of ground state cyclohexyl to form 1-hexen-6-yl, which competes with direct H-loss. Experimentally determined branching ratios were $(\text{H-loss})_{slow}$:$(\text{H-loss})_{fast}$:(C_5H_3 + CH_3):(C_4H_7 + C_2H_4) = $1 : 0.7^{+1.6}_{-0.4} : 0.015^{+0.005}_{-0.005} : 0.86^{+0.10}_{-0.07}$. The slow:fast H-loss ratio of ∼0.7:1 is very similar to findings in other alkyl radicals, and the ground-state channels are formed in excellent agreement with RRKM calculations. The 1-buten-4-yl (C_4H_7) radical was formed with sufficient energy to dissociate further, proceeding exclusively to C_4H_6 + H within the experimental detection capabilities.

The dynamics of evaporation and scattering from aqueous and organic liquid surfaces has important implications for atmospheric chemistry occurring at surface coatings and aerosol interfaces. Modifications to the photodissociation apparatus enable the generation of free-flowing, flat liquid jets of water and hydrocarbons in vacuum. Measurements of the kinetic energy and angular distributions of evaporation of the neat liquid and dissolved species reveal dynamical signatures of the thermal desorption process governing evaporation. Fundamentally interesting in their own right, the manifestation of thermal desorption isolated in these experiments develops experience that can be applied during scattering experiments, where impulsive scattering and trapping-desorption are prototypical surface-scattering processes. Preliminary results on scattering from the liquid-vacuum interface show promise for this technique, and several future research directions are discussed.

To my wife

"You may have heard the world is made up of atoms and molecules, but it's really made up of stories."

- William Turner

Contents

List of Figures

List of Tables

Acknowledgments

From a young and curious boy exploring the idyllic beaches of Barbados to a somewhat less young (but still curious) boy receiving his doctorate in California it has been a truly remarkable and privileged journey. Even now, I remain lucky enough to occasionally visit and explore the beaches! The journey has also been a long one, throughout which I have been continually guided and supported by a tremendous number of people.

First, I must offer my sincerest gratitude to Dan Neumark. Thank you for welcoming me into your research group six years ago, even after I yawned through your research presentation on the visit weekend (courtesy of my visit to an unnamed university across the bay the night prior). For allowing me to join the X-Beam project, to which I was so genuinely interested in contributing, and to take the helm of an apparatus of such stature and so storied as the B-Machine. For mentoring me as a scientist, fostering my analytical abilities, and instilling a rigor into my work that was always for the better. For allowing me to stay at Berkeley for an extra semester at a time when COVID-19 had upended the job market and thrown the immigration status of international students into disarray. For always being available to answer questions, field concerns, and provide thoughtful advice when challenges arose. Thank you for your large role in shaping me into who I am today.

Particular thanks to Michelle Haskins for keeping Dan's group running so smoothly, and for always being willing and available to solve problems over the last 6 years, whether they be with campus or with LBNL. It would have been much more difficult without you, and I wish you the best in your retirement.

Along the way, my research in Dan's group has been buoyed by many wonderful individuals. Thanks to the senior student on X-Beam when I joined, Mark Shapero, who taught me everything about B-Machine and the photodissociation experiment. For taking the time to talk through so many aspects of the experiment and data analysis in such a thorough manner. Thanks to Chin Lee for joining the X-Beam project, and for bringing such great enthusiasm to the laboratory. You have been a dynamic force in driving the liquid jet experiments forward, for which I have nothing but gratitude. Thanks to Marvin Pohl for joining us as a post-doc. For bringing liquid jet experience, design creativity, and the internationally-renowned German sense of humor to Latimer D10. I could not be leaving the project in better hands than those of Chin and Marvin.

Thanks too for the contributions from all of the Neumark group members, so many of whom I have solicited for advice, assistance, and camaraderie. Thanks to Holly Williams, Marissa Weichmann, Weili Li, Alice Kunin, Bethan Nichols, Jessalyn Devine and Katherine Lunny. Thanks to the members of my cohort, Erin Sullivan and Ashley Fidler, with whom I shared so many of the same experiences. Thanks to the younger students in the group for bringing additional flair to the Latimer Dungeon, to Mark Babin and Blake Erickson, to

Zach Heim, Steve Saric, Marty DeWitt, and Megan Asplund. Best wishes to you all as you navigate your own doctoral journeys.

My work at Berkeley would not have been possible without the technical support from many members of the College. Thanks to Doug and Clint for their excellent work in the machine shop, and for taking time and care on the design and manufacture of so many parts we have needed from them. Thanks to Yimin in the pump shop for keeping the vacuum pumps spinning, and to Jim in the glass shop for keeping our bubblers bubbling. Thanks to Hasan for support in the NMR facility, and to Kathy Durkin for computational support in the MGCF.

Special thanks must be reserved for the friends and family who have greatly enriched my entire life. My parents are to be commended for shipping me off to Costa Rica and the wider world at the tender age of just 16. Thank you for always believing in me, and for always being there to support me. Thanks to everyone for taking an interest in my success, and for teaching me so much about life, love, and the things that truly matter. Thanks to the late Mike Hagerman for being a mentor and a friend over so many years, since the day I joined his research group at Union College. I will always cherish the times we spent together. Thanks to Nick Stoute, for 25 years of friendship and counting, for all the adventures we have taken together, and for being a constant positive presence throughout my whole life. I have learned more from you than I could ever say. Thanks to all of my friends, both here and abroad, for the countless good times. For the lunchtime burgers, tacos, beers, and margaritas. For trips to the bar and the sauna, and to the beaches and the mountains, and the myriad others.

Finally, thanks to Yi Cao for choosing to spend so much of this journey with me. For letting me live in your dorm room with you for an entire year after I graduated college. For making the improbable trip with me from upstate New York to the Bay Area for graduate school. For all of your patience and support throughout the years, without which none of this would be possible. Thank you for your excitement and your enthusiasm to explore all that life has to offer. I can't wait to embark on the next adventure with you.

Part I

Background and Methods

Chapter 1

Introduction

This dissertation discusses two broad types of inquiry into fundamental molecular dynamics – ultraviolet photodissociation, and molecular scattering at the liquid-vacuum interface. Free radicals feature prominently in much of the work presented here, given their central importance to so many of the theatres within which chemistry plays out. This section motivates the types of experiments undertaken in this dissertation and highlights relevant information about the experimental techniques used to measure various physical phenomena.

1.1 Molecular Beams

The idea that collisions between molecules were integral to chemistry extends back to the formal origin of the discipline. Pondering the constituent building blocks of matter, Robert Boyle remarked that they ought to:[1]

> "continue in a state of rest til some external force put it out of that state, and to concur to the production of divers Changes in the bodies that hit against it, by either quite stopping or lessening their Motion (whilst the body formerly at Rest Receives all or part of it into itself) or else by giving a new Byass, or some other Modification, to Motion, that is, To the Grand and Primary instrument whereby Nature produces all the Changes and other Qualities that are to be met with in the World."

The ensuing centuries of physical chemical research have only confirmed the idea that collisions underpin chemistry and are often a very good way to study it. Yet the numerous random collisions between particles also obscures the detailed physical and chemical dynamics of the brief sojourns of atoms and molecules. To disentangle the fundamental and state-specific interactions from the crude averages offered by thermodynamics, the ability to suppress or directly control collisions was crucial.

Molecular beams were thus a revolutionary development in the study of atomic and molecular physics, contributing to a tremendous array of fundamental discoveries. Though gas-phase dynamics of ions were under study as early as the late 1800's, collimated beams of neutral particles were possibly first employed by Dunoyer in 1911, using an effusive source

of alkali metals to ascertain whether particles traveled through vacuum in straight lines.[2] However, the generalized conceptualization of molecular beams arguably appears exactly one century ago in 1921, when Hartmut Kallman and Fritz Reiche considered the utility of true *molecular* beams in support of experiments investigating whether molecular dipoles were intrinsic properties of molecules, or rather induced through intermolecular interactions.[3]

Importantly, a pre-print of this article came across the desks of Otto Stern and collaborator Walther Gerlach, whereafter the eponymous Stern-Gerlach experiment was swiftly conceived by the former and performed mostly by the latter. By February 1922, this pair had succeeded in using an inhomogeneous magnetic field to split an effusive beam of silver atoms into two spatially localized components.[4] This experiment demonstrated for the first time that atoms possessed an intrinsic angular momentum, and that the angular momentum was quantized. As we now know, the intrinsic spin angular momentum of the electron is responsible for the doublet resolved by Stern and Gerlach.

The Stern-Gerlach experiment generated great enthusiasm for using electromagnetic fields to manipulate atomic and molecular beams,[5] and none of these experiments will be described here save for the following example. Coupling of an ammonia beam into a microwave cavity in 1954-1955 provided an effective means of amplifying microwave emission through a stimulated emission process (maser).[6,7] Molecular beams had led to the development of the laser, described at the time as a "solution seeking a problem," whereas today problems for which lasers are not a suitable solution are scarce.

While molecular beams also found important use in applications other than electromagnetic manipulation experiments, the effusive beams utilized then had broad velocity distributions comparable to a Maxwell distribution (Figure 1.1). Narrow distributions can be achieved by directing the beam through a series of velocity selectors at the expense of losing a significant proportion of the beam.[8] Of significance for this work, therefore, was the realization of high-intensity, supersonic molecular beams by Jim Anderson and John Fenn.[9] Supersonic molecular beam sources are particularly appealing because they produce a high density of molecules in a collision-free environment and with a very low internal temperature (and thus a well-defined initial quantum state). This is achieved by converting the enthalpy of gas behind the valve orifice into a highly directional beam with a large flow velocity.[10] Collisions in the valve orifice during expansion align particles in the beam along its flow axis and accelerate them into a velocity distribution of the form

$$N(v) \propto v^2 \; e^{-S^2\left(\frac{v-V_o}{V_o}\right)^2} \tag{1.1}$$

where V_o is the average flow velocity of the beam and S is the speed ratio (a measure of the beam velocity divided by the spread in velocities). For any experiment measuring some property related to the velocity distribution of particles in the beam, both V_o and S are the key parameters to determine in order to properly treat experimental data. Since S is a measure of $V/\Delta V$, higher speed ratios indicate a smaller velocity spread within the co-moving gas pulse – the molecules in the beam are colder. While V_o could take on many different values depending on the gas species and expansion conditions, for an ideal, monoatomic gas

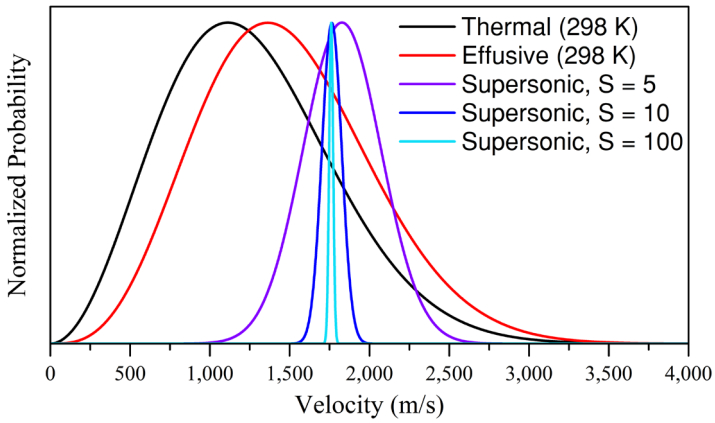

Figure 1.1: Velocity distributions of effusive and supersonic nozzle expansions compared to a Maxwell thermal distribution for helium. Supersonic beams with several different speed ratios are featured, with higher ratios representing narrower distributions.

of mass m in a reservoir at temperature T_o, such an adiabatic, isentropic expansion provides the terminal velocity $\langle v_{max} \rangle$ according to

$$\langle v_{max} \rangle = \sqrt{\frac{5RT_o}{N_A m}} \tag{1.2}$$

where R is the universal gas constant, and $N_A = 6.022 \times 10^{23}$ mol^{-1} is Avogadro's number. Figure 1.1 shows the velocity distribution of several supersonic beams of helium with different expansion conditions, peaked at ∼1760 m/s as Equation 1.2 predicts. Entrainment of small quantities of heavy gases in molecular beams also leads to high densities and cold internal temperatures for these species with terminal velocities close to those of the carrier gas (the converse also being true for light gases seeded in heavy ones).

Supersonic molecular beams were a key enabling technology in the development of the universal crossed molecular beam scattering machine by Yuan T. Lee,[11] the second iteration of which, Machine B, is the instrument used for the work in this dissertation. The gas source used herein for both photodissociation and surface scattering experiments is a molecular beam produced through supersonic expansion of an appropriate species (often a gas mix). For photodissociation experiments, molecules of interest in recent years have typically been free radicals. Given their high reactivity, radicals are not available 'off-the-shelf,' which is either a dismaying or exciting prospect depending on one's sensibilities. Radical production therefore involves selection of a suitable precursor from which to create a molecular beam, which is then modified in some way to produce the radical of interest. Common ways of producing radical beams include electric discharge,[12] photolysis,[13] and pyrolysis in a heated reactor[14] just outside the nozzle orifice. The pyrolysis method is typically chosen in our lab as it affords a dense source of radicals with a low internal temperature, free from contamination by interfering species.

It is worthwhile to briefly consider different types of molecular beam scattering experiments. Molecular beam photodissociation reactions can be thought of as the second half of a scattering process; crossed molecular beams study the physics and chemistry of collisions between isolated pairs of gaseous species; while molecular beam-surface scattering experiments probe the interactions of gas particles with condensed matter matrices, either in the solid or liquid phases. Kinematic ('Newton') diagrams for these three increasingly complex cases are shown in Figure 1.2. Quantities in black are laboratory frame velocities and angles, while those in the center-of-mass frame are shown in red. In each case, unravelling the dynamics of the relevant interaction is aided by the properties of the molecular beams. These properties combine with the dynamical processes taking place in the experiment to prescribe expectations and impose constraints on the velocities and scattering angles of product species. These kinematic constraints are represented in Figure 1.2 by the blue shaded regions. The instrument used in this dissertation no longer performs the crossed molecular beams scattering experiments it was originally designed for, and this case is included in Figure 1.2 for illustrative purposes only. Further details of the photodissociation and surface scattering cases are given in their respective sections below.

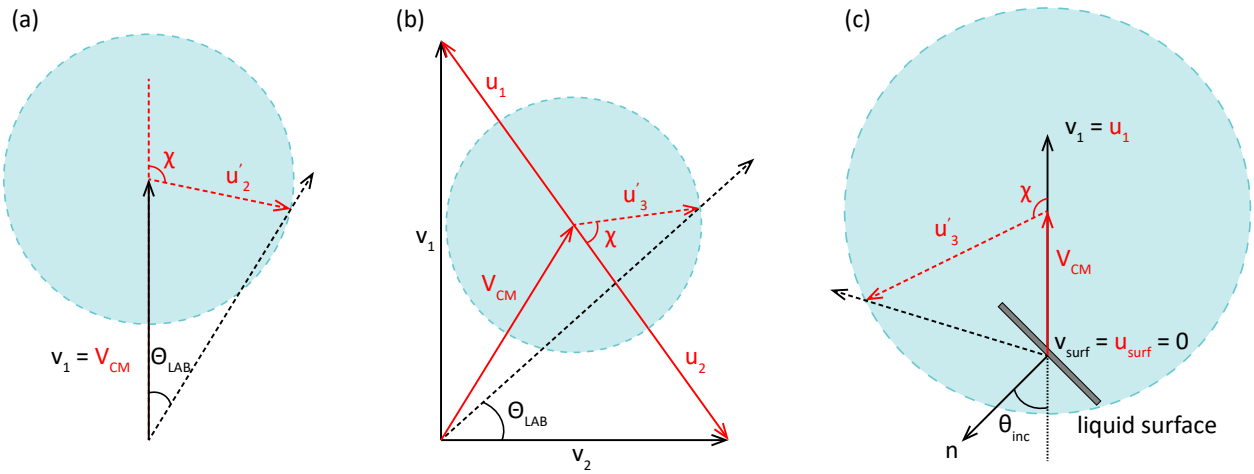

Figure 1.2: Kinematic diagrams for (a) a photodissociation 'half-scattering' process, (b) a crossed molecular beam collision, and (c) collision between a molecular beam with a condensed phase surface. Blue shaded areas are constructed from all possible vectors of the scattered products subject to conservation of energy and momentum constraints. Note that in the case of gas-surface collisions a substantial part of this kinematically accessible space is actually physically blocked by the surface. While satisfactory for very fast beams, the validity of this framework for thermal velocities is unclear given the motion of surface molecules. In most cases for surface scattering experiments, the surface normal is the natural reference vector rather than the incident beam velocity.

1.2 Photochemistry and Photodissociation

Electronic Absorption

The first step of any photochemical reaction is the absorption of a photon by the reactant molecule. Photon absorption requires that the initial and final states of the molecule can be coupled through the electromagnetic field of the photon by a non-zero transition moment integral. In general, the intensity I of a transition is proportional to

$$I \propto |\langle \Psi_n^f | \Psi_n^i \rangle|^2 \; |\langle \Psi_e^f | \mu_e | \Psi_e^i \rangle|^2 \tag{1.3}$$

where Ψ_n and Ψ_e are nuclear and electronic wave functions for the initial state i and final state f, and μ_e is the transition dipole moment.[15] For absorption to occur both of the integrals in this expression must be non-zero. The first integral is the Franck-Condon factor, which states that the initial and final states must have non-negligible overlap of their nuclear wavefunctions under the Born-Oppenheimer approximation, since nuclei are essentially motionless on the timescale of electronic transitions. In the limit of low spin-orbit coupling, decomposing the second integral into separate terms corresponding to the electronic orbital and electronic spin angular momenta provides the usual selection rules for electronic spectroscopy:[16] the total spin cannot change during the transition, $\Delta S = 0$, e.g. singlet-triplet excitations are formally forbidden (these transitions may nevertheless be enabled by spin-orbit or nonadiabatic couplings); and the triple direct product of the irreducible representations of the transition dipole moment, initial and final states must contain the totally symmetric representation of the point group containing the molecule, $\Gamma(\Psi^f) \otimes \Gamma(\mu_e) \otimes \Gamma(\Psi^i) \supseteq A$ (here A refers very generally to the totally symmetric representation of any point group). Having large values for the nuclear overlap and transition dipole integrals leads to a large transition intensity, suggesting that the experimental absorption cross-section will be large for the transition.

The photodissociation experiments reported in this dissertation are induced by absorption of ultraviolet photons containing energies exceeding typical bond dissociation energies (D_o) of molecules. For a polyatomic molecule ABC, there are often several possible primary photoproducts in a variety of final quantum states that can be formed during dissociation:

$$\begin{aligned} ABC \xrightarrow{h\nu} ABC^* \; &\rightarrow AB + C \\ &\rightarrow A + BC \\ &\rightarrow A + B + C \\ &\vdots \end{aligned}$$

The interactions between dissociating fragments depend on the shape of the potential energy surface (PES) along which the molecule evolves. The PES thus determines the relative yields of different product channels, and governs the state-specific distribution of energy partitioned into translational, rotational, vibrational, and electronic degrees of freedom in the photofragments.

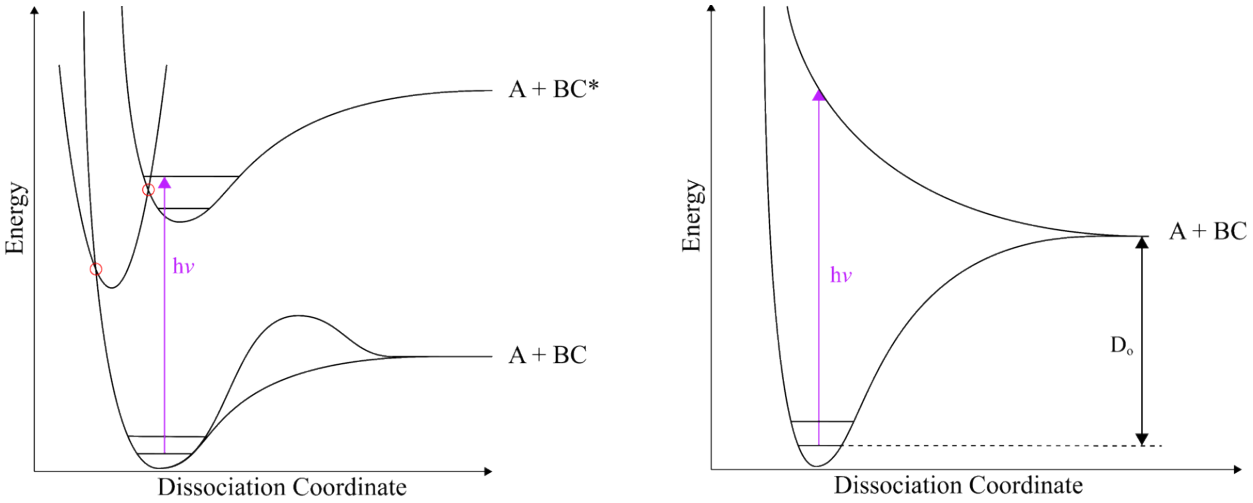

Figure 1.3: Schematic potential energy curves showing absorption of an ultraviolet photon and several states that may facilitate photodissociation. Crossings between states corresponding to the location of conical intersections are highlighted by red circles. In the left panel, the ground state is shown both with and without an exit barrier, whereas in the right panel only the barrierless curve is shown.

Various schematic potential energy curves for a model triatomic ABC are shown in Figure 1.3, highlighting some of the general aspects of photochemistry described above. A molecule in its ground vibronic state may absorb a photon and populate an excited state which is bound along the dissociation coordinate (left panel). Notice that the potential energy minima of the ground and excited states occur at different positions along the dissociation coordinate. The overlap between the nuclear wave functions for the two vibronic states connected by the photon is the Franck-Condon factor, $\langle \Psi_n^f | \Psi_n^i \rangle$. Following photoexcitation, a newly energized molecule may dispose of its energy in a number of ways; it need not dissociate at all if other deactivation mechanisms are much faster, or if it is unable to do so (e.g. if $E < D_o$ for bond energy D_o). Broadly speaking, there are two common non-dissociative relaxation mechanisms available to a photoexcited molecule: it may return to the ground or some other lower electronic state by emitting a photon via fluorescence; or, if connected to a bath, it may transfer its energy through repeated collisions until the energy is dispersed. The study of radiative[17] and collisional[18] deactivation each represent a significant segment of molecular physics inquiry, contributing enormously to our understanding of the behavior of chemical systems, but in general neither leads to dissociation. If instead a molecule does dissociate, some of the energy is consumed in breaking the chemical bond and the rest is distributed into the product degrees of freedom. There are a number of mechanisms through which dissociation may proceed, each contributing to a set of products with unique distributions of the available energy.

Photodissociation Mechanisms

The schematic potential energy diagrams shown in Figure 1.3 illustrate the common photodissociation mechanisms available to excited molecules. Dissociation may lead to both products formed in their ground electronic states, or to one or both products in an excited electronic state depending on the mechanism and on the coupling between different potential energy curves in the accessible region of the potential energy surface.

The excitation depicted in the left panel of Figure 1.3 forms an excited bound state with insufficient energy to overcome the bond energy in this state ($E < D_o$). If the photon energy were greater, dissociation from the upper bound state would result in at least one product being formed in one of its excited electronic states. Nevertheless, a molecule excited to this state can still dissociate by crossing between potential energy curves at the location of a conical intersection (CI). At a CI the electronic states become degenerate, the potential surface has a local double-cone topology in the multidimensional coordinates, and the Born-Oppenheimer approximation breaks down.[19,20] For our illustrative triatomic molecule a conical intersection occurs at a single point, but for an N-atom molecule the CI is actually a $(3N-8)$-dimensional seam in the full potential energy surface. While some conical intersections are required due to symmetry considerations, the importance of so-called 'accidental' intersections has increasingly been recognized, being more numerous but harder to locate (for researchers) without the guidance of symmetry constraints. The significance of conical intersections to photochemistry has prompted advances in both experimental and theoretical research in an attempt to better understand their influence on photochemical dynamics.

Conical intersections may connect the excited state to the ground state directly, or through successive intersections mediated by additional electronic states as depicted in Figure 1.3. The radiationless passage through these intersections from upper states to lower states is known as internal conversion, and the result is a molecule in its ground electronic state with a large amount of internal energy. The process by which the photon energy is distributed through the molecule is intramolecular vibrational redistribution (IVR): energy concentrated in specific modes by absorption and internal conversion becomes distributed amongst the other vibrational degrees of freedom via couplings between these modes.[21,22] The outcome of complete IVR is a molecule with a statistical distribution of energy amongst its internal modes. Dissociation then relies on statistical fluctuations in this internal energy distribution to concentrate an amount of energy $E \geq D_o$ into the dissociation coordinate. Since increasingly large energy concentrations have decreasing probability, dissociation from the 'hot' ground state potential yields products with generally low relative kinetic energies but high degrees of internal excitation, provided the photon energy is sufficiently greater than D_o.

For reactions with exit barriers along the dissociation coordinate, statistical fluctuations must overcome the barrier height in order to facilitate dissociation. Alternatively, quantum mechanical tunneling provides a means of traversing a barrier for energies below the barrier height. Tunneling processes will have slower rates as the potential barrier becomes wider, and the importance of tunneling would increase as the barrier width decreases closer to its apex. Regardless of how a molecule overcomes a potential barrier, the exit of the barrier

is characterized by a decrease in potential energy along the dissociation coordinate. This repulsive potential promotes greater relative kinetic energies of the photofragments, exerting a force on the fragments proportional to the gradient of the potential surface as they separate. The impulse exerted on the molecule along the repulsive portion of the barrier may also lead to excitation of molecular rotations and vibrations depending on the dissociation vector.

The right panel in Figure 1.3 shows another dissociation mechanism whereby photon excitation populates an excited state which is repulsive with respect to the dissociation coordinate. A molecule situated on the steeply repulsive potential shown here will have a very short lifetime in this state, and the rapidly formed products will be endowed with high relative kinetic energy and a correspondingly small degree of internal excitation. As with dissociation over an exit barrier, some excitation in certain molecular rotations and vibrations can still occur depending on the dissociation vector. Note that the repulsive state and ground state lead to the same ground state products along the dissociation coordinate shown.

The discussion above has made mention of how different dissociation mechanisms influence the kinetic and internal energy distributions of the photoproducts. Figure 1.4 shows model forms of translational energy distributions for these different mechanisms. Statistical ground state distribution for a barrierless reaction is peaked very close to zero relative translational energy, and the likelihood of a dissociation event producing larger kinetic energies decays quickly. Dissociation over an exit barrier is shown to result in the distribution peaking at higher E_T and leading to a broadening of the overall distribution. The fairly low energy of the peak of this distribution implies the exit barrier is of only moderate size. Finally, dissociation from the repulsive state yields very high kinetic energy fragments, with essentially zero likelihood of slow-moving products. The peak of this distribution roughly implies the energy difference between the product asymptote and the excited state energy.

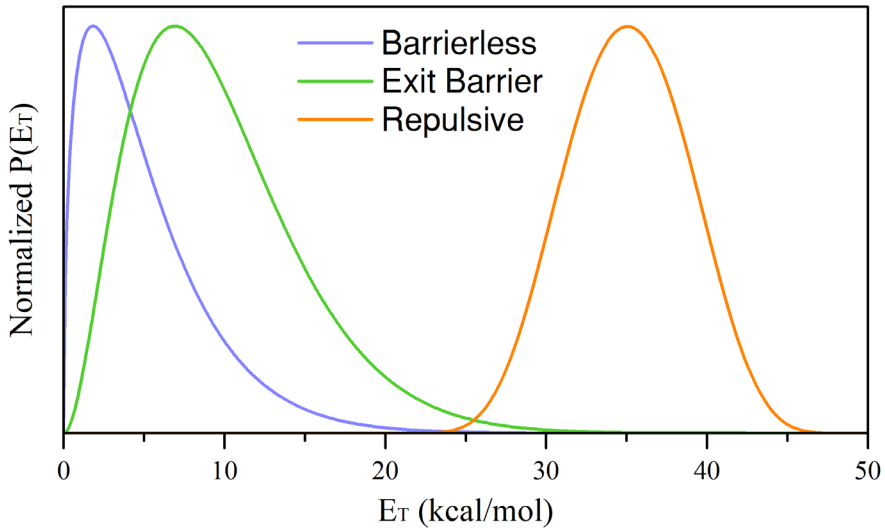

Figure 1.4: Model $P(E_T)$ distributions for dissociation from a bound state with and without an exit barrier, and from a repulsive state.

It is clear that although internal conversion to the ground state and direct dissociation from the repulsive state will produce identical products in our model system, the significant difference in their final quantum states presents an opportunity to distinguish these mechanisms. Greater detail around the manifestation of these dissociation processes within real molecular systems can be found in the chapters dealing with photodissociation dynamics in Part II, which contain distributions very similar to these examples given the observation of each of these mechanisms. The relationship between the unique mechanisms and the resultant product translational energy distributions forms the basis of photofragment translational spectroscopy, the technique used herein to study photodissociation dynamics of molecules.

Photofragment Translational Spectroscopy

To discuss the photofragment translational spectroscopy (PTS) technique, consider a reactant R that absorbs a photon and dissociates into fragment pairs A_n and B_n of the n^{th} reaction channel

$$R(r_i) \xrightarrow{\mathrm{h}\nu} R(r_f) \rightarrow A(a) + B(b)$$

where r_i and r_f are respectively the initial and final quantum states of reactant R during photon absorption, and a and b are the quantum states of products A and B respectively. The state-to-state rate constant $k_n^d\left(r_f \rightarrow a_n, b_n\right)$ determines how fast the photoexcited reactant dissociates into pairs of photoproducts. The formation of the reactant excited state during absorption, and its subsequent reaction to form fragments A_n and B_n, are fully described by the following system of differential equations:

$$\begin{aligned}
\frac{\mathrm{d}N_{\mathrm{R}}(\mathbf{v}_{\mathrm{R}}, \omega_{\mathrm{R}}, \mathbf{X}, r_f, t)}{\mathrm{d}t} &= \sum_i k_{if} N_{\mathrm{R}}(\mathbf{v}_{\mathrm{R}}, \omega_{\mathrm{R}}, \mathbf{X}, r_i, t) - \sum_n \sum_{a_n, b_n} k_n^d(r_f \rightarrow a_n, b_n) N_{\mathrm{R}}(\mathbf{v}_{\mathrm{R}}, \omega_{\mathrm{R}}, \mathbf{X}, r_f, t) \\
\frac{\mathrm{d}N_{\mathrm{A}_n}(\mathbf{v}_{\mathrm{A}_n}, \omega_{\mathrm{A}_n}, \mathbf{X}, a_n, t)}{\mathrm{d}t} &= \sum_{f, b_n} \int\limits_{\{\mathbf{v}_{\mathrm{A}_n}, \omega_{\mathrm{A}_n}\}} k_n^d(r_f \rightarrow a_n, b_n) N_{\mathrm{R}}(\mathbf{v}_{\mathrm{R}}, \omega_{\mathrm{R}}, \mathbf{X}, r_f, t) \mathrm{d}\mathbf{v}_{\mathrm{R}} \mathrm{d}\omega_{\mathrm{R}} \qquad (1.4) \\
\frac{\mathrm{d}N_{\mathrm{B}_n}(\mathbf{v}_{\mathrm{B}_n}, \omega_{\mathrm{B}_n}, \mathbf{X}, b_n, t)}{\mathrm{d}t} &= \sum_{f, a_n} \int\limits_{\{\mathbf{v}_{\mathrm{B}_n}, \omega_{\mathrm{B}_n}\}} k_n^d(r_f \rightarrow a_n, b_n) N_{\mathrm{R}}(\mathbf{v}_{\mathrm{R}}, \omega_{\mathrm{R}}, \mathbf{X}, r_f, t) \mathrm{d}\mathbf{v}_{\mathrm{R}} \mathrm{d}\omega_{\mathrm{R}}
\end{aligned}$$

In these rate equations, $N_Y(\mathbf{v}_Y, \omega_Y, \mathbf{X}, y, t)$ is the density of species Y with respect to laboratory-frame velocity $\mathbf{v}_Y$ and solid angle ω_Y, three-dimensional spatial coordinate $\mathbf{X}$, in quantum state y at reaction time t. Quantities in curly braces under the integral indicate constraints placed on the integration.

A typical PTS experiment measures the arrival time distribution of photofragment signal in the detector, and so yields none of the above quantities directly. The dissertation of Xinsheng Zhao provides a detailed description of how this system of equations is converted into a form concordant with the observables of a PTS experiment and outlines assumptions

that must be made about the experiment during this derivation.[23] The derived expression for the number density of a given photoproduct A_n is

$$N_{\mathrm{A}_n}(\mathbf{v}_{\mathrm{A}_n},\omega_{\mathrm{A}_n})d\mathbf{v}_{\mathrm{A}_n}d\omega_{\mathrm{A}_n} = \int_{\{\mathbf{v}_{\mathrm{A}_n},d\mathbf{v}_{\mathrm{A}_n},\omega_{\mathrm{A}_n},d\omega_{\mathrm{A}_n}\}} C_n^o P_n(E_{T,n},\Omega_n) N_R^o(\mathbf{v}_{\mathrm{A}_n},\omega_{\mathrm{A}_n})d\mathbf{v}_{\mathrm{A}_n}d\omega_{\mathrm{A}_n}dE_{T,n}d\Omega_n \tag{1.5}$$

where $N_R^o(\mathbf{v}_{\mathrm{A}_n},\omega_{\mathrm{A}_n})$ describes the initial population of all reactant states of molecules contained within the interaction region before irradiation; C_n^o describes the photon absorption and dissociation processes over the quantum state population in the molecular beam; $P_n(E_{T,n},\Omega_n)$ is the joint center-of-mass translational and angular distribution of the photoproducts; and the product of C_n^o and $P_n(E_{T,n},\Omega_n)$ yields the absolute number of dissociation events. A primary goal of most PTS experiments is to extract $P_n(E_{T,n},\Omega_n)$, as the shape of this distribution directly encodes the detailed dissociation mechanism.

We now need to relate $N_{A_n}(\mathbf{v}_{A_n},\omega_{A_n})$ to the distribution of photofragments entering a detector with solid angle ω_D as a function of arrival time t after traversing flight distance L between the interaction region and the detector, given by

$$N_{A_n}(t,\omega_D)\mathrm{d}t = \left(\int_{\{\omega_D\}} N_{A_n}(\mathbf{v}_{A_n},\omega_{A_n})\left|\frac{\delta\mathbf{v}_{A_n}}{\delta t}\right|\mathrm{d}\omega_{A_n}\right)\mathrm{d}t \tag{1.6}$$

where $\mathrm{v}_{A_b} = {}^{L}\!/_{t}$ gives the Jacobian for the velocity to time transformation

$$\left|\frac{\delta\mathbf{v}_{A_n}}{\delta t}\right| = \left|\frac{\delta}{\delta t}\frac{L}{t}\right| = \frac{\mathrm{v}_{A_n}}{t} \tag{1.7}$$

The distribution $N_{A_n}(\mathbf{v}_{A_n},\omega_{A_n})\mathrm{d}\mathbf{v}_{A_n}\mathrm{d}\omega_{A_n}$ is still defined in the molecular center-of-mass frame. To convert this expression from center-of-mass variables $(E_{T,n},\Omega_n)$ to laboratory frame variables $(\mathrm{v}_{A_n},\omega_{A_n})$ we use

$$E_{T,n} = \frac{1}{2}\frac{m_R m_{A_n}}{m_{B_n}}\mathbf{u}_{A_n}^2 \tag{1.8}$$

where m_Y is the mass of species Y, and the Jacobian transformation

$$\frac{\partial(\mathbf{u}_{A_n},\Omega_n)}{\partial(\mathbf{v}_{A_n},\omega_{A_n})} = \frac{\mathbf{v}_{A_n}^2}{\mathbf{u}_{A_n}^2} \tag{1.9}$$

is defined purely in terms of the center-of-mass frame velocity $\mathbf{u}_{A_n}$ and laboratory frame velocity $\mathbf{v}_{A_n}$. Thus, the time-of-flight distribution of photofragment A_n arriving at the detector is

$$N_{A_n}(t,\omega_D) = C_n^o\frac{v_{A_n}^3}{t}\frac{m_R m_{A_n}}{m_{B_n}}\int_{\{t,\omega_D\}}\frac{P_n(E_{T,n},\Omega_n)}{\mathbf{u}_{A_n}}N_R^o(\mathbf{v}_R,\omega_R)\mathrm{d}\mathbf{v}_R\mathrm{d}\omega_R\mathrm{d}\omega_{A_n} \tag{1.10}$$

Finally, the mass spectrometer detectors used in typical PTS experiments cannot directly measure the neutral photoproducts, and rely on ionization of the photofragments. The experiments described in this thesis use electron impact ionization to produce cations, where the ionization probability is a function of the fragment velocity:

$$\eta_{A_n}(\mathbf{v}_{A_n}) = \frac{\eta^o_{A_n}}{\mathbf{v}_{A_n}} \tag{1.11}$$

where $\eta^o_{A_n}$ is a constant that depends on the molecular properties of the fragment (e.g. its ionization cross section) and on the operation conditions of the ionizer (e.g. the chosen emission current). Taking this ionization term into account gives

$$N^+_{A_n}(t,\omega_D) = C^o_n \eta^o_{A_n} \frac{\mathbf{v}^2_{A_n}}{t} \frac{m_R m_{A_n}}{m_{B_n}} \int\limits_{\{t,\omega_D\}} \frac{P_n(E_{T,n},\Omega_n)}{\mathbf{u}_{A_n}} N^o_R(\mathbf{v}_R,\omega_R)\mathrm{d}\mathbf{v}_R\mathrm{d}\omega_R\mathrm{d}\omega_{A_n} \tag{1.12}$$

which describes the relationship between the center-of-mass joint translational and angular distribution, which characterizes the photochemical reaction and the measured arrival time distribution of ions produced from photofragments entering the detector.

In practice, the $P_n(E_{T,n},\Omega_n)$ distribution is constructed by guessing its form and performing a forward convolution to produce a simulated time-of-flight spectrum. This guess is iteratively updated until the simulation provides satisfactory agreement with the time-of-flight distributions of all photofragments measured in the experiment. To simplify this process, the assumption is made that the joint distribution for channel n can be decoupled into separate translational energy and angular distributions:

$$P(E_T,\Omega) = P(E_T)I(\Omega) \tag{1.13}$$

Given a known form of $I(\Omega)$, only the translational energy distribution, $P(E_T)$ needs to be guessed. For one-photon electric dipolar transitions described herein, $I(\Omega)$ takes the form of a dipole radiation pattern[24]

$$I(\Omega) = \frac{1}{4\pi}\left[1 + \beta \mathrm{P}_2(\cos\Omega)\right] \tag{1.14}$$

where $\mathrm{P}_2(a) = 1/2\,(3a^2-1)$ is the second Legendre polynomial and β is the anisotropy parameter. The value of β ranges from -1 to 2, yielding respectively a $\sin^2\Omega$ and a $\cos^2\Omega$ angular distribution. These two limiting values correspond respectively to electronic transitions where the transition dipole moment μ is aligned perpendicular and parallel to the dissociation vector within the molecule. Many experiments find $\beta = 0$, corresponding to an anisotropic angular distribution. This is usually an indication that the dissociation timescale exceeds the timescale of molecular rotations (typically $\sim 10^{-11}$–10^{-10} s), resulting in the excitation and dissociation vectors becoming uncorrelated.

Secondary Dissociation

The discussion above concerns the dissociation of a molecule induced by absorption of a single photon by that same molecule. At the ultraviolet wavelengths used in this study, photons may contain energies in great excess compared to the strength of chemical bonds. If the internal energy contained within a photofragment after dissociation exceeds bond strengths within that molecule then dissociation will occur in the absence of other relaxation mechanisms:

$$\begin{aligned} ABC &\xrightarrow{\mathrm{h}\nu} AB^* + C \\ AB^* &\longrightarrow A + B \end{aligned}$$

In this reaction scheme, AB^* is a photofragment containing enough internal energy to dissociate further, and this process is referred to as spontaneous secondary dissociation.

Another possible source of secondary photofragments exists when the primary photoproducts are able to absorb the same laser wavelength used for excitation of the original reactant molecule. If the primary photodissociation process takes place within the duration of the laser pulse, then products of the primary photochemical reaction are exposed to photons that they may absorb, potentially leading to further dissociation:

$$\begin{aligned} ABC &\xrightarrow{\mathrm{h}\nu} AB + C \\ AB &\xrightarrow{\mathrm{h}\nu} A + B \end{aligned}$$

This process is referred to as secondary photodissociation, and the degree to which it occurs depends on properties of the molecule (e.g. their state-specific absorption cross-sections) and on the experimental conditions (e.g. laser intensity, pulse duration, etc.).

A detailed explanation of how the rate equations governing these processes are converted into expressions related to directly observable quantities in a PTS experiment has also been described in detail previously.[23,25] In either case, if a primary photofragment A_n produces secondary photofragments via the w^{th} secondary dissociation channel

$$A_n \rightarrow G_{nw} + H_{nw}$$

the secondary photofragment time-of-flight distribution is described according to

$$\begin{aligned} N^+_{G_{nw}}(t,\omega_D) = C^o_{nw} C^o_n \eta^o_{G_{nw}} \frac{\mathbf{v}^2_{G_{nw}}}{t} \frac{m_R m_{A_n}}{m_{B_n}} \frac{m_{G_{nw}} m_{A_n}}{m_{H_{nw}}} \int\limits_{\{t,\omega_D\}} P_n(E_{T,n},\Omega_n)\mathbf{u}_{A_n} \cdot \\ \frac{P_{nw}(E_{T,nw},\Omega_{nw})}{\mathbf{u}_{G_{nw}}} N^o_R(\mathbf{v}_R,\omega_R)\,\mathrm{d}\mathbf{u}_{A_n}\,\mathrm{d}\Omega_{A_n}\,\mathrm{d}\mathbf{v}_R\,\mathrm{d}\omega_R\,\mathrm{d}\omega_R\,\mathrm{d}\omega_{G_{nw}} \end{aligned} \tag{1.15}$$

Although this expression describes both spontaneous secondary dissociation and secondary photodissociation, C^o_{nw} and $P_{nw}(E_{T,nw}, \Omega_{nw})$ are defined in each case according to different dynamical quantities that characterize the two processes. Note that the secondary dissociation process occurs in the center-of-mass frame of the dissociating primary photofragment rather than of the original reactant. The assumption is made that the secondary $P_{nw}(E_{T,nw}, \Omega_{nw})$ distribution is independent of the primary $P_n(E_{T,n}, \Omega_n)$ distribution, and the two distributions are convolved with one another during simulation of secondary photofragment time-of-flight spectra.

Illustrative Newton diagrams for secondary dissociation are shown in Figure 1.5 to highlight some of the features of this process. The left panel shows a cut through the three-dimensional Newton sphere of the primary photofragment, along with an example of a secondary dissociation vector originating from the primary photofragment and scattered towards the detector. The right panel shows a cut through the scattering plane, with the dashed black Newton circle arising from primary photodissociation. The orange circles represent secondary dissociation taking place along the full perimeter of the primary photofragment Newton circle, demonstrating the many contributions typically detected for a secondary dissociation reaction. In this example, only translational vectors of a single magnitude are considered. In reality, this process will occur across the surface of all Newton spheres generated by all possible primary product velocity vectors, subject to constraints required for energy and momentum conservation.

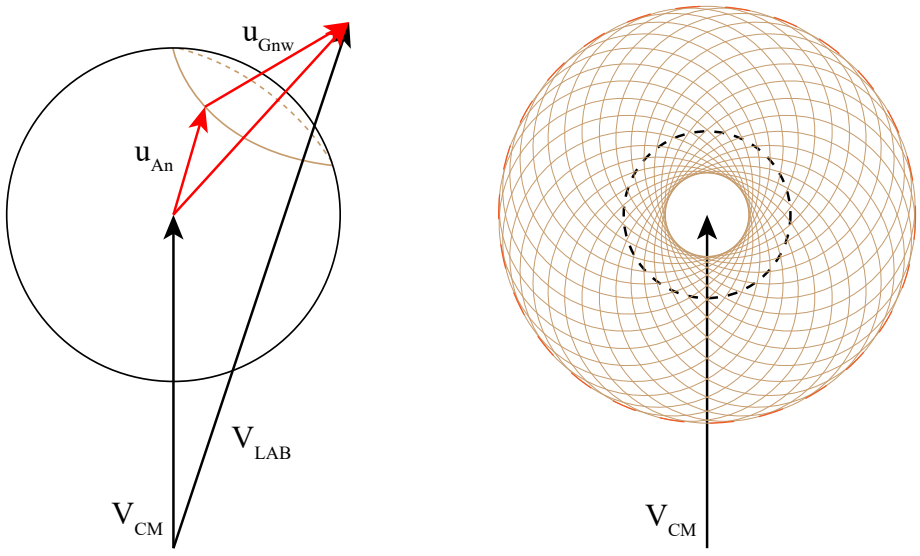

Figure 1.5: Kinematic diagrams for secondary dissociation processes. The left panel shows an arbitrary cut through the Newton sphere of the primary photofragment. The right panel shows a cut through the scattering plane, with the primary Newton circle shown in black and secondary Newton circles shown in orange.

Throughout the remainder of this dissertation, the quantity $N_Y^+(t, \omega_D)$ (any measured time-of-flight distribution) is simply referred to as $N(t)$. This is done for the sake of brevity and cleaner notation, since all time-of-flight spectra correspond to the detection of ionized photofragments, and since both the detected particle mass and the laboratory-frame scattering angles are specified for each spectrum.

1.3 Interfacial Chemistry and Surface Scattering

Heterogeneous reactions occur at phase boundaries, and are important in a number of different contexts. Of particular consequence for humanity is the chemistry taking place in the atmosphere, of which heterogeneous chemistry represents disproportionate importance. Molina and co-workers demonstrated that the reaction of chlorine nitrate ($ClONO_2$) at the surface of atmospheric ice crystals within polar stratospheric clouds is catalyzed in the presence of HCl.[26] The chlorine molecules thus produced lead to increased numbers of Cl radicals formed through Cl_2 photolysis:

$$\begin{aligned} HCl_{(s)} + ClONO_{2(g)} &\longrightarrow Cl_{2(g)} + HNO_{3(s)} \\ Cl_2 + h\nu &\longrightarrow 2\,Cl \end{aligned}$$

Chlorine and bromine radicals were already known to catalytically decompose ozone. A mechanistic understanding of the above reaction represented an important step in discerning the cause of the stratospheric ozone destruction in Earths atmosphere in the late twentieth and early twenty-first centuries.[27] While solid surfaces play an large role in myriad other heterogeneous processes, the surfaces of liquids are by no means less important.

The Liquid-Vapor Interface

Although enormously important in many contexts, and particularly in terrestrial atmospheric chemistry, the liquid-vapor interface can be a challenging system to study in detail. By virtue of the molecular flow properties of liquids, the surface of a liquid is a highly fluxional environment. It actively changes as particles strike and depart from it, rise up from or sink back into the bulk, and it undulates due to local molecular density fluctuations. Consider the clusters of 500 water molecules shown in Figure 1.6, generated from molecular dynamics (MD) simulations with temperatures at and well below the bulk freezing point of 273 K. The cluster at 273 K has many molecules residing off the periphery of the cluster proper – this behavior is due to the vapor pressure of water at its freezing point supporting moderate evaporation. The molecules at 240 K are held more closely to the surface as a result of the substantially reduced vapor pressure at this super-cooled temperature (the cluster is too small to freeze). In these clusters, it is not always clear which molecules correspond to the bulk and which to the interface, although in general it is manifestly more clear at 240 K than at 273 K.

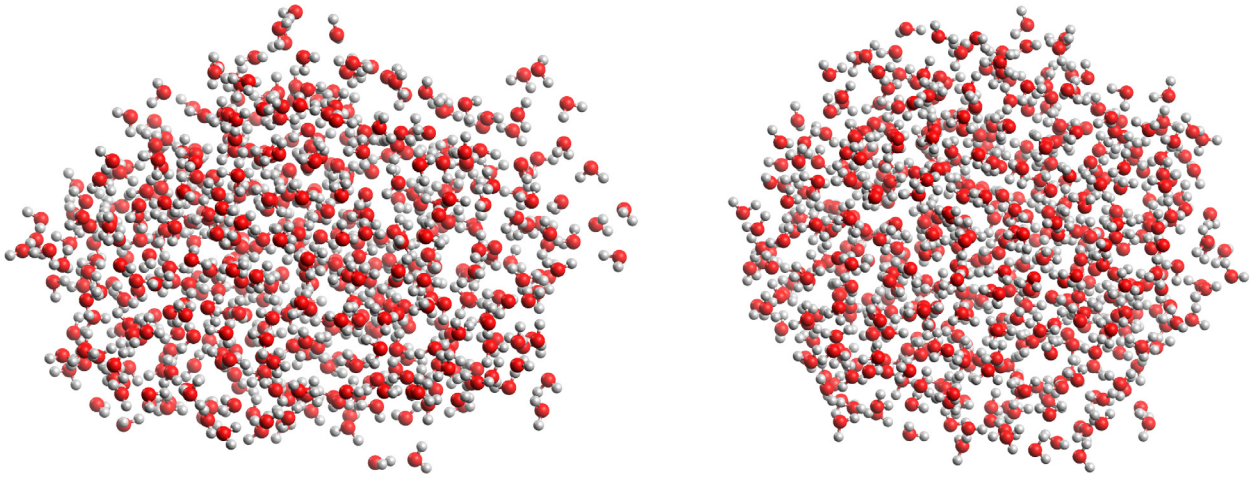

Figure 1.6: MD simulations of 500 molecule water clusters using the Amber99 force field[28] implemented in the Q-Chem 5.1 software package.[29] The 500 molecule input was equilibrated for 50 ps at 325 K to thoroughly randomize the structure (not shown), followed by 50 ps at 273 K (left), and finally 200 ps at 240 K (right). Thermal equilibration was achieved using Langevin thermostats applied over 1 fs time steps.

The clusters in Figure 1.6 represent a single snapshot in time, and are not well-suited to understanding the average properties of such a dynamic system. Taking a time-average as the structure evolves will produce an equilibrium density profile where density varies smoothly from the liquid density inside the cluster to the vapor density far away from the cluster. While the location of the interface is arbitrary, it is often defined in terms of the Gibbs dividing surface: a plane separating the limiting liquid and vapor density values at their midpoint in the density profile.[30,31] To better reflect fluctuations taking place across liquid surfaces, more realistic treatments define a non-planar instantaneous interface that varies over time as fluctuations perturb the surface.[32] The influence of such fluctuations on the surface geometry has significant implications for the dynamics undergone by particles incident on liquid surfaces, affecting their adsorption and scattering dynamics.[33,34]

An intriguing property of the interface is the fundamental asymmetry of its chemical environment. Reactivity at interfaces can differ substantially from the bulk phase as a result of this asymmetry, which may favor certain molecular orientations over others, modify diffusive transport rates, and result in local enrichment of molar composition.[35,36] Although chemistry in the bulk constitutes the bulk of chemistry, chemistry at the interface is anything but superficial.

Surface Accommodation and Desorption

Accommodation

When gas-phase molecules impinge onto a surface there is a chance that they will stick to or penetrate into the interface. This adsorption process is commonly referred to as 'accomomodation' in the atmospheric science community, and often as 'trapping' in the language of vacuum surface science. Particles residing at the interface will eventually thermalize with the surface, acquiring an internal energy distribution according to the characteristic temperature of the surface. For atmospheric aerosol particles, surface accommodation of volatile compounds is their primary growth mechanism, especially for water in response to increases in relative humidity.[37]

The accommodation of incident particles into a liquid is parameterized by the accommodation coefficient, α, given by the ratio of the number of molecules which enter the liquid phase to the total number which impinge upon the surface. The maximum flux, J, that can be accommodated into the surface is then

$$J = \alpha n \bar{v}/4 \tag{1.16}$$

where n is the number density of the vapor and $\bar{v}$ is average molecular speed describing an equilibrium system. The sticking coefficient can be determined by monitoring depletion of incident particles or an increase of these species in the liquid. Equation 1.16 is normalized per unit surface area, so knowledge of the interaction area of incident particles with the liquid is necessary to provide an experimental value for α.

Measurements of accommodation as liquid surfaces can be complicated by surface fluctuations as described above – at higher temperatures, larger fluctuations lead to increased roughening of the surface which result in greater accommodation of impinging particles as the exposed surface area and the chance to undergo multiple collisions with the surface increase.[33,34] Although the surface may be preferentially covered by some particles, any individual particle trapped at the surface will eventually either diffuse into the bulk liquid, or will desorb back into the vapor phase.

Desorption

Desorption describes the transfer of particles that reside in the interfacial layer into the surrounding vapor phase. For evaporation from liquids, it is expected that the desorbing particles will depart the surface with a Maxwellian velocity distribution corresponding to the surface temperature. In the following, it will be satisfactory to proceed using the speed distribution rather than the velocity distribution. The Maxwell speed distribution is usually encountered in the form

$$f(v) = n \left(\frac{m}{2\pi k_B T} \right)^{3/2} v^2 \exp\left[-\frac{m v^2}{2 k_B T} \right] \mathrm{d}v \tag{1.17}$$

where n is the gas density, k_B is Boltzmann's constant, T is the temperature and m is the mass of the particle. However, Equation 1.17 describes specifically the instantaneous distribution of speeds for particles contained within a volume of space. In order to describe the evaporation process, which involves molecules passing through a surface during an interval of time, the Maxwellian flux distribution is instead required:[38]

$$f(v,\theta) = n\left(\frac{m}{2\pi k_B T}\right)^{3/2} v^3 \cos\theta \exp\left[-\frac{mv^2}{2k_B T}\right]\mathrm{d}v \tag{1.18}$$

which depends on v^3 rather than v^2, and where the flux is proportional to $\cos\theta$ for departing velocities along angle θ relative to the surface normal.[39] The average energy of the flux distribution Equation 1.18 is $2RT$ compared to $3/2RT$ for Equation 1.17 – i.e. the evaporating particles are more energetic than those in an equilibrium gas. Note that Equation 1.18 as presented has already been normalized to flux per unit solid angle. The velocity distribution is converted to a time-of-flight distribution according to

$$N(t) = f(v)\frac{\mathrm{d}v}{\mathrm{d}t} \tag{1.19}$$

Once again, making use of the definition $v = L/t$ and the Jacobian transformation

$$\left|\frac{\delta v}{\delta t}\right| = \left|\frac{\delta}{\delta t}\frac{L}{t}\right| = \frac{L}{t^2}$$

the velocity-dependent distribution can be related to the expected time-of-flight distribution:

$$N(t) = n\left(\frac{m}{2\pi k_B T}\right)^{3/2} \frac{L^4}{t^5} \exp\left[-\frac{m}{2k_B T}\frac{L^2}{t^2}\right]\cos\theta \tag{1.20}$$

Finally, considering once again the velocity-dependent ionization behavior

$$\eta(v) = \frac{\eta^o}{v}$$

and factoring in the additional $1/v$ dependence thus imposed, the experimental time-of-flight spectrum becomes

$$N(t) = n\ \eta^o \left(\frac{m}{2\pi k_B T}\right)^{3/2} \frac{L^3}{t^4} \exp\left[-\frac{m}{2k_B T}\frac{L^2}{t^2}\right]\cos\theta \tag{1.21}$$

where the overall measured intensity is weighted by a factor of $\cos\theta$ depending on the observation angle.

If the corresponding translational energy distribution $P(E_T)$ is desired it may be readily obtained by direct inversion of an $N(t)$ distribution:

$$P(E_T) \propto t^2\ N(t) \tag{1.22}$$

and using the definition $E_T = {}^1\!/_2\ m\ ({}^L\!/_t)^2$. For Maxwell-Boltzmann desorption, the translational energy distribution is[40]

$$P(E_T) = \frac{E_T}{(RT)^2}\ \exp\left[-\frac{E_T}{RT}\right] \tag{1.23}$$

which represents a useful comparison to experimental data on desorbing species.

While the desorption of molecules from liquid surfaces dynamically interesting in its own right, it also presents a significant impediment to the ability to probe liquid surfaces via molecular scattering. Volatile liquids have vapor pressures high enough to represent an appreciable desorption flux, and placing such liquids in a vacuum environment establishes a thick sheath of high-density vapor above the liquid surface. This vapor sheath has a low enough density to transmit photons and photoelectrons of most energies,[41] but the much larger scattering cross-sections of atoms and molecules make molecular beam experiments challenging. Sections presented later in this dissertation describe various strategies aimed at minimizing the number of collisions experienced during evaporation and scattering experiments.

Surface Scattering

The above discussion concerns molecules which adsorb onto surfaces, and which may eventually desorb from them. An incident molecule need not be accommodated by the surface at all, and may instead recoil back into the vapor phase following the collision. Scattering reactions at the liquid interface allow us to probe the structure, properties, and reactivity of liquid-vapor interface. One of the most fundamental questions we can ask about a collision between a gas-phase particle and a liquid surface concerns how much energy is transferred during the collision. The simplest model for describing energy transfer treats the surface as a collection of hard cubes, each with an effective surface mass m_{surf}. The energy transfer, $\Delta E = E_i - E_f$, during a collision is given simply by[42]

$$\frac{\Delta E}{E_i} = \frac{4\mu}{(\mu+1)^2} \tag{1.24}$$

where E_i is the kinetic energy of the incident gas particle, and μ is the mass ratio of the colliding partners, ${}^{m_g}\!/_{m_{surf}}$. While providing qualitatively good predictions of gas-surface collision dynamics and capturing many overall trends, major shortcomings of this model include its treatment of the surface as perfectly smooth and rigid, devoid of intermolecular interactions, and only allowing for energy transfer normal to the surface.

Real scattering systems in general have collision partners which both contain internal degrees of freedom, and from the description of the interface given above it should be clear that the surfaces are typically not smooth, and will be compliant to some degree under the impact of incident particles. The soft-sphere kinematic model for energy transfer is developed to include these effects during gas-liquid collisions:[43]

$$\frac{\Delta E}{E_i} = \frac{2\mu}{(\mu+1)^2}\left[1 + \mu\sin^2\chi + \frac{E_{int}}{E_i}\left(\frac{\mu+1}{2\mu}\right) - \cos\chi\sqrt{1-\mu^2\sin^2\chi - \frac{E_{int}}{E_i}(\mu+1)}\right] \quad (1.25)$$

where the deflection angle χ is the angle between the incident and scattered velocity vectors (see Figure 1.2), and E_{int} is the internal excitation imparted to the surface molecules during the collision. Note that m_{surf} (the denominator in the definition of μ) is not a quantity that is readily available *a priori*. For example, in the scattering of Ar atoms at the surface of squalane (a $C_{30}H_{62}$ alkane), m_{surf} is found to be 162 amu, whereas squalane has a molecular weight of ∼423 amu.[43] Furthermore, in similar collisions with hydrocarbon and fluorocarbon self-assembled monolayers (often used as proxies for true liquids), m_{surf} is greater for the hydrocarbon surface despite fluorine atoms being 19 times heavier than H atoms. Moreover, m_{surf} varies with quantities such as the kinetic energy of the incident particle and whether the scattered products are detected within or outside of the scattering plane. The collision is best thought of as

Thus, m_{surf} must usually be determined experimentally from a plot of $\Delta E/E$ vs. χ using μ and E_i as fitting parameters. Using the Newton diagram vector analysis shown in Figure 1.2 for experimental scattering data does indeed find that impulsively scattered signal lies along a circle arc whose origin is taken to be the center-of-mass as for crossed-beam scattering.[43] By combining the known incident particle mass and velocity with the center-of-mass velocity obtained from the above analysis it is trivial to obtain m_{surf}. Knowledge of m_{surf} also provides the center-of-mass collision energy, and thus the amount of energy transferred to internal excitation of the surface and scattered particle, $E_{int} = E_{COM} - E_T$.

Experiments in the Nathanson and other groups have found that most TOF spectra can be simulated by a two-component distribution including thermal desorption (TD) and faster, "impulsive"- or "inelastic"-type scattering (IS) features:

$$P(E_T) = \alpha P_{TD}(E_T) + (1-\alpha)P_{IS}(E_T) \quad (1.26)$$

where $P_{TD}(E_T)$ is given by Equation 1.23, allowing for the commonly encountered scenario in which a fraction of the incident particles become trapped and thermalize prior to departing the surface. In practice, the IS scattering component is often simply taken to be the difference between the $P(E_T)$ producing the best simulation to measured data and the $P_{TD}(E_T)$ component.

1.4 Liquids in Vacuum

Vacuum-compatible liquid sources

The development of good vacuum systems allowed molecular beams to find use in characterizing the interactions between gases and condensed phase surfaces. Early work focused on solid surfaces, which had relevance to ongoing development of high-vacuum techniques

Table 1.1: Vapor pressures of select liquids.

Liquid	**P_{vap} (Torr)**
Krytox (perfluoropolymer)	10^{-13}
Sn, Ga, In (500 K)	10^{-11}-10^{-9}
Squalane ($C_{30}H_{62}$)	10^{-8}
70-99% H_2SO_4	10^{-4}
Glycerol	10^{-4}
Salty water (LiBr)	10^{-3}-10^{-1}
Dodecane ($C_{12}H_{26}$)	10^{-1}
Water	18
NH_3 (200 K)	75
^{4}He (4.2 K)	760

and aerospace design and were relatively easy samples to prepare.[44] Extending this type of inquiry to liquid surfaces in general was a much more difficult challenge owing to the large vapor pressures exhibited by many liquids (see Table 1.1, spanning 17 orders of magnitude, and all of which have been studied in vacuum).

Liquid metals and polymer melts are fairly simple to prepare and represent the initial foray into desorption and gas-liquid scattering studies. Excellent vacuum levels are readily achievable by simply placing an open reservoir of these liquids inside of a chamber. These experiments have provided important details about physical interactions and energy transfer processes involved when particles impinge on the non-rigid surfaces of liquids. This class of readily accessible liquids has recently been broadened with the inclusion of modern room-temperature ionic liquids, and continues to be an area of active research.[45–47]

The real technical problems begin to arise when the liquid vapor pressure begins to compromise the ability to maintain adequate vacuum levels, perhaps about 10^{-5} Torr (about 10^{-3} Pa) as a somewhat arbitrary threshold. A means to circumvent this problem was introduced by Sandra Lednovich and John Fenn (of supersonic molecular beam fame) in 1977 in the form of a wetted wheel.[48] By partially submerging a rotating disc in liquid it is possible to expose a continuously renewed, clean sample of liquid to a vacuum chamber through a small aperture. In doing so, the limit of accessible vapor pressures is increased to perhaps $\sim 10^{-3}$ Torr, and many small molecular liquids become feasible targets.

In order to study high vapor pressure liquids, even the wetted wheel technique becomes insufficient. The key to unlocking high volatility liquids is to produce diminutive jets of free-flowing liquid, pioneered by Manfred Faubel and typically referred to as liquid microjets.[49] With careful consideration of experimental design, microjets can in principle be used to

study liquids of almost arbitrary vapor pressure. Perhaps most importantly, liquid jets of water either neat or containing solutes can be subjected to a wide array of powerful vacuum analytical techniques.

Cylindrical jets

Liquid microjets are most commonly encountered as cylindrical filaments formed by forcing pressurized fluid through a capillary with a circular orifice. Being relatively well-studied (compared to flat jets), analytical expressions exist for the distance such jets travel before hydrodynamic forces cause their breakup, as well as how much evaporative cooling occurs within the chamber. Because of the greater body of literature studying cylindrical jets, and to make comparisons to the data acquired from flat jets, it is sometimes desirable to generate liquid cylindrical jets in our laboratory.

As indicated earlier, the greatest challenge associated with volatile liquid jets is the significant evaporative cooling they undergo. For water, cooling rates in excess of 10^5 K/s are the norm.[50,51] This cooling results in large quantities of gas admitted to the vacuum environment, as well as potentially supercooling the liquid, which then has a tendency to freeze onto any surface it encounters. For a cylindrical jet traveling through a vacuum chamber, the evaporative cooling along the length of the flow direction z of the jet is given by[49,52]

$$\frac{dT}{dz} = -\sqrt{\frac{32m}{\pi RT}}\frac{\Delta H_{vap}(T)P_{vap}(T)}{C_p(T)\rho(T)r_{jet}v_{jet}} \tag{1.27}$$

where m is the molecular mass, R is the gas constant, T is the temperature, $\Delta H_{vap}(T)$ is the enthalpy of vaporization, $C_p(T)$ is the heat capacity, $P_{vap}(T)$ is the vapor pressure, $\rho(T)$ is the liquid density, r_{jet} is the jet radius, and v_{jet} is the jet velocity. Although many of these quantities are functions of the changing temperature, values at a single reference temperature are usually sufficient since $\rho(T)$ and the ratio $\Delta H_{vap}(T)/C_p(T)$ change very little over fairly wide temperature ranges, as noted previously.[50] Incorporating the temperature dependence of $P_{vap}(T)$ will be required for accurately modeling jet cooling depending on the initial conditions, since this quantity varies more strongly over certain temperature ranges. To illustrate this, the left panel in Figure 1.7 shows predictions from Equation 1.27 for a cylindrical jet cooling under its temperature-dependent vapor pressure compared to the unrealistic scenario where cooling always occurs according to the 273 K vapor pressure of 4.6 Torr. The latter predicts (incorrectly) liquid temperatures some 50 K colder over the computed distance. The right panel of Figure 1.7 shows a comparison of the cooling of volatile water, slightly volatile dodecane, and non-volatile squalane: dodecane undergoes an almost imperceptible cooling, while squalane cooling is essentially non-existent. Under most flow conditions these jets break up within just a few millimeters of travel due to hydrodynamic instabilities.[52]

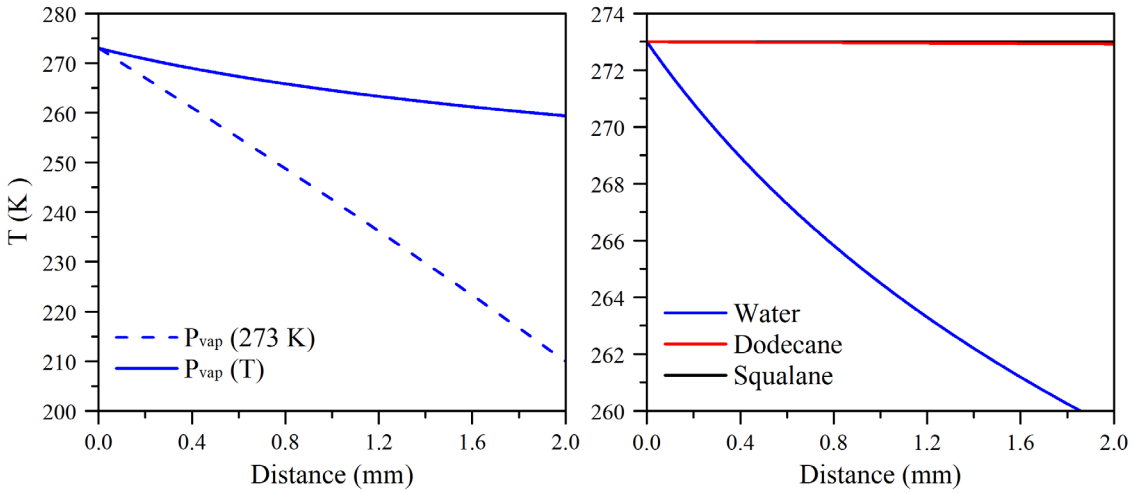

Figure 1.7: Evaporative cooling for cylindrical microjets (r_{jet} = 12.5 μm, v_{jet} = 20 m/s). The left panel shows the effect of incorporating the changing vapor pressure of water as the jet cools, instead of using a reference value. The right panel shows water, dodecane, and squalane microjets cooling according to their temperature-dependent vapor pressures (note the change of the temperature scale).

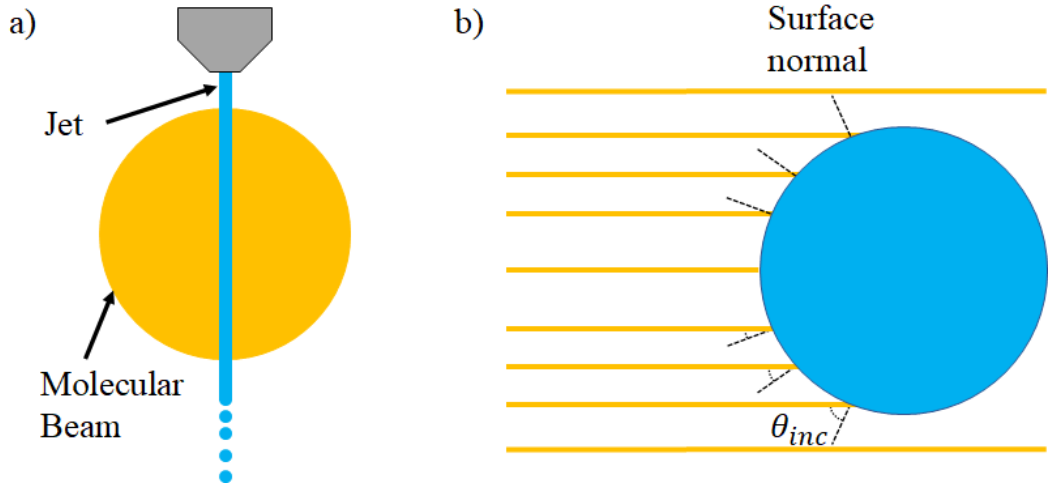

Figure 1.8: (a) Spatial mismatch between liquid jet and molecular beam, and (b) broad range of incident angles on a cylindrical surface.

Despite making important contributions to understanding evaporation, sticking, and scattering dynamics at the surfaces of volatile liquids, cylindrical jets are not ideal for molecular beam scattering experiments owing to spatial mismatching between the beam and jet, as well as the lack of a well-defined incident angle θ_{inc} onto the liquid surface (Figure 1.8). For typical microjet and molecular beam sizes the area ratio $^{A_{MB}}/_{A_{jet}} \approx$ 50-100, and impacting a cylindrical surface gives $\langle\theta_{inc}\rangle = 33^o \pm 22^o$. In principle these issues can be avoided by using a molecular beam much smaller than the liquid jet, but signal levels would be undetectable in almost all cases. The solution to both of these problems is to use a liquid flat jet.

Flat jets

Creating liquid jets with 'flat' geometries is not a new idea – fluid dynamicists have expressed formal interest in characterizing the flow behavior of colliding liquid jets and of liquids emanating from elliptical and rectangular orifices with large aspect ratios since as early as 1833.[53] The formation and breakup of liquid sheets has relevance to varied practical applications ranging from dye laser design[54,55] to any process involving atomization of liquid sprays such as irrigation, fuel combustion, and aerosol sprayers.[56,57]

Spectroscopic characterization of samples in the soft X-ray to extreme ultraviolet has driven the more recent adoption of volatile liquid flat jets for vacuum analytical experiments owing to the significant opacity of liquids at these wavelengths. Flat jets were initially prepared as vacuum-compatible X-ray targets by colliding two cylindrical microjets into each other at an oblique angle.[58] Conservation of momentum in the fluid causes it to spread out into a comparatively large, thin, leaf-like structure in the plane perpendicular to the two liquid filaments.[59] Surface tension draws liquid from the sheet into thick rims of cylindrical cross-section that bound the sheet and eventually pull the liquid back in on itself. This functions like a subsequent collision of two 'liquid filaments,' and a chain of progressively smaller leaves are formed until surface tension can no longer be overcome or until the jet breaks up. Liquid sheets can be made several millimeters in size, with micrometer to sub-micrometer thickness. The major drawback of colliding cylindrical jets is the potential for misalignment of the filaments with respect to one another, or obstructions altering the flow rate through one or both nozzles. Misalignment or obstruction invariably results in large liquid volumes spraying into the vacuum chamber and compromising the vacuum environment.

Integration of the fluid channels into a solid 'chip' substrate with converging channels eliminates any potential for misalignment. Convergence may occur through two separate channels that merge with one another, or through a single channel that tapers towards the nozzle exit. In either case the physical formation of the liquid sheet structure is analogous to the case of colliding free liquid streams: as the fluid flow converges in the nozzle exit the liquid is forced into the transverse plane, and surface tension acts as described above.

A fluid dynamical description of the flow properties of flat jets is more complicated than their cylindrical counterparts, and most descriptions of the geometry of flat jets rely on empirical relations. Experimental relations established by Santiago and co-workers[60] between nozzle geometry, flow conditions, and jet size are helpful in providing jet dimensions while

removing the need for computational fluid dynamics simulations using the Navier-Stokes equations. These empirical relations for the maximal jet length l_{max} and width w_{max} are:

$$l_{max} = 0.23\ d\ \mathrm{We}_e\ \mathrm{Ca}_e^{-0.1}(1+1.5\alpha^2)^{-0.5}\ \left[1+\cot(0.67\ \theta)\right]^{-0.5} \tag{1.28}$$

$$w_{max} = 0.074\ d\ \mathrm{We}_e\ \mathrm{Ca}_e^{-0.2}(1+1.5\alpha^2)^{-1}\ \left[1+\cot(0.67\ \theta)\right]^{-1} \tag{1.29}$$

In the above expressions, d and w_o are the width and depth of the liquid nozzle orifice and $\alpha = d/w_o$ its aspect ratio, θ is the convergence angle of the liquid relative to the jet flow axis, and the Weber number $\mathrm{We}_e = \rho Q^2/\sigma d^2 w_o$ accounts for the influence of surface tension, while the capillary number $\mathrm{Ca}_e = \mu Q/\sigma d w_o$ further incorporates effects of viscosity on the flow dynamics. Within We_e and Ca_e, ρ is the liquid density, σ is the surface tension, Q is the volumetric flow rate of the liquid, and μ is the dynamic viscosity. Additionally, the thickness profile $h(z)$ along the jet center-line is given by

$$h(z) = 0.36\ \frac{d\ w_o}{z}\ (1+1.5\alpha^2)\ \left[1+\cot(0.67\ \theta)\right] \tag{1.30}$$

These scaling relations for the jet sheet size and thickness profile are validated for ethanol, water, and ethylene glycol/water mixtures over a large range of flow rates, collision angles and nozzle aspect ratios, and consequently over a large range of Reynolds, Weber, and capillary numbers. A very robust correlation is achieved within these ranges.

An expression describing the evaporative cooling of flat jets does not seem to be available in the literature. One would expect that the much larger surface area exposed by a flat jet will result in more substantial cooling of the liquid. Experimental observations support this expectation,[58] with water flat jets contributing a vapor throughput into the vacuum chamber approximately 3-4 times greater than an isolated pair of cylindrical jets, while exposing a surface area approximately 3-4 times larger than such a pair. As a cautionary note, this crude measure of evaporation should only be used to develop a rough sense of a jet's thermal properties owing to the complex flow taking place within a flat jet as the thinning sheet of fluid is subsumed into the thick bounding rims.

Jet instabilities and breakup

The breakup of liquid jets has arisen several times in the preceding sections, occurring through varied and sometimes visually spectacular mechanisms (see the fishbone instability[61]). While a detailed description of liquid jet breakup modes is beyond the scope of this work and the expertise of this author, a brief mention of key instabilities is warranted. The most important breakup mode for the cylindrical microjets under the present experimental conditions is due to the Plateau-Rayleigh instability.[62–66] The amplitude of random sinusoidal perturbations grows as the jet travels, leading to periodic bulges and contractions in the cross-sectional area of the filament. Surface tension increases the amplitude of these oscillations, minimizing surface energy by further shrinking the neck of the contracted sections. This capillarity eventually results in the neck pinching off, producing a train of separated liquid

droplets. In the case of flat jets, it has also been noted that the largest amplification factors belong to short-wave instabilities caused by viscosity stratification across the sheet due to the non-uniform temperature profile established by evaporative cooling.[67] Aside from the growth of perturbations due to white-noise fluctuations, imperfections in the nozzle aperture may also produce instabilities that can propagate through the jet structure.

Many studies prominently discuss instabilities of the Kelvin-Helmholtz type[64,65] brought about by interactions of a liquid surface with quiescent or moving ambient gas, important for practical applications of liquid jets. These phenomena are not relevant to the liquid jets flowing through a vacuum environment in this work. Developing a refined understanding of the fluid dynamics of these jets is a significantly involved affair, and is not particularly important for the experiments described herein. The main takeaway should be that there are many geometrical variations in the experimental setup that can alter the shape and size of the jet, but jets cannot be produced with arbitrary dimensions. As an important consequence of this, the final temperature achievable in a jet will always face limitations due to the inability to undergo an arbitrary degree of evaporative cooling before it fragments. Indeed, the cooling process itself has been attributed as the cause of the principal instability affecting fluid sheets in vacuum.

1.5 Neutral Free Radicals

Molecular species exhibiting high reactivity have always held a place of interest for scientists. While many aspects of molecular physics and chemistry can lead to pronounced reactivity, neutral free radicals in particular possess a great propensity to react with the environment surrounding them. Both because of and despite their high reactivity, radicals are important in many different fields and processes, including atmospheric chemistry, combustion, planetary science and astronomy, industrial activities, and in biology. A brief flavor of these is provided here through select examples, while others are included in various chapters of this dissertation.

Earth's atmosphere is a dynamic system comprising a large number of different species engaged in rich chemical interplay. Ultraviolet photochemistry is ultimately responsible for the production of most of these radicals, often directly at higher altitudes and indirectly at lower ones. An important radical reaction in the stratosphere is the interconversion between oxygen and ozone, initiated by ultraviolet light and mediated by collisions with other molecules. Ozone in the troposphere also features prominently in other radical processes,[68] for example

$$\begin{aligned} NO_2 + O_3 &\longrightarrow NO_3 + O_2 \\ NO_3 + NO_2 + M &\rightleftharpoons N_2O_5 + M \end{aligned}$$

where M is any third-body collision partner (typically O_2 or N_2). The NO_2 and NO_3 species are both radicals important to tropospheric pollution.

The N_2O_5 product in the above reaction scheme has further implications for atmospheric chemistry, able to promote acid-rain formation by reacting heterogeneously with water to form two equivalents of nitric acid, HNO_3.[68] Heterogeneous reactions are of enormous importance to atmospheric chemistry because of the complexity of the chemical environment and potential for catalysis in surface coatings and aerosol particles. Atmospheric radicals including NO_3, OH, O_3, and Cl may rebound from, stick to, or react with aqueous and organic interfaces they come into contact with. Organic molecules in particular are subject to oxidation through H-abstraction or addition pathways, depending on their structure and the presence of unsaturated functional groups. Both of these reactions produce organic radicals, further contributing to the dizzying array of molecules driving aerosol chemistry. A less geocentric bias might prompt one to instead highlight the atmospheric importance of the chloroformyl peroxyl radical to Venus,[69] the methyl radical to Titan,[70] or the sulfur monoxide radical to Io.[71] Radicals play an even more prominent role in the rarefied environments around comets and in the interstellar medium,[72] as well as in the circumstellar envelopes of carbon-rich asymptotic giant branch stars.[73]

Radical reactions also feature prominently in hydrocarbon combustion, where a vast number of aliphatic and aromatic radicals are produced that contribute to soot formation.[74] Combustion can be considered in terms of two very general phases, beginning with low-temperature autoignition (∼600-900 K) and progressing into the high-temperature regime (>1100 K), which primarily differ in their prevailing chemistry and respective rate-limiting processes.[75] The necessary presence of oxidizing species such as O_2 and OH in the combustion chamber leads to H-abstraction and addition reactions that are critical for starting the combustion process. Addition reactions of O_2 during low-temperature combustion have been extensively studied for their role during low-temperature autoignition in converting hydrocarbons with radicals at one site ($R^\bullet$) into increasingly oxygenated species with radicals at other sites ($Q^\bullet$).[76] This takes place through successive oxidative additions and internal H-abstractions: $R^\bullet \rightarrow ROO^\bullet \rightarrow {}^\bullet QOOH \rightarrow {}^\bullet OOQOOH \rightarrow HOOQ^\bullet OOH$. Such pathways ultimately contribute to chain-branching by liberating up to two highly reactive OH radicals from each $HOOQ^\bullet OOH$, from which subsequent abstraction reactions are key drivers of autoignition.

In the high-temperature combustion regime, the internal energy of molecules becomes great enough to induce spontaneous decomposition of hydrocarbon radicals in addition to the abstraction/addition reactions described above. A prominent decomposition pathway of nascent hydrocarbon radicals is β-scission, where a bond adjacent to the radical site is homolytically cleaved. In alkyl radicals, typical bond energies for C_β–C_γ and C_β–H are on the order of just 20-35 kcal/mol and 35-45 kcal/mol respectively.[75] In fact, it is by this means whereby combustion actually converts much of the aliphatic species into conjugated and aromatic ones – the decomposition of alkyl species leads to unsaturated groups that proliferate since their bond energies are typically much higher than for their saturated counterparts, and thus more resilient to decomposition or abstraction reactions. In this way, radical reactions may produce increasingly large unsaturated molecules, resulting in soot formation and poor combustion efficiencies. Without the requisite mechanistic understanding to control the

reactions characterizing both low-temperature autoignition and high-temperature combustion, their products are invariably discharged into the atmosphere. More recently, the application of neural-network based molecular dynamics simulations have shown promise in generating complex combustion reaction networks, providing evidence for new reaction pathways and illuminating areas warranting greater focus within the experimental community.[77]

As a final example, industrial manufacturing processes also employ radical chemistry to create modern technology. Consider chemical vapor deposition used to grow metallic and semiconductor materials used for computing and sensor architectures. Silicon films grown in silane (SiH_4) plasma must contend with the chemistry of SiH_{1-3} and Si_2H_{1-5} radicals.[78] A similar situation prevails for germanium films grown from GeH_4 derivatives,[79] in addition to many more.[80,81]

1.6 Systems Discussed

The systems explored in this work represent a varied cross-section of different classes of molecules and processes. Ultraviolet photodissociation studies were carried out on fulvenallene and the fulvenallenyl radical, the methylsulfinyl radical, and the cyclohexyl radical, with both ground and excited electronic state photochemical dynamics observed across these systems. In the second part of this work, evaporation from neat water and dodecane microjets was studied for these solvent molecules, as well as dissolved gases contained in these liquids. The speed and angular distributions of the desorbing particles were characterized in these evaporation experiments. Finally, the scattering configuration of the apparatus was validated by scattering He, Ar, and N_2 from a silicon wafer, and He scattering from the surface of a water flat jet was successfully measured.

Chapter 2

Experimental

The photodissociation and surface scattering experiments described here were conducted using the same crossed molecular beam machine, with relevant modifications to enable each type of experiment. This section describes the apparatus and highlights differences between the two experiment types. Very broadly, the layout and operation of the vacuum chambers for the different experiments is described, including techniques for generating molecular and laser beams and liquid jets, along with their interaction geometries. Relevant calibration and alignment procedures are also described for each component of the apparatus. The modularity of components needed for the different experiments makes switching between the two relatively straightforward.

2.1 The Crossed Beam Machine

History

The crossed molecular beam scattering apparatus was developed by Yuan T. Lee in 1968 during his tenure as a postdoctoral fellow at Harvard under the guidance of Dudley Herschbach.[11] On his acceptance of a faculty position at University of California Berkeley, Lee brought the machine with him to begin a spectacularly successful research program interrogating the fundamental interaction dynamics during atomic and molecular collisions.[82] Expanding this research, Cheuk-Yiu Ng in 1974 drafted the blueprints for the second iteration scattering chamber, Machine B. Lee's former graduate student Daniel Neumark was entrusted with this very apparatus early in his own research career at Berkeley as Lee departed for Taiwan. Neumark's graduate student Jason Robinson assumed the unenviable task of moving the colossal apparatus and all of its components from Giauque Hall to the specially-built room D10 of Latimer Hall where it lives to this day.

Over the years, Machine B has received upgrades to almost all of its components to improve its capabilities and enable new experiments. In addition to crossed molecular beam scattering experiments, it has performed a considerable number of ultraviolet and infrared

photodissociation experiments. The extension of this work to include interrogation of reactive free radicals marked another large chapter in its catalogue of scientific output. Its continued contributions to science over its nearly half-century long lifetime are a testament both to its superlative design at the hands of Lee and Ng, as well as the prudence of its stewardship at the hands of so many generations of graduate students. This dissertation in part describes the beginning of its modification to study scattering dynamics at the surfaces of volatile liquid jets. The reflections of future graduate students on the history of Machine B will judge the significance of this effort.

Apparatus

Machine B is made up of three separate vacuum chambers: the source chamber is where the molecular beam is generated; the main chamber is where dissociation and scattering experiments take place; and the detector chamber housed within the main chamber contains the ionizer, mass filter, and detector components. The main and source chamber are differentially pumped, and the detector chamber consists of three differentially pumped stages (RI-RIII). All chambers are made out of non-magnetic stainless steel. The general layout of the vacuum chambers is described below and shown in Figure 2.1, and the additional configurations supporting photodissociation and liquid jet experiments are outlined separately thereafter. Typical pressures achieved within these sections of the machine are shown in Table 2.1 for passive standby operation and during different experiments. Large changes in the source chamber pressure occur depending on the pulsed valve operating conditions.

The source chamber is a stainless steel enclosure situated within the main chamber. Within the source chamber is a water-cooled mount housing the pulsed valve used to generate molecular beams. A 10" ASA stainless steel removable tee chamber attaches to the source chamber through the exterior wall of Machine B with greased viton o-rings creating the

Table 2.1: Comparison of typical pressures within different sections of Machine B during standby operation, and during photodissociation and liquid jet experiments. Pressures are given in units of Torr. Values for detector regions RI-RIII during experiments correspond to the detector gate valve open to the 'large' 3x3 mm aperture.

Chamber	**Passive**	**Photodissociation**	**Liquid jet scattering**
Source	5×10^{-8}	6×10^{-5}	6×10^{-5}
Main	4×10^{-7}	6×10^{-7}	$4–12 \times 10^{-6}$
RI	1×10^{-11}	3×10^{-9}	10^{-8}–10^{-6}
RII	10^{-13}–10^{-12}	1×10^{-12}	10^{-12}–10^{-11}
RIII	$4\text{-}5 \times 10^{-11}$	$4\text{-}5 \times 10^{-11}$	$4\text{-}7 \times 10^{-11}$

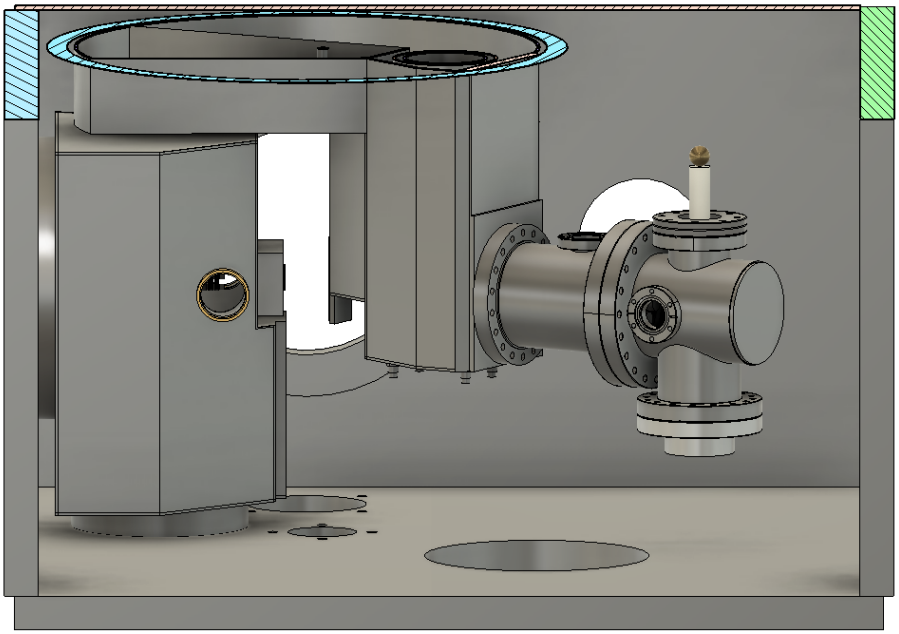

Figure 2.1: Accurate three-dimensional computer model of Machine B. The author wishes to acknowledge Chin Lee for converting the large stack of Ng's original blueprints into the highly detailed model showcased here.

vacuum seal. This tee supports the gas and electrical vacuum feedthroughs for the pulsed valve, as well as the Seiko Seiki STP-A2203 2200 L/s turbomolecular pump used to achieve vacuum conditions in the source chamber. This turbomolecular pump has chromium-plated fan blades to provide corrosion resistance against the numerous reactive species admitted in large quantities into the source chamber. Windows in the sides of the source chamber allow laser light to be transmitted to the outlet of the pulsed valve to enable photolytic generation of radical beams. Differential pumping between the source and main chambers is then achieved by mounting a 1 mm conical beam skimmer onto the source chamber wall.

The 96 cm × 96 cm × 76 cm main chamber of Machine B is an imposing structure. Achieving vacuum within the 0.7 m^3 of internal volume necessitates the use of another large 2200 L/s turbomolecular pump. The large chamber size is to accommodate the rotatable detector housing, which can sweep through ∼140°. The detector is a removable unit that sits on the roof of the machine. It sits on two spring-loaded graphite/PTFE gaskets evacuated by an Edwards E2M18 pump to 10^{-2}-10^{-1} Torr. This 'tec-ring' allows the detector to rotate through its full angular range without affecting the vacuum levels in the main chamber. With such a large size, the walls and floor of the main chamber are 3.7 cm thick stainless steel to resist being crushed by atmospheric pressure – a job they perform to within about 0.5 mm of distortion. The roof of the machine is much thicker at 6.7 cm to support the considerable weight of the detector.

There are a number of ports situated across the floor and walls supporting various electrical and cooling water feedthroughs and access to the interior of the chamber. One entire wall adjacent to the source chamber wall is removable, and the wall opposite the source chamber has an enormous 21" diameter circular port. All of the vacuum seals for these ports are made with greased viton o-rings.

The detector rotates around an axis running between the roof and floor of the machine. The point where this axis intersects the scattering plane containing the molecular beam and detector is referred to as the interaction region. It is the point where all physical interactions should occur during an experiment – this zone is always equidistant from the detector, and changes in physical detector angle correspond exactly to changes in the laboratory frame detection angle.

The detector is sealed from the main chamber by a gate valve, which can slide open to expose the detector to the main chamber through either a 100 μm diameter circular aperture or a 3×3 mm square aperture. The three differentially pumped regions RI-RIII are each pumped by 400 L/s turbomolecular pumps (a Leybold Turbovac 361 and two Seiko Seiki STP-400 units respectively). These three pumps are collectively backed by a 360 L/s turbomolecular pump (Leybold Turbovac 360). Backing the three region-specific turbomolecular pumps with a fourth provides two advantages. Firstly, it increases the compression ratio of the first set of pumps to make the ultrahigh vacuum regime accessible. It also has the unintended benefit that if failure ever occurs in any one of the pumps (which unfortunately it does), the entire system remains under high vacuum. Pumping back down to ultrahigh vacuum then takes less than 24 hours. All of these pumps are mounted atop the rotatable tec-ring.

Particles entering the detector find themselves in RI, which is just a large buffer region that begins lowering the vacuum to the ultrahigh regime. It is separated from RII by a wall with an aperture. the first thing encountered in RII is actually the entrance to RIII, which extends from the roof of the machine down into RII and houses the ionizer. The RIII wall is connected to a reservoir that is gravity-fed by a liquid nitrogen dewar, which improves the ultimate pressure in RII and RIII. This insert also has an array of copper fins filling the space in RIII above the ionizer assembly to increase the cryopumping surface area.

The ionizer is an axial design with a thoriated-iridium ring-filament producing electrons that ionize gas molecules to form cations. Details about this ionizer may be found elsewhere.[83] While usually operated at 80 eV electron energy, this unit is fully tunable down to electron energies as low as 4-5 eV. The utility of soft ionization using low electron energies to suppress confounding effects of dissociative ionization and ionization of interfering species on time-of-flight signals has been demonstrated previously.[83,84] Ionization efficiency curves formed by measuring the ion signal dependence on the electron energy are a useful characterization tool for species in the molecular beam, as well as for photofragments if signal intensities are high. Onset of ion signal is expected to occur once the electron energy surpasses the ionization potential of the species in the ionizer. The ions produced by the ionizer are focused by a series of einzel lenses and directed out of the ionizer assembly and back into RII.

The ions re-entering RII are mass-selected by a quadrupole mass filter connected to one of two different radio-frequency oscillators. The 1.2 MHz oscillator can filter ions with m/z

ratios up to 300, but the resolving power is insufficient to fully separate species with mass differences of 1 amu. A 2.1 MHz oscillator is able to filter ions with m/z ratios up to 120 and has no overlap between peaks with 1 amu spacing. The entrance and exit sides of the quadrupole have small additional sections of rod called the front and rear tri-filters. The tri-filters are held at a constant voltage and help with smoothing out stray electric fields in the vicinity of the quadrupole.

Finally, mass-selected cations are detected using a Daly-style ion detector.[85] The ions exiting the quadrupole section encounter a metal surface (the 'doorknob' on account of its shape) held at -30 kV potential. The ions are accelerated towards this surface and impact it with enough kinetic energy to liberate several electrons. The electrons are accelerated away from the doorknob and collide with a plastic scintillator, which produces photons. Photons are detected by a photomultiplier tube interfaced to a discriminator and a level adaptor. The TTL output can be shown to the user as a mass spectrum over the mass range repeatedly swept by the oscillator, or interfaced to a multichannel scalar (MCS) to record signal arrival time distributions.

All of the turbomolecular pumps on Machine B are backed by Welch 1397 mechanical pumps, and an Edwards Roots blower provides increased pumping capacity to the source chamber mechanical pump. The manifold that delivers gas to the stagnation reservoir behind the pulsed valve is also connected to a Welch 1397 mechanical pump. Modifications or additions to the above description for experiment-specific configurations of the machine are outlined below.

Photodissociation configuration

The machine configuration used for photodissociation experiments is shown in Figure 2.2. Photodissociation experiments require exposing the molecular beam to light. This is accomplished by using a periscope to steer the output of the excimer lasers into the scattering plane and intersecting the molecular beam in a perpendicular orientation. Light is focused to an approximately 6 mm $\times$ 2 mm spot in the interaction region by a short-wavelength-compatible lens, removed through a window on the opposing wall of the chamber, and disposed of using a beam dump. The photodissociation studies in this dissertation use photons at 248 nm and 193 nm, produced from the KrF^* and ArF^* excimers respectively. The path between the laser output and beam dump is fully enclosed to prevent lab exposure to stray excimer light. The lens mount is heated using heating tape to ensure a more uniform temperature gradient across the lens, preventing distortion of the laser spot by localised optical heating.

A spinning, slotted disk is used for determining the velocity of particles in the molecular beam (described later). This 'chopper wheel' was located between the source chamber and the interaction region during photodissociation experiments. Wheel rotation is driven by a three-phase synchronous motor (Globe, #75A1004-2) attached to a retractable mount allowing vertical translation into and out of the molecular beam path. The motor is water-cooled for vacuum operation.

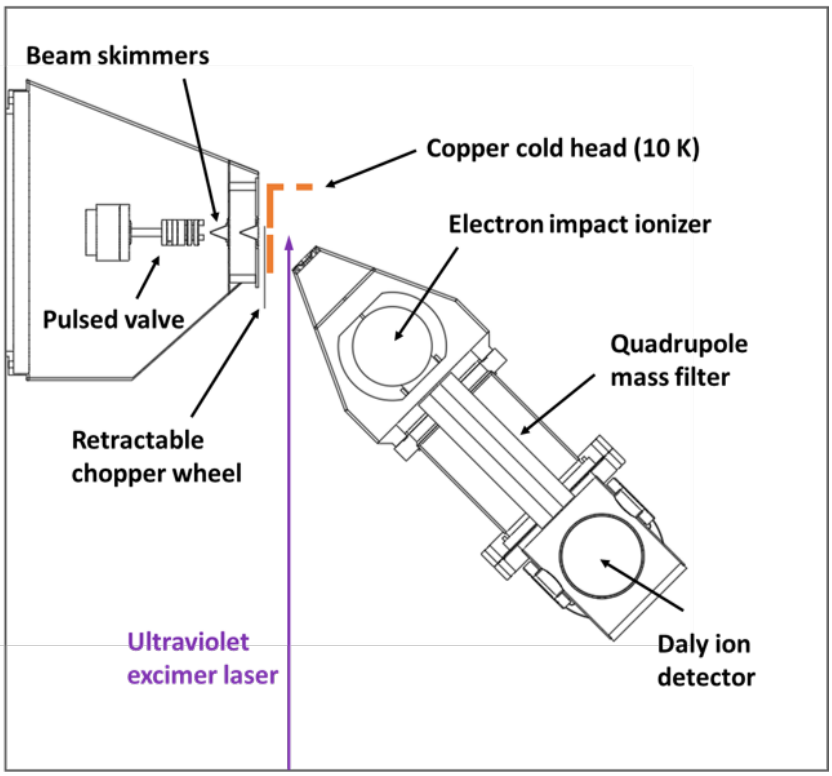

Figure 2.2: Configuration of Machine B supporting ultraviolet photodissociation experiments.

Finally, the photofragment yield in photodissociation experiments is often extremely low. To suppress contributions from the main chamber environment to the scattering time-of-flight signal, a copper block is mounted in the beam path and cooled to 10 K by a Leybold Coolpak 6200 helium compressor. This 'cold head' has cutouts to allow transmission of the molecular and laser beams. Background signal is minimized by a roughly 10-fold reduction in main chamber pressure during operation of the cold head, and by further collimation of the molecular beam as it passes through the cold head en route to the interaction region. The L-shaped geometry of the cold head also means that for all detector angles accessible during photodissociation experiments the detector is 'looking at' the 10 K surface, thus no reflected particles enter the detector along the same axis as the species under investigation.

Liquid jet configuration

Configuring Machine B for success in liquid jet experiments involves a much greater number of components than for photodissociation. The design of these capabilities has resulted in a set of components that is somewhat modular and fairly well-integrated with one another. Switching back and forth between photodissociation and liquid jet experiments should in principle be achievable within 1 or 2 days. The machine configuration used for the

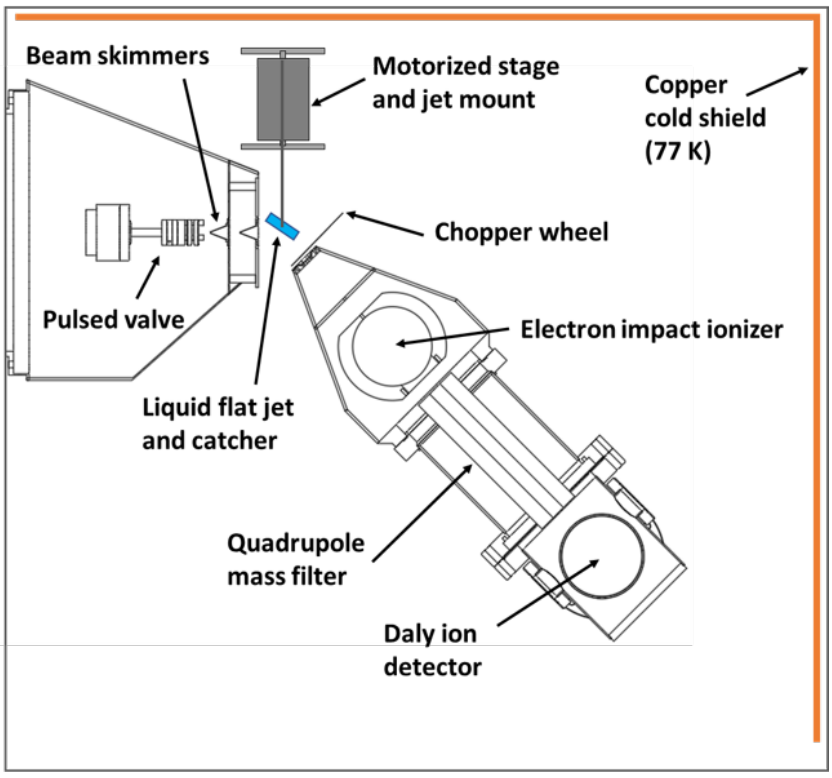

Figure 2.3: Configuration of Machine B supporting liquid jet evaporation and scattering experiments.

liquid jet experiments described in this dissertation is shown in Figure 2.3.

To produce liquid jets, liquid is pressurized and pumped using a high-performance liquid chromatography (HPLC) pump. This liquid travels through a counter-current heat-exchanger to adjust the temperature of the liquid. The heat-exchanger spans the wall of the vacuum chamber to minimize temperature changes after exiting the heat-exchanger. The liquid is then delivered to an adaptor that interfaces the polyether ether ketone (PEEK) tubing carrying the liquid to the liquid nozzle. The details of operating various types of liquid nozzles are described in a later section. The liquid jet is a free-flowing stream of liquid that travels through the main chamber upon exiting the liquid nozzle.

Ordinarily, it is preferable to direct the liquid jet into a collection reservoir so that only the section of the jet to be experimentally probed is exposed to the vacuum chamber. This is done in order to reduce the gas load contributed by volatile liquids, which is often achieved by directing the jet through a small aperture separating the main chamber from a collection reservoir that is cooled with liquid nitrogen to 77 K. Unfortunately, this was not a feasible solution for Machine B. We were not keen on cutting a port through the thick floor of the machine underneath the interaction region, nor, incidentally, was the machinist when we brought this idea up to him. But beyond that, there is another port on the floor of Machine

B used for the retractable chopper wheel mount that is slightly offset from the interaction region. It is too far away to be used for liquid collection, but close enough that any new port would need to be so small that it might not function appropriately.

The solution was to use a compact beryllium copper ($CuBe_2$) catcher (Microliquids GmbH) to collect the jet liquid. This catcher has the general form of a conical beam skimmer, although it is mostly solid with only a narrow through-hole, 0.5 mm in our case. For flat jets, the catcher entrance should be placed at the node where surface tension pulls the sheet back to a minimal diameter. The catcher has a built-in heating unit that can be connected to a power supply to heat the catcher. This is a strict necessity when working with highly volatile liquids such as water, which readily super-cool below their freezing points during transit through the vacuum chamber. The CuBe material is chosen to provide robustness in machining tiny through-holes, as well as high thermal conductivity to avoid cold spots. Without a liquid jet the catcher easily heats up to over 90 °C. With a water flat jet directed into it the same power dissipation results in catcher temperatures of ∼10 °C.

The bottom of the catcher is connected to a flexible plastic hose that takes liquid out of the main chamber and into a collection bottle. This bottle usually sits in an ice-bath and is pumped by a Welch 1397 mechanical pump in series with a 4 L liquid nitrogen-cooled foreline trap. The collection reservoir pressure is thus maintained at ∼0.2-2 Torr under most conditions. A 2 L liquid nitrogen-cooled foreline trap is also placed between the main chamber mechanical and turbomolecular pumps during liquid jet experiments. These traps are cooled when water jets are used, but often not for dodecane jets where the vapor pressure is much lower. For more expensive liquids, a peristaltic pump can be used to transfer the liquid from the collection reservoir back into the HPLC solvent bottle. Latimer D10 contains a Masterflex peristaltic pump that could be used for this purpose in the future.

With the heat-exchanger for liquid pre-cooling, the jet catcher, and the assorted pumping capabilities described above, operating a typical water flat jet (2.5 mL/min flow rate) results in an ultimate pressure of approximately 4×10^{-4} Torr in the main scattering chamber. This is not an acceptable pressure to expose the detector to for long periods of time, and the mean-free path in the main chamber is also relatively short. The pressures reported in Table 2.1 are achieved by installing a large copper panel in the main chamber, cooled by a gravity-fed liquid nitrogen dewar. The pumping speed of this 'cold shield' is given by[86]

$$S = \alpha_s A_{surf} \bar{v}/4 \tag{2.1}$$

where α_s is the temperature-dependant sticking coefficient, A_{surf} is the surface area of the cold panel, and $\bar{v}$ is the average velocity of the gas species. This cold shield has an area of approximately 0.98 m^2, and for molecular liquids of interest the sticking coefficient is essentially unity. For dodecane at 273 K the pumping speed of the cold shield is ∼40,000 L/s, while for water at the same temperature it is ∼122,000 L/s. The pressure reduction observed with the cold shield installed is consistent with this factor of increase in pumping speed. Cooling down of the cold shield normally begins after the main chamber turbomolecular pumps have reached maximum speed and the main chamber pressure is ∼4-5 $\times 10^{-4}$ Torr.

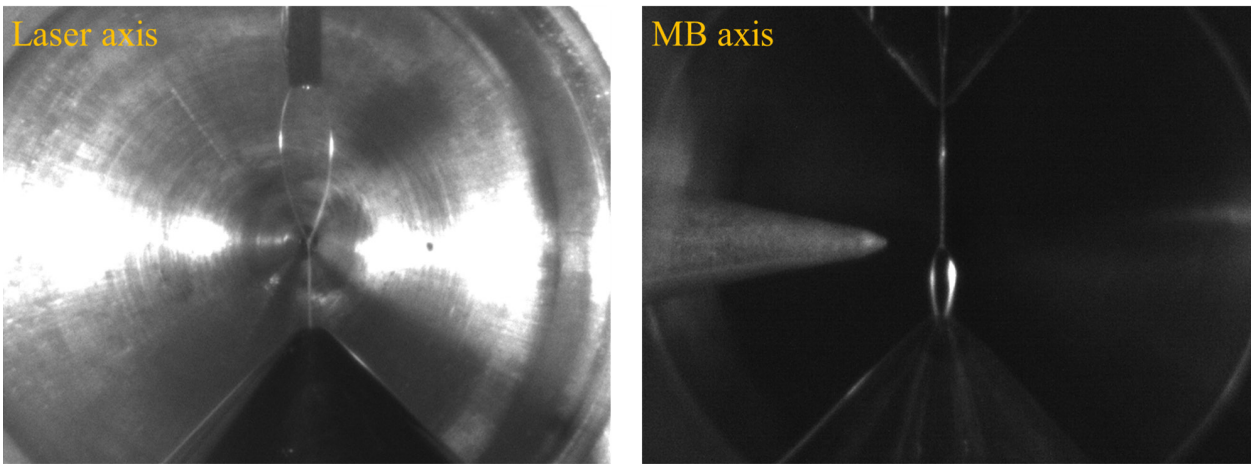

Figure 2.4: A liquid dodecane flat jet (2.9 mL/min flow rate) as viewed from the two lab cameras. Two of the orthogonal liquid sheets are exposed to the vacuum in these images.

A complicating factor in the design of the liquid jet configuration is the inability to start volatile liquid jets when the main chamber is already under vacuum. The jets must be started with the chamber open and operated continuously until the daily experiment has concluded. The jet assembly is mounted on a collection of picomotor-driven translation stages, which allow control over the three-dimensional positioning of both the catcher relative to the jet, as well as the jet + catcher pair relative to the interaction region. A high-repeatability stepper motor mounted on a long rail enables retracting the jet and catcher several centimeters away from the molecular beam axis to allow characterization of the beam prior to scattering experiments. The positions of the jet and catcher are monitored using two cameras with zoom lenses. One camera views along the molecular beam axis, while the other views along the 'laser' axis. Although the laser is not used in the liquid jet experiments, the laser axis is still used in practice as a reference during experiments. An example of the simultaneous views obtained from these two cameras is shown in Figure 2.4. A compact rotation stage (Standa, #8MR174-11-20) allows the jet to be rotated about the same axis as the detector, allowing on-line changes to the incident angle of the molecular beam, and increasing the accessible range of scattering angles.

Machine Parameters

Analysis of photodissociation and scattering process kinematics requires measuring the velocity distribution of the product species. Fundamentally, this is accomplished by measuring the arrival time distribution of ion signal at the detector and using the relation $v_{LAB} = {}^{L}/_{t}$. Thus, we need to know the neutral flight length L, and to measure the time taken to traverse this distance. In practice, the measured flight time t_{meas} includes a number of parameters that depend on the machine geometry. The true flight time of the neutral species, t_{true}, the

flight time that we desire to know in an experiment, is related to t_{meas} according to

$$t_{meas} = t_{true} + \alpha_{ion}\sqrt{m} + E_o \pm M_o \tag{2.2}$$

where m is the mass, α_{ion} is the ion flight constant, and E_o and M_o are the electronic and mechanical offsets respectfully.

The flight time to the detector has two components - the neutral particle first travels from the main scattering chamber to the ionizer, and then the ion is transmitted through the mass filter towards the detector chamber. The ion flight time, given by the $\alpha_{ion}\sqrt{m}$ term, is found by measuring the arrival time for several ions which arrive at the ionizer with the same neutral flight time. This is achieved by choosing a molecule that undergoes dissociative ionization within the ionizer to yield daughter ions spanning the mass range of interest. Since all ions originate from the same parent molecule, the only difference in their arrival time at the detector is due to their ion flight time. Plotting the arrival time of these ions as a function of $\sqrt{m}$ yields a line with a slope equal to α_{ion}. Values of α_{ion} typically range from 4.5 to 7.5 μs amu$^{-1/2}$ depending on the ion energy set by the ionizer conditions.

The velocity of the molecular beam is determined by using a rotating disk containing small slits to 'chop' a narrow section of the beam and then measuring the arrival time of these particles at the detector. The presence of a chopper slit is measured using an emitter-photodiode pair mounted with an angular offset from the detector aperture. By using the known wheel rotation speed and angular offset, the time this slit will be centered on the detector aperture is readily calculated, thus determining the appropriate time $t = 0$. For example, with a 200 Hz wheel rotation frequency and the emitter-photodiode pair mounted 90^o from the detector, it is expected that the slit will be detected 1250 μs prior to being centered on the detector aperture. The implementation of the mechanical chopper wheel introduces the electronic and mechanical offsets to the measured flight time as described below.

The E_o term arises due to the electronic triggering scheme used to determine when a slit passes the emitter-photodiode pair, and this timing offset contains two components. The first arises due to the difference in time between the rising edge of the photodiode trigger signal and the center of the chopper slit. A digital delay generator is used to adjust the delay between when the photodiode trigger signal is received and when the MCS trigger signal is generated. By overlapping these two signals this component of E_o is removed. Additionally, the built-in signal amplifier within the photodiode has a propagation delay time of 5.0 μs that elapses before the trigger signal confirming passage of a slit is produced.[87] Consequently, E_o = 5.0 μs for the chopper wheel component as currently implemented in Machine B.

The M_o term results from angular misalignments in the physical mounting of the chopper and emitter-photodiode pair relative to the detector aperture. For the 200 Hz wheel frequency used in Machine B, a contribution of $\sim$14 μs per degree of misalignment is made to M_o. The value of M_o thus changes slightly when the chopper wheel and emitter-photodiode pair are moved during machine maintenance. For the retractable chopper wheel mount used during photodissociaton experiments M_o was typically 5-10 μs, while the chopper mounted to the

underside of the detector during liquid jet experiments has $M_o \simeq 18$ μs. Since M_o is due to angular misalignment, its sign depends on which direction the chopper wheel is spinning. The experimental determination of M_o is achieved by measuring the difference in flight time with the wheel spinning clockwise vs. counter-clockwise, which corresponds to $2M_o$. For the rotation direction giving faster arrival times M_o is positive, while M_o is negative for the slower direction. This ensures that the flight time is independent of the chopper rotation direction, as it should be.

To calibrate the neutral flight length, the flight time is measured for pure beams of several noble gases. The terminal velocities $\langle v_{max} \rangle$ of these beams are determined by the enthalpy in the stagnation volume before the nozzle orifice and are easily calculated using Equation 1.2. While the flight time measurement of a single gas with known velocity is in principle sufficient to determine L, a more robust method relies on the use of several noble gases. Substituting $\langle v_{max} \rangle$ and t_{meas} into $v = {}^{L'}/_{t}$ and simplifying yields

$$t_{meas} = \left(\frac{L'}{\sqrt{5 k_B T}} + \alpha_{ion} \right) \sqrt{m} + E_o \pm M_o \tag{2.3}$$

where L′ is the distance between the chopper wheel and the ionizer. Thus, for a collection of noble gases, the arrival time is a linear function of $\sqrt{m}$, with the slope of this plot providing L′ and the time-axis intercept occurring at ($E_o \pm M_o$). Calibrating the neutral flight length with the above prescription gives a value L′ = 22.8 cm for photodissociation and 17.2 cm for liquid jet experiments, and ($E_o \pm M_o$) generally agrees very well with individually determined values for these quantities. The distance L between the interaction region and the ionizer is found by adjusting L′ to account for the distance between the chopper wheel and the interaction region, measured using a ruler or from a calibrated camera image. With this methodology, the neutral flight length of Machine B is found to be 21.1 cm.

2.2 Molecular Beam Generation

Pulsed molecular beams are admitted into the vacuum chamber using a piezoelectric disk translator to open and close the o-ring vacuum seal, usually at a 200-400 Hz repetition rate. Stagnation conditions within the valve reservoir are typically 286 K and 700-900 Torr, leading to supersonic expansion of the gas mix through an 800 μm orifice when the valve is opened. For generating radical beams, the valve must be modified to convert a suitable precursor molecule into the radical of interest. Electric discharge, laser photolysis, and flash vacuum pyrolysis have all been implemented on Machine B in the past.[88] Electric discharge often leads to a highly contaminated radical beam, which is unsuitable for neutral particles that cannot easily be separated from one another. In situ photolysis often results in low number densities of radicals in a very small portion of the beam, reducing overall signal levels and introducing complications where precursor and radical absorb photons at the same wavelength. Pyrolysis is thus the only method of radical generation routinely employed in Machine B.

The flash vacuum pyrolysis modification to the pulsed valve is described in detail elsewhere.[14,83,88] It consists of a silicon carbide (SiC) tube about 15 mm long spanning two molybdenum electrodes. The electrodes are electrically insulated from the valve and from each other except through the SiC tube. A current-regulated power supply is used to dissipate a fixed power through the tube during operation. The temperature of this source is not usually of interest and is seldom measured. Weak bonds such as the ∼40 kcal/mol O–NO bonds in alkyl nitrites[89] can be pyrolyzed by dissipating about 25-30 W, while much stronger bonds such as the 64 kcal/mol CH_3–O bond in anisole[90] require as much as 70-75 W dissipation. The latter case corresponds to electric currents of about 6-7 A through the SiC tube, which greatly decreases its usable lifespan. Supersonic expansion occurs from the valve reservoir into the pyrolysis tube where the gas heats up and the precursor is pyrolyzed during a residence time of ∼10 μs. A subsequent supersonic expansion into the source chamber then occurs. The hot tube conditions and large ∼1 mm diameter of the tube results in a supersonic expansion of diminished quality, and fairly low speed ratios are the norm for radical beams. Seeding the carrier gas with a few percent of molecular species such as N_2 results in superior cooling of the radical vibrational temperatures in particular.[91]

However, pyrolysis as implemented is unsuitable for generating some types of reactive species. Criegee intermediates such as CH_2O_2 are of particular interest to our and to other labs due to their high reactivity and their integral role in the atmospheric fate of unsaturated hydrocarbons. These molecules are routinely produced via photolysis of geminal diiodoalkanes (e.g. CH_2I_2) in the presence of O_2.[92] Attempts to produce CH_2O_2 via flash pyrolysis of gas mixtures containing both CH_2I_2 and O_2 were unsuccessful. At temperatures lower than those required to induce I-atom loss from CH_2I_2, the surface of the SiC tube became susceptible to attack by O_2. This leads to the generation of prodigious amounts of CO_2, and converts the tube surface to non-conductive SiO_2. Pyrolysis tubes made from ZrO_2 are compatible with strongly oxidizing environments, but must be pre-heated since ZrO_2 is an insulator at room temperature.[14] The alternative is to rely on in situ photolysis to generate Criegee intermediates, as many other laboratories do, with the drawbacks mentioned above.

2.3 Excimer Lasers

The Latimer D10 laboratory contains two excimer lasers that may be used for photolysis: a large Lambda Physik LPX 220i and a smaller GAM EX100/500. The LPX 220i is a powerful system capable of substantial output of excimer light, and was the photolysis laser used for all of the photodissociation experiments reported herein. The GAM EX100/500 is a lower intensity light source, and is usually employed when the higher intensity output of the LPX leads to multi-photon excitations in the molecular beam. From these lasers, ultraviolet light with a wavelength of 248 nm is produced by the KrF^* excimer, while ArF^* gives 193 nm photons. The LPX 220i is capable of around 2-3 times greater output at 248 nm than at 193 nm, up to around 60 mJ/pulse at 248 nm compared to around 25 mJ/pulse at 193 nm at a typical 200 Hz repetition rate following a new gas fill of the lasing cavity. The built-in

power meter in the LPX 220i is slightly inaccurate when measuring 248 nm output and does not work for measuring 193 nm output. To get an accurate measure for both wavelengths a portable power meter is used to measure the laser power right before it enters the vacuum chamber.

The unpolarized light obtained from these excimer lasers is a limitation when characterizing dissociation occurring faster than the rotational period of a molecule, where, as discussed previously, the excitation and dissociation vectors are correlated. With polarized light, certain polarization angles result in a greater number of photofragments scattering towards the detector depending on the transition dipole vector. It is thus occasionally useful to control the polarization of the laser to produce the most pronounced effect in the measured time-of-flight data. This is achieved using a stack of 8 quartz plates held at Brewster's angle, which yields a 9:1 ratio of the two linear polarization directions.[83]

2.4 Liquid Jet Generation

For experiments probing the evaporation and scattering from liquid surfaces, there are a number of options introducing volatile liquids into the vacuum chamber. While the injection of droplets of volatile liquids into vacuum is advantageous for various other types of inquiry,[50,93] it is not well-suited to scattering experiments. Cylindrical microjets have historically been used for introducing volatile liquids into vacuum due to the manageable vapor-load they generate in the chamber. While flat jets are the desired scattering target for most experiments planned on Machine B, both flat and cylindrical jets are used depending on the experiment. Whether the liquid is new or being recycled after collection in the reservoir, it is pre-filtered through a 2-5 μm fritted glass filter before use.

In all cases, the liquid is pumped using an Agilent 1260 Infinity II isocratic HPLC pump capable of providing flow rates of 0.001-10 mL/min at backing pressures up to 600 bar. Flow rates of 0.1-3.5 mL/min typically used herein result in pressures between ∼10-60 bar depending on the jet nozzle and the liquid used. Liquid is drawn into the HPLC pump through a 0.2 μm filter to remove any particulate matter from the liquid in the solvent reservoir. A 0.5 μm inline filter is often also connected to the tube carrying liquid to the nozzle. In addition to trapping particles that may make it past a compromised inlet filter, it increases the backing pressure of the HPLC pump resulting in better flow stability. The HPLC pump is usually controlled by a 1200 Infinity Series Instant Pilot handheld controller that includes read-back displays for monitoring the liquid flow rate and pump head pressure during operation. Alternatively, if can be controlled using the Lab Adviser software package, which provides additional functionality, especially for troubleshooting issues.

Cylindrical jet nozzles

A free-flowing cylindrical filament of liquid can be produced in vacuum by forcing a pressurized liquid through a micrometer-scale capillary. Interest in cylindrical jets in our lab

is usually only for the purposes of comparison to flat jets, or to compare results we obtain with previously published results from other research groups. The low signal levels and poor angular resolution intrinsic to the use of cylindrical jets is discussed in Section 1.4 of the Introduction chapter. There are numerous commercially available capillaries with a wide range of capillary diameters. The very limited work that has been done using cylindrical capillaries in our lab typically used 50-100 μm capillaries. For routine generation of cylindrical jets we use a microfluidic chip discussed later.

Colliding cylindrical jets

A flat liquid sheet is easily afforded by the collision of two cylindrical jets. Forming high quality sheets requires precise alignment of the two filaments with respect to one another. To test this jet generation technique in our vacuum chamber, Marvin Pohl designed and 3D-printed a flexible holder onto which was mounted two cylindrical capillaries and a picomotor to adjusts their relative alignment. Unfortunately, it is difficult to make this design compact enough to satisfy space restrictions around the interaction region in Machine B. Jet misalignment due to complete or partial blockage of the individual capillaries remains a problem with flat sheets formed by colliding free cylindrical jets. In such instances there is a grave danger of electrical arcs from high-voltage components within the main chamber that can damage electronics within the detector. Ultimately, colliding free-flowing cylindrical jets was deemed to be unsuitable to the needs of a scattering experiment within our instrument. This technique was therefore not used for any of the data reported herein.

Flat nozzles

The potential for jet misalignment discussed above is a significant drawback for flat jets created from a pair of colliding cylindrical jets. A more reliable solution uses converging flows emanating from rectangular orifices to create flat sheets, with the downside that the collision angle is fixed during the nozzle design. There are a number of both commercial and custom-built nozzle designs that can be used to generate flat jets, most of which have been prototyped and tested in some form in our laboratory.

The greatest flexibility in nozzle design is obviously achieved by designing one's own nozzles. A relatively simple option involves cutting the converging channel out of a sheet of polyimide (Kapton) film, which is then sandwiched between metallic mounting plates supporting fluid delivery to the enclosed channel.[60,94] While the low-cost and easily prepared polyimide sheets allow for maximal nozzle design flexibility, a noted problem in these designs is micrometer-scale misalignments in the mounting plates resulting in sheet instabilities. Nozzles may be produced using high-resolution 3D printers, enabling exquisite control over very intricate geometric features.[95,96] Unlike the Nanoscribe GmbH 3D printers used in the preceding references, the 3D printers in the machine shop were incapable of printing precise features on the micrometer scale. All attempts to 3D print our own nozzles were therefore unsuccessful.

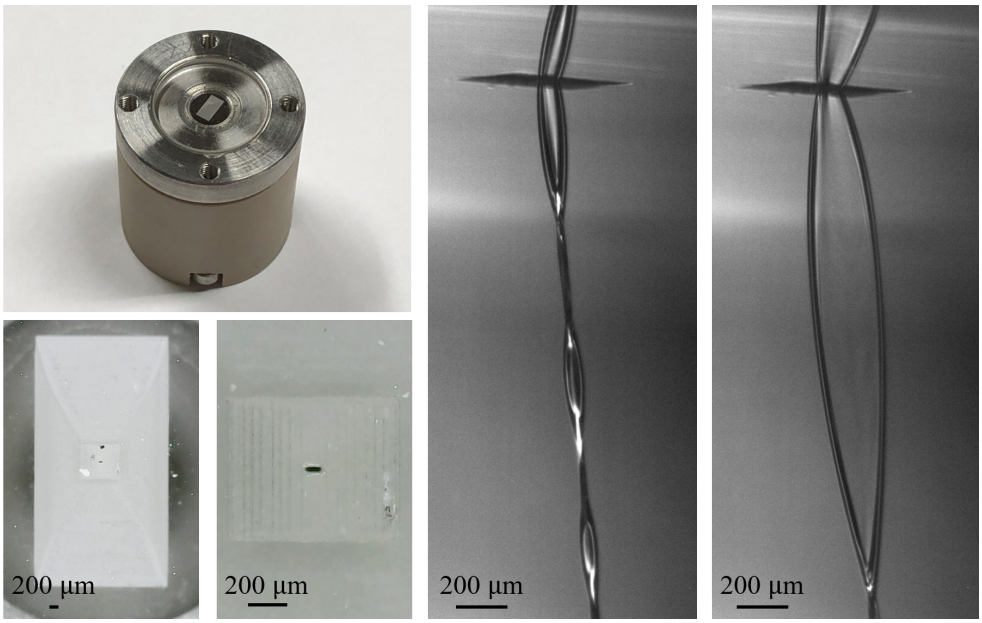

Figure 2.5: Dimensions of the sapphire nozzle containing a converging fluid channel, and successive magnified views of the nozzle aperture. In the right panels a chain of multiple flat sheets fits within the camera frame at low flow rate, while a higher flow rate exposes a much larger sheet.

While nozzle prototypes were not constructed from polyimide film, a converging channel nozzle was tested through a collaboration with Bernd Abel of the University of Leipzig and the Leibniz Institute of Surface Engineering. These nozzles consisted of a sapphire disk into which fluid channels were cut using a laser. The convergence geometry is more complicated, with the liquid flow converging along two dimensions rather than just one. An example of such a nozzle with a 20 μm $\times$ 80 μm aperture is shown in Figure 2.5. The jets produced by this nozzle have a very high-quality appearance, but often suffer from large tilts in their flow axis (i.e. a vertically aligned nozzle may produce a jet that shoots 'sideways'). This is a complicating factor for removing liquid from the chamber without a gimbal-capable mount. Another problem is the large aspect ratio of the jet, with such slender widths being problematic as molecular beam scattering targets. Challenges in production of these nozzles meant that it was quite slow to work through different prototypes, and cracks caused by the high-pressure liquid behind the nozzle often lead to long delays before another sapphire disk could be received.

The flat jet nozzle routinely used in our lab is a microfluidic chip made by etching channels into borosilicate glass, developed by Micronit Microtechnologies BV in collaboration with SLAC National Accelerator Laboratory. The dimensions of this nozzle are shown in Figure 2.6, and the flat jets shown in Figure 2.4 were produced using this nozzle design. The nozzle has a central channel connected to one inlet port, along with another inlet port that diverges

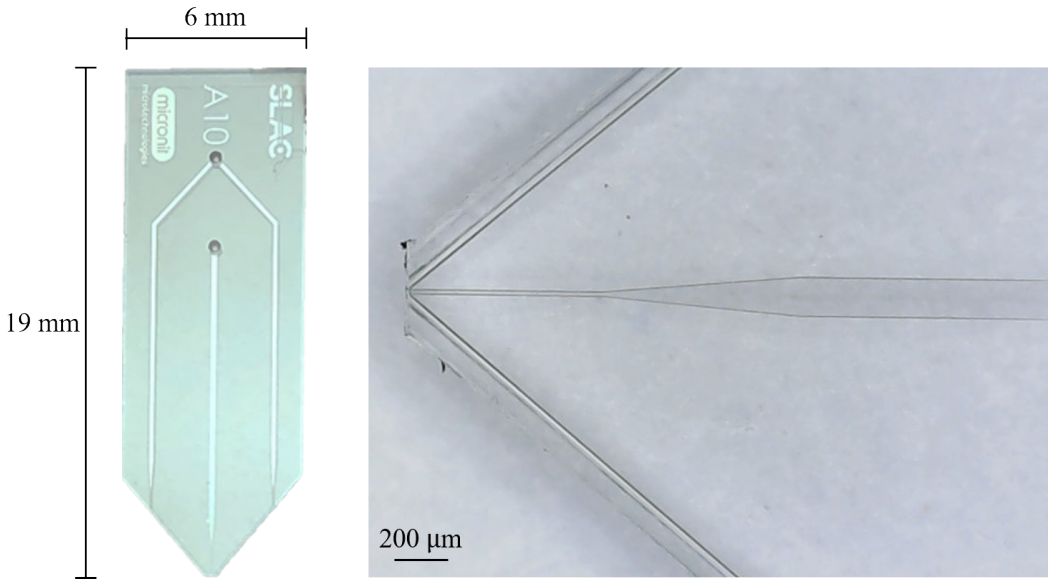

Figure 2.6: Dimensions of the Micronit/SLAC liquid nozzle chip, showing the two liquid channels supported within the chip. The right panel shows a magnified view of the exit side of the nozzle where the jet originates.

into two channels that later re-converge on the central channel. The central channel and outer channels have dimensions of 20 μm $\times$ 30 μm and 50 μm $\times$ 60 μm respectively, while the nozzle exit is 130 μm $\times$ 50 μm. This nozzle was designed to operate as a gas dynamic virtual nozzle, using high-pressure gas in the outer channels to squeeze liquid from the central channel into extremely thin sheets ($<$ 20 nm).[97] Gas dynamic jet operation is obviously not compatible with a molecular scattering experiment. Instead, during operation in colliding jet mode, liquid is pumped through the outer channels while the inner channel is left unused.

As a commercial product, no control over the jet collision angle exists, but the 40^o collision half-angle of these nozzles produced jets with dimensions compatible with molecular beams. The sizes of the first two liquid sheets for both dodecane and water flat jets created from different volumetric flow rates using this nozzle are shown in Figure 2.7. Also shown are jet dimension predictions of the model employed by Santiago and coworkers.[60] Unaltered, these models do not accurately predict the size of jets from the chip nozzles, which have a different convergence geometry than those used to establish the model. Additionally, many of the flow parameters for our jets fall outside the range of those parameters on which the model was validated. Nevertheless, multiplication of these predictions by a constant results in excellent agreement between predicted and experimental jet dimensions. The scaling constants for the maximal width and lengths of flat jets of water and dodecane are collected in Table 2.2. The value of the scaling constant differs for the first and second flat sheets, with the second sheet being approximately half the dimensions of the first. The scaling constants for the two liquids are also in generally good agreement. The experimental and model dimensions

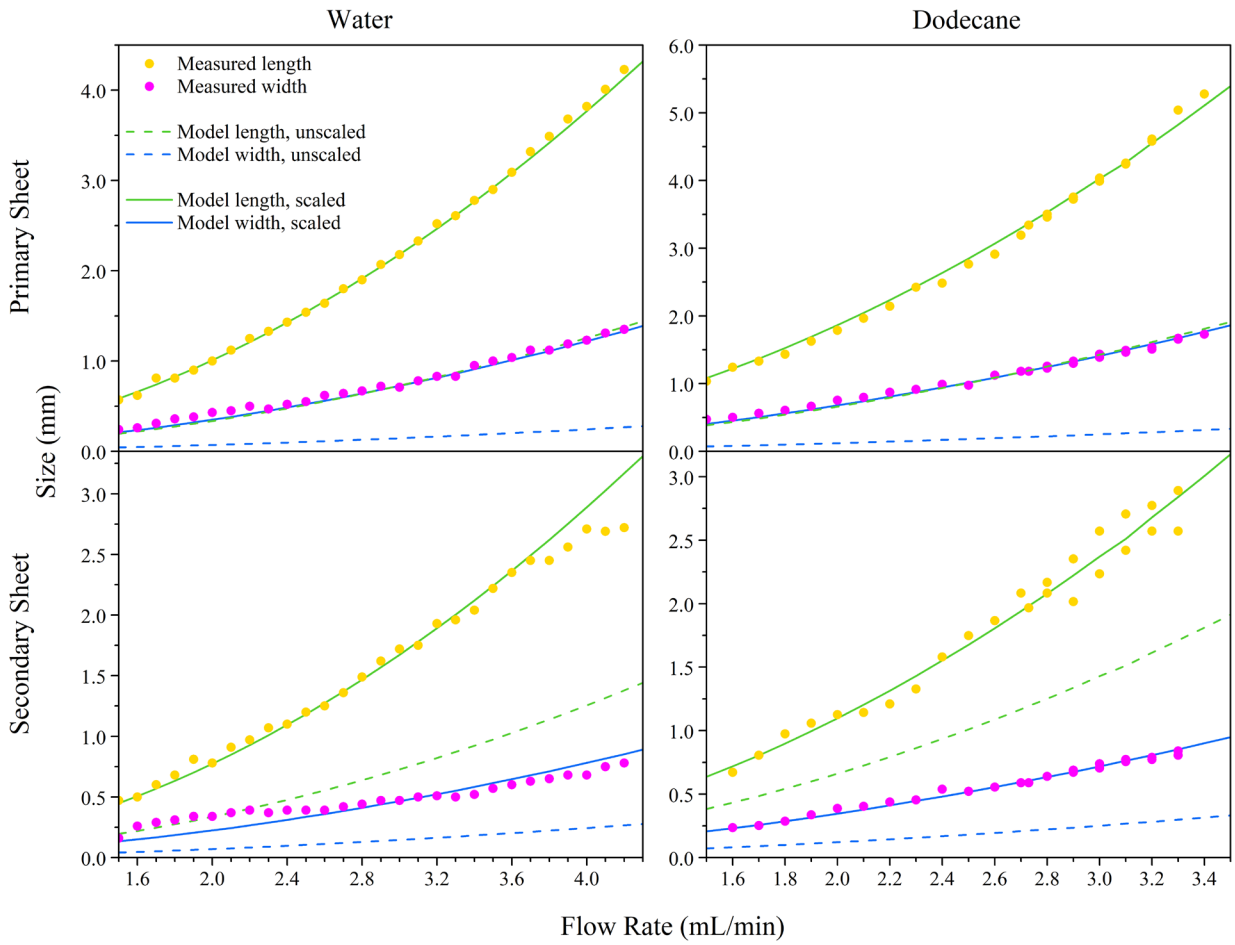

Figure 2.7: Scaling relation between jet flow rate and flat sheet dimensions for the Micronit/SLAC chip nozzles. The left and right panels correspond respectively to water and dodecane flat jets, while the top and bottom plot show data for the primary and secondary flat sheets respectively.

include both the flat sheet and the rims bounding it.

Cylindrical jets can also be produced very easily by swapping the liquid inlet from the split outer channels to the single central channel. The dimensions of this channel lead to a cylindrical jet approximately 28 μm in diameter. A major advantage of these nozzles is their extremely compact design compared to individual colliding cylindrical nozzles or the sapphire disks. Their low cost (~\$145/chip at the time of writing) is also a large benefit when testing out different experiment implementations, which frequently leads to breakage of the nozzles.

Table 2.2: Scaling constants for dimensions of flat jets produced using the Micronit/SLAC chip nozzles.

Liquid	**Scaling constant**	
	Width	Length
Water		
Primary sheet	5.0	3.0
Secondary sheet	3.2	2.3
Dodecane		
Primary sheet	5.6	2.8
Secondary sheet	2.9	1.7

Pulse Damper

The HPLC pump contains two pumping chambers enclosing reciprocating sapphire pistons that drive fluid through the pump. Between these chambers is a pulse damper that reduces fluctuations in the fluid pressure during pump operation. For low flow rates below about 1.5 mL/min, the pistons sweep through the pumping volume fairly slowly, and the built-in damper is able to keep pressure fluctuations at around 1%. When higher flow rates are used this built-in damper is no longer sufficient – as an example, a 2.5 mL/min water jet will have pressure fluctuations of ∼2%, which leads to visually-apparent pulsation in the size of the liquid sheet occurring at a frequency matching the piston motion. Typical flow rates for generating flat jets lead to the pump operating at ∼1.5 Hz. The volume of fluid moved per stroke of the pump is then about 30 μL, and a fluctuation of 2% amounts to only 0.6 μL of additional liquid volume that must be accommodated.

To overcome this issue, the pulse damper shown in Figure 2.8 is installed perpendicular to the fluid flow travelling between the HPLC pump and the jet nozzle. The damper is based on a previous design,[98] and consists of a flexible stainless steel ballast reservoir (Swagelok, SS-FM4SL4SL4-75CM) with an internal volume of ∼35 mL. This reservoir is essentially a fairly stiff bellows that responds elastically to transient changes in liquid pressure. Alternatively, the ballast reservoir can be operated as a gas-damper by leaving a small volume of headspace in the reservoir when it is filled with liquid. This headspace is pressurized to the liquid pressure during pump operation, and pressure pulses are damped by the compression and expansion of the gas.

The pulse damper works well in both operation modes, and the ∼2-20 m of PEEK capillary tubing that takes liquid from the pulse damper to the liquid nozzle also helps in dissipating fluctuations. Under typical experimental conditions the pressure fluctuation experienced in the liquid pump head is usually below 0.8%. Pressure fluctuations downstream from the

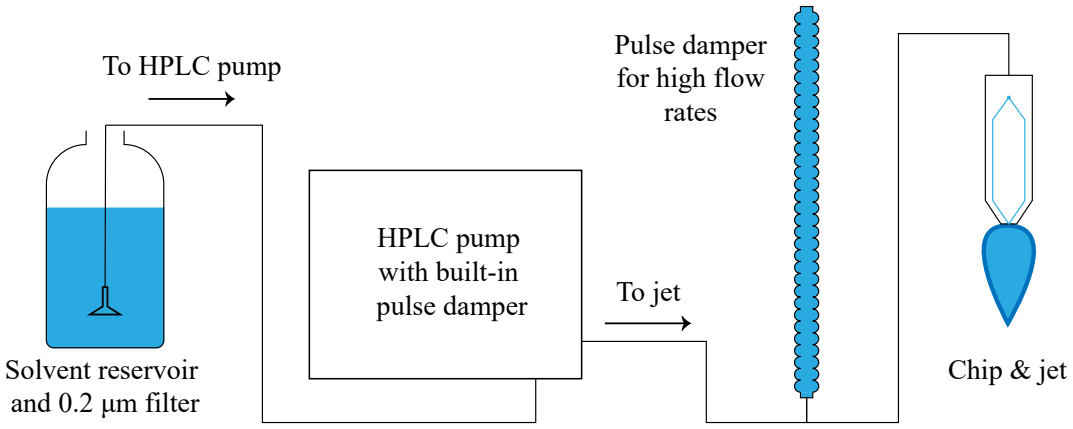

Figure 2.8: Schematic of the liquid path from solvent reservoir to jet showing the location of the pulse damper and its orientation to the flow path.

damper have not been measured, but are expected to be very minimal. Any visual evidence of pulsations in the liquid sheet is eliminated.

2.5 Physical Alignment of the Instrument

Success in photodissociation and surface scattering experiments requires all of the components within the apparatus to be aligned with respect to one another. Machine B has several grooves machined into the walls of the machine, which the two molecular beam source chambers were attached to, as well as on the opposing walls, which facilitate routine alignment of the instrument components. By spanning the machine walls with a vertically and a horizontally positioned string fixed into these grooves, a set of 'cross-hairs' on each end of the machine is established along which alignment takes place. A stable viewpoint centered along the alignment axis may be achieved with a telescopic objective which is used to monitor the positioning of components relative to this axis during the alignment procedure. This has historically been done using an adjustable telescope mounted atop a rugged, movable base, but more recently uses the two cameras installed to monitor the liquid jet (providing the views in Figure 2.4). For experiments where very tight alignment is required the older telescope is still the preferred method, since the field of view is more stable to adjustments of the focal plane, has a longer focal length (so the closer pair of alignment strings still appear very thin, and therefore tighter alignment is more easily achieved), and can provide a sharper focus. The drawback is that alignment along each axis defining the scattering plane must be done step-wise and, once relocated, the scope takes several hours to physically settle into a stable position which will not shift during the alignment process. The components are then inserted into the vacuum chamber in order of decreasing distance to the viewing setup. Regardless of the viewing optics, the procedure for aligning components to the cross-hairs is as follows.

The molecular beam source is inserted into its mount within the source chamber. The valve is aligned using a pair of vertical set screws and one horizontally positioned set screw to adjust the pitch and yaw of the valve and secure it in place. Next, a molecular beam skimmer is screwed into a pre-aligned mount that centers the skimmer aperture along the alignment axis once fixed. Pre-alignment of this mount would involve mounting the skimmer and adjusting the mount to the alignment axis before tightening it in place, a process that is necessary only very infrequently. A subsequent skimmer is mounted to a movable plate adjusted by vertical and horizontal set screws to the alignment axis.

The ultraviolet laser beam is aligned using a piece of receipt paper mounted in the interaction region. Brief exposure of the paper to the laser by the researcher (e.g. by quickly flashing a piece of card in and out of view) results in a dark spot formed where the laser hit the paper. The faster the laser light can be blocked following exposure the better, since this results in a smaller spot highlighting the position of the most intense part of the laser beam. The periscope mirrors may then be used to adjust the pitch and yaw of the laser beam to steer it onto the correct alignment axis.

The translational capabilities of the liquid jet are described in an earlier section. Each time the jet is run it is positioned into the correct alignment, and the liquid catcher is positioned below the jet to collect all of the liquid using the translation stages. It is sometimes necessary to check that the flow axis of flat liquid jets are orthogonal to the scattering plane. If the jet were to be tilted relative to this plane impinging molecules will be preferentially scattered either above or below the scattering plane. Other than having a tilt in the nozzle mounting geometry, such a tilt may occur because of physical imperfections in the nozzle orifice or due to unequal flow rates of the two liquid streams if a colliding design is used. This angle can be checked by using the same periscope mirrors for the ultraviolet lasers to steer the beam of a small, low-power, green HeNe laser into the scattering plane and reflect it off the jet. By slightly rotating the jet so the flat sheet is not perfectly normal to laser axis a fraction of the light is reflected back towards the laser with a small spatial displacement. The height of this reflected spot compared to the incident beam is easy to check by letting it hit one of the strings used to define the alignment axis. A tilt stage mounted to the jet rotation stage can be used to correct any tilt in the jet while keeping rotations strictly centered about the interaction region.

The detector rotates around the interaction region by design, requiring no alignment with respect to this position in the chamber (actually, the rotation axis defines this position). The detector skimmer and chopper wheel can be aligned easily along the laser axis using the telescope or the laser axis camera. No other components in the machine need to be aligned outside of exceptionally rare circumstances.

Part II

Photodissociation Dynamics

Chapter 3

Photodissociation dynamics of fulvenallene and the fulvenallenyl radical at 248 and 193 nm

The content and figures of this chapter are reprinted or adapted with permission from
Ramphal, I. A.; Shapero, M.; Haibach-Morris, C; Neumark D. M., "Photodissociation dynamics of fulvenallene and the fulvenallenyl radical at 248 and 193 nm," Phys. Chem. Chem. Phys., 2017, 19, 29305.

Abstract

Photofragment translational spectroscopy was used to study the photodissociation of fulvenallene, C_7H_6, and the fulvenallenyl radical, C_7H_5, at 248 nm and 193 nm. Starting from fulvenallene, only the H-atom loss channel producing the fulvenallenyl radical, C_7H_5, was observed. Fulvenallene dissociation occurs on the ground state surface with no exit barrier, and there is good agreement between our experimentally determined photofragment translational energy distribution and a prior distribution for a statistical process. Subsequent absorption at both wavelengths by fulvenallenyl enabled investigation of the photodissociation of this radical. Two channels were observed: C_5H_3 + C_2H_2 and C_4H_2 + C_3H_3. The photofragment translational energy distributions for these channels are peaked away from 0 kcal/mol, which is consistent with ground state dissociation over an exit barrier. At 248 nm, the C_3H_3-loss channel accounted for 85 ± 10% of fulvenallenyl dissociation, while at 193 nm it accounted for 80 ± 15%. The experimental branching between these channels is in reasonable agreement with Rice-Ramsperger-Kassel-Marcus theory calculations, which predict C_3H_3 to account for 70% and 63% of dissociation for 248 nm and 193 nm, respectively.

3.1 Introduction

Fulvenallene is the global minimum of the C_7H_6 potential energy surface (PES)[99] and plays a key role in the combustion chemistry of aromatic compounds.[100,101] It has been detected in large quantities in toluene flames by photoionization mass spectrometry.[100,102] Shock tube experiments have identified H-atom loss to produce a C_7H_6 product as the most important thermal decomposition reaction for the benzyl radical.[103,104] Fulvenallene is also the primary 248 nm photodissociation product of the benzyl radical.[105] Hence, elucidation of the unimolecular dissociation pathways of fulvenallene is of considerable interest. To this end, we investigate the ultraviolet photodissociation dynamics of both fulvenallene and its primary photodissociation product, the fulvenallenyl radical (Figure 3.1).

Fulvenallene was first observed and isolated by flash vacuum pyrolysis of suitable precursors.[106,107] Its infrared and microwave spectra have been reported,[108,109] and its gas phase and condensed phase chemistry has been investigated.[110–113] Photoelectron spectroscopy[114,115] and, more recently, photoionization mass spectrometry[116] find the ionization potential (IP) of fulvenallene to be 8.22 eV. Theoretical investigations of fulvenallene decomposition have found the following two lowest energy channels:[117]

$$C_7H_6 \rightarrow C_7H_5 + H \qquad \Delta H(0K) = 82.5\ kcal/mol \qquad \text{(CH1)}$$

$$\rightarrow C_5H_4 + C_2H_2 \qquad \Delta H(0K) = 92.7\ kcal/mol \qquad \text{(CH2)}$$

Channel 1 corresponds to loss of an allenic H-atom and production of the resonance-stabilized fulvenallenyl radical; it proceeds through a loose transition state with no exit barrier. Channel 2 involves an intersystem crossing from the singlet to the triplet state, followed by dissociation over an exit barrier to yield cyclopentadienylidene and acetylene. A simplified C_7H_6 PES is shown in Figure 3.10 of the Supporting Information (Section 3.7). Calculations have suggested that decomposition via channel 2 following intersystem crossing to the triplet state occurs with comparable probability to H-atom loss.[117]

Velocity-map imaging experiments on the H-atom product of fulvenallene photodissociation (channel 1) in the 245-255 nm energy range (assigned to the $\widetilde{D}\ ^1A_1 \leftarrow \widetilde{X}\ ^1A_1$ transition) were conducted by Giegerich and Fischer.[118] The H atoms were produced with a translational

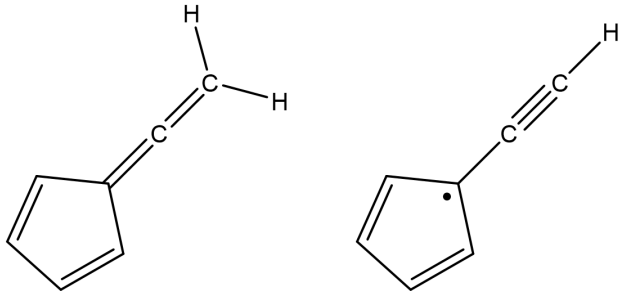

Figure 3.1: Structures of fulvenallene and the fulvenallenyl radical.

energy distribution peaked close to 0 kcal/mol, and with no dependence on excitation laser polarization. These results supported statistical and isotropic photodissociation dynamics subsequent to internal conversion to the electronic ground state. This work postulated that there must be a low probability of intersystem crossing in order to account for the large H-atom signal measured in these experiments. No attempts to measure channel 2 have been reported.

The fulvenallenyl radical product from channel 1 is greatly stabilized by electron delocalization over the cyclopentadienyl and propargyl moieties and is the global minimum of the C_7H_5 PES.[119] Fulvenallenyl was detected experimentally by Steinbauer *et al.*[116] by flash pyrolysis of a suitable precursor followed by photoionization mass spectrometry. Additionally, the IP of fulvenallenyl was found to be 8.19 eV using threshold photoelectron spectroscopy. An electronic absorption spectrum of the fulvenallenyl radical in a cryogenic Ne matrix has recently been reported, with an absorption band at 401 nm attributed to the origin of the $\widetilde{A}\ ^2B_1 \leftarrow \widetilde{X}\ ^2B_1$ transition.[120] The present study considers transitions at energies much higher than in any previous reports.

Theoretical investigations of the C_7H_5 PES predict the following as the lowest energy decomposition channels:[121]

$$C_7H_5 \rightarrow n\text{–}C_5H_3 + C_2H_2 \qquad \Delta H(0K) = 74.1\ kcal/mol \qquad \text{(CH3)}$$

$$\rightarrow i\text{–}C_5H_3 + C_2H_2 \qquad \Delta H(0K) = 75.2\ kcal/mol \qquad \text{(CH4)}$$

$$\rightarrow C_4H_2 + C_3H_3 \qquad \Delta H(0K) = 77.0\ kcal/mol \qquad \text{(CH5)}$$

In addition, several H-atom loss channels exist with $\Delta H(0\ \text{K}) > 90$ kcal/mol. A simplified C_7H_5 PES is shown in Figure 3.11 of the Supporting Information (Section 3.7). There are multiple pathways to the products of channels 3-5, with a minimum of two isomerization steps prior to dissociation in each case. There are exit barriers for each of these channels, ∼13-22 kcal/mol for channel 3, ∼15-17 kcal/mol for channel 4, and ∼8-10 kcal/mol for channel 5. The dissociation products of channels 3-5 and their subsequent recombination processes have important implications for terrestrial combustion processes, as well as atmospheric photochemistry and molecular weight growth in the outer planets and their moon systems.[100,122–128]

The flash pyrolysis/photoionization experiments in which fulvenallenyl was observed yielded smaller mass fragments as well;[116] subsequent work proposed that these originated from fulvenallenyl dissociation via channels 3-5 in the pyrolysis source.[129] A detailed combustion kinetics model[100,101] based on theoretical work[117,119,130,131] produced good agreement with the concentration *vs.* temperature profiles of the species in channels 1-5 that were produced from toluene in combustion flow reactors and detected by photoionization mass spectrometry. The importance of these models to understanding the combustion of aromatic hydrocarbons demands closer inspection of the constituent reactions.

As the previous study of fulvenallene photodissociation was only sensitive to H-atoms, and because such studies on the fulvenallenyl radical are non-existent, we investigated the ultraviolet photodissociation dynamics of both of these species *via* molecular beam

photofragment translational spectroscopy at 248 nm and 193 nm. In principle, all reaction products of channels 1-5 can be detected by this technique.

For fulvenallene photodissociation at both wavelengths, we only observe evidence for channel 1. The fulvenallenyl photoproduct from this channel then absorbs another photon, and evidence for channels 3-5 is observed for the radical photodissociation. Each process is consistent with a statistical mechanism on the ground electronic state, with dissociation occurring directly for channel 1 from fulvenallene, and over exit barriers for channels 3-5 from the fulvenallenyl radical. These assignments are based on consideration of the experimental product translational energy distributions and their comparison to results from statistical theories of reactivity.

3.2 Experimental

Fulvenallene synethesis

Fulvenallene was produced via flash vacuum thermolysis of homophthalic anhydride vapor at the surface of a resistively heated wire.[113,132] The product of the reaction was isolated as a yellow crystalline solid in a liquid N_2 cold trap, warmed to 0 ^oC, and transferred to an evacuated cylinder (usually 3-5 Torr) that was then filled to 3000 Torr with Ar or He. NMR spectroscopy confirmed the successful production of fulvenallene, ^{1}H-NMR (400 MHz, C_6H_6, Me_4Si): δ (ppm) 4.75 (2H, s, =CH2), 6.27 (2H, m, *meta*–CH), 6.47 (2H, m, *ortho*–CH). The NMR data match spectra reported previously.[113]

A typical mass spectrum of fulvenallene measured in our instrument is provided in Figure 3.12 of the Supporting Information (Section 3.7), and shows good agreement with a previously reported electron impact ionization mass spectrum.[106] The IP of $m/z = 90$ was determined by measurement of an electron impact ionization efficiency curve (IEC) as reported previously.[105] The appearance potential of 8.3 eV determined using this technique closely matches the previously measured adiabatic IP of 8.22 eV.[116]

Photodissociation experiments

Photodissociation studies of fulvenallene and the fulvenallenyl radical were carried out on a modified crossed molecular beam apparatus with a fixed source and rotatable detector as described previously.[11,133,134] A pulsed molecular beam of fulvenallene in a noble gas carrier was produced by supersonic expansion through the orifice of a piezoelectric valve. The molecular beam was collimated *via* passage through two skimmers. A retractable, slotted chopper wheel enabled characterization of the beam velocity, typically 1700 m/s in He and 600 m/s in Ar carrier gas; typical speed ratios, *i.e.* the ratio of the beam velocity to velocity spread, were found to be 12-18. The molecular beam was crossed orthogonally with a focused, unpolarized laser pulse from a Lambda Physik LPX 220i excimer laser at either 248 nm or

193 nm. Operation of the laser at half the 200 Hz repetition rate of the pulsed valve allowed for shot-to-shot subtraction of the background signal.

Photofragments were collected as a function of laboratory scattering angle, Θ_{LAB}, in the plane defined by the laser and molecular beam. An electron impact ionizer nested within three differentially pumped regions and operated at 80 eV produced cations that were mass selected by a quadrupole filter and detected with a Daly style ion detector.[85,135] The additional capability to tune the electron energy to as low as 4 eV enabled measurement of IECs.[105] A multichannel scalar collected and binned ion signal as a function of arrival time to produce time-of-flight (TOF) spectra.

Center-of-mass translational energy distributions, $P(E_T)$, were determined via a forward convolution method in the PHOTRAN program,[136] whereby TOF spectra are simulated using a trial $P(E_T)$ that is iteratively adjusted until agreement with all experimental TOF spectra is reached. In the case of secondary photodissociation of primary photoproducts, the trial distribution is additionally convoluted over the primary photodissociation $P(E_T)$ in the CMLAB2 program[137] to obtain the simulated TOF spectra.

Computational methods

Electronic Structure. Optimized geometries were calculated at the B3LYP/6-31G++(d,p) level implemented in Gaussian 09.[138] Time-dependent density functional theory (TD-DFT) using this functional and basis set were used to calculate electronic excited state energies and oscillator strengths of fulvenallene and the fulvenallenyl radical, as shown in Table 3.4. For these excited state properties the current TD-DFT method and functional produces good agreement with more sophisticated EOM-CCSD calculations, which themselves agree well with experimental results.[139,140]

RRKM Kinetics. Isomerization and dissociation kinetics were calculated using the full C_7H_5 surface developed by da Silva and Trevitt.[121] All dissociation and isomerization pathways on this surface involve passage over barriers that we treat as tight transition states. Stationary point energies and vibrational modes calculated by da Silva and Trevitt using G3SX B3LYP/6-31G(2df,p) were used, with internal rotational modes treated as hindered rotors.

Unimolecular rate constants for reactions across this surface were calculated using Rice-Ramsperger-Kassel-Marcus (RRKM).[141–143] The RRKM rate constant is given by

$$k(E) = \sigma \frac{W^{\ddagger}(E - E_o)}{h\rho(E)} \tag{3.1}$$

where σ is the reaction path degeneracy,[144] $W^{\ddagger}(E\text{-}E_o)$ is the sum of states of the transition state, h is the Planck constant, and $\rho(E)$ is the rovibrational density of states of the reactant at energy E. The steady-state approximation is applied to the concentration of intermediates, and the product channels 3-5 and the H-loss channels are treated as sinks. Ratios of asymptotic

product concentrations give branching in the statistical limit among the various product channels. The RRKM calculations were implemented using a custom-written code.

3.3 Results

All TOF experimental data are shown normalized by on-axis $m/z = 90$ signal intensity (per 1000 counts) and then scaled to counts per 10^6 laser shots. Spectra with low signal are further scaled for comparison purposes as specified on an individual basis. Based on the known energetics, the maximum laboratory frame scattering angles Θ_{LAB} for the heavy photofragment from fulvenallene dissociation channels 1 and 2 under different experimental conditions are shown in Table 3.1.

Fulvenallene photodissociation

For photodissociation of fulvenallene seeded in an Ar beam, $m/z = 89$ ($C_7H_5^+$) TOF spectra were measured at laboratory scattering angles from 3^o up to 12^o at 248 nm and up to 15^o at 193 nm. No signal was observed at higher scattering angles. Figures 3.2 and 3.3 show representative TOF spectra collected at 4^o and 10^o with laser fluences of $\Phi_{248nm} = 25$ mJ cm^{-2} per pulse and $\Phi_{193nm} = 300$ mJ cm^{-2} per pulse respectively. The higher fluence at 193 nm was necessitated by considerably lower signal levels at that wavelength, reflecting the lower oscillator strength (Table 3.4). Data collected for very long scans at lower fluence, $\Phi_{193nm} = 50$ mJ cm^{-2}, do not present any deviations from the data included here. All spectra in Figures 3.2-3.3 are comprised of a single peak.

Table 3.1: Heavy photofragment maximum scattering angles for fulvenallene photodissociation channels 1-2 for different excitation wavelengths and carrier gases. The C_2H_2-loss photoproducts are not constrained when Ar is the carrier.

Channel	**Maximum Θ_{LAB}**	
	He	Ar
H-loss		
248 nm	6	18
193 nm	9	26
C_2H_2-loss		
248 nm	34	-
193 nm	61	-

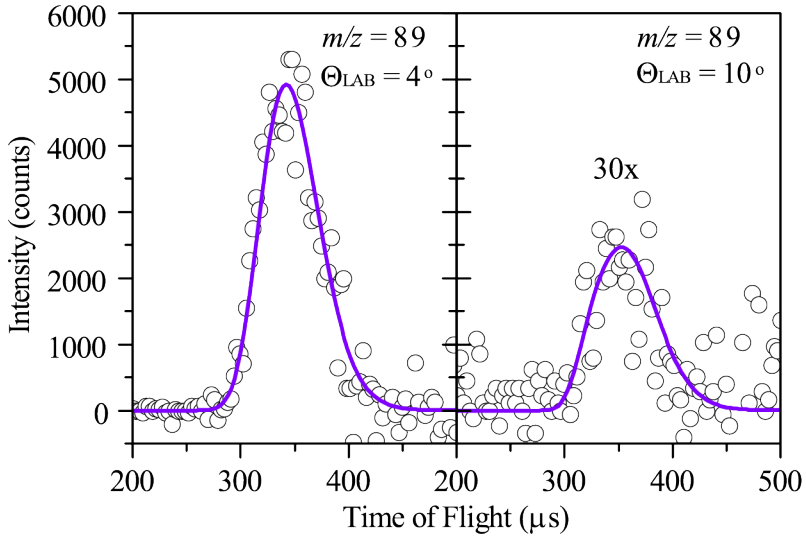

Figure 3.2: TOF spectra for $m/z = 89$ at $\Theta_{LAB} = 4^o$ and 10^o ($\Phi_{248nm} = 25$ mJ cm^{-2}). The solid line simulations are generated using the experimental H-atom loss *P(E$_T$)* in Figure 3.8.

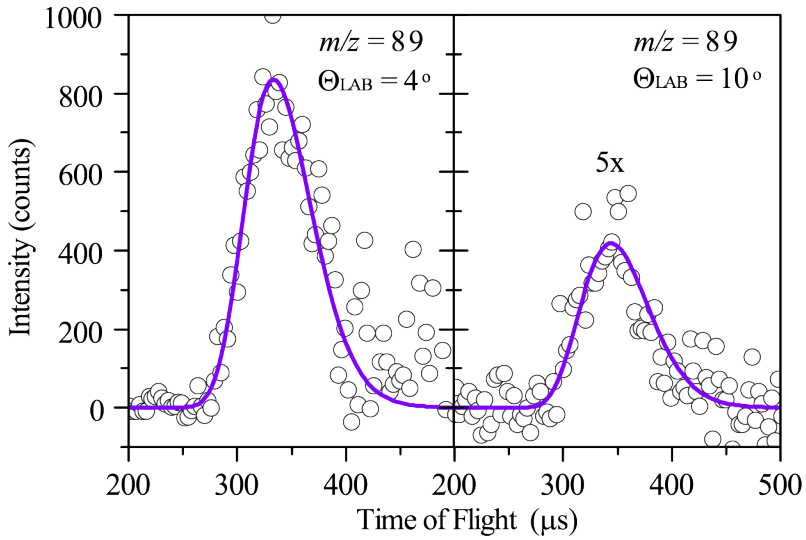

Figure 3.3: TOF spectra for $m/z = 89$ at $\Theta_{LAB} = 4^o$ and 10^o ($\Phi_{193nm} = 300$ mJ cm^{-2}). The solid line simulations are generated using the experimental H-atom loss *P(E$_T$)* in Figure 3.8.

The H-atom counter-fragment for this dissociation channel cannot be detected due to its short residence time in the ionizer and extremely large Newton sphere, coupled with high background signal at $m/z = 1$. No evidence for the predicted cyclopentadienylidene + acetylene dissociation products (channel 2) is observed.[117]

Primary photofragment characterization

The large signal at $m/z = 89$ enables physical characterization of this primary photofragment. Figure 3.4 shows IECs for $m/z = 89$ along the molecular beam axis with no photodissociation, as well as 4^o away from the molecular beam axis with the 248 nm dissociation laser turned on. Along the molecular beam axis, the IEC intercepts the energy axis at 12.1 eV and $m/z = 89$ signal is attributed to dissociative ionization (DI) of fulvenallene in the ionizer. When the IEC for $m/z = 89$ is collected at $\Theta_{LAB} = 4^o$, the appearance potential shifts to 8.4 eV, in acceptable agreement with the experimentally measured value of 8.19 eV for the adiabatic IP of the fulvenallenyl radical.[116] The fragmentation pattern of the $m/z = 89$ radical is shown in Figure 3.13 of the Supporting Information (Section 3.7). This spectrum was collected by measuring TOF spectra at $\Theta_{LAB} = 5^o$ with m/z values covering all possible combinations of up to seven C atoms and five H atoms, using an electron impact ionization energy of 80 eV. The signal for each spectrum was normalized by the $m/z = 89$ signal at 5^o that was continually remeasured throughout the experiment.

At 248 nm, there is insufficient internal energy following dissociation to allow for isomerization to other C_7H_5 isomers on the reported PES.[121] The next lowest energy isomer lies 38.7 kcal/mol above fulvenallenyl (**12**, Figure 3.11), while $E_{avail} = 33$ kcal/mol at 248nm. Although isomerization is possible at 193 nm ($E_{avail} = 66$ kcal/mol), C_7H_5 molecules with enough translational energy to scatter into $\Theta_{LAB} > 3^o$ will have insufficient internal energy to surmount the 64.5 kcal/mol isomerization barrier, and we report only data collected at $\Theta_{LAB} \geq 4^o$. These considerations further support our assertion that the $m/z = 89$ signal should be attributed solely to the fulvenallenyl radical.

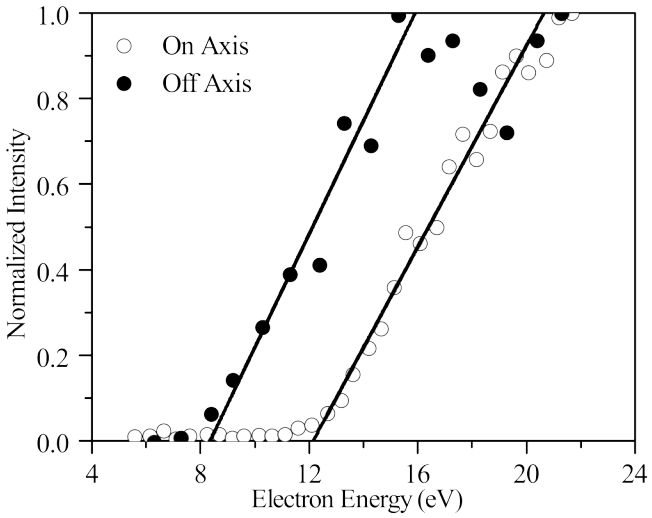

Figure 3.4: Ionization efficiency curves for $m/z = 89$ taken along the molecular beam axis with the laser off (○) and 4^o off the molecular beam axis with the laser on (●). On axis the appearance potential is 12.1 eV, whereas off axis it is 8.4 eV.

Evidence for secondary photodissociation

While studying fulvenallene photodissociation, there initially seemed to be evidence for acetylene-loss via channel 2. This channel should produce signal at $m/z = 64$ ($C_5H_4^+$) and $m/z = 26$ ($C_2H_2^+$), and there was extremely weak signal observed at $m/z = 64$ ($C_5H_4^+$) up to 30^o. The $m/z = 26$ ($C_2H_2^+$) fragment was observed over the full $\sim 45^o$ angular range accessible by our apparatus. However, the observed counts for $m/z = 64$ were consistent with the expected ^{13}C isotope ratio for C_5H_3 based on counts for this species at $m/z = 63$, and the TOF spectra were identical. In addition, $m/z = 63$ ($C_5H_3^+$) was observed at LAB angles as large as 40^o in the experiment, which exceeds the maximum $\Theta_{LAB} = 34^o$ for channel 2 following 248 nm photoexcitation of fulvenallene (see Table 3.1). These observations suggest that the signals at $m/z = 64$ and 63 do not arise from channel 2.

The TOF spectra for masses below $m/z = 64$ taken within the allowed angular range for H-atom loss from fulvenallene (Table 3.1) display at least two features that have different laser fluence dependence, as shown in Figure 3.5. There is a fast feature apparent for both $m/z = 62$ ($C_5H_2^+$) and $m/z = 50$ ($C_4H_2^+$) at high laser fluence that disappears at lower laser fluence. The slower feature present at all laser fluences is due to DI of fulvenallenyl. If two dissociation channels were both active and caused by single-photon dissociation of fulvenallene, the relative intensity of both features would be independent of laser fluence. The differing fluence dependences for the two peaks suggests that the faster peak in the TOF spectra for $m/z < 64$ arises from secondary photodissociation of fulvenallenyl radicals that absorb a second photon after they are produced; a model showing that such a mechanism is consistent with the observed fluence dependences is discussed in more detail in the Supporting Information (Section 3.7).

Fulvenallenyl photodissociation

Secondary photodissociation of the fulvenallenyl primary photofragment was studied at 248 and 193 nm at laser fluences $\Phi_{248nm} = 420$ mJ cm^{-2} and $\Phi_{193nm} = 300$ mJ cm^{-2}. These experiments were performed using He as the carrier gas. For channels 3-5, the Newton circles are such that the laboratory angular range over which scattering can occur is not kinematically constrained, in contrast to channel 1 for fulvenallene photodissociation.

Figures 3.6 and 3.7 show TOF spectra collected for m/z = 63 ($C_5H_3^+$), $m/z = 50$ ($C_4H_2^+$), $m/z = 39$ ($C_3H_3^+$) and $m/z = 26$ ($C_2H_2^+$) at $\Theta_{LAB} = 10^o$ for photoexcitation at 248 nm and 193 nm, respectively. These TOF spectra were collected beyond the Newton circles for H-loss from fulvenallene, and therefore do not contain the slow feature due to DI of the fulvenallenyl radical seen in Figure 3.5. Additional TOF spectra at $\Theta_{LAB} = 30^o$ are shown in Figure 3.14. These ion masses correspond to the parent fragments of the lowest energy dissociation pathways of the fulvenallenyl radical, channels 3-5. For both wavelengths, these features were observed over the full $\sim 45^o$ angular range accessible by our apparatus. Signal collected at $m/z = 88$ was entirely consistent with DI of fulvenallenyl, and no signal that could be attributed to the H-atom loss channels available to the fulvenallenyl radical was observed.

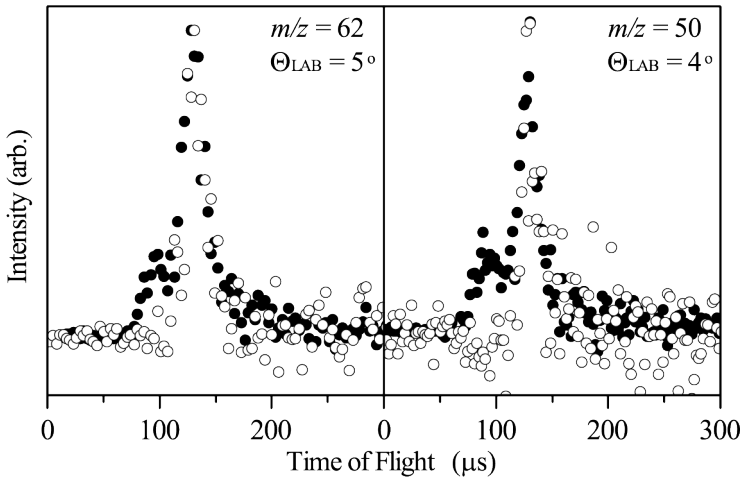

Figure 3.5: Left panel: $m/z = 62$ at 330 mJ cm^{-2} ($\bullet$) and 50 mJ cm^{-2} ($\circ$) per pulse at $\Theta_{LAB} = 5^o$, right panel: $m/z = 50$ at 330 mJ cm^{-2} ($\bullet$) and 25 mJ cm^{-2} ($\circ$) per pulse at $\Theta_{LAB} = 4^o$. The 248 nm excimer is used for these measurements. These spectra are normalized to the slow, intense feature due to DI of the fulvenallenyl radical in the ionizer.

Beyond the Newton circles for fulvenallene H-atom loss, there is no dissociative ionization signal from the primary photofragment (fulvenallenyl), and thus no signal for $m/z > 64$. TOF spectra were collected at $m/z = 64$, 63, 62, 61, 60, 52, 51, 50, 49, 48, 39, 38, 37, 36, 27, 26, 25, 24, 16, 15, 13, and 12. It is not possible to measure signal at $m/z = 40$, $m/z = 28$ and $m/z = 14$ due to high argon and nitrogen background in the ionizer. These TOF spectra allow a construction of the fragmentation patterns of the $m/z = 63$ and $m/z = 50$ photofragments by normalizing the signal collected at each m/z value (Figure 3.15 of the Supporting Information, Section 3.7).

3.4 Analysis

Primary photodissociation of fulvenallene

For each dissociation channel, the TOF spectra are governed by the center-of-mass (CM) angular and translational energy distribution, P(E_T, Θ), which we assume are uncoupled to yield

$$P(E_T, \Theta) = P(E_T)I(\Theta) \tag{3.2}$$

Here P(E_T) is the CM translational energy distribution and I(Θ) is the CM angular distribution. All TOF spectra can be adequately simulated by assuming isotropic angular distributions. For a given dissociation channel, conservation of linear momentum ensures both photofragments are simulated by the same P(E_T) distribution.

At 248 nm, a fulvenallene molecule dissociating via H-atom loss channel 1 will have E_{avail} = 33 kcal/mol available for internal and translational energy partitioning. At 193 nm, E_{avail} = 66 kcal/mol for this channel. The $P(E_T)$ distributions that best simulate $m/z = 89$ ($C_7H_5^+$) TOF spectra at all observed laboratory angles are shown in Figure 3.8. For these distributions, the peak translational energy, average translational energy $\langle E_T \rangle$, maximum translational energy $E_{T,max}$, and average fraction of the available energy that goes into product translation $\langle f_T \rangle$, are shown in Table 3.2. These characteristics for the $P(E_T)$ distribution measured by Giegerich and Fischer for the H-atom counter-fragment of this channel collected at 247 nm are also shown for comparison.[118]

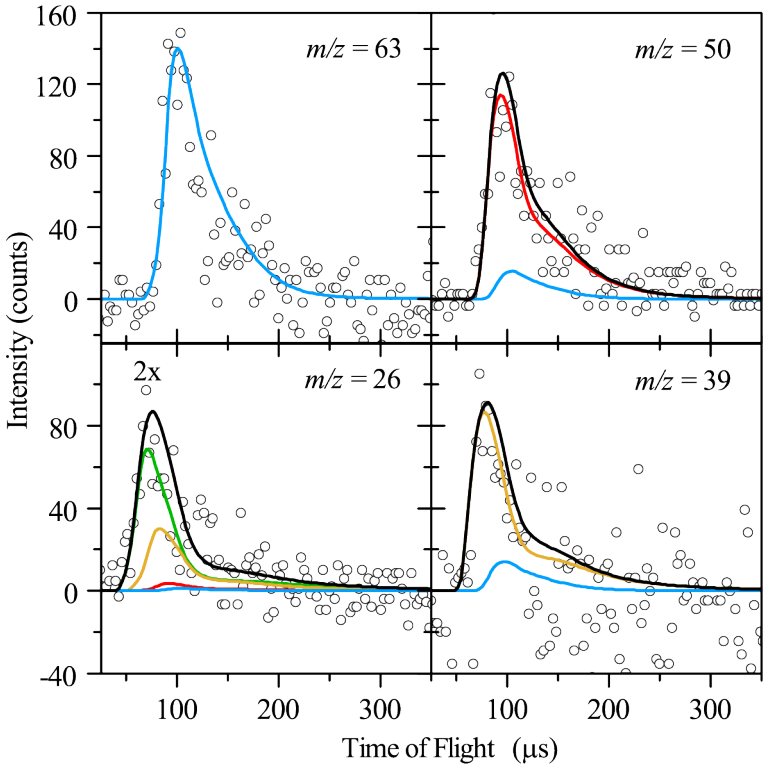

Figure 3.6: TOF spectra for $m/z = 63$, $m/z = 50$, $m/z = 39$ and $m/z = 26$ at $\Theta_{LAB} = 10^o$ at 248 nm (Φ_{248nm} = 420 mJ cm^{-2}). The blue ($m/z = 63$) and green ($m/z = 26$) simulations are generated using the $P(E_T)$ in Figure 3.9a, while the red ($m/z = 50$) and yellow ($m/z = 39$) simulations are generated using the $P(E_T)$ in Figure 3.9b. For TOF spectra with multiple features, the total simulation is shown in black. Note that DI of the three heavier fragments along with ionization of C_2H_2 contribute to the $m/z = 26$ TOF spectrum, as indicated by the presence of all four colors.

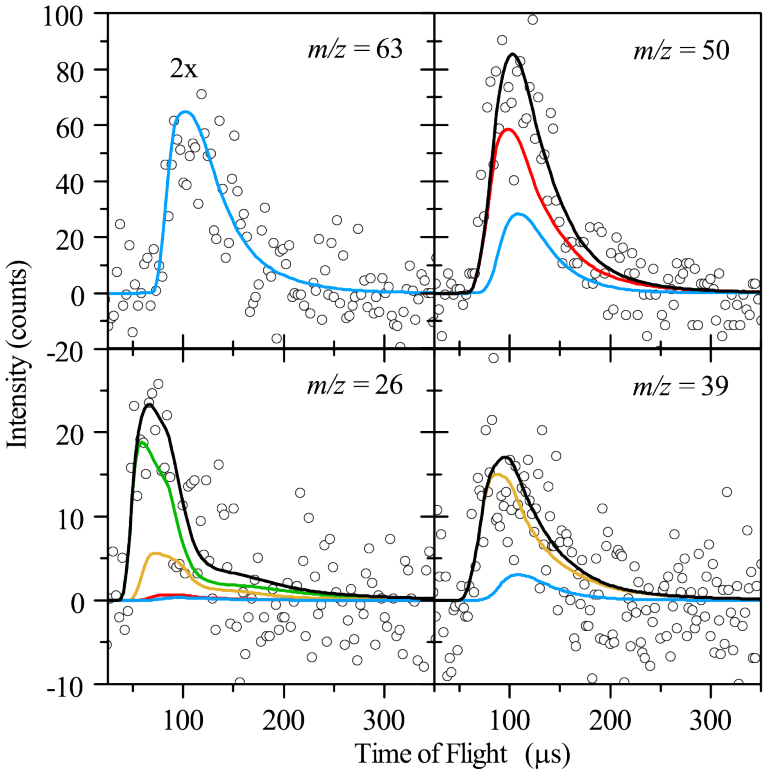

Figure 3.7: TOF spectra for $m/z = 63$, $m/z = 50$, $m/z = 39$ and $m/z = 26$ at $\Theta_{LAB} = 10^o$ at 193 nm ($\Phi_{193nm} = 300$ mJ cm^{-2}). The blue ($m/z = 63$) and green ($m/z = 26$) simulations are generated using the $P(E_T)$ in Figure 3.9c, while the red ($m/z = 50$) and yellow ($m/z = 39$) simulations are generated using the $P(E_T)$ in Figure 3.9d. For TOF spectra with multiple features, the total simulation is shown in black.

A statistical dissociation process with no exit barrier is expected to produce a P(E_T) distribution similar to the prior distribution,[145] which has the analytical form

$$P(E_T) \propto E_T^{1/2}\ \rho_{vib}(E_{avail} - E_T) \tag{3.3}$$

In Equation 3.3, ρ_{vib} is the vibrational density of states evaluated as a function of $E_{avail} - E_T$, where E_{avail} is the difference between the absorbed photon energy and the activation barrier for the reaction, and E_T is the translational energy of the fulvenallenyl product.[145] There is reasonable agreement both at 248 nm and 193 nm between the $P(E_T)$ that best simulates the experimental TOF spectra and their respective single-photon prior distributions shown in Figure 3.8.

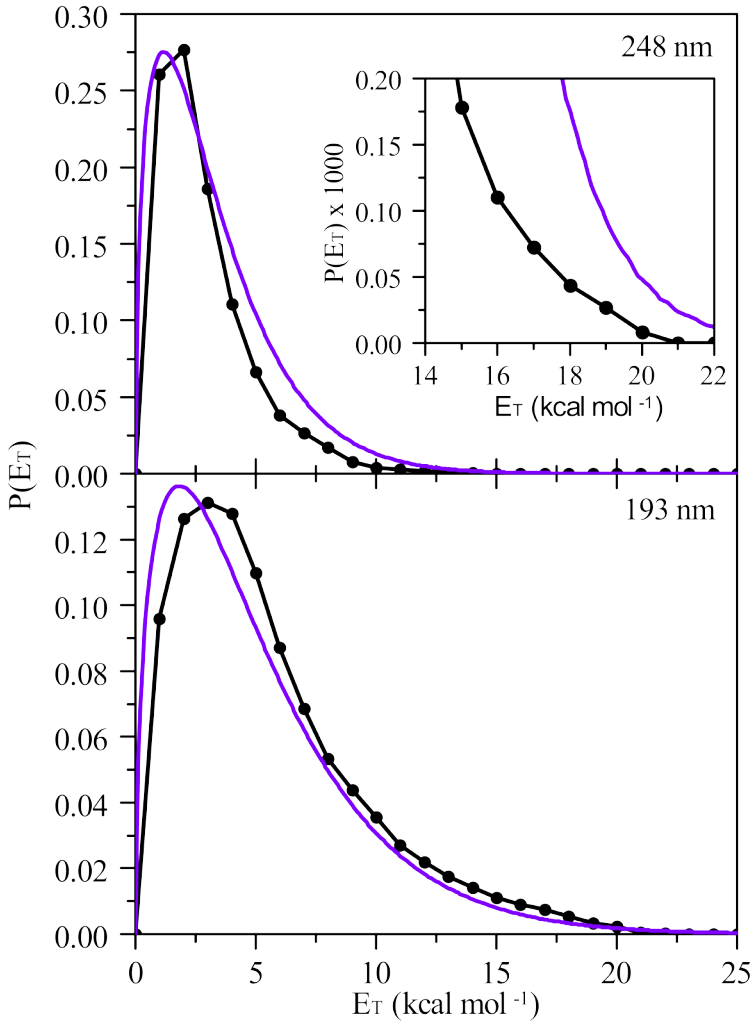

Figure 3.8: The $P(E_T)$ distributions that best match experimental data (black) and one-photon prior distributions (purple) for fulvenallene H-atom loss following photoexcitation at 248 nm (top) and 193 nm (bottom). The tail at high E_T is necessary to adequately simulate all TOF spectra at 248 nm.

Secondary photodissociation of the fulvenallenyl radical

Fulvenallenyl radicals that absorb a second photon will have sufficient energy to undergo secondary photodissociation. These radicals are produced with a distribution of internal energies determined by the $P(E_T)$ distributions for H-atom loss from fulvenallene (Figure 3.8). In order to obtain the correct $P(E_T)$ distributions for the secondary photodissociation of fulvenallenyl, it is necessary to convolute the secondary $P(E_T)$ distributions over these primary H-loss distributions, which can be done in the analysis program CMLAB2. Fulvenallenyl dissociation via channels 3+4 gives rise to parent ion signals at $m/z = 63$ ($C_5H_3^+$) and

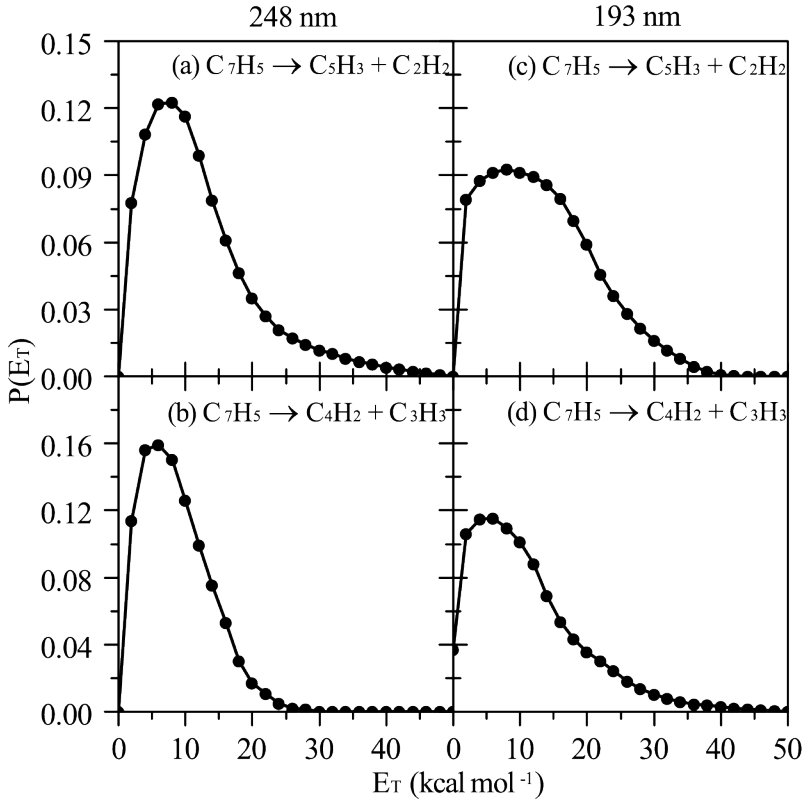

Figure 3.9: Center-of-mass $P(E_T)$ distributions for secondary photodissociation of the fulvenallenyl radical at 248 nm (left) and 193 nm (right) to produce C_5H_3 + C_2H_2 (top) and C_4H_2 + C_3H_3 (bottom).

m/z = 26 ($C_2H_2^+$), while channel 5 produces parent ion signals at m/z = 50 ($C_4H_2^+$) and m/z = 39 ($C_3H_3^+$). Conservation of linear momentum requires the two fragments from each channel to be simulated by the same $P(E_T)$. This condition is satisfied for the $P(E_T)$ distributions shown in Figures 3.9a-d; the characteristics of these distributions are listed in Table 3.3. The fitting procedure in now described in more detail.

As the heaviest secondary photofragment, the m/z = 63 ($C_5H_3^+$) TOF spectra can be used to construct the full $P(E_T)$ for the fulvenallenyl → C_5H_3 + C_2H_2 channel without having to contend with DI signal from other fragments. As such, the m/z = 63 ($C_5H_3^+$) TOF spectra shown in Figures 3.6 and 3.7 are adequately simulated using only contributions from the m/z = 63 ($C_5H_3^+$) secondary photoproduct, i.e. the $P(E_T)$ distributions in Figures 3.9a and 3.9c.

The m/z = 50 ($C_4H_2^+$) and m/z = 39 ($C_3H_3^+$) TOF spectra shown in Figures 3.6 and 3.7 differ significantly from the simulation produced for DI of m/z = 63 ($C_5H_3^+$), which does not adequately simulate the fast edge of the peak. Agreement with the experimental m/z = 50 ($C_4H_2^+$) TOF spectra requires simulations including contributions from the m/z = 50 ($C_4H_2^+$)

Table 3.2: Characteristics of the $P(E_T)$ distributions in Figure 3.8 determined for C_7H_5, and the 247 nm $P(E_T)$ for H measured by Giegerich and Fischer.[118] At 248 nm and 193 nm, E_{avail} = 33 kcal/mol and 66 kcal/mol respectively.

Fragment	**Peak (kcal/mol)**	$\langle E_T \rangle$ **(kcal/mol)**	$E_{T,max}$ **(kcal/mol)**	$\langle f_T \rangle$
248 nm				
C_7H_5	1.5	2.9	21	0.09
H[a]	1.2	3.2	23	0.09
prior	1.2	3.2	-	0.09
193 nm				
C_7H_5	3.1	5.6	22	0.09
prior	1.8	5.1	-	0.08

a. Data from Ref. [118].

Table 3.3: Characteristics of the $P(E_T)$ distributions in Figure 3.9.

Channel	**Peak (kcal/mol)**	$\langle E_T \rangle$ **(kcal/mol)**	$E_{T,max}$ **(kcal/mol)**	E_{avail} **(kcal/mol)**	$\langle f_T \rangle$
248 nm					
C_2H_2 loss	7.0	12.1	48	74	0.16
C_3H_3 loss	6.0	9.1	28	71	0.13
193 nm					
C_2H_2 loss	8.0	13.3	42	139	0.10
C_3H_3 loss	5.0	11.3	48	137	0.08

photofragment of channel 5, as well as DI from $m/z = 63$ ($C_5H_3^+$). Simulation of the $m/z = 39$ ($C_3H_3^+$) TOF spectra include contributions from the momentum-matched propargyl counter-fragment for channel 5, as well as DI signal from $m/z = 63$ ($C_5H_3^+$).

Construction of the $P(E_T)$ for C_4H_2 + C_3H_3 is complicated by the fact that the parent ions and all DI fragments produced by either of these photofragments are also formed by DI of $m/z = 63$ ($C_5H_3^+$). The $P(E_T)$ distributions for this channel (Figures 3.9b,d) are constructed by finding the distribution that best simulated $m/z = 50$ ($C_4H_2^+$) and $m/z = 39$ ($C_3H_3^+$) signal across the entire angular range, and which all have a consistent weighting of

the $m/z = 63$ ($C_5H_3^+$) contribution.

The TOF spectra for $m/z = 26$ ($C_2H_2^+$) are simulated using a contribution from the momentum-matched acetylene counter-fragment for the C_5H_3 + C_2H_2 dissociation channel, Figures 3.9a and 3.9c, as well as DI signal from the $m/z = 63$ ($C_5H_3^+$), $m/z = 50$ ($C_4H_2^+$), and $m/z = 39$ ($C_3H_3^+$) fragments. Given that all other photofragments dissociatively ionize to $m/z = 26$ ($C_2H_2^+$), the weighting of each contribution to these TOF spectra are calculated using the product branching ratio (details below). The major contributor to these TOF spectra is the parent ion from the acetylene photofragment produced through channels 3+4.

The experimental branching ratio (BR) between channel 5 and channels 3+4 can be calculated according to

$$BR\left(\frac{CH(3+4)}{CH(5)}\right) = \frac{W_{CH(3+4)}}{W_{CH(5)}}\frac{\sigma_{CH(5)}}{\sigma_{CH(3+4)}}\frac{f_{CH(5)}}{f_{CH(3+4)}} \tag{3.4}$$

In Equation 3.4, W_i is the weighted fraction of the $P(E_T)$ of channel i used to simulate the experimental spectra, σ_i is the ionization cross-section of the species i, calculated according to Fitch and Sauter,[146] and f_i is the relative fraction of the m/z value in the mass spectrum of the parent species.

To obtain f_i requires a mass spectrum for each photofragment used for the BR calculation. The fragmentation pattern collected off-axis (see Figure 3.15) was used for the C_5H_3 photofragment, while previously reported mass spectra[147,148] were used for C_4H_2. The fragmentation pattern collected off-axis for the mass 50 photofragment (Figure 3.15) is in excellent agreement with the mass spectrum for diacetylene. For C_3H_3, we used the fragmentation pattern for scattered products from allene photodissociation at 193 nm (see Figure 3.16), since the dominant channel is H-atom loss to produce propargyl radicals.[149] The experimental data indicate that C_3H_3-loss (channel 5) accounts for 85 ± 10% and 80 ± 15% of fulvenallenyl decomposition at 248 nm and 193 nm respectively. The uncertainty in these branching ratios comes from the different weightings that can be used to adequately simulate the $m/z = 50$ and $m/z = 39$ TOF spectra.

The branching ratio calculated using Equation 3.4 can be compared with the results given by an RRKM calculation that represents the statistically expected branching ratio. Such a calculation requires consideration of the internal energy remaining in the primary photofragment. The fulvenallenyl radical internal energy is taken into account by integrating the RRKM analysis over the primary $P(E_T)$ distributions. The RRKM analysis predicts that C_3H_3-loss accounts for 70% and 63% of fulvenallenyl decomposition at 248 nm and 193 nm respectively. The RRKM predictions are in reasonable agreement with the experimentally determined branching ratio between the C_3H_3-loss and C_2H_2-loss channels. The experimental and theoretical branching ratios display the same qualitative trend in which the contribution from C_2H_2-loss increases slightly for higher excitation energy.

The RRKM calculations also predict that the combined H-atom loss channels accessible to the fulvenallenyl radical are negligible (< 1% of dissociation) at both wavelengths used in

this study. For the two acetylene-loss channels, the n-C_5H_3 isomer is calculated to account for 53 % and 46 % of the C_5H_3 signal at 248 nm and 193 nm respectively.

3.5 Discussion

This experiment was aimed at elucidating the primary photodissociation channels of fulvenallene at 248 and 193 nm. During the course of these investigations, it became clear that some of the fulvenallenyl radical produced from fulvenallene absorbs an additional photon and subsequently dissociates. In this section, the dynamics of the primary and secondary dissociation channels are considered in more detail.

The fulvenallene H-atom loss channel was previously measured by Giegerich and Fischer.20 The characteristics of the $P(E_T)$ that best simulates all of our 248 nm C_7H_5 TOF data are in excellent agreement with their study (Table 3.2) in which the H-atom counter-fragment was detected, with both distributions peaking close to 0 kcal/mol.[118] Our experimental $P(E_T)$ also compares reasonably well to a prior distribution for an idealized statistical ground state process. It is therefore likely that this channel proceeds *via* internal conversion to the ground electronic state, followed by IVR and then dissociation, consistent with the mechanism proposed by Giegerich and Fischer. While no previous work has been done on the photodissociation of fulvenallene at 193 nm, the dynamics appear to be similar to 248 nm in occurring through a statistical ground state mechanism. The lack of evidence for acetylene-loss from fulvenallene suggests a low probability for intersystem crossing[117] relative to H-atom loss.

The C_7H_5 photoproduct from fulvenallene dissociation was identified as the fulvenallenyl radical based on agreement with the previously measured ionization potential.[116] Measurements by Giegerich and Fischer give a 100 ns lifetime for fulvenallenyl formation, with counts rising to 70% of their maximum value within the 30 ns duration of our laser pulse,[118] and the lifetime should be even shorter at 193 nm. It is therefore likely that nascent fulvenallenyl is formed in time to absorb a second photon. The experimentally observed laser fluence dependence of the $m/z = 89$ signal agrees quite well with a consecutive two-photon dissociation reaction (see the Supporting Information, Section 3.7). This is consistent with the interpretation that the fulvenallenyl radical undergoes secondary photodissociation following absorption of a second ultraviolet photon.

The only previous study on the UV photophysics of the fulvenallenyl radical probed electronic transitions down to 365 nm.[120] The present study demonstrates that absorption also occurs at 248 nm and 193 nm. Theoretical work on the C_7H_5 surface identified the lowest energy dissociation pathways of acetylene-loss (+ i/n-C_5H_3) and propargyl-loss (+ C_4H_2), along with several higher energy H-atom loss channels.[121] Both of the heavy fragment channels were observed in this study, with no evidence for H-atom loss. The unimportance of H-atom loss and the dominance of propargyl-loss are consistent with the RRKM branching ratios and with previous theoretical investigations.[129] The diacetylene photoproduct is specifically identified by the excellent agreement between the mass spectrum constructed from data

collected off-axis for the $m/z = 50$ fragment and its dissociative ionization (Figure 3.15) and previously reported mass spectra for this species.[147,148]

Production of i-C_5H_3 and n-C_5H_3 isomers from Channels 3 and 4 is expected,[150] but these isomers cannot be distinguished due to their similar IP values of 8.28 eV and 8.19 eV, respectively, and because of the similar energetics of their dissociation. Previous calculations[129] show higher concentrations of the n-C_5H_3 isomer over a large temperature and pressure range, whereas the RRKM analysis conducted here finds each isomer to be of comparable importance. The fragmentation pattern constructed for the $m/z = 63$ fragment from data collected off-axis (Figure 3.15) shows significant differences from a previously measured mass spectrum for n-C_5H_3.[151] While most the same mass fragments appear in the two mass spectra, the relative intensities of the peak clusters around the parent ion mass and $m/z = 50$ are reversed. This discrepancy may reflect production of appreciable amounts of both i-C_5H_3 and n-C_5H_3 during fulvenallenyl photodissociation, which is consistent with the RRKM prediction. In calculating the product channel branching ratios, the ionization cross sections of these two isomers are weighted according to their RRKM branching.

At both 248 nm and 193 nm, the distributions for the two secondary photodissociation channels peak away from 0 kcal/mol. The characteristics of these distributions are consistent with internal conversion to the ground state followed by statistical dissociation over an exit barrier. The $P(E_T)$ distributions for 193 nm secondary photodissociation are much broader and peak at slightly higher energies than at 248 nm, in line with expectations for higher E_{avail}. There is only a modest decrease in $\langle f_T \rangle$ with the much higher E_{avail} conferred by two 193 nm photons. At both dissociation wavelengths, the peak and average positions of these distributions are in line with calculated exit barrier heights of ∼16-17 kcal/mol for C_2H_2-loss and ∼8-10 kcal/mol for C_3H_3-loss (there are multiple pathways to each of these dissociation channels),[121] since one generally expects only part of the exit barrier height to be channeled into product translation.[152] In addition, the $P(E_T)$ distribution for channel 5, which is predicted to have the smaller exit barrier, peaks at lower E_T than for channels 3+4.

The general agreement between the RRKM and experimentally determined product branching ratios supports the assignment of statistical dissociation mechanisms for the product channels. The statistical nature of the dissociation reactions studied here leads to product branching ratios that agree reasonably well with those calculated by da Silva *et al.* for thermal decomposition of fulvenallenyl.[129]

3.6 Conclusion

Fulvenallene photodissociates exclusively via H-atom loss following 248 nm and 193 nm photoexcitation to produce the fulvenallenyl radical, $C_7H_6 \rightarrow C_7H_5 + H$. The analysis of the TOF spectra supports internal conversion to the ground state followed by statistical dissociation. The lack of signal corresponding to the cyclopentadienylidene + acetylene dissociation channel demonstrates that the probability of intersystem crossing is low.

Secondary photodissociation of the primary fulvenallenyl photofragment occurs at both wavelengths and results in at least two dissociation channels: acetylene-loss to produce a C_5H_3 radical (i- and n-isomers both predicted), $C_7H_5 \rightarrow C_5H_3 + C_2H_2$; and propargyl radical loss to produce diacetylene, $C_7H_5 \rightarrow C_4H_2 + C_3H_3$. Based on the consistency between the $P(E_T)$ distributions for these channels and the calculated exit barrier heights, and the reasonable agreement between the experimental branching ratios with those calculated using RRKM theory, it appears that the photodissociation of fulvenallenyl proceeds by internal conversion followed by ground state statistical dissociation for the radical. The predicted H-atom loss channels at much higher energy were not observed, and do not appear to play a meaningful role in the dissociation dynamics of the fulvenallenyl radical.

The dissociation channels reported here encompass the most important unimolecular photochemistry for fulvenallene and the fulvenallenyl radical. The statistical nature of these reactions suggests they are also the most important unimolecular thermal decomposition reactions for these species.

3.7 Supporting Information

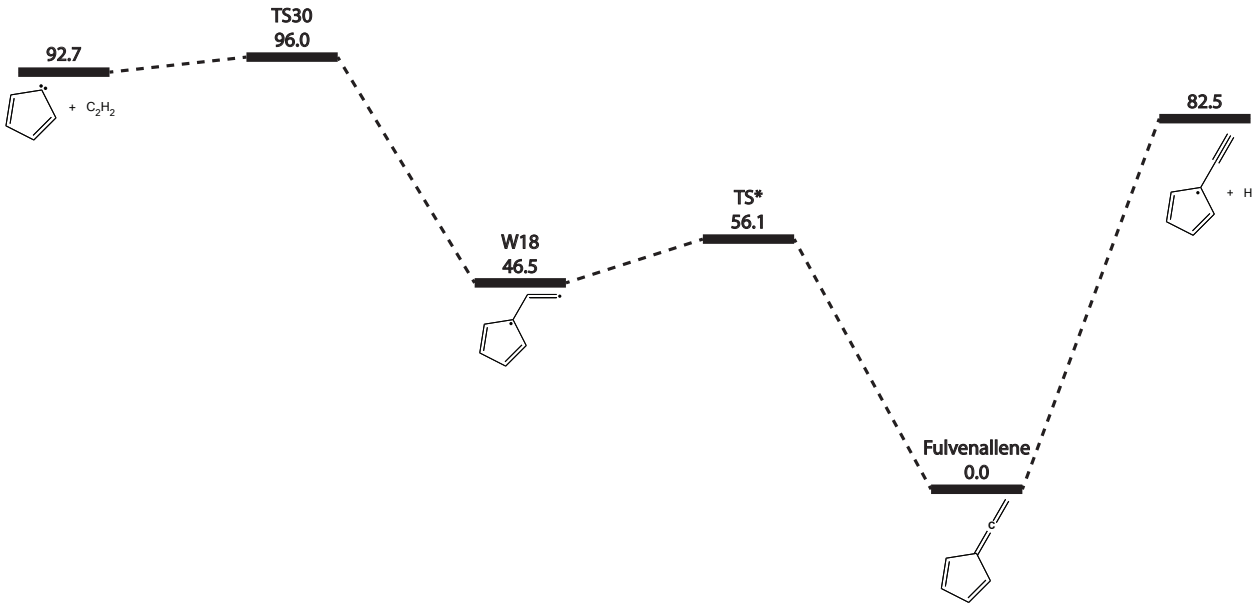

Figure 3.10: A simplified C_7H_6 potential energy diagram showing the production of C_7H_5 + H and C_5H_4 + C_2H_2 according to predictions by Polino and Cavalotti.[99] The molecular naming scheme of the original work is used here. TS* separates the singlet and triplet surfaces.

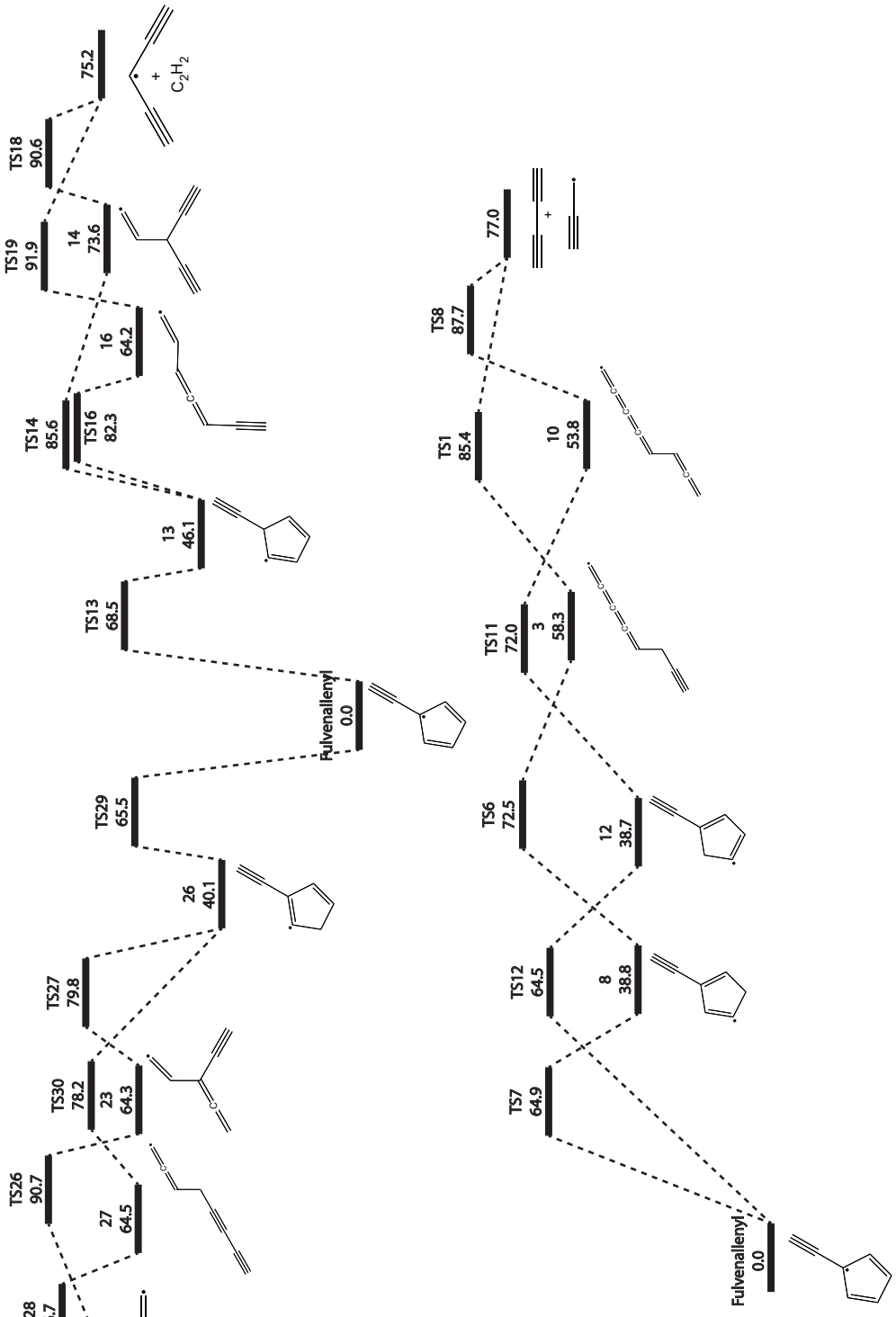

Figure 3.11: A simplified C_7H_5 potential energy diagram showing the production of $C_5H_3 + C_2H_2$ (top) and $C_4H_2 + C_3H_3$ (bottom) according to predictions by da Silva and Trevitt.[121] The molecular naming scheme of the original work is used here. The RRKM calculations done in this study use the full potential energy surface from the original work.

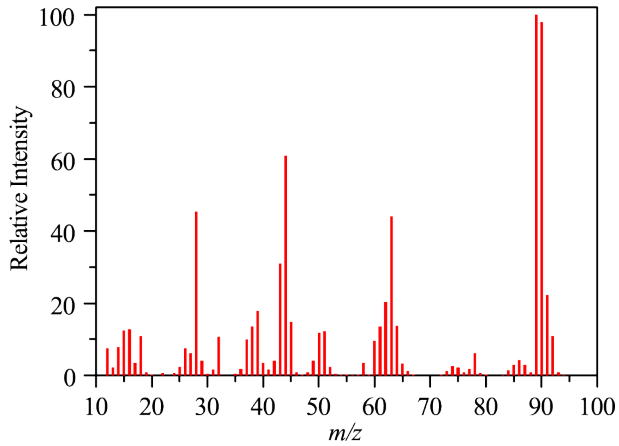

Figure 3.12: Mass spectrum of fulvenallene in the standardized format used by NIST, collected with 80 eV electron energy and normalized to the $m/z = 89$ signal intensity. There is likely an appreciable contribution to the signal at $m/z = 28$ and 14 due to high N_2 background in the detector.

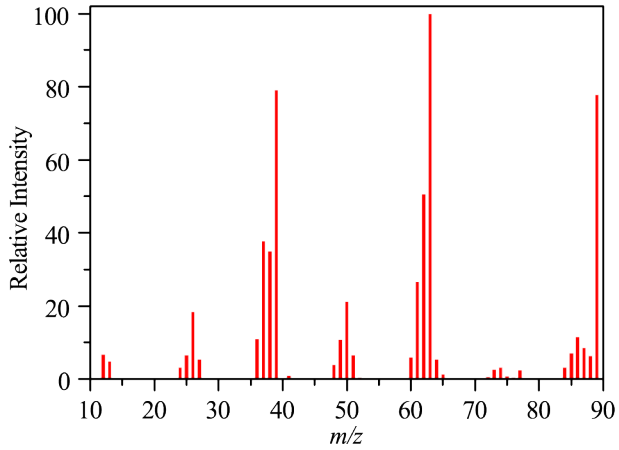

Figure 3.13: Mass spectrum of the fulvenallenyl radical in the standardized format used by NIST, collected with 80 eV electron energy and normalized to the $m/z = 63$ signal intensity. Values of $m/z < 12$ were not measured. High detector background at $m/z = 28$ and 14 from N_2^+ and N_2^{2+}/N^+ respectively and at $m/z = 40$ from Ar^+ preclude measurement of these signals. This spectrum was collected by measuring TOF spectra with m/z of all possible combinations of up to seven C atoms and five H atoms at $\Theta_{LAB} = 5^o$. The signal for each spectrum was normalized by the $m/z = 89$ signal at 5^o that was continually remeasured throughout the experiment.

Table 3.4: Oscillator strengths and orbital symmetries for vertical transitions of fulvenallene and fulvenallenyl in the vicinity of 248 nm and 193 nm, calculated using time-dependent DFT at the B3LYP/6-311G++(d,p) level.

	Fulvenallene		**Fulvenallenyl**	
Absorption energy	241 nm	197 nm	254 nm	191 nm
Oscillator Strength	0.436	0.024	0.219	0.007
Transition Symmetry	$4\ ^1A_1 \leftarrow \widetilde{X}\ ^1A_1$	$11\ ^1B_1 \leftarrow \widetilde{X}\ ^1A_1$	$5\ ^2A_1 \leftarrow \widetilde{X}\ ^2B_1$	$15\ ^2A_1 \leftarrow \widetilde{X}\ ^2B_1$

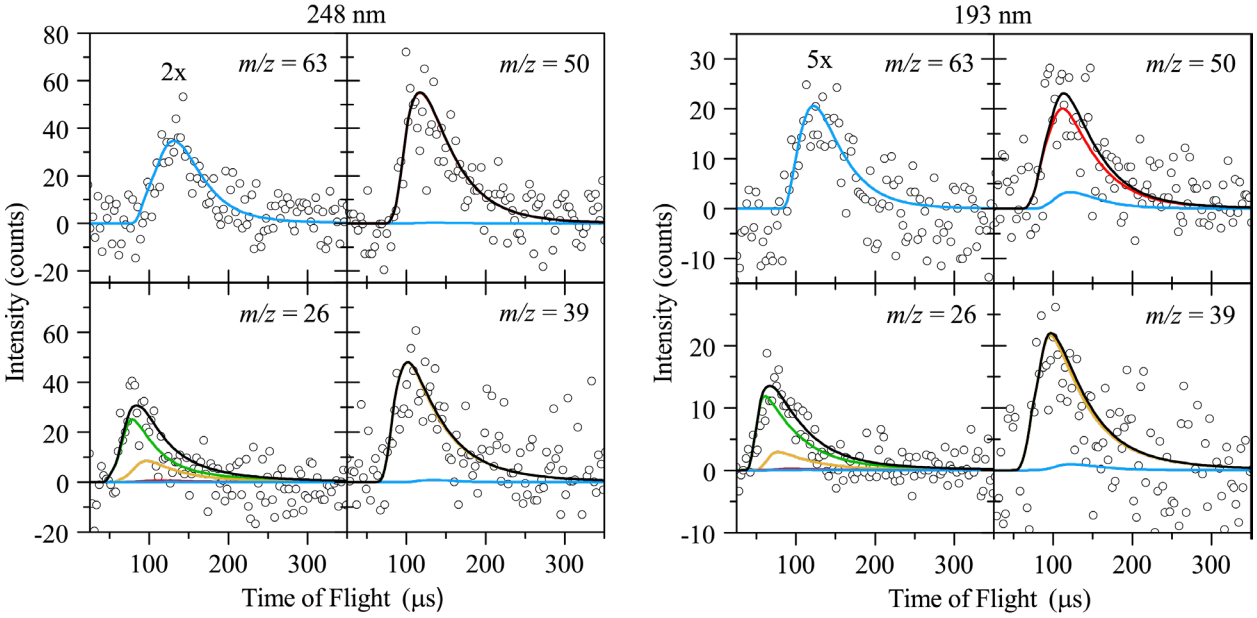

Figure 3.14: TOF spectra for $m/z = 63$ (top left panels), $m/z = 26$ (bottom left panels), $m/z = 50$ (top right panels) and $m/z = 39$ (bottom right panels) at $\Theta_{LAB} = 30^o$ ($\Phi_{248nm} = 420$ mJ cm^{-2}, $\Phi_{193nm} = 300$ mJ cm^{-2}). The blue ($m/z = 63$) and green ($m/z = 26$) simulations are generated using the $P(E_T)$ in Figures 3.9a and 3.9c, while the red ($m/z = 50$) and yellow ($m/z = 39$) simulations are generated using the $P(E_T)$ in Figures 3.9b and 3.9d. For TOF spectra with multiple features, the total simulation is shown in black.

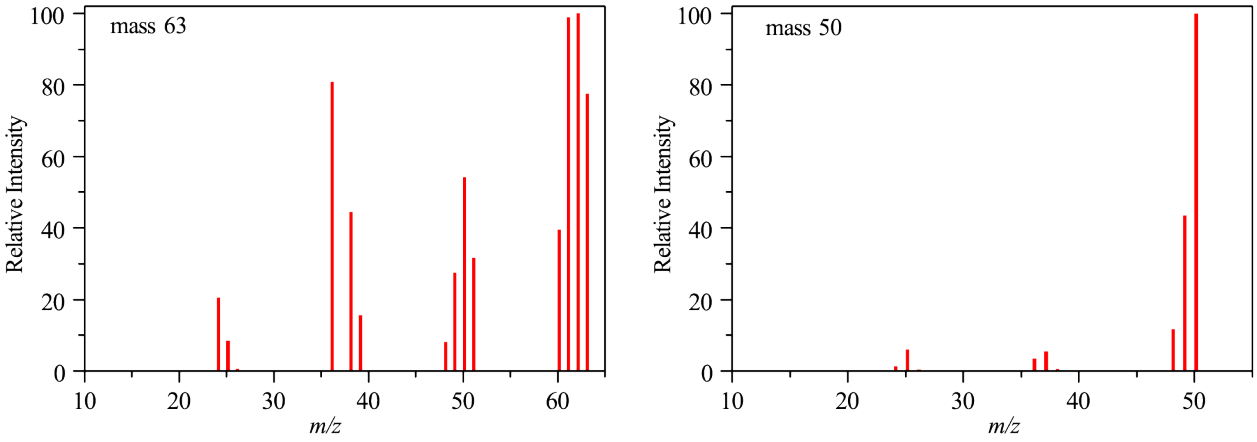

Figure 3.15: Mass spectrum of the mass 63 (left) and 50 (right) photofragments in the standardized format used by NIST, collected with 80 eV electron energy and normalized to the $m/z = 62$ and 50 signal intensities respectively. Values of $m/z < 12$ were not measured. High detector background at $m/z = 14$ from N_2^{2+}/N^+ precludes measurement of these signals. The same technique described in Figure 3.13 was used to collect these spectra, with measurements taken at $\Theta_{LAB} = 10^o$. This angle is beyond the fulvenallene H-atom loss Newton sphere so that any contributions from this channel to the TOF signal are removed.

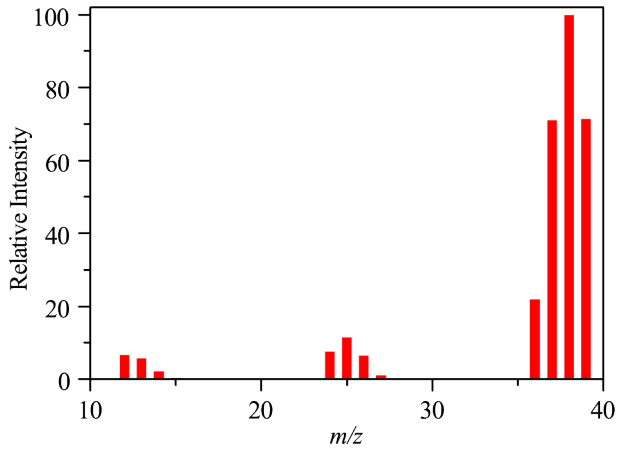

Figure 3.16: Mass spectrum of the propargyl radical in the standardized format used by NIST, collected with 180 eV electron energy and normalized to the $m/z = 38$ signal intensity. Values of $m/z < 12$ were not measured. The same technique described in Figure 3.13 was used to collect this spectrum. These previously unpublished data were collected during studies of allene photodissociation, for which loss of an H atom to form the propargyl radical is the dominant channel.[149]

Consecutive photodissociation processes

Figure 3.5 shows that photofragments with $m/z < 64$ have a different laser fluence dependence than the $m/z = 89$ ($C_7H_5^+$) feature produced by fulvenallene H-atom loss. This behavior is suggestive of the presence of secondary photodissociation. For an experiment in which primary photoproducts undergo secondary photodissociation in the consecutive reaction scheme

$$A \rightarrow B \rightarrow C$$

where A is fulvenallene, B is fulvenallenyl, and C is the sum of secondary dissociation channel products, the rate equations governing concentration changes in each species are

$$\begin{aligned}
\frac{dA(t)}{d(t)} &= -\frac{\sigma_A \phi(t)}{h\nu} A(t) \\
\frac{dB(t)}{d(t)} &= \frac{\sigma_A \phi(t)}{h\nu} A(t) - \frac{\sigma_B \phi(t)}{h\nu} B(t) \\
\frac{dC(t)}{d(t)} &= \frac{\sigma_B \phi(t)}{h\nu} B(t)
\end{aligned} \tag{3.5}$$

In Equation 3.5, σ_A and σ_B are the absorption cross-sections of fulvenallene and the fulvenallenyl radical respectively and $\phi(t)$ is the intensity of the laser pulse as a function of time. We assume dissociation is instantaneous. Integrating $\phi(t)$ over the duration of the laser pulse gives the total intensity Φ contained in the pulse. Solving for the concentrations of A, B, and C after the laser pulse has finished gives

$$\begin{aligned}
A &= A_o e^{-\sigma_A \Phi/h\nu} \\
B &= A_o \frac{\sigma_A}{\sigma_B - \sigma_A} \left(e^{-\sigma_A \Phi/h\nu} - e^{-\sigma_B \Phi/h\nu} \right) \\
C &= A_o \left[\frac{\sigma_B}{\sigma_B - \sigma_A} \left(1 - e^{-\sigma_A \Phi/h\nu} \right) - \frac{\sigma_A}{\sigma_B - \sigma_A} \left(1 - e^{-\sigma_B \Phi/h\nu} \right) \right]
\end{aligned} \tag{3.6}$$

Given the results of the TD-DFT calculations (Table 3.4), we expect that the ratio of calculated oscillator strengths for electronic excitations compares approximately to the ratio of absorption cross-sections such that for 248 nm excitation ${}^{\sigma_A}/_{\sigma_B} \approx 2$ and for 193 nm excitation ${}^{\sigma_A}/_{\sigma_B} \approx 3$.[153] Therefore, the only free parameter in these functions is σ_A, the absorption cross-section of fulvenallene. From the TD-DFT results we also expect that ${}^{\sigma_{A,248}}/_{\sigma_{A,193}} \approx 18$.

The laser fluence dependence of the $m/z = 89$ ($C_7H_5^+$) and $m/z = 50$ ($C_4H_2^+$) TOF features is shown in Figure 3.17. The $m/z = 50$ ($C_4H_2^+$) data were collected beyond the fulvenallene H-loss Newton circle, and so contain no DI signal from fulvenallenyl. The expected linear

dependence of signal intensity for a single-photon absorption process is not observed, nor is the quadratic dependence that should arise were fulvenallene to absorb two photons. Best fits of Equation 3.6 to select data, obtained by varying σ_A, are shown in Figure 3.17, with the experimentally derived cross-sections presented in Table 3.5. The fitting routine involves a global fit to the $m/z = 89$ ($C_7H_5^+$) and $m/z = 50$ ($C_4H_2^+$) data, as well as similar data for $m/z = 62$ ($C_5H_2^+$, not shown) at each wavelength.

The consecutive two-photon model matches well with the observed laser fluence dependence. Fitting the photofragment signal dependence on incident laser fluence with this model produced good fits at each wavelength for both species having absorption cross-sections in

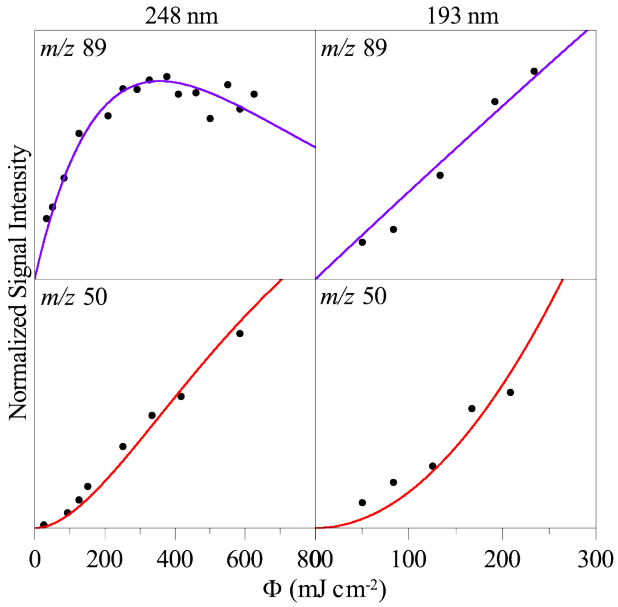

Figure 3.17: Laser fluence dependence of primary photofragment $m/z = 89$ (top) and secondary photofragment $m/z = 50$ (bottom) upon photoexcitation of fulvenallene at 248 nm (left) and 193 nm (right). Fits to the data are made using Equations 3.6 for primary and secondary photofragment concentration as a function of laser fluence.

Table 3.5: Absorption cross-sections of fulvenallene and fulvenallenyl determined by fitting the laser power dependence of primary and secondary photoproducts.

λ **(nm)**	σ **(×** 10^{-19} **cm^2 per molecule)**	
	Fulvenallene	*Fulvenallenyl*
248	31 ± 1	16.0 ± 0.5
193	1.70 ± 0.05	0.52 ± 0.02

the range of 10^{-20}-10^{-18} cm^2 per molecule (Table 3.5). For fulvenallene, $\sigma_{248nm} = (3.1 \pm 0.1) \times 10^{-18}$ cm^2 compares quite well with a previously reported experimental value of $\sigma_{266nm} = (3.4 \pm 0.5) \times 10^{-18}$ cm^2 for a similar energy absorption.[104]

A competing, concerted two-photon process whereby fulvenallene absorbed two ultraviolet photons and dissociated to produce the fulvenallenyl radical, which then further dissociates, is conceivable. Our fulvenallene H-loss $P(E_T)$'s do not match well with two-photon prior distributions at 248 nm or at 193 nm. If this process were to occur the laser fluence dependence should be quadratic for the m/z = 63, 50, 39 and 26 photofragments, contrary to what is observed experimentally.

Chapter 4

Photodissociation dynamics of the methylsulfinyl radical at 248 nm

The content and figures of this chapter are reprinted or adapted with permission from Ramphal, I. A.; Lee, C; Neumark D. M., "Photodissociation dynamics of the methylsulfinyl radical at 248 nm," Mol. Phys., 2019, 117, 3043.

Abstract

The photodissociation dynamics of jet-cooled methylsulfinyl radicals, CH_3SO, at 248 nm have been investigated using molecular beam photofragment translational spectroscopy. The primary channel is CH_3S + O, which occurs via the initially prepared excited CH_3SO state by rapid cleavage of the S-O bond to produce ground state products. The minor SO + CH_3 channel has two components in comparable proportions: a fast feature corresponding to rapid C-S cleavage on the excited state to produce CH_3 and electronically excited SO, and a slow feature due to internal conversion of CH_3SO followed by statistical dissociation on the ground electronic state. Statistical ground state dissociation also produces small amounts of CH_2SO, likely sulfine, and H-atoms.

4.1 Introduction

The gaseous transport of volatile sulfur-containing small molecules is a key step in the global sulfur cycle, with significant implications for physical and chemical processes taking place in the atmosphere.[154,155] Biogenic sulfur is primarily released in the form of dimethylsulfoniopropionate, $(CH_3)_2S^+CH_2CH_2CO_2^-$, produced directly by marine algae and higher plants,[156–159] and subsequently metabolized to small, volatile sulfur-containing species such as H_2S, CH_3SCH_3 and CH_3SH.[160] These molecules exhibit a rich chemistry with important atmospheric gases such as O_3, OH and NO_x to form many reactive radical and closed-shell species, of which sulfuric acid is perhaps the most important, and further impact the atmosphere through heterogeneous processes such as formation and uptake into aerosol particles.[161–165] Sulfur-containing species also feature prominently in the atmospheric chemistry of other planetary bodies and their satellites.[166–169]

The present work is concerned with ultraviolet (UV) photodissociation of the methylsulfinyl radical, CH_3SO, a key intermediate in the oxidation of volatile sulfur-containing species such as CH_3SCH_3 and H_2S in the atmosphere.[165] Despite the apparent importance of this species, there is currently a dearth of information in the literature. Electron spin resonance spectroscopy has shown that the majority of the unpaired spin density resides in the p_z orbital of the internal S atom, in contrast to the much higher spin densities on the terminal atoms for CH_3OO and CH_3SS radicals.[170–175] This is in agreement with infrared spectra, which find that the stretching frequency for the S-O bond in CH_3SO, 1071 cm^{-1}, is similar to a double bond such as that found in a sulfoxide rather than a single bond as in a sulfenic ester (1103 cm^{-1} for dimethyl sulfoxide and 724 cm^{-1} for CH_3SOCH_3).[176–179] Electronic transitions at 530 nm ($\widetilde{A}\,^2A' \leftarrow \widetilde{X}\,^2A''$) and 250 nm ($\widetilde{B}\,^2A'' \leftarrow \widetilde{X}\,^2A''$) have been observed in a cryogenic Ar matrix, and irradiation with UV light near 250 nm results in the disappearance of the infrared and UV/visible absorption bands of methylsulfinyl.[179] High-level computations (up to CCSDT(Q)/cc-pV(5+d)Z for the ground state and EOM-CCSD(T)/ANO2 for electronic transitions) corroborate all of these observations, except for the 250 nm transition, which was not reported.[180] Photoionization studies have determined that the ionization potential of methylsulfinyl is 8.99 eV.[181,182]

The most important atmospheric reactions that form methylsulfinyl are likely those of CH_3S with NO_2 and with O_3.[161,183] Laboratory investigations into the chemistry of CH_3SO have focused on reactions with these species as well as O_2.[161,164,183–185] Theoretical work has explored reactions of CH_3SO with NO and XO (X = F, Cl, Br),[186,187] implicated the CH_3SO + O_3 reaction in atmospheric SO_x formation,[188] and assessed the heterogeneous aerosol nucleation chemistry of CH_3SO/HOCl and $CH_3SO/H_2SO_4/(H_2O)_{0-2}$ clusters.[189,190] Although isomerization on the CH_3SO potential energy surface has been studied on one occasion,[191] no dedicated experimental or theoretical effort has yet been carried out to characterize the unimolecular dissociation dynamics of CH_3SO. In the ultraviolet photodissociation of dimethyl sulfoxide, a major product is internally hot CH_3SO in its ground and first excited electronic states, of which the former was observed to undergo statistical secondary dissociation yielding CH_3 + SO and CH_2SO + H in a 93:7 ratio.[192–196]

In this study, we explore the photodissociation dynamics of methylsulfinyl at an excitation wavelength of 248 nm in order to determine the formation mechanisms of different product channels and to assess their relative importance. This work is motivated in part by our previous investigations into CH_3SS and CH_3OO photodissociation.[197,198] The potential energy diagram in Figure 4.1 shows the three excited electronic states of methylsulfinyl that are within the energetic range of a 248 nm photon. Also included are the energies of both ground state and excited state accessible products that do not require isomerization of methylsulfinyl; other channels are presented in the Supporting Information (Section 4.8). In Figure 4.1, the formation of SO + CH_3 is the lowest energy channel, followed by H-atom loss to form sulfine, CH_2SO.

We find that the dissociation dynamics occur primarily on an excited state, producing CH_3S + O and lesser amounts of CH_3 + SO. A small fraction (< 15%) of methylsulfinyl radicals internally convert to the ground electronic state where they dissociate into CH_3 + SO and CH_2SO + H.

4.2 Experimental

Precursor synthesis and characterization

Flash vacuum pyrolysis of allyl methyl sulfoxide (AMSO, Figure 4.2) has previously been demonstrated as a suitable means of producing methylsulfinyl radicals, and AMSO itself does not absorb at 248 nm.[179,206,207] The preparation of AMSO has been described elsewhere.[179] The successful production of the precursor sample was determined by NMR spectroscopy (400 MHz, $CDCl_3$, Me_4Si), ^{1}H-NMR: δ (ppm) 2.58 (3H, s, CH_3), 3.50 (2H, t, α-CH_2), 5.46 (2H, m, γ-CH_2), 5.92 (1H, m, β-CH), and ^{13}C-NMR: δ (ppm) 37.2 (CH_3), 57.9 (α-CH_2), 123.9 (γ-CH_2), 125.5 (β-CH). These NMR spectra agree well with previous measurements,[208] and do not show evidence of the allyl methyl sulfone byproduct that can sometimes be formed during AMSO synthesis.[179]

Photodissociation experiments

The photodissociation of methylsulfinyl was carried out on the modified universal crossed molecular beam apparatus with a fixed source and rotatable mass spectrometer detector as described above and previously.[11,133,134] A reservoir of AMSO was warmed to ∼50-60 ^{o}C to increase its vapor pressure to approximately 0.03 Torr.[209] A pulsed molecular beam of methylsulfinyl radicals was produced by flash vacuum pyrolysis of AMSO undergoing supersonic expansion into a resistively heated SiC tubular reactor through the nozzle of a piezoelectric valve.[14] During pyrolysis, a current regulated power supply was used to ensure the SiC tube dissipated a fixed power of 25 W. This power was found to fully deplete the AMSO precursor peak at m/z = 104 since the allyl C-S bond energy is only 37 kcal/mol.[179] By comparison, the weakest bond in CH_3SO is the C-S bond with a bond energy of ∼52

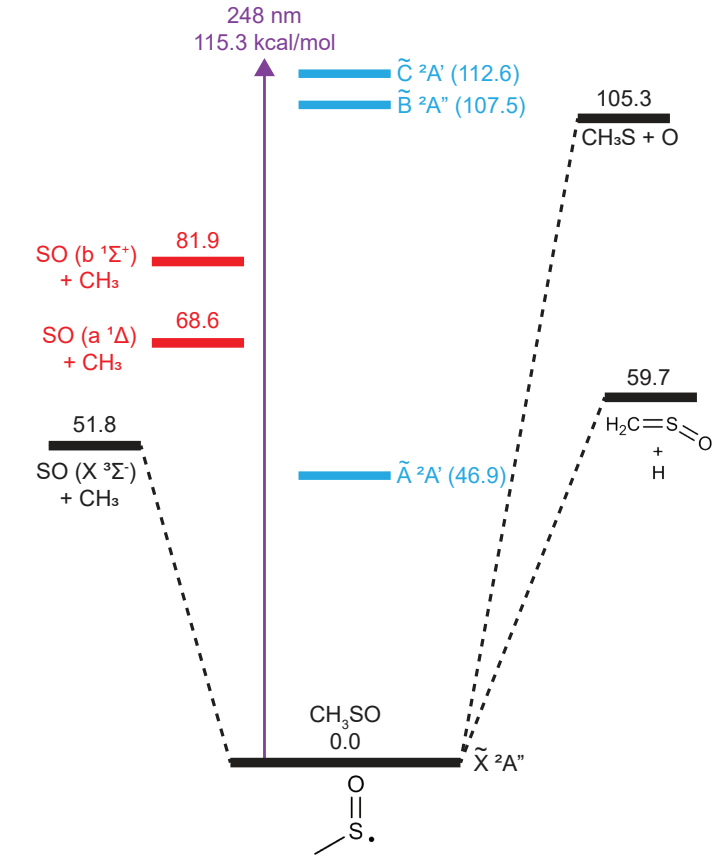

Figure 4.1: A simplified CH_3SO potential energy diagram with the energy of a 248 nm photon represented by the purple arrow. All energies are in units of kcal/mol. Species on the ground electronic state are indicated in black. The excited electronic states of CH_3SO are indicated in blue, and excited product states are indicated in orange. Ground state energies are determined from experimental heats of formation,[192,199–201] except for CH_2SO for which the assumptions made in deriving the experimental value likely lead to overestimation.[202,203] The energies of excited states of CH_3SO are taken from calculations reported herein (see Section 4.4), and the energies of the excited SO product states are experimental values taken from Refs. [204] and [205].

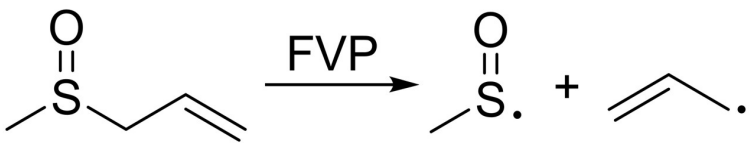

Figure 4.2: Generation of methylsulfinyl and allyl radicals by pyrolysis of AMSO.

kcal/mol.[193,195] Entrainment in a He carrier gas seeded with 10% N_2 has been shown to more effectively cool radicals produced by pyrolysis than pure He.[91] Passage through two skimmers separating the source and main scattering chambers collimates the radical beam, whose velocity distribution is characterized by time-of-flight (TOF) measurements with respect to a retractable slotted spinning disk. Typical beam velocities in this experiment were 1900 m/s, with speed ratios, defined as the velocity divided by the spread in velocities, of 5-6. The radical beam was then crossed orthogonally with the focused 248 nm output of an LPX $220i$ excimer laser. Typical pulse energies were 45 mJ/pulse, which gives a photon fluence of approximately 375 mJ/cm^2. Operation of the laser at half the 400 Hz repetition rate of the pulsed valve enabled shot-to-shot subtraction of any signal not induced by the laser pulse.

Photofragments were collected as a function of laboratory scattering angle, Θ_{LAB}, relative to the molecular beam axis in the plane defined by the laser and molecular beams. The detector includes an electron impact ionizer nested within three differentially pumped regions and operated at 80 eV to produce cations that are mass-selected using a quadrupole filter and detected using the Daly style ion detector.[85,135] The ionizer has the ability to tune electron energies to as low as 5 eV whereby the appearance potential for different ion signals can be determined from the resulting ionization efficiency curve (IEC) of ion signal as a function of electron energy for a fixed emission current.[84,105] A multichannel scalar collects and bins ion signal as a function of time relative to the laser-molecular beam interaction to produce TOF spectra.

Global simulation of the product TOF spectra using an iterative forward convolution program yields the center-of-mass translational energy distributions, $P(E_T)$, for different product channels.[136] The photofragment angular distributions, $I(\theta)$, were determined at a fixed Θ_{LAB} by rotating the angle ϕ of the laser electric field with respect to the plane defined by the molecular beam and detector axes using a stack of eight quartz plates held at Brewster's angle and measuring the relative ion signal as described previously.[197]

4.3 Theoretical Methods

Unimolecular reaction rates for methylsulfinyl isomerization and dissociation on its ground electronic state were calculated using microcanonical Rice-Ramsperger-Kassel-Marcus (RRKM) theory, in which the reaction rate constant $k(E)$ is given by:[141]

$$k(E) = \sigma \frac{W^{\ddagger}(E - E_o)}{h\rho(E)} \tag{4.1}$$

In this expression, σ is the reaction path degeneracy,[144] h is the Planck constant, $\rho(E)$ is the density of rovibrational states of the reactant at energy E, and $W^{\ddagger}(E - E_o)$ is the sum of accessible rovibrational states at the transition state. Terms in Equation 4.1 were evaluated using the Beyer-Swinehart algorithm.[142,143] The branching ratio between different product channels was determined by applying the steady-state approximation to the concentration of intermediate species and solving for the relative reaction rate for each channel.

The RRKM analysis requires the molecular geometries, vibrational modes, and relative energies to calculate rate constants. These properties were determined using the chemically accurate Gaussian-4 (G4) composite method implemented in Gaussian 09.[138,210] There were no imaginary frequencies at minimum energy points. For transition states, a single imaginary frequency was identified corresponding to the reaction coordinate, and intrinsic reaction coordinate scans verified connectivity between the correct reactant and product minima. In the absence of a recombination barrier, the location of the transition state was determined using the variational RRKM method to minimize the rate constant. These stationary points produce a potential energy diagram highlighting the isomerization and dissociation pathways available to energized methylsulfinyl radicals on the ground electronic state. Reasonable product channels not included in Figure 4.1 but which might be operative in methylsulfinyl photodissociation include CH_3O + S, CH_2S + OH, CH_2O + SH, CH_2 + HSO, and H_2 + HCSO. Tunneling rates were not considered for any reactions in this study.

Excited states of methylsulfinyl were calculated using the EOM-CCSD/aug-cc-PVDZ level of theory and the ground state geometry from the G4 calculation. These calculations provide several key features of the excited states, including their vertical energy difference, electronic symmetry, oscillator strength from the ground state, and transition electric dipole vectors.

4.4 Results

Methylsulfinyl radical production

The mass spectrum for AMSO (Figure 4.3a, blue trace) agrees well with the known mass spectrum for this species.[211] During pyrolysis (Figure 4.3a, red trace), peaks corresponding to AMSO are depleted and a large increase in the relative intensity of $m/z = 63$ is observed, corresponding to ionization of methylsulfinyl. Other peaks in good agreement with the known mass spectrum of the allyl radical are also clearly present (e.g. at m/z = 39-41).[212]

The IECs for several m/z ratios with pyrolysis on and off are shown in Figure 4.3b-d. In Figure 4.3b, the IEC for $m/z = 104$ ($C_4H_8SO^+$) intercepts the energy axis at an appearance potential of 8.7 eV, in excellent agreement with the calculated vertical ionization potential of 8.64 eV for AMSO. Daughter ion fragments from dissociative ionization are also produced. In Figure 4.3c and 2d, the solid data points correspond to CH_3SO^+ and $C_3H_5^+$ ions that are formed from dissociative ionization of AMSO, with appearance potentials of 11.7 eV and 10.2 eV respectively. When pyrolysis is turned on, AMSO decomposes to CH_3SO and C_3H_5, leading to appearance potentials of 9.3 eV for CH_3SO^+ and 8.1 eV for $C_3H_5^+$, in excellent agreement with the experimentally determined ionization potentials of 8.99 eV and 8.1 eV for these respective species.[148,181]

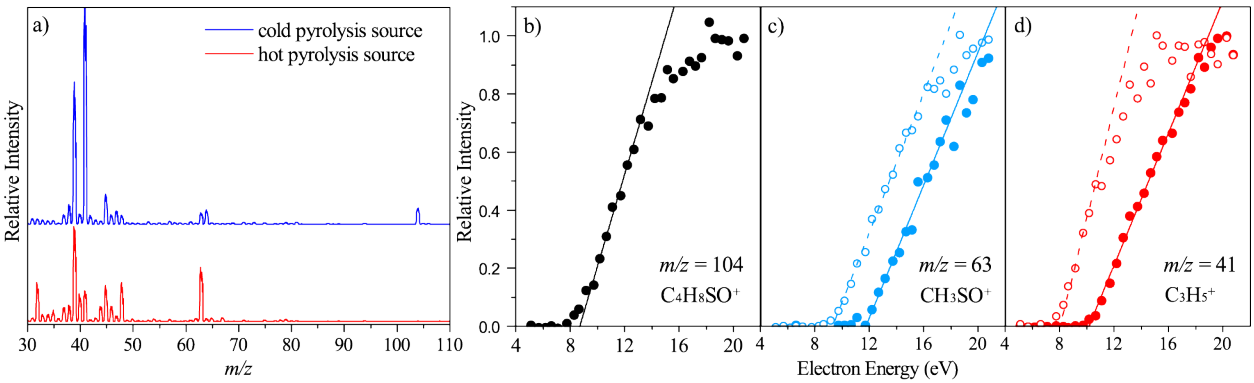

Figure 4.3: (a) Mass spectra of the molecular beam collected with the pyrolysis source off (blue) and on (red). When pyrolysis is turned on the AMSO peaks are fully depleted and replaced with those of CH_3SO and C_3H_5. The right panel contains IECs for (b) $m/z = 104$, (c) $m/z = 63$, and (d) $m/z = 41$. Filled circles are data collected with no pyrolysis, and open circles are collected with pyrolysis on. There is no IEC for $m/z = 104$ with pyrolysis on because this ion signal is fully depleted in the mass spectrum.

Photofragment translational spectroscopy

TOF spectra of fragments from the photodissociation of CH_3SO were measured at multiple scattering angles for ion masses expected from this process. Representative data are shown in Figures 4.4-4.6. All experimental spectra are shown normalized by the on-axis $m/z = 63$ signal intensity and then scaled to counts per 10^9 laser shots. Additional scaling for spectra with low signal is specified on an individual basis.

The largest photodissociation signal was observed at $m/z = 47$ (CH_3S^+) for Θ_{LAB} ranging from 5^o up to 20^o, with representative TOF spectra shown in Figure 4.4. These spectra comprise a single feature. The counter-fragment for CH_3S formation is an O atom. Attempts to measure ion signal for O^+ at $m/z = 16$ were unsuccessful.

Ion signal was also detected at $m/z = 48$ (SO^+) for Θ_{LAB} ranging from 5^o up to 40^o, with representative TOF spectra shown in Figure 4.5. The counter-fragment for SO formation is the methyl radical, CH_3. Some evidence of signal for this fragment at $m/z = 15$ was observed (see Figure 4.14). As discussed in Section 4.5, two dynamical pathways contribute to this channel.

The heaviest possible photofragment originating from methylsulfinyl is CH_2SO whose parent ion is $m/z = 62$. Representative TOF spectra are shown in Figure 4.6. The ion signal measured here is very low, giving a poor signal-to-noise ratio, and no signal was observed for $\Theta_{LAB} > 8^o$. These TOF spectra appear to comprise a single feature.

The dependence of the $m/z = 47$ and 48 TOF data on laser polarization angle φ with respect to the scattering plane was investigated at $\Theta_{LAB} = 15^o$ and 20^o respectively (Figure 4.7). The signal intensity for each ion was determined by integrating the entire TOF spectrum. Inspection of the TOF spectra did not reveal any qualitative changes in the

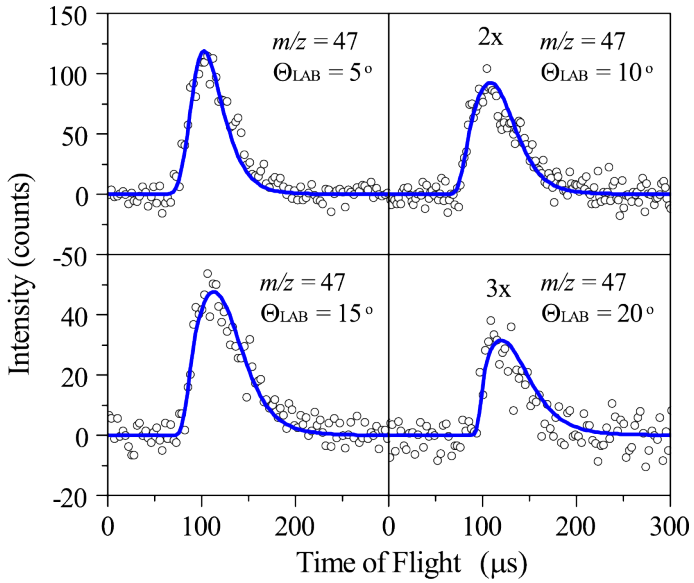

Figure 4.4: TOF spectra for $m/z = 47$ (CH_3S^+). The experimental data are shown as open circles, and the blue line is a forward convolution simulation generated using the $P(E_T)$ in Figure 4.10 and anisotropy parameter $\beta = 1.74$ (see Section 4.5).

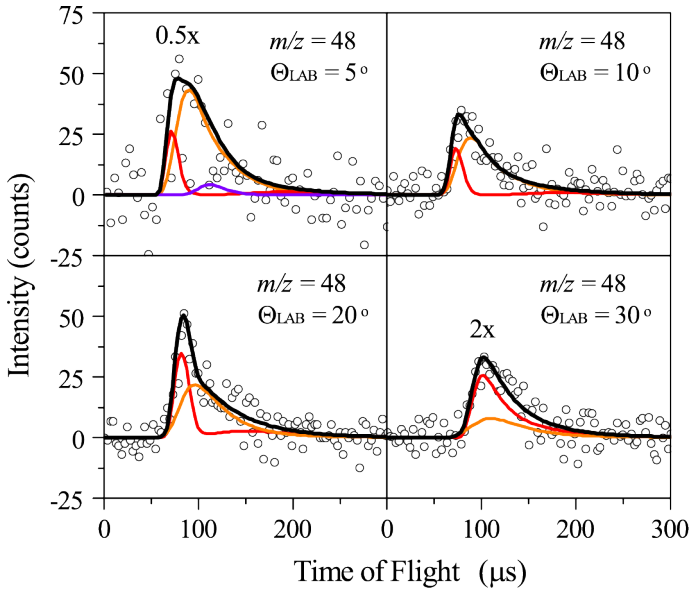

Figure 4.5: TOF spectra for $m/z = 48$ (SO^+). The experimental data are shown as open circles, and the smooth lines are forward convolution simulations. The orange, red, and purple simulations are produced from the $P(E_T)$ distributions in Figures 4.11 and 4.12 and isotropic angular distributions. The total simulation is shown in black.

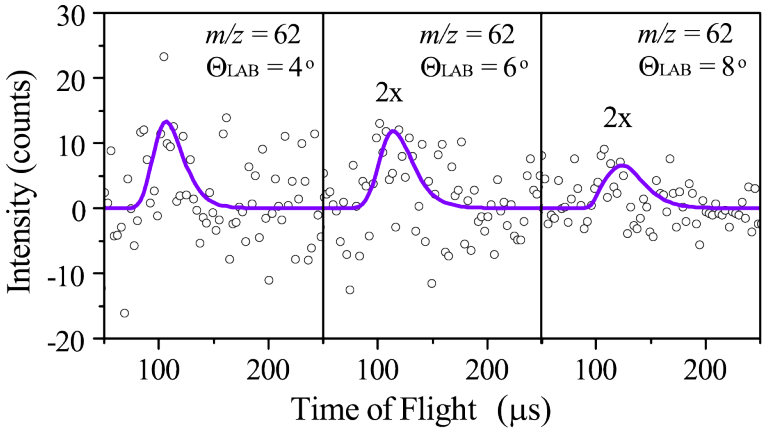

Figure 4.6: TOF spectra for $m/z = 62$ (CH_2SO^+). The experimental data are shown as open circles, and the purple line is a forward convolution simulation generated using the $P(E_T)$ in Figure 4.12 and an isotropic angular distribution.

shape of the TOF peaks as the polarization was changed. Signal levels for $m/z = 48$ did not appear to depend on the laser polarization, whereas the $m/z = 47$ signal demonstrated a moderate decrease in ion signal as the polarization was rotated from 0^o to 90^o. Due to the very poor signal-to-noise ratio for the $m/z = 62$ data, it was not possible to conduct a similar polarization study for this channel.

The existence of several other channels was investigated. Reasonable photofragments would include S ($m/z = 32$) + CH_3O ($m/z = 31$), OH ($m/z = 17$) + CH_2S ($m/z = 46$), SH ($m/z = 33$) + CH_2O ($m/z = 30$), H_2 ($m/z = 2$) + HCSO ($m/z = 61$), and CH_2 ($m/z = 14$) + HSO ($m/z = 49$). For the mass-to-charge ratios indicated above, signal was only observed at $m/z = 46$ and $m/z = 49$. The $m/z = 46$ feature was entirely consistent with dissociative ionization of the CH_3S photofragment to CH_2S^+ based on the virtually identical TOF spectra, and the $m/z = 49$ feature is due to photofragments containing heavy isotopes of sulfur (see below). None of the aforementioned reactions appear to be operative with 248 nm photoexcitation of methylsulfinyl.

The most straightforward way to determine a branching ratio between two channels on this apparatus is to measure the TOF spectrum for some m/z signal that contains contributions from both channels. The only daughter ion shared by the dissociative ionization of CH_3S and SO is S^+ with $m/z = 32$. Low signal coupled with high detector background signal at $m/z = 32$ renders extraction of a branching ratio infeasible. However, naturally occurring sulfur includes two heavy isotopes of reasonable abundance, with ^{33}S and ^{34}S constituting 0.75% and 4.25% of natural abundance respectively. Consequently $m/z = 49$ will exhibit ion signal from both of these channels due to $^{33}SO^+$ and $^{34}SCH_3^+$. Figure 4.8 shows TOF spectra taken at $\Theta_{LAB} = 15^o$ and 20^o for $m/z = 49$ which show evidence of both $^{33}SO^+$ and $^{34}SCH_3^+$ ion signal.

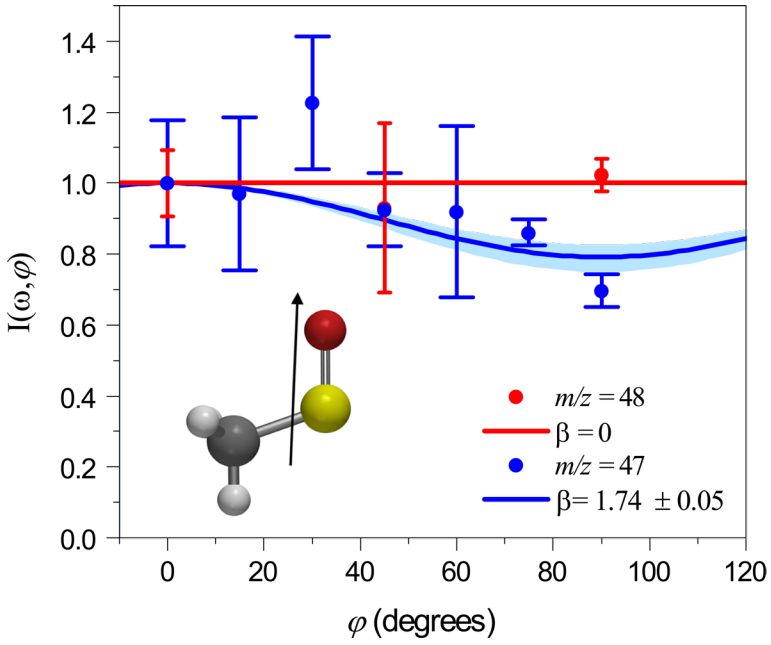

Figure 4.7: Photofragment ion signal at $m/z = 47$ (blue) and $m/z = 48$ (red) as a function of φ. Intensities are normalized to $\varphi = 0^o$. Error bars represent the standard deviation from the average intensity for three repeated values of φ. The solid line curves are plots of $I(\omega, \varphi)$ for the indicated values of β, also normalized to $\varphi = 0^o$ (see Section 4.5). The $m/z = 48$ and 47 data shown here correspond to $\omega = 62^o$ and 82^o respectively; this is the angle between the center-of-mass product recoil axis and the molecular beam and is discussed further in Section 4.5. The methylsulfinyl radical is shown in the bottom left along with the transition electric dipole vector for the $\widetilde{B}\,^2A'' \leftarrow \widetilde{X}\,^2A''$ transition.

Excited electronic state properties

The key results of the EOM-CCSD/aug-cc-PVDZ calculations of excited state properties for methylsulfinyl are shown in Table 4.1. The EOM-CCSD calculations employed here predict slight shifts in the energies of these two states that causes them to switch order as compared to previous work.[179] Specifically, this experiment is probing the $\widetilde{B}\,^2A'' \leftarrow \widetilde{X}\,^2A''$ transition as in the analogous CH_3OO radical. Inspection of the transition electric dipole vectors shows that the $\widetilde{A}\,^2A' \leftarrow \widetilde{X}\,^2A''$ and $\widetilde{C}\,^2A' \leftarrow \widetilde{X}\,^2A''$ transitions are perpendicular to the S-O bond axis, while the $\widetilde{B}\,^2A'' \leftarrow \widetilde{X}\,^2A''$ transition is near-parallel.

Ab initio potential energy surface

In addition to the reactions shown in Figure 4.1, calculations using the G4 composite method were used to produce the CH_3SO ground electronic state potential energy diagrams in Figures 4.15-4.17. There are many accessible product channels at 248 nm excitation. As

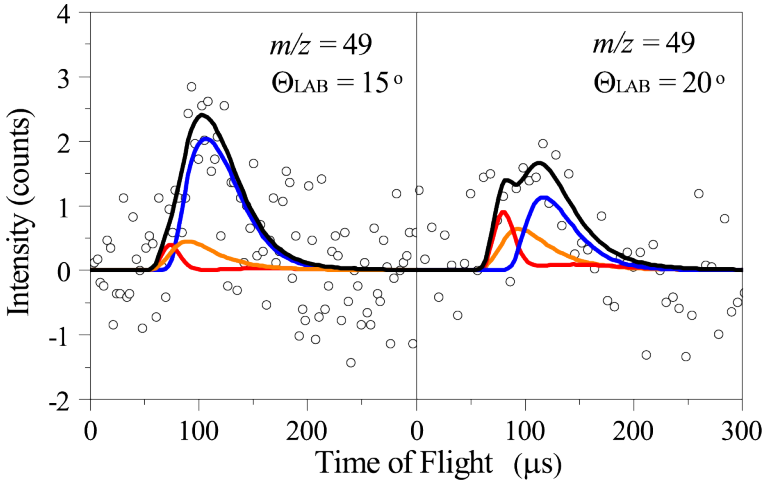

Figure 4.8: TOF spectra for $m/z = 49$, corresponding to $^{33}SO^+$ and $^{34}SCH_3^+$ ions. The experimental data are shown as open circles and the smooth lines are forward convolution simulations. The blue, orange, and red simulations are produced from the $P(E_T)$ distributions in Figures 4.10 and 4.11 and the anisotropy parameters determined from Figure 4.7. The total simulation is shown in black.

Table 4.1: Excited state properties of CH_3SO calculated at the EOM-CCSD/aug-cc-PVDZ level of theory.

Excited State	**Energy** ($^{\text{kcal}}/_{\text{mol}}$)	**Oscillator strength (from $\widetilde{X}\,^2A''$)**	**Angle with S-O bond**
$\widetilde{A}\,^2A'$	46.9	0.0004	90^o
$\widetilde{B}\,^2A''$	107.5	0.0435	4.6^o
$\widetilde{C}\,^2A'$	112.6	0.0000	90^o

shown in Figure 4.1, fragmentation to SO + CH_3 and to sulfine + H are the simplest reactions available to CH_3SO, although Figures 4.15-4.17 show several less endoergic channels. Both are found to proceed via simple bond fission mechanisms through loose transition states analogous to methyl loss from CH_3OO and CH_3SS,[213,214] and without the recombination barriers suggested by previous work.[193] Cleavage of the S-O bond to produce CH_3S + O is also expected to proceed through a loose transition state, but is highly endoergic and therefore not expected to be competitive with other channels on the ground electronic state. In contrast to CH_2OH, the CH_2SH isomer is higher in energy than the methylthio radical, CH_3S, and requires 111.6 kcal/mol to form.[215] Attempts to locate a transition state directly connecting methylsulfinyl to oxathiirane + H or to HCSO + H_2 were unsuccessful.

As shown in Figures 4.15-4.17, CH_3SO is surrounded by isomerization barriers on the ground state surface that are high compared to the direct dissociation reactions. For methylsulfinyl radicals that do isomerize, there are generally smaller barriers to reform methylsulfinyl than to dissociate or isomerize further. The most notable exception is the $CH_3SO \rightarrow H_2CSOH$ reaction with a barrier of only 54.1 kcal/mol, enabling the formation of CH_2S + OH with only 52.5 kcal/mol through a loose transition state. The two lowest energy product channels are thioformic acid + H (38.5 kcal/mol) and H_2CO + SH (24.0 kcal/mol), but these require surmounting a ∼80 kcal/mol barrier before any CH_3SO isomers capable of facilitating these reactions can be formed. Reaction pathways to other energetically accessible channels were excluded due to either the presence of prohibitively high energetic barriers to isomerization or product formation, or due to the requirement for many isomerization reactions before dissociation is possible.

4.5 Analysis

The center-of-mass velocity (V_{CM}) and available energy (E_{avail}) for different product channels impose constraints on the allowed laboratory scattering angles for photofragments. Conservation of energy during photodissociation requires

$$E_{avail} = h\nu + E_i - D_o = E_{int} + E_T \tag{4.2}$$

for photon energy $h\nu$, initial reactant energy E_i, and bond dissociation energy D_o, and this available energy is then partitioned into internal energy E_{int} and relative translational energy E_T according to the detailed reaction mechanism. We assume $E_i \approx 0$ kcal/mol due to cooling of the radical beam during supersonic expansion,[91] in which case $E_{avail} = h\nu - D_o$. A kinematic diagram for the observed product channels is shown in Figure 4.9, in which energy and momentum conservation constrain the photofragment signal to be bound within the so-called Newton circles. Only the heavy photofragments are included since there are no kinematic constraints on scattering angle for any of the light counter-fragments. These constraints assume all products are formed in their respective ground electronic states. Excited state products will necessarily be bound within smaller circles.

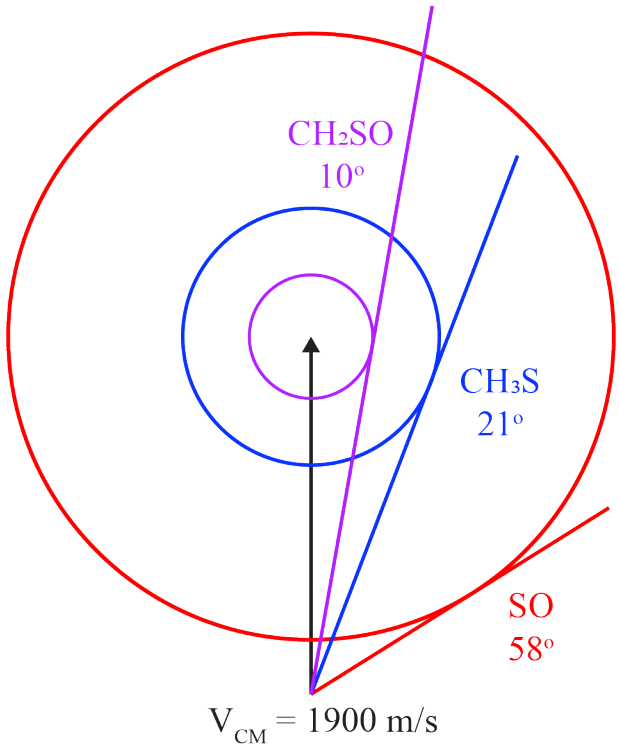

Figure 4.9: Kinematic diagram for the heavy fragments of methylsulfinyl photodissociation at 248 nm. Each circle represents the maximum center-of-mass frame velocities of the photofragment with the resulting maximum laboratory frame scattering angles indicated. The purple circle is for sulfine formed by H-atom loss, the blue circle is for CH_3S formed by O-atom loss, and the red circle is for SO formed by CH_3 loss.

The product TOF spectra are governed by the joint center-of-mass translational energy and angular distribution, $P(E_T, \theta)$. We assume this can be decoupled into separate translational and angular distributions according to

$$P(E_T, \theta) = P(E_T) \times I(\theta) \tag{4.3}$$

The center-of-mass photofragment angular distribution $I(\theta)$ has the functional form

$$I(\theta) = \frac{1}{4\pi} \left[1 + \beta P_2(\cos\theta)\right] \tag{4.4}$$

where β is the anisotropy parameter, $P_2(a) = \frac{1}{2}(3a^2 - 1)$ is the second Legendre polynomial, and θ is the center-of-mass scattering angle with respect to the laser electric field polarization direction.[24,216] It is more convenient to rewrite $I(\theta)$ as $I(\omega, \varphi)$ in which ω is the angle between the center-of-mass product recoil axis and the molecular beam in the scattering plane, φ is the angle between the electric field vector of the laser beam and the scattering plane, and $\cos\theta = \cos\omega \cos\varphi$.

For the experimental geometry used here, $I(\omega, \varphi)$ becomes

$$I(\omega, \varphi) = \frac{1}{4\pi}\left[\frac{3}{2}\beta(\cos^2\omega)[x\cos^2\varphi + (1-x)\sin^2\varphi] + \left(1 - \frac{\beta}{2}\right)\right] \tag{4.5}$$

where $x = 0.9$ is the dominant fraction of light polarization produced by the quartz polarizer.[197] To determine ω for each photofragment, the ion signal is assumed to come from a single center-of-mass velocity corresponding to the peak of the TOF spectrum. For the $m/z = 48$ spectra collected at $\Theta_{LAB} = 20^o$, this yields $\omega = 62^o$, while $\omega = 82^o$ for $m/z = 47$ spectra collected at $\Theta_{LAB} = 15^o$. The anisotropy parameter β is then found by fitting $I(\omega, \varphi)$ to the data in Figure 4.7. The best fit of Equation 4.5 to the $m/z = 47$ data yields $\beta = 1.74 \pm 0.05$, corresponding to a near-parallel transition. For the $m/z = 48$ data, $\beta = 0$ was used since there is no significant deviation of the data from a horizontal line.

The $m/z = 47$ TOF spectra were simulated using the $P(E_T)$ distribution in Figure 4.10 and $\beta = 1.74$ as determined above. Despite significant effort, it was not possible to collect a TOF spectrum for the O-atom counter-fragment at $m/z = 16$ because of high detector background at $m/z = 16$ as well as the small ionization cross-section and short residence time of O-atoms in the ionizer. The available energy for this channel is 10.0 kcal/mol, with the $P(E_T)$ in Figure 4.10 extending very slightly beyond this.

If dissociation is prompt, the anisotropy parameter depends on the angle α between the transition electric dipole moment and the dissociation vector[216,217]

$$\beta = 2P_2(\cos\alpha) \tag{4.6}$$

For S-O cleavage, α is the angle between the S-O bond and the transition dipole indicated in Table 4.1 for the $\widetilde{B}\,^2A'' \leftarrow \widetilde{X}\,^2A''$ transition. This gives $\beta = 1.99$ for cleavage of the S-O bond following 248 nm absorption, providing excellent agreement with the parallel nature of the transition derived from the experimental measurement of β.

The $m/z = 48$ TOF spectra were simulated using the bimodal $P(E_T)$ in Figure 4.11, which is deconvoluted into a fast and a slow feature, and taking $\beta = 0$. Without introducing the cusp in the distribution at $E_T = 14$ kcal/mol, it is not possible to adequately simulate TOF spectra around $\Theta_{LAB} = 20^o$. The slow feature is taken to be a statistical prior distribution for cleavage of the C-S bond of the form

$$P(E_T) \propto E_T^{1/2}\rho(E_{avail} - E_T) \tag{4.7}$$

It is expected that for an ideal statistical process with no recombination barrier, a prior distribution should approximately describe the partitioning of available energy into internal and relative translational energy of the photofragments.[145] The fast feature is peaked at a much higher translational energy of 24 kcal/mol.

Some evidence for the CH_3 counter-fragment is shown in Figure 4.14 in the Supporting Information (Section 4.8) that was collected for an extremely long time, but this fragment is difficult to collect for the same reasons given above for O-atoms. The energy available to ground state SO and CH_3 products is 63.5 kcal/mol, while the energies available for the

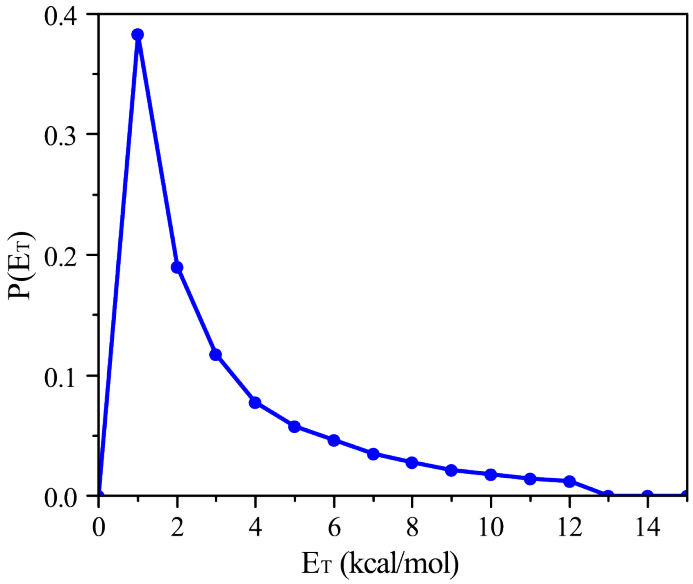

Figure 4.10: Center-of-mass $P(E_T)$ distribution for $CH_3SO \rightarrow CH_3S + O$.

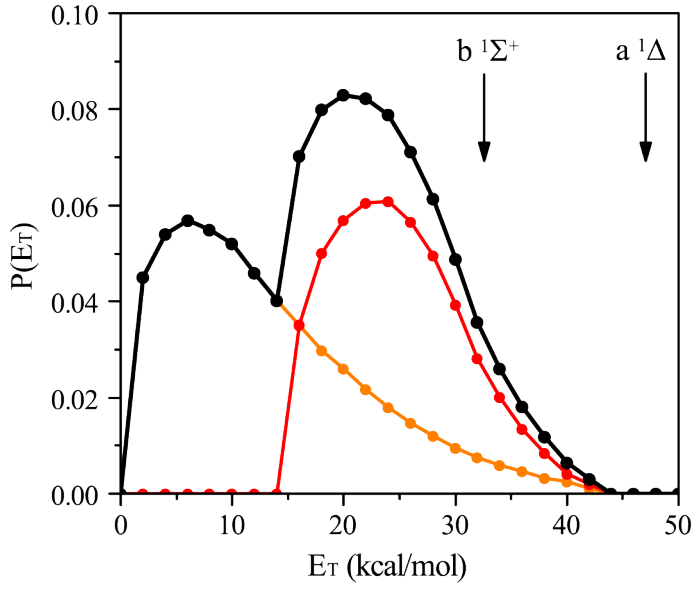

Figure 4.11: Center-of-mass $P(E_T)$ distribution for $CH_3SO \rightarrow SO + CH_3$. Simulations of the black distribution provide the best agreement with experimental TOF spectra. The slow orange component of the distribution is a prior distribution for C-S bond cleavage. The red distribution is the difference between the total experimental distribution and the slow orange component.

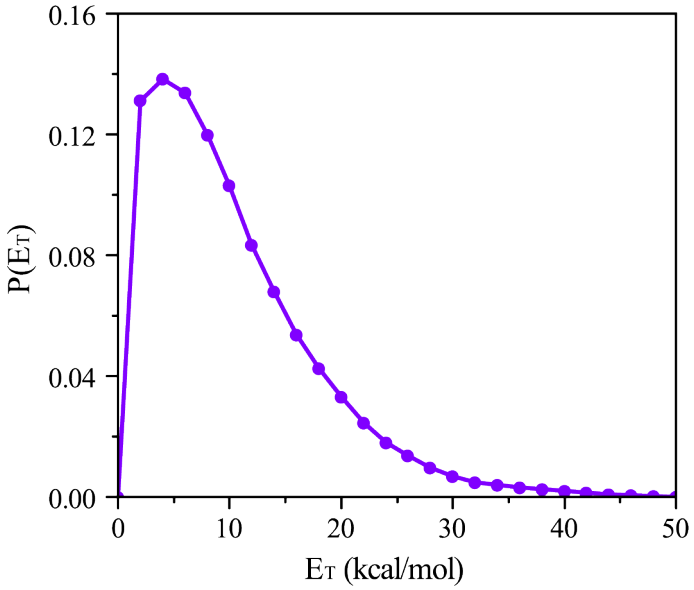

Figure 4.12: Center-of-mass $P(E_T)$ distribution for $CH_3SO \rightarrow CH_2SO + H$.

formation of the $a\,^1\Delta$ and $b\,^1\Sigma^+$ states of SO are indicated by arrows on the figure. The fast feature terminates just below the energetic cut-off for the $a\,^1\Delta$ state.

The $m/z = 62$ (CH_2SO^+) TOF spectra were simulated using a statistical prior distribution for direct H-atom loss from ground state CH_3SO, shown in Figure 4.12. Although it was not possible to measure the dependence of these TOF spectra on laser polarization, all spectra could be adequately simulated by assuming an isotropic angular distribution ($\beta = 0$). The H-atom counter-fragment could not be collected because of the same difficulties for O atoms and CH_3 fragments. Depending on the CH_2SO isomer formed, the available energy for this process can range from ~56-77 kcal/mol.

Insight into the mechanisms of the dissociation reactions is gained by inspecting various characteristics of the $P(E_T)$ determined here. Table 4.2 shows a comparison of the peaks of the distributions, the average translational energy, $\langle E_T \rangle$, the maximum translational energy, $E_{T,max}$, and the fraction of the available energy partitioned into relative product translational motion, $\langle f_T \rangle$.

The product branching ratio for competing dissociation pathways can be obtained by measuring TOF spectra that contain contributions from each channel of interest.[218] The branching ratio between two channels A and B is then given by

$$BR\left(\frac{A}{B}\right) = \frac{W_A}{W_B} \times \frac{\sigma_B}{\sigma_A} \times \frac{f_B}{f_A} \tag{4.8}$$

in which W_i is the weighting of the $P(E_T)$ for channel i, σ_i is the ionization cross section for product i that is estimated according to an empirical scheme unless otherwise stated,[146] and f_i is the fraction of product i that dissociatively ionizes to the detected ion during electron

Table 4.2: Characteristics of the $P(E_T)$ distributions for methylsulfinyl dissociation. All values are in kcal/mol except for $\langle f_T \rangle$ which is a dimensionless quantity ranging from 0 to 1. For the CH_3 + SO data the $\langle f_T \rangle$ reported for the slow and fast channels assumes formation of the X $^3\Sigma^-$ and $a\ ^1\Delta$ product states of the SO fragment respectively.

Channel	**Peak**	$\langle E_T \rangle$	$E_{T,max}$	$\langle f_T \rangle$
CH_2SO + H	4	10	56	0.18
CH_3 + SO				
Slow	6	13	44	0.20
Fast	24	25	44	0.54
CH_3S + O	1	3	12	0.25

impact ionization. The f_i values for the SO fragment are taken from the published mass spectrum.[219] The CH_3S mass spectrum was produced by measuring the relative ion signal at m/z = 47 (0.17), 46 (0.03), 45 (0.27), and 44 (0.29) and to the best of our ability at m/z = 32 (0.24). Despite the difficulties faced in collecting this mass spectrum, the fraction of parent ions calculated for CH_3S is similar to that for the analogous CH_3O radical,[220] and CH_3OH and CH_3SH both produce almost identical mass spectra when accounting for the difference in mass between O and S.[148] In the CH_3S/SO branching ratio calculation, the f_i values are corrected for the natural abundances of ^{33}S and ^{34}S for the SO and CH_3S channels respectively since both products are detected at m/z = 49, leading to a CH_3S/SO branching ratio of $3.5^{+2.1}_{-1.1}$. The uncertainty is determined by varying W_i for each component until the simulation no longer agrees with the experimental TOF spectra.

To determine the branching ratio between the fast and slow SO + CH_3 channels, we assume that f_i is the same regardless of the product state of the nascent SO molecules. For σ_i we assume that the ratio of electron impact ionization cross sections for the X $^3\Sigma^-$ ground state (4.95 Å^2 at 80 eV)[219] and the $a\ ^1\Delta$ excited state scale according to theoretical calculations for the analogous electronic states in O_2.[221] With these assumptions we find that $SO_{fast}/SO_{slow} = 0.8 \pm 0.2$ according to Equation 4.8. These branching ratio results are summarized in Table 4.3.

The theoretical branching ratio for statistical ground state dissociation is found from the RRKM analysis, which yields 87% SO + CH_3, 11% CH_2SO + H, and 2% CH_2S + OH. If we assume that the CH_2SO and SO_{slow} are both produced from ground state statistical reactions proceeding at rates according to RRKM theory, then $CH_2SO/SO_{slow} = 0.13$ is expected. These results are included in Table 4.3 for comparison with experiment. Note that the total "experimental" contribution from H + CH_2SO is based on the RRKM ratio between that channel and slow SO + CH_3. Other product channels amounted to significantly less than 0.1% of the total dissociation in all cases.

Table 4.3: Comparison of experimental and RRKM branching ratios for CH_3SO photodissociation. For the SO + CH_3 channel the total contribution to dissociation is further split into the slow and fast channels observed in the experiment.

Channel	**Percent of Dissociation**	
	Experimental	**RRKM**
CH_3S + O	77 ± 8	2×10^{-3}
SO + CH_3		
Total	22 ± 7	-
Slow	12 ± 4	87
Fast	10 ± 3	-
CH_2SO + H	1.5 ± 0.5	11
CH_2S + OH	Not observed	2

Although the ion signal for $m/z = 62$ is very weak, dissociative ionization of this fragment to SO^+ could be expected to appear in the TOF spectrum for $m/z = 48$ at $\Theta_{LAB} = 5^o$ in Figure 4.5. This contribution, indicated as the purple line, is added by assuming the RRKM branching ratio to form sulfine is correct, and that f_i at $m/z = 48$ is the same for CH_2SO as it is for CH_3CHSO.[222]

4.6 Discussion

This experiment sought to determine the photochemistry of methylsulfinyl radicals, including the reaction mechanisms and relative importance of different product channels. Dissociation forms primarily CH_3S + O (77%), with some SO + CH_3 (22%) and small amounts of CH_2SO + H (estimated at ∼1%) also contributing.

On the ground state, the RRKM calculations show that cleavage of the S-O bond, which results in the CH_3S + O channel, is virtually nonexistent due to the large reaction enthalpy of 105.3 kcal/mol, but this is the dominant product channel, accounting for 77% of total dissociation. Hence, this channel must arise from excited state dynamics as does the analogous channel in CH_3OO and CH_3SS photodissoiciation.[197,198] The laser polarization results support this assignment in finding an anisotropic angular distribution of photoproducts that suggests prompt bond cleavage. The experimentally determined anisotropy parameter indicates a near-parallel transition that is consistent with excitation to the $\widetilde{B}\,^2A''$ electronic state. While the $\widetilde{C}\,^2A'$ state has very similar excitation energy, this transition carries no oscillator strength and the perpendicular nature of the transition would lead to $\beta < 0$ in the limit of prompt dissociation.

Despite the apparent prompt recoil of CH_3S and O, the $P(E_T)$ distribution for this channel is peaked close to 0 kcal/mol. Such a result is rationalized by the very close proximity in the energies of the methylsulfinyl $\widetilde{B}\,^2A''$ state and the CH_3S + O products, which makes it unlikely that the potential energy surface would have a steep slope along the S-O reaction coordinate. Motion along a more gently sloped surface would be expected to less efficiently partition the available energy into relative translational motion of the products, resulting in an overall slower $P(E_T)$ distribution.

The SO + CH_3 channel, which dominates for ground electronic state dissociation, accounts for only ∼22% of methylsulfinyl dissociation in this experiment. Furthermore, adequate simulation of the TOF spectra requires a $P(E_T)$ distribution that comprises two features, taken in Figure 4.11 to be a prior distribution and a fast channel. The $P(E_T)$ distribution for the fast channel peaks at 24 kcal/mol and extends from 14-44 kcal/mol. The peak of the distribution is far from 0 kcal/mol but much less than the 63.5 kcal/mol of available energy for formation of ground state SO, so this likely corresponds to SO fragments produced in either the $a\,^1\Delta$ state, or a mixture of the $a\,^1\Delta$ and $b\,^1\Sigma^+$. By analogy with CH_3OO,[223] the $\widetilde{B}\,^2A''$ state populated by 248 nm absorption correlates adiabatically with the $a\,^1\Delta$ SO product state, for which the energy cut-off agrees with the largest E_T in the experimental $P(E_T)$ distribution. The $\widetilde{C}\,^2A'$ state correlates adiabatically with the $b\,^1\Sigma^+$ SO product state, but has negligible oscillator strength. Hence, the most likely scenario is that excited state dissociation produces SO exclusively in the $a\,^1\Delta$ state.

The slow component of the $P(E_T)$ distribution in Figure 4.11 is a statistical prior distribution for $CH_3SO \rightarrow$ SO + CH_3. The slow SO + CH_3 feature is therefore assigned to a ground state statistical mechanism. Theoretical calculations support passage through a loose transition state without the recombination barriers suggested by an earlier experiment.[193]

Previous work on dimethyl sulfoxide photolysis observed production of hot ground state CH_3SO radicals that proceeds to dissociate statistically to SO + CH_3 and CH_2SO + H, in excellent agreement with the RRKM predictions in this work.[192,193] The presence of ground state statistical dissociation of CH_3SO to SO + CH_3 suggests that there should also be small amounts of H-atom loss occurring, and weak ion signal at $m/z = 62$ (CH_2SO^+) is indeed observed in this experiment. The assumption that the ground state branching ratio between these two channels is consistent with RRKM theory suggests that the CH_2SO + H channel accounts for only ∼1% of the measured dissociation in this experiment. Allowing H-atom loss to account for more than a few percent of dissociation compromises the ability to simulate the small angle $m/z = 48$ TOF spectra. The statistical nature of this channel is corroborated by the adequate simulation of the TOF spectra for $m/z = 62$ using a prior distribution for $CH_3SO \rightarrow$ H + sulfine. This agreement also supports passage through a loose transition state with no recombination barrier, in agreement with the theoretical calculations. The energy available to H + sulfine is insufficient to produce either fragment in an excited electronic state.

The experimental results of this study suggest that all four dissociation channels proceed through simple bond fission mechanisms, and that isomerization of methylsulfinyl does not

occur to an appreciable degree on the timescale of statistical ground state dissociation. For the ground state CH_3 + SO and CH_2SO + H reactions, this agrees with expectations based on the potential energy diagram in Figure 4.1 and Figures 4.15-4.17 that show dissociation mechanisms to proceed directly through loose transition states to products with comparatively low asymptotic energies. The only other non-negligible product predicted by RRKM theory for statistical ground state dissociation is ∼2% CH_2S + OH. Evidence of this reaction was not observed, and would be expected to produce even smaller signal than the H-atom loss channel in addition to being kinematically disfavored. If there are small amounts of this reaction, the dissociative ionization of CH_3S would fully obscure the signal. As such, there is no evidence that this reaction has any importance in the photochemistry of methylsulfinyl radicals.

It is interesting to compare the photodissociation dynamics of CH_3SO with the isovalent CH_3OO and CH_3SS radicals. Whereas CH_3OO and CH_3SS seem to exhibit exclusively excited state photochemistry for 248 nm absorption,[197,198] CH_3SO has a modest ground state contribution to its photodissociation. For all three molecules, the dominant channel involves impulsive cleavage of the chalcogen bond on an excited state. The minor channels show more variation: CH_3OO undergoes abstraction-dissociation on the $\widetilde{A}\,^2A'$ state to form formaldehyde and hydroxyl radical, CH_3SS eliminates S_2 to form methyl radicals through an unknown mechanism, while CH_3SO forms excited electronic state SO (likely $a\,^1\Delta$) with ground state methyl radical, and also undergoes statistical ground state dissociation to form SO + CH_3 and sulfine + H. Given the similarities in the various data between the S_2-loss in Ref. [197] and the SO-loss reported here, it is interesting to consider whether the broad CH_3 + S_2 distribution for CH_3SS dissociation actually comprises both ground state and excited state S_2 features that are less well resolved than in the present work. An equally plausible explanation is that the different electronic structure of CH_3SS, as described in Section 4.1, results in a different dynamical pathway to dissociation.[224]

4.7 Conclusions

The methylsulfinyl radical has a rich photochemistry at 248 nm. Prompt dissociation to CH_3S + O on an excited electronic state is the dominant channel, accounting for ∼77% of all dissociation. The CH_3S and O fragments are formed in their ground electronic states. Formation of SO + CH_3 makes up ∼22% of dissociation, and is split roughly equally between excited state and ground state mechanisms. Both mechanisms produce ground state CH_3 radicals, while the excited state mechanism leads to electronically excited SO, likely in its $a\,^1\Delta$ state. The excited state mechanisms of O-loss and SO-loss occur in a roughly 87:13 ratio. H-atom loss is a minor channel attributed to ground state dissociation producing sulfine, and accounts for the final ∼1% of dissociation events based on the expectation of statistical ground state dissociation.

4.8 Supporting Information

Photofragment ion signal dependence on laser fluence

The dependence of $m/z = 48$ signal on laser fluence is shown in Figure 4.13. The plot is linear with an intercept very close to the origin, supporting the assumption that all photochemistry occurs by single-photon excitation. Similar data for $m/z = 47$ shows the same linear dependence on laser fluence. It was not possible to determine the laser fluence dependence of $m/z = 62$ ion signal due to the poor signal-to-noise in the TOF spectra, but the data for this channel are consistent with the energy input of a single 248 nm photon.

Ion signal at $m/z = 15$

The co-fragment product for SO is the methyl radical which should be detected at $m/z = 15$ (CH_3^+). The TOF spectrum in Figure 4.14 for $m/z = 15$ shows some evidence for signal of this ion at $\Theta_{LAB} = 40^o$. The simulation for the CH_3 photofragment is produced using the $P(E_T)$ in Figure 4.11 which is determined from the much higher quality TOF spectra for the SO photofragment. This simulation coincides very well with a consistent rise in ion counts over a $\sim$50 μs wide region centered at an arrival time of 45 μs. This spectrum has a very poor signal-to-noise ratio due to the lower ionization cross-section and shorter residence time in the ionizer of CH_3 relative to the heavier SO fragment, and this makes TOF spectra at $m/z = 15$ prohibitively difficult to collect.

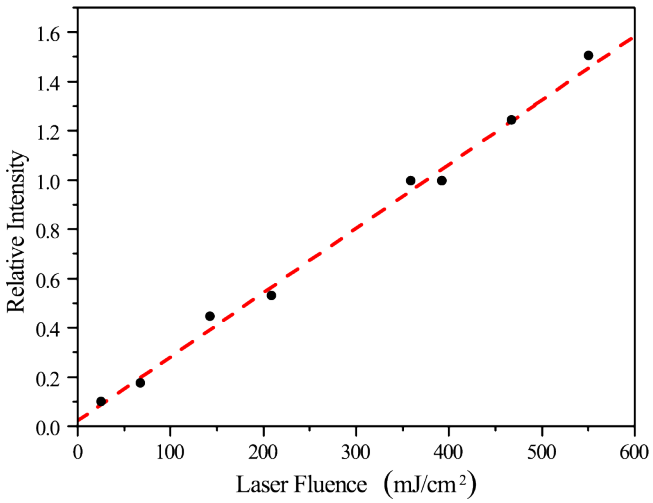

Figure 4.13: Dependence of ion signal at $m/z = 48$ (SO^+) on laser fluence normalized to the integrated signal collected for 375 mJ/cm^2. The dashed line is a linear fit to the experimental data points.

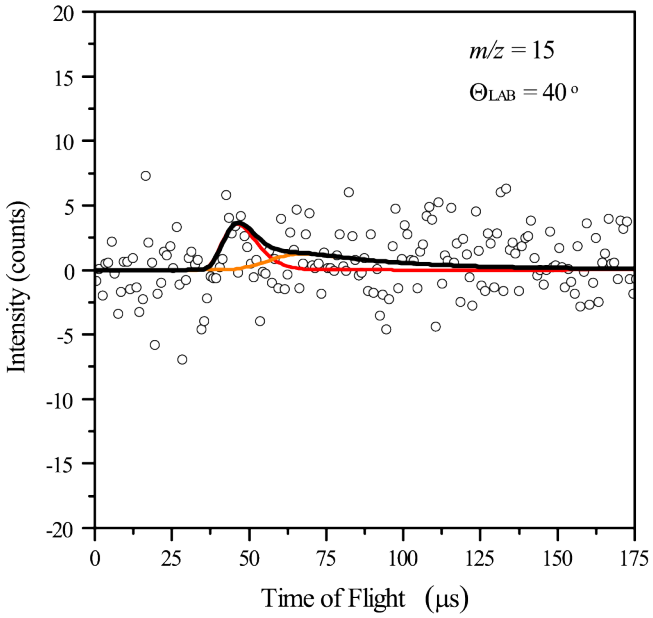

Figure 4.14: TOF spectrum for $m/z = 15$ (CH_3^+) at $\Theta_{LAB} = 40^o$. The experimental data are shown as open circles, and the black line is the total simulation generated using the $P(E_T)$ in Figure 4.11. This simulation is deconvoluted to yield a fast and a slow distribution which produce the red and orange simulations respectively.

G4 *ab initio* potential energy diagrams

Many isomerization and product channels were investigated using the G4 composite method. The relevant pathways are included in Figures 4.15-4.17, showing the most facile reactions and pathways to otherwise important products (for example the formation of the minimum energy isomer for a particular reaction). The potential energy diagram is split into one figure showing the formation of CH3 + SO (Figure 4.15), one for H-atom loss reactions (Figure 4.16), and one for reactions that eliminate O atoms, OH molecules, or SH molecules (Figure 4.17).

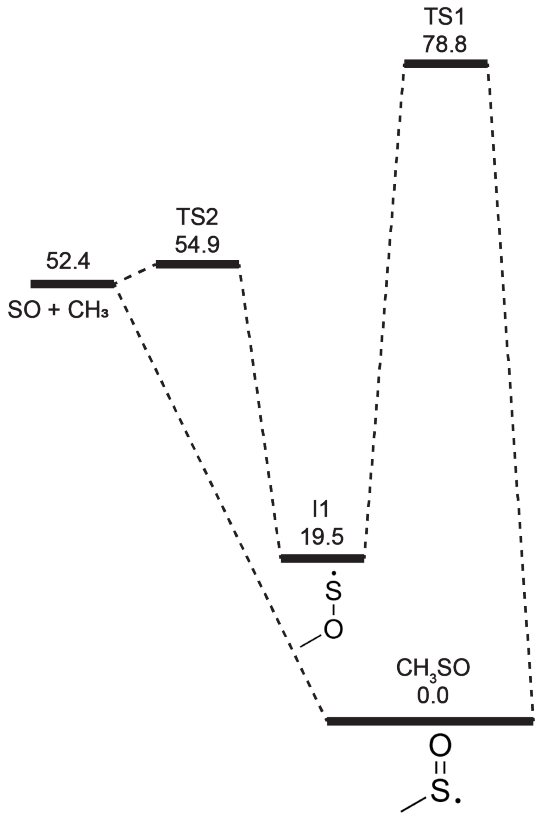

Figure 4.15: Ground state CH_3SO potential energy diagram showing the formation of SO ($X\ ^3\Sigma^-$) + CH_3.

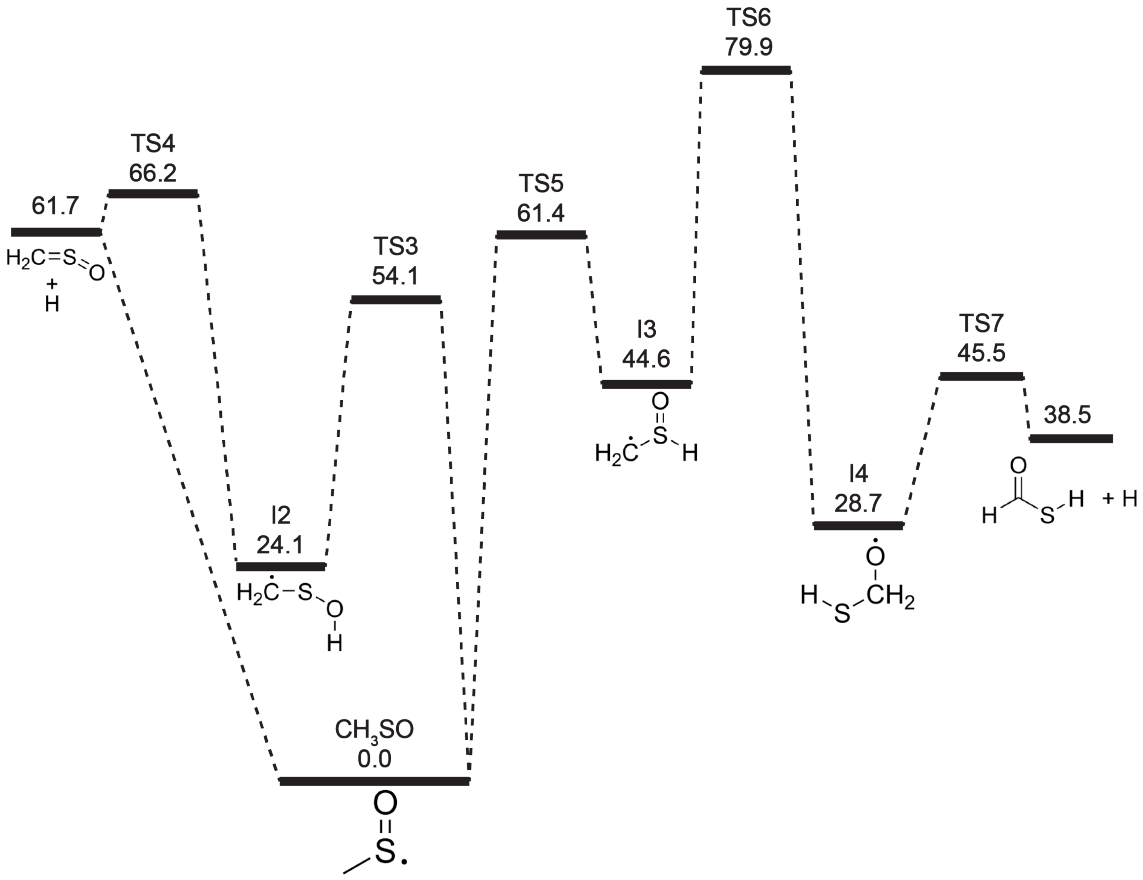

Figure 4.16: Ground state CH_3SO potential energy diagram showing the formation of sulfine, the most facile CH_2SO product, and thioformic acid, the lowest energy CH_2SO product.

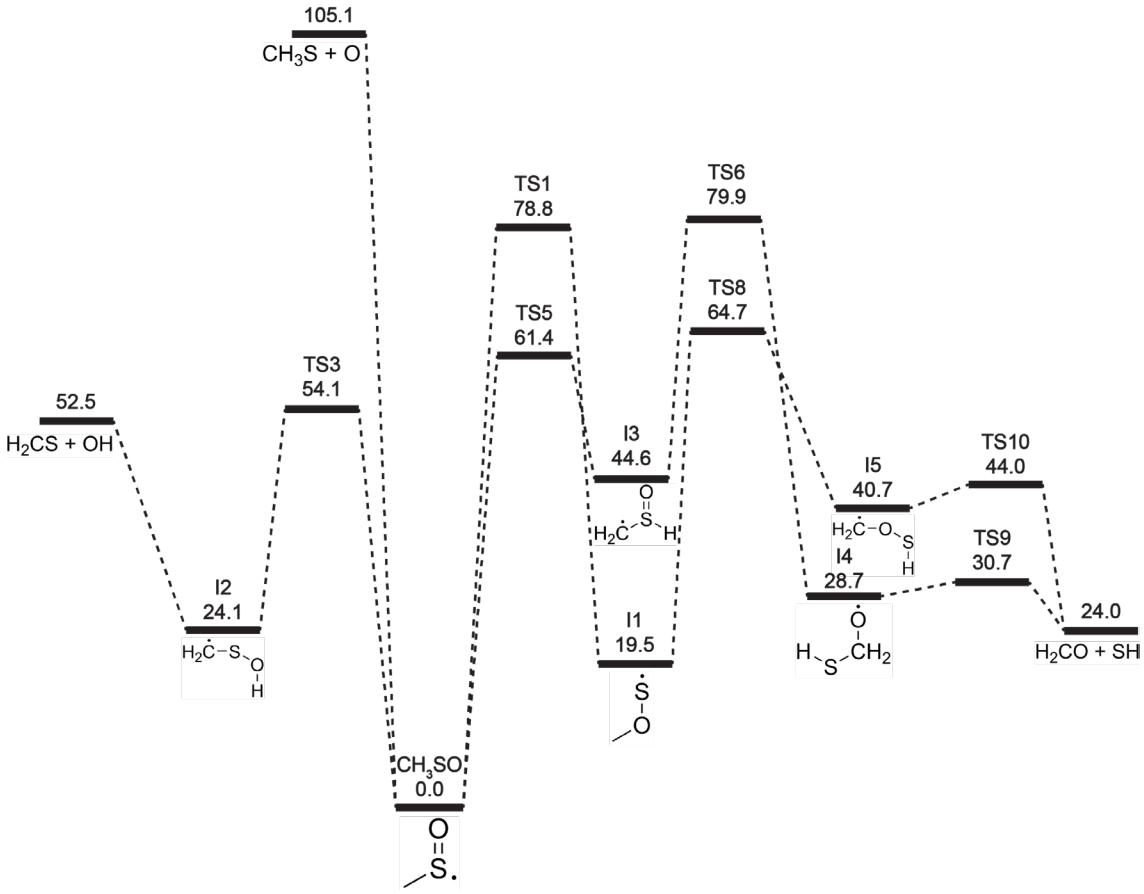

Figure 4.17: Ground state CH_3SO potential energy diagram showing the most facile pathways for CH_3S + O, CH_2S + OH, and CH_2O + SH product channels.

Stationary point geometries and vibrational frequencies from G4 calculations

The results of the G4 calculations for species relevant to this work are included below. Frequencies are in units of cm^{-1} and the molecular geometries use units of Å.

Minima:

CH_3SO:

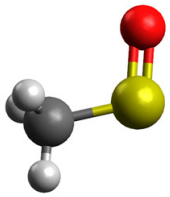

Frequencies:
127, 324, 664, 883, 942,
1057, 1320, 1446, 1460,
3041, 3140, 3143

	Geometry		
S	0.6559605	1.1688942	0.0000000
O	2.0458185	0.5840222	0.0000000
C	−0.5026875	−0.2372958	0.0000000
H	−0.3406095	−0.8425488	0.8948240
H	−1.5178725	0.1694772	0.0000000
H	−0.3406095	−0.8425488	−0.8948240

I1:

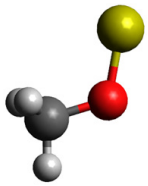

Frequencies:
83, 374, 777, 1025, 1152,
1189, 1461, 1478, 1485,
3038, 3123, 3140

	Geometry		
S	−1.857426	−1.050652	0.000000
O	−0.985846	0.327098	0.000000
C	0.445881	0.194332	0.000000
H	0.842306	1.212182	0.000000
H	0.777543	−0.341479	0.893628
H	0.777543	−0.341479	−0.893628

I2:

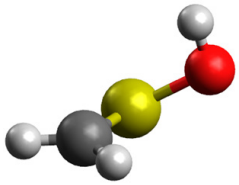

Frequencies:
286, 308, 379, 511, 721,
836, 900, 1178, 1383,
3147, 3272, 3752

	Geometry		
S	−0.348734	−1.026180	−0.138205
O	−1.683583	−0.007167	−0.178345
C	0.968042	0.028312	−0.099150
H	0.961683	0.949614	−0.669914
H	−1.773823	0.372126	0.706842
H	1.876413	−0.316704	0.378772

I3:

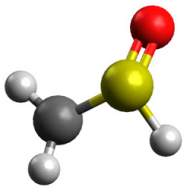

Frequencies:
219, 333, 526, 676, 778,
955, 1054, 1144, 1372,
2277, 3140, 3274

	Geometry		
S	−0.776177	−0.445193	−0.293303
O	−1.914688	0.467725	−0.035152
C	0.769156	0.311527	−0.050515
H	1.629459	−0.347121	0.020487
H	−0.593782	−1.309616	0.781069
H	0.886033	1.322680	−0.422587

I4:

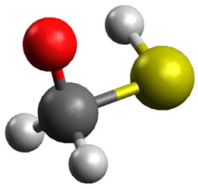

Frequencies:
279, 305, 545, 786, 1034,
1120, 1181, 1258, 1528,
2687, 2965, 3024

	Geometry		
S	1.317496	−0.328414	−0.292622
O	−1.097186	−0.833411	−0.285774
C	−0.436552	0.320109	−0.140587
H	1.281233	−1.022711	0.860355
H	−0.539950	0.825309	0.830081
H	−0.525042	1.039117	−0.971455

I5:

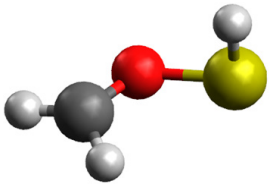

Frequencies:
203, 248, 389, 633, 701,
992, 1173, 1192, 1449,
2599, 3123, 3268

	Geometry		
S	−1.661365	−0.145216	−0.223252
O	−0.120973	−0.804561	−0.130798
C	0.921724	0.082700	−0.088597
H	0.769640	1.070323	−0.510429
H	−1.790741	0.216445	1.076503
H	1.881715	−0.419691	−0.123426

Transition States:

TS1:

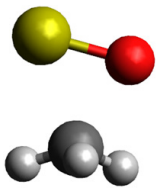

Frequencies:
980*i*, 234, 447, 812, 879, 920, 1254, 1398, 1470, 3055, 3149, 3272

	Geometry		
S	−1.711709	−0.092821	−0.001915
O	−0.746005	1.260741	−0.002844
C	0.415280	−0.204558	0.007838
H	0.670892	−0.203929	1.058575
H	0.350097	−1.200374	−0.437227
H	1.021445	0.440943	−0.624428

TS2:

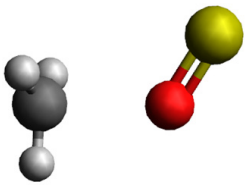

Frequencies:
134*i*, 18, 148, 312, 332, 632, 1060, 1410, 1412, 3130, 3313, 3316

	Geometry		
S	−2.573234	−0.002619	0.000000
O	−1.306198	0.824049	0.000000
C	0.927473	−0.187591	0.000000
H	1.406377	0.780964	0.000000
H	0.772790	−0.707402	0.934833
H	0.772790	−0.707402	−0.934833

TS3:

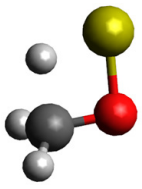

Frequencies:
1587*i*, 269, 559, 674, 880, 1019, 1112, 1160, 1474, 1754, 3057, 3177

	Geometry		
S	1.754787	0.221994	0.016253
O	0.258715	1.093707	0.036742
C	−0.559235	−0.020051	0.018595
H	−1.329741	−0.005453	−0.753321
H	0.686848	−0.841094	−0.308726
H	−0.811374	−0.449103	0.990455

TS4:

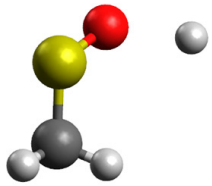

Frequencies:
873*i*, 165, 371, 415, 614, 756, 870, 967, 1113, 1397, 3154, 3279

	Geometry		
S	−0.310535	−0.989708	−0.068274
O	−1.577996	−0.226672	−0.318749
C	1.025284	−0.070552	−0.151248
H	1.003772	0.977610	−0.425295
H	−2.104093	0.873575	0.887968
H	1.963567	−0.564254	0.075600

TS5:

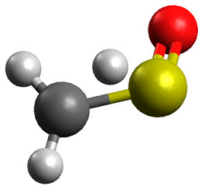

Frequencies:
1669*i*, 318, 332, 506, 709, 867, 1016, 1141, 1343, 1920, 3135, 3282

	Geometry		
S	0.916989	−0.649028	−0.158985
O	2.021993	0.339459	−0.153169
C	−0.688183	0.135776	−0.167915
H	−1.503307	−0.329850	−0.710737
H	−0.006382	−0.658418	1.014394
H	−0.741111	1.162059	0.176411

TS6:

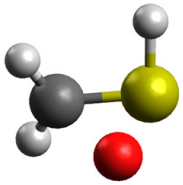

Frequencies:
1040*i*, 389, 495, 663, 833, 855, 908, 1065, 1407, 2332, 3156, 3301

	Geometry		
S	−1.087952	0.198335	−0.259302
O	−0.069794	1.538563	−0.064142
C	0.556811	−0.239474	−0.170759
H	−1.472550	−0.520704	0.860765
H	0.968567	−0.672811	0.733204
H	1.104920	−0.303911	−1.099766

TS7:

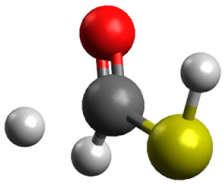

Frequencies:
870*i*, 281, 355, 407, 516, 624, 910, 997, 1349, 1712, 2683, 2948

	Geometry		
S	−1.374917	−0.252883	−0.202603
O	1.305406	−0.623072	−0.161612
C	0.404130	0.162127	−0.320274
H	−1.157801	−1.498925	0.261813
H	0.515971	1.158804	−0.785167
H	0.307213	1.053949	1.207842

TS8:

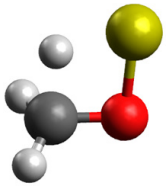

Frequencies:
1587*i*, 269, 559, 674, 880, 1019, 1112, 1160, 1474, 1754, 3057, 3177

	Geometry		
S	1.754787	0.221994	0.016253
O	0.258715	1.093707	0.036742
C	−0.559235	−0.020051	0.018595
H	−1.329741	−0.005453	−0.753321
H	0.686848	−0.841094	−0.308726
H	−0.811374	−0.449103	0.990455

TS9:

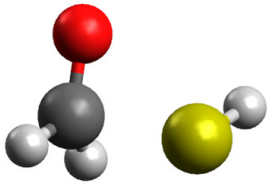

Frequencies:
292*i*, 214, 272, 590, 746, 1081, 1222, 1434, 1597, 2696, 2939, 3003

	Geometry		
S	1.529298	−0.266203	−0.278602
O	−1.045682	−0.853330	−0.294187
C	−0.645158	0.317668	−0.136728
H	1.395849	−1.017331	0.831317
H	−0.621513	0.789810	0.859338
H	−0.612795	1.029388	−0.981139

TS10:

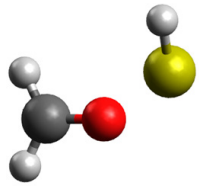

Frequencies:
379*i*, 129, 315, 374, 622, 879, 1141, 1175, 1494, 2658, 3095, 3223

	Geometry		
S	1.706835	−0.130263	−0.269815
O	0.032222	−0.773993	0.000757
C	−0.981203	0.048701	−0.164432
H	−0.953686	1.047552	0.263111
H	−1.751255	−0.242561	−0.874925
H	1.947088	0.050564	1.045304

Variational TSA: $CH_3SO \rightarrow CH_3 + SO$

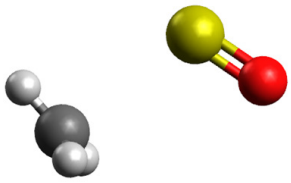

Frequencies:
178*i*, 92, 193, 486, 516, 822, 1115, 1416, 1420, 3131, 3313, 3318

	Geometry		
S	0.000000	0.787201	0.000000
O	1.489118	0.634938	0.000000
C	−1.310599	−1.935861	0.000000
H	−0.861349	−2.247951	0.933016
H	−2.326651	−1.563645	0.000000
H	−0.861349	−2.247951	−0.933016

r_{C-S} = 3.0 Å

Variational TSB: $CH_3SO \rightarrow CH_2SO + H$

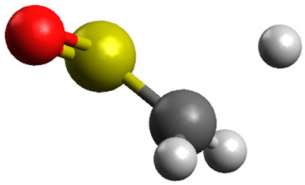

Frequencies:
1257*i*, 359, 435, 603, 783, 828, 890, 926, 1128, 1382, 3148, 3273

	Geometry		
S	0.195962	−0.460267	0.048241
O	1.287672	0.549250	−0.018760
C	−1.315387	0.229541	−0.199955
H	−1.390667	1.223045	−0.628173
H	−2.126875	−0.474951	−0.350237
H	−2.026913	0.844935	1.556356

r_{C-H} = 2.0 Å

Variational TSC: $CH_3SO \rightarrow CH_3S + O$

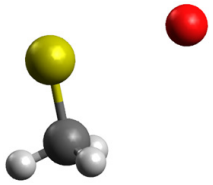

Frequencies:
200*i*, 65, 78, 707, 863,
1207, 1326, 1468, 1746,
3021, 3104, 3186

Geometry			
S	0.475222	−0.728718	0.000000
O	−2.353273	0.294569	0.000003
C	1.186317	0.926380	0.000009
H	0.915622	1.479669	0.900899
H	2.275360	0.784457	−0.001193
H	0.913748	1.480531	−0.899780

r_{S-O} = 3.0 Å

Variational TSD: $CH_2SOH \rightarrow CH_2S + OH$

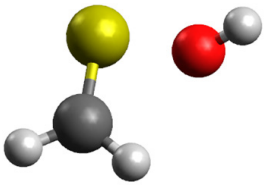

Frequencies:
335*i*, 170, 334, 541, 850,
915, 934, 1026, 1445,
3081, 3167, 3673

Geometry			
S	0.235836	−0.579690	0.031710
O	−1.621061	0.383677	−0.152293
C	1.307129	0.622715	0.000522
H	2.264986	0.538155	−0.515749
H	1.126039	1.579106	0.494179
H	−2.038688	0.352070	0.729420

r_{S-O} = 2.1 Å

Molecular Products:

CH_2SO (sulfine):

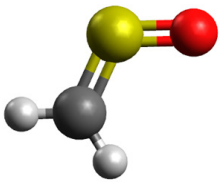

Frequencies:
389, 645, 793, 874, 1005,
1195, 1404, 3151, 3274

Geometry			
S	−0.646547	0.871071	0.000000
O	−1.991429	0.263510	0.000000
C	0.589741	−0.166894	0.000000
H	0.468819	−1.244297	0.000000
H	1.579417	0.276610	0.000000

CH_2SO (thioformic acid):

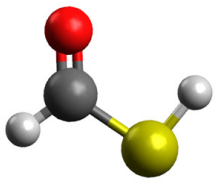

Frequencies:
424, 431, 658, 938, 948,
1385, 1810, 2684, 2958

	Geometry		
S	−0.635681	−1.127679	0.000000
O	1.060398	0.945011	0.000000
C	−0.078238	0.579002	0.000000
H	−0.951885	1.256859	0.000000
H	0.605405	−1.653192	0.000000

CH_3S (methylthio):

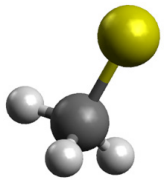

Frequencies:
572, 713, 859, 1328, 1372,
1470, 3022, 3098, 3123

	Geometry		
S	0.019515	−1.667092	0.000000
C	0.019515	0.137845	0.000000
H	−0.532606	0.485534	0.879752
H	1.026180	0.558181	0.000000
H	−0.532606	0.485534	−0.879752

CH_2S (thioformaldehyde):

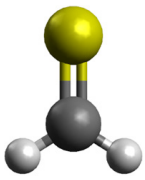

Frequencies:
995, 1033, 1090, 1489,
3071, 3155

	Geometry		
S	0.000000	0.000000	1.500011
C	0.000000	0.000000	−0.110707
H	0.000000	0.922054	−0.694652
H	0.000000	−0.922054	−0.694652

CH_2O (formaldehyde):

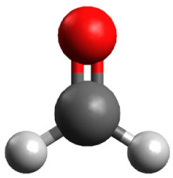

Frequencies:
1202, 1272, 1544, 1847,
2883, 2930

	Geometry		
O	0.000000	0.000000	1.198238
C	0.000000	0.000000	−0.001723
H	0.000000	0.937108	−0.598258
H	0.000000	−0.937108	−0.598258

CH_3:

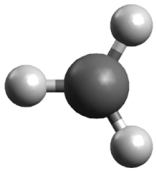

Frequencies:
470, 1407, 1407, 3123,
3306, 3306

	Geometry		
C	0.000000	0.000000	0.000000
H	0.000000	1.081308	0.000000
H	−0.936440	−0.540654	0.000000
H	0.936440	−0.540654	0.000000

SO:

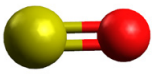

Frequencies:
1148

	Geometry		
S	0.000000	0.000000	0.748412
O	0.000000	0.000000	−0.748412

SH:

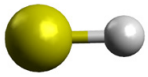

Frequencies:
2679

	Geometry		
S	0.000000	0.000000	0.675033
H	0.000000	0.000000	−0.675033

OH:

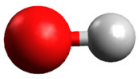

Frequencies:
3696

	Geometry		
O	0.000000	0.000000	0.488066
H	0.000000	0.000000	−0.488066

Other Species:

C_4H_8SO (allyl methyl sulfoxide):

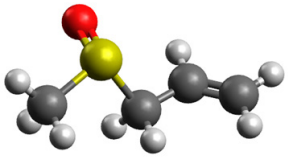

Frequencies:
70, 91, 181, 201, 267, 346, 359, 410, 564, 650, 722, 864, 929, 936, 958, 973, 1040, 1080, 1121, 1213, 1221, 1318, 1324, 1430, 1447, 1462, 1466, 1712, 3031, 3043, 3101, 3144, 3145, 3152, 3170, 3230

	Geometry		
S	1.094824	0.580857	−0.610054
O	1.356685	1.872081	0.089363
C	2.376407	−0.601379	−0.057127
H	2.423988	−0.598438	1.034566
H	2.149294	−1.599863	−0.439806
H	3.324234	−0.252453	−0.470930
C	−0.310284	−0.234046	0.293310
H	−0.432969	−1.239606	−0.121093
H	0.018775	−0.298493	1.336935
C	−1.546337	0.592600	0.152926
H	−1.472074	1.602171	0.549474
C	−2.670868	0.178067	−0.423462
H	−2.772213	−0.824092	−0.830800
H	−3.539461	0.822593	−0.503299

C_3H_5 (allyl):

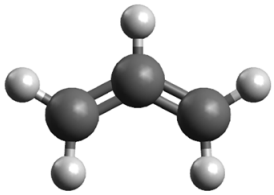

Frequencies:
422, 537, 556, 784, 808, 932, 1023, 1041, 1220, 1271, 1421, 1509, 1519, 3139, 3149, 3155, 3247, 3250

	Geometry		
C	1.227542	−0.163407	0.000000
H	1.297433	−1.246580	0.000000
H	2.156813	0.393018	0.000000
C	0.000000	0.472391	0.000000
H	0.000000	1.561546	0.000000
C	−1.227542	−0.163407	0.000000
H	−1.297433	−1.246580	0.000000
H	−2.156813	0.393018	0.000000

Chapter 5

Photodissociation dynamics of the cyclohexyl radical from the 3p Rydberg state at 248 nm

The content and figures of this chapter are reprinted or adapted with permission from Ramphal, I. A.; Shapero, M.; Neumark D. M., "Photodissociation dynamics of the cyclohexyl radical from the 3p Rydberg state at 248 nm," J. Phys. Chem. A, 2021, 125, 3900.

Abstract

The photodissociation of jet-cooled cyclohexyl was studied by exciting the radicals to their 3p Rydberg state using 248 nm laser light and detecting photoproducts by photofragment translational spectroscopy. Both H-atom loss and dissociation to heavy fragment pairs are observed. The H-atom loss channel exhibits a two-component translational energy distribution. The fast photoproduct component is attributed to impulsive cleavage directly from an excited state, likely the Rydberg 3s state, forming cyclohexene. The slow component is due to statistical decomposition of hot cyclohexyl radicals that internally convert to the ground electronic state prior to H-atom loss. The fast and slow components are present in a ∼0.7:1 ratio, similar to findings in other alkyl radicals. Internal conversion to the ground state also leads to ring-opening followed by dissociation to 1-buten-4-yl + ethene in comparable yield to H-loss, with the C_4H_7 fragment containing enough internal energy to dissociate further to butadiene via H-atom loss. A very minor ground-state C_5H_8 + CH_3 channel is observed, attributed predominantly to 1,3-pentadiene formation. The ground-state branching ratios agree well with RRKM calculations, which also predict C_4H_6 + C_2H_5 and C_3H_6 + C_3H_5 channels with similar yield to C_5H_8 + CH_3. If these channels were active it was at levels too low to be observed.

5.1 Introduction

Alkanes comprise a large fraction of chemical species in hydrocarbon fuel mixes, including substantial amounts of cycloalkanes.[225,226] Given their abundance, a detailed understanding of hydrocarbon combustion requires knowledge of possible decomposition pathways available to alkanes, in which alkyl radicals are crucially important. Alkanes emitted directly into the atmosphere by industrial activities are oxidized through an array of homogeneous and heterogeneous chemical transformations involving radicals.[227,228] Alkyl radical photochemistry is also important to consider, both on earth and in other planetary atmospheres where hydrocarbons are abundant.[229,230] In this study, we investigate the photodissociation of the cyclohexyl radical at 248 nm to determine its primary photochemistry and dissociation mechanisms using photofragment translational spectroscopy.

Alkyl radical photochemistry is of fundamental interest,[231–233] and the electronic absorption spectra of alkyl radicals have previously been characterized.[234] The lowest lying electronic excited states available to alkyl radicals are the 3s and $3p_z$ (henceforth referred to as 3p) Rydberg states. While there has been a great deal of historical interest in the photodissociation dynamics of methyl[235–237] and ethyl[238–241] radicals, larger alkyl radicals have only been addressed more recently. Furthermore, to date the ultraviolet photodissociation dynamics of cycloalkyl radicals remains virtually uncharacterized.

Previous photodissociation studies from the 3s and 3p Rydberg states of ethyl by Zhang, Fischer, Bañares and co-workers detected H atoms ejected with a bimodal kinetic energy distribution.[238–241] The 'fast' H atoms result from direct dissociation from the excited electronic state, while the 'slow' population is attributed to statistical dissociation following internal conversion to the ground state. The observation of angular distributions that are anisotropic for the fast H atoms and isotropic for the slow H atoms supports these mechanisms. These fast and slow dissociation channels occur in a roughly 0.4:1 ratio depending on the initial and final states of ethyl used in the experiment. For ethyl excited to the 3s state, the fast dissociation channel has a dissociation time constant of ∼300 fs, while for the slow channel it is ∼6-7 ps.[242]

Photodissociation of *n*-propyl, *i*-propyl, *n*-butyl, *s*-butyl, *t*-butyl, and 1-pentyl radicals have all produced data that are consistent with the same H-loss mechanisms outlined above for the ethyl radical.[232,243–245] For all of these radicals as for ethyl, the fast and slow H-loss channels occur in a 0.2-0.7:1 ratio, assuming H atoms with different speeds are detected with equal efficiency. Similar experiments on cyclohexyl radical were carried out by Zhang and co-workers.[246] Initially, only fast H-atom photofragments were seen, but more recent work suggests evidence for the slow channel, too.[247] In addition, for most studies on the photodissociation dynamics of alkyl radicals, the detection scheme is only sensitive to H atoms, and cannot yield direct information about potential competing dissociation pathways. A notable exception is photodissociation of *t*-butyl radical excited to the 3p state, which produced CH_3 + dimethylcarbene in roughly equal amounts to H + 2-methylpropene (*i*-butene).[134]

Numerous studies concerning the thermal decomposition of cyclohexyl radical have appeared in the context of understanding the decomposition pathways of cyclohexane during

combustion.[248–252] Of particular interest is the competition between direct H-atom loss adjacent to the radical site to form cyclohexene and C–C β-scission yielding the radical-terminated linear alkene 1-hexen-6-yl:

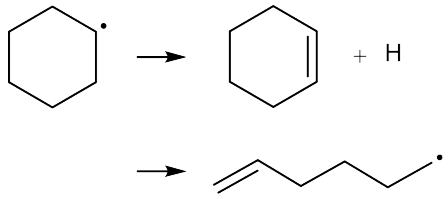

Shock tube and flame studies on cyclohexane find data consistent with a preponderance for ring-opening, with the direct H-loss to ring-opening branching ratio ∼0.3-0.9:1 depending upon experimental conditions.[248,249] Low-pressure (30 Torr) pyrolysis of cyclohexane in a flow reactor, probed with VUV photoionization mass spectrometry, found a similar 0.25:1 ratio for these reactions.[250] Comparably low-pressure chemical activation studies also yielded cyclopentylmethyl radical, formed either by ring-contraction of cyclohexyl through a tight transition state, or stepwise by the recyclization of 1-hexen-6-yl.[251,252] However, pyrolysis of cyclohexyl radicals under unimolecular conditions produced no evidence for cyclopentylmethyl in photoionization spectra.[253]

While all the C_6H_{11} isomers described above can decompose by H-atom loss, ring-opening to 1-hexen-6-yl facilitates many additional dissociation channels. Various experimental and theoretical studies on decomposition of both cyclohexane and 1-hexene have implicated 1-hexen-6-yl in the following:[248–250,253–260]

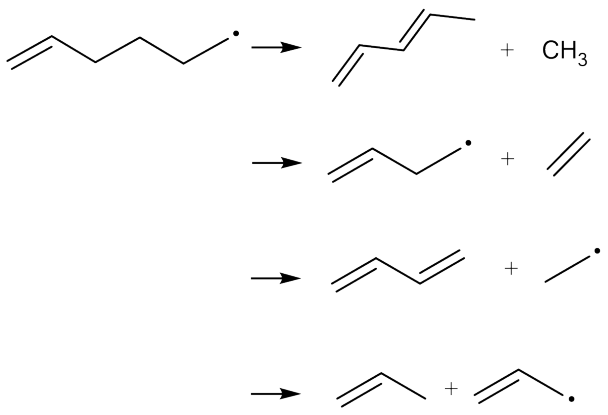

Aside from the 1-buten-4-yl + ethene channel, all of the above reactions require further isomerization to other C_6H_{11} species before dissociation can occur. Goldsmith et al.[257] and Gong et al.[258] in particular provide a detailed picture of many isomerization and dissociation reactions on the C_6H_{11} potential energy surface. The relative energies of these product channels compared to cyclohexyl are shown in Table 5.1.

Cyclohexyl radicals adopt the chair conformer equilibrium geometry with C_s symmetry, and a 5.6 kcal/mol isomerization barrier separating the two chair conformers.[261] The most

Table 5.1: Asymptotic energies for cyclohexyl dissociation channels. All channels except H + cyclohexene require ring-opening to proceed. Energies are reported in units of kcal/mol and taken from Ref. [258], except for H + 1,5-hexadiene which was calculated here.

Product Channel	**ΔH (0 K)**
H + cyclohexene	31.3
H + 1,5-hexadiene	55.7
C_5H_8 + CH_3	34.6
C_4H_7 + C_2H_4	44.1
C_4H_6 + C_2H_5	37.2
C_3H_6 + C_3H_5	27.9

stable conformation has a nearly planar geometry about the radical site, with the α-hydrogen in the equatorial position. Electron impact has determined the ionization potential to be 7.66 eV.[262] The absorption spectrum of cyclohexyl radicals shows a broad feature around 250 nm corresponding to the 3p Rydberg excited state.[234,263]

Given that most photodissociation studies on alkyl radicals rely heavily on H-atom-specific detection schemes, and the lack of studies concerning the photodissociation of cycloalkyl radicals altogether, this work seeks to characterize the photochemistry of cyclohexyl radicals excited at 248 nm to the 3p Rydberg state. The universal detection scheme utilized herein for photofragment translational spectroscopy is capable of detecting all possible photoproducts. In addition to H-atom loss, we find evidence for C_5H_8 + CH_3, and C_4H_7 + C_2H_4 dissociation channels, and no evidence of the C_4H_6 + C_2H_5 or C_3H_6 + C_3H_5 channels. Comparison to previous work on the ethyl radical suggests that the initially prepared 3p state converts to the 3s Rydberg state, followed by passage through a conical intersection with the ground state.[241] Traversing the conical intersection either liberates H atoms directly or results in hot ground state cyclohexyl that dissociates according to statistical energy partitioning. The C_4H_7 fragment is formed with enough internal energy to further decompose, proceeding almost exclusively to 1,3-butadiene + H.

5.2 Experimental

Precursor synthesis and characterization

Flash vacuum pyrolysis of alkyl nitrites yields alkyl radicals via sequential loss of NO and CH_2O (Figure 5.1). Cyclohexylmethyl nitrite was synthesized from cyclohexanemethanol by reaction of the alcohol with HONO, and collected as a viscous, pale yellow liquid.[264] The production and purity of cyclohexylmethyl nitrite was verified using NMR spectroscopy

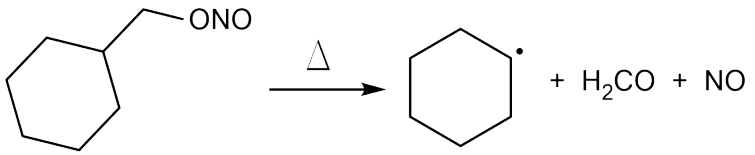

Figure 5.1: Generation of cyclohexyl radicals by pyrolysis of cyclohexylmethyl nitrite. This two-step reaction proceeds via NO-loss followed by liberation of formaldehyde to afford cyclohexyl.

(400 MHz, C_6D_6, $(CH_3)_4Si$), ^{1}H-NMR: δ (ppm) 0.68 (2H, q, *o*-CH axial), 0.97 (3H, m, *m,p*-CH axial), 1.33 (1H, m, α-CH), 1.47 (5H, m, *o,m,p*-CH equatorial), 4.12 (2H, s, —CH_2ONO), and ^{13}C-NMR: δ (ppm) 25.5 (*m*-CH_2), 26.1 (*p*-CH_2), 29.3 (*o*-CH_2), 37.2 (α-CH), 73.2 (—CH_2ONO). The chemical shifts, splitting patterns, and integrated peak intensities were consistent with expectations for cyclohexylmethyl nitrite, and the ^{1}H-NMR peak at 1.58 ppm due to the alcohol group is absent from the product spectrum. Cyclohexylmethyl nitrite was stored at ≤ 5 ^{o}C and away from light to minimize decomposition.

Photodissociation experiments

Photodissociation of cyclohexyl was studied using the modified crossed molecular beam instrument with a fixed source and a rotatable detector.[11,133] Cyclohexylmethyl nitrite was entrained in ∼900 Torr of a carrier gas mix consisting of 10% N_2 in He bubbled through an ice-water cooled reservoir of the nitrite, resulting in a ∼0.5% nitrite beam. Supersonic expansion through a piezoelectric pulsed valve introduced the molecular beam directly into a resistively heated SiC tubular reactor,[14] set to dissipate a fixed amount of power using a current-regulated power supply. During operation of the molecular beam the source chamber was kept at a fixed pressure of 6.0×10^{-5} Torr. Two skimmers separated the source chamber and main scattering chamber, and collimated the molecular beam.

In the main chamber, the beam passed through an aperture in a copper cold head held at 10 K by a He compressor. This surface further collimates the beam and lowers background signal in the detector, maintaining a main chamber pressure of $\sim 5 \times 10^{-7}$ Torr. The detector lies within a triply differentially pumped chamber. A tunable electron impact ring-filament ionizer typically operated at 80 eV creates cations.[135] These ions are extracted and focused into a quadrupole mass filter which selectively transmits ions according to their m/z value. Mass-selected ions are detected using the Daly-style ion detector.[85]

The molecular beam can be characterized by directing it into the detector, where dissociative ionization following electron impact will produce a mass spectrum characteristic of molecules within the beam. The ionizer can be operated as low as ∼4 eV, and measuring ion signal response to changes in electron impact energy with a fixed emission current generates an ionization efficiency curve (IEC).[84,105] The energy-intercept of this curve yields an appearance potential that is expected to match the ionization potential of the species

in the beam. Finally, a multichannel scaler interfaced to the ion detector can collect and bin ion signal as a function of time. Insertion of a slotted spinning disk into the molecular beam path thus enables determination of the molecular beam velocity profile. Cyclohexyl radical beams typically had a velocity of 1600 m/s and speed ratios, defined as the beam flow velocity divided by the velocity spread, of ∼5.

During photodissociation experiments, the focused 248 nm output of an LPX 220i excimer laser crossed the molecular beam at 90^o with a fluence of 375 mJ/cm^2. The laser was operated at half of the 400 Hz repetition rate of the pulsed valve to enable shot-to-shot background subtraction of signal not attributable to the laser pulse. Photoproduct TOF spectra were collected as a function of detector laboratory angle Θ_{LAB} relative to the molecular beam by rotating the detector within the plane defined by the laser and molecular beams. Typical TOF spectra were collected using a few 10^5-10^6 laser shots and simulated using a forward convolution program to determine center-of-mass translational energy distributions for photoproducts.[136]

5.3 Theoretical Methods

The large photon energy in this study motivated consideration of isomerization and dissociation pathways which were not included by Goldsmith et al.[257] and Gong et al.[258] in previous work. Energies and vibrational frequencies for the additional minima and transition states were calculated using the ωB97X-D functional[265] with the aug-cc-PVTZ basis set[266,267] implemented in Gaussian 16.[268] Excited electronic states of cyclohexyl were found using the EOM-CCSD/aug-cc-PVDZ level of theory.[269]

Unimolecular reaction rates for ground-state isomerization and dissociation of cyclohexyl radicals were calculated using microcanonical Rice-Ramsperger-Kassel-Marcus (RRKM) theory,[141] where elementary rate constants $k(E)$ are given by:

$$k(E) = \sigma \frac{W^{\ddagger}(E - E_o)}{h\rho(E)} \tag{5.1}$$

In the above expression, σ is the reaction path degeneracy,[144] $W^{\ddagger}(E - E_o)$ is the sum of rovibrational states accessible to the transition state, $\rho(E)$ is the reactant rovibrational density of states, and h is Planck's constant. It is important to treat internal rotors appropriately in the density of states evaluation given their plentitude in many C_6H_{11} isomers. To determine $\rho(E)$, the rotational density of states for a collection of u 1-D and p 2-D internal rotors was first calculated according to

$$\rho_R(E) = \frac{\pi^{u/2}}{\Gamma(p + u/2)} \, E^{p+u/2-1} \prod_{i=1}^{u} \frac{1}{\sigma_i} \left(\frac{1}{B_i}\right)^{1/2} \prod_{j=1}^{p} \frac{1}{\sigma_i B_i} \tag{5.2}$$

where σ_i is the symmetry number of the internal rotor and B_i is the rotational constant.[143,270] With the prepared $\rho_R(E)$ as a starting point, the Beyer-Swinehart direct-count algorithm was

then used to fold in the vibrational density of states to evaluate the full $\rho(E)$ and $W^{\ddagger}(E-E_o)$ required in Equation 5.1.[142] Tunneling effects on reaction rates were neglected. Relative product yields were determined by numerically solving the full system of differential equations describing isomerization and dissociation of cyclohexyl.

5.4 Results

Cyclohexyl radical production

The mass spectrum of cyclohexylmethyl nitrite without pyrolysis is shown in Figure 5.2. As is typical for electron impact ionization of alkyl nitrites, the parent ion of this species at $m/z = 147$ is not observed.[271] The peak at $m/z = 97$ is due to $C_7H_{13}^+$ formed when cyclohexylmethyl nitrite cracks in the ionizer. When pyrolysis is turned on this peak is depleted, leaving $m/z = 83$ as the heaviest ion in line with expectations for cyclohexyl radical. It is important to fully deplete the parent nitrite, since photodissociation of alkyl nitrites can interfere with the ability to determine radical photodissociation channels.[272] Full nitrite depletion requires dissipating ∼28-30 W in the pyrolysis source. The resulting mass spectrum agrees well with a previously reported partial mass spectrum for cyclohexyl radical produced by H-abstraction from cyclohexane.[273]

Further confirmation of cyclohexyl production is obtained by measuring the IEC with and without pyrolysis (Figure 5.2). Cracking of cyclohexylmethyl nitrite in the ionizer produces $m/z = 83$ with an appearance potential of 11.2 eV based on extrapolation of the linear portion of the IEC. When pyrolysis is used to deplete the precursor nitrite, the appearance potential for $m/z = 83$ shifts to 7.4 eV, close to the known ionization potential of 7.66 eV for cyclohexyl radical.[262] Increasing the pyrolysis source power from 30 W to 35 W produces an IEC with at least two features. The first has an appearance potential ∼7.8 eV and is attributed to cyclohexyl radicals, while the second has an appearance potential ∼9 eV and is likely caused by isomerization of cyclohexyl to other C_6H_{11} species via ring-opening. The pyrolysis source was therefore operated close to 30 W at all times to ensure no other isomers contaminated the molecular beam.

Photofragment translational spectroscopy

Photofragment product TOF spectra were collected at several angles for many different m/z values. Figure 5.3 shows representative examples for $m/z = 82$ ($C_6H_{10}^+$), $m/z = 81$ ($C_6H_9^+$), $m/z = 68$ ($C_5H_8^+$), $m/z = 67$ ($C_5H_7^+$), $m/z = 55$ ($C_4H_7^+$), $m/z = 54$ ($C_4H_6^+$), $m/z = 41$ ($C_3H_5^+$), $m/z = 39$ ($C_3H_3^+$), $m/z = 27$ ($C_2H_3^+$) and $m/z = 15$ (CH_3^+). The ionizer was operated at 80 eV during collection of these spectra.

The heaviest possible photofragments from cyclohexyl radical are C_6H_{10} isomers produced by H-atom loss and having $m/z = 82$ parent ions. Ion signal at $m/z = 82$ ($C_6H_{10}^+$) and $m/z = 81$ ($C_6H_9^+$) was detected out to $\Theta_{LAB} = 12^o$. Both ions give essentially identical TOF

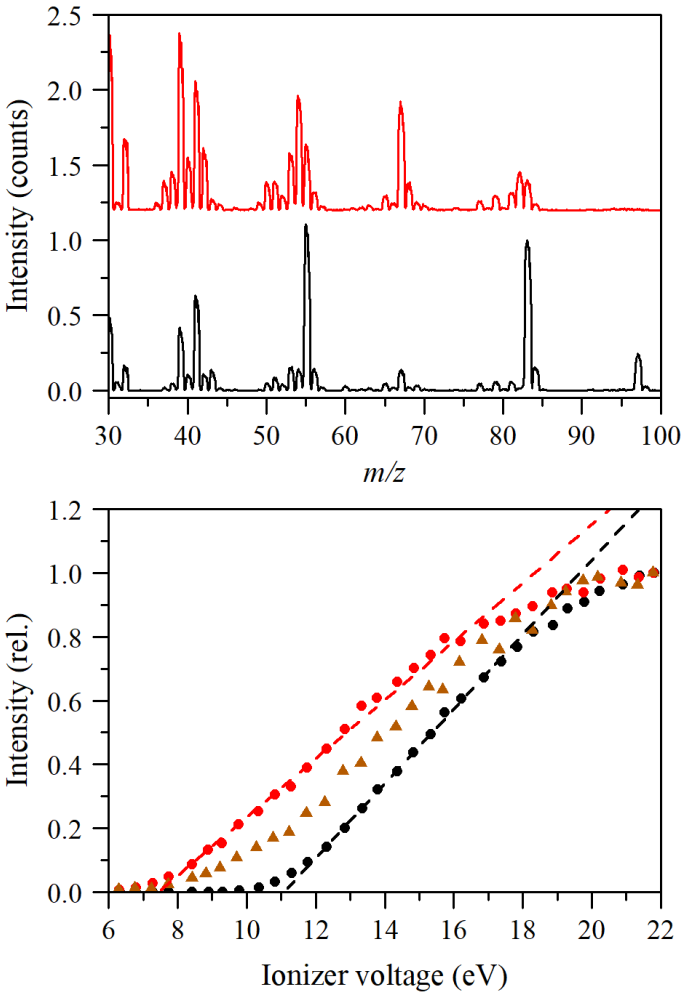

Figure 5.2: Mass spectra (top) and ionization efficiency curves (IEC, bottom) demonstrating cyclohexyl production. Data for the pyrolysis source off are shown in black, while data for 30 W power dissipation are shown in red. Lines are extrapolations of the linear portion of the curves to yield appearance potentials. An IEC is included for 35 W dissipation power (brown triangles) showing beam contamination under these conditions (extrapolated lines omitted for clarity).

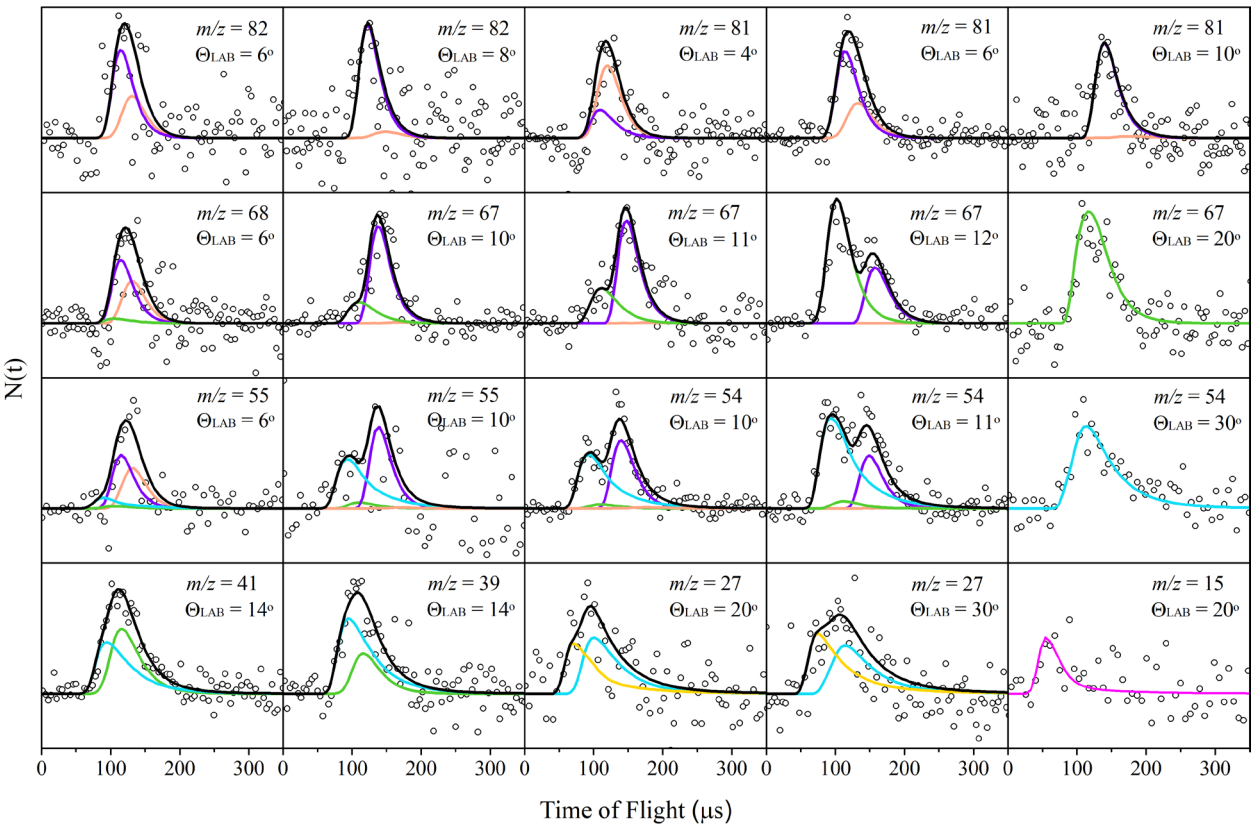

Figure 5.3: Select TOF spectra for cyclohexyl radical photodissociation. The individual ion m/z values and laboratory-frame scattering angles are indicated on each spectrum. Simulations are forward convolutions from the $P(E_T)$ distributions in Figure 5.5 (purple and orange), Figure 5.6 (green and magenta), and Figure 5.7 (blue and gold). For TOF simulations containing multiple components, the total simulation is shown in black.

spectra, suggesting that $C_6H_9^+$ originates from dissociative ionization of $C_6H_{10}^+$ ions, and not from an H_2-loss pathway. Higher quality TOF spectra were collected at $m/z = 81$ given lower background counts for this ion, possibly as a consequence of undissociated cyclohexyl radical preferentially forming $m/z = 82$ in the ionizer (see Figure 5.2). Collecting TOF data for the H-atom counter-fragment is not feasible on this apparatus under these experimental conditions.

For photofragments lighter than C_6H_{10}, the TOF spectra collected at $\Theta_{LAB} < 8^o$ are in general dominated by a feature with a similar arrival time as the $m/z = 82$ and 81 spectra. For $8^o \leq \Theta_{LAB} \leq 12^o$, a faster feature is observed in many of the TOF spectra, and for $\Theta_{LAB} > 12^o$ only the faster feature remains. These faster TOF features extend across a large range of scattering angles (typically up to our maximum accessible $\Theta_{LAB} \approx 45^o$) and are indicative of photoproducts caused by dissociation channels other than H-atom loss. No TOF signal was observable for $m/z = 42$ ($C_3H_6^+$) or $m/z = 29$ ($C_2H_5^+$) despite considerable effort.

All TOF features measured in this experiment are attributed to single-photon excitations based on a linear signal response to changes in laser fluence. Determination of which reaction pathways contribute to TOF signal at different m/z values and at different scattering angles is covered in Section 5.5.

Calculations

The ground-state geometry of cyclohexyl radical is shown in Figure 5.4a, demonstrating the roughly trigonal planar geometry of the α-carbon site. Also shown in Figure 5.4b is a transition state on the ground-state surface with an H atom forming a bridge between two adjacent carbon atoms. The relevance of this structure to cyclohexyl photochemistry is discussed later. The Supporting Information includes isomerization and dissociation pathways previously neglected by Gong et al. and Goldsmith et al.,[257,258] and calculated for the ground-state surface herein. Many additional H-loss channels were identified, as well as two additional CH_3-loss channels. It is important to include these to ensure that statistical calculations produce realistic predictions for different product yields.

The EOM-CCSD calculations provided excited state properties for cyclohexyl radical. The first excited state is located at 4.54 eV excitation energy, with an oscillator strength of 0.0033 and A′ symmetry. The second excited state lies 5.08 eV above the ground state, with oscillator strength of 0.0357 and also A′ symmetry. Isosurfaces of the orbitals carrying the greatest amplitude for these excitations are shown in Figure 5.4c and 5.4d respectively, both

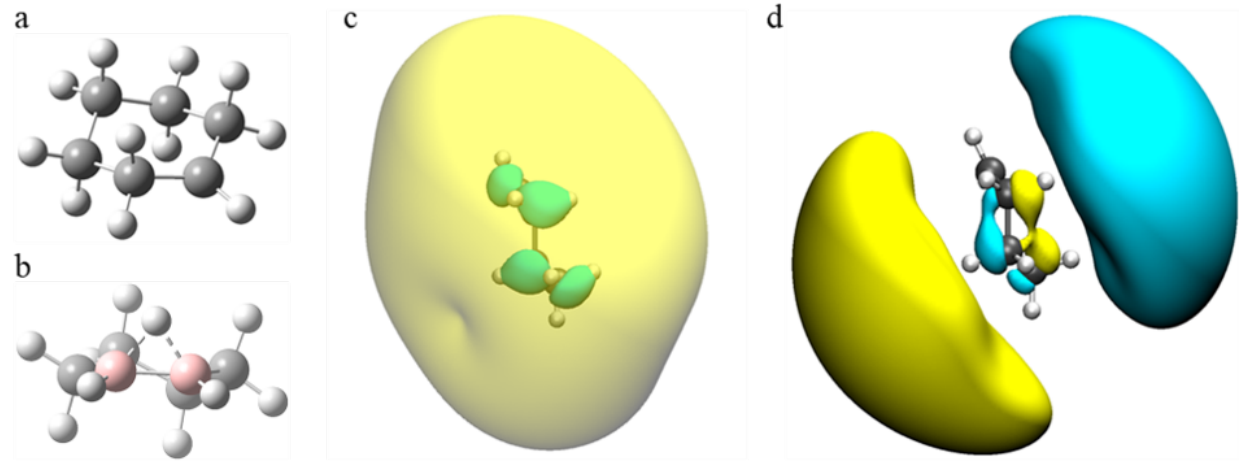

Figure 5.4: (a) Ground-state equilibrium geometry of cyclohexyl, (b) ground state local maximum with an H atom bridging two carbons (highlighted pink for viewing clarity), (c) Rydberg 3s orbital isosurface, and (d) Rydberg $3p_z$ orbital isosurface. The Rydberg orbitals are shown with a side-on view of the cyclohexyl ring, with the radical carbon situated in the upper-left (isovalue = 0.01 a.u.).

of which are extremely large and diffuse. The lower excitation is to a Rydberg 3s orbital ($\widetilde{A}\ ^2\mathrm{A}'$), while the higher is to a Rydberg $3p_z$ orbital ($\widetilde{B}\ ^2\mathrm{A}'$). The latter carries a large oscillator strength and lies very close to the excitation laser energy of 5.0 eV used in this experiment.

5.5 Analysis

Conservation of energy during photodissociation requires

$$E_{avail} = h\nu + E_i - D_o = E_{int} + E_T \tag{5.3}$$

for photon energy $h\nu$, reactant energy E_i, and dissociation energy D_o. We assume $E_i \approx 0$ kcal/mol for the radical beam following supersonic expansion, in line with previous findings.[91,274,275] During dissociation, the available energy E_{avail} is partitioned into either product internal energy E_{int} or relative product translational energy E_T. Conservation of momentum in each dissociation event requires that photofragment pairs acquire equal and opposite momenta. These conservation requirements impose kinematic constraints on the laboratory-frame scattering angles accessible for each dissociation channel.

For H-atom loss to produce cyclohexene, the maximum laboratory angle for the C_6H_{10} photofragment is $\Theta_{LAB} = 12^o$, with no constraint on the H-atom fragment. The possible production of H-atoms from other reasonable C_6H_{11} isomers does not change this angular constraint significantly. A similar analysis for methyl-loss indicates a maximum $\Theta_{LAB} = 52\text{-}61^o$ for different C_5H_8 fragments, with no constraint on CH_3. Other dissociation channels have no kinematic constraints on accessible scattering angles.

Product TOF spectra for each dissociation channel are governed by the joint center-of-mass translational energy and angular distribution, $P(E_T, \Theta)$. Decoupling this distribution into separate center-of-mass translational energy and angular distributions yields

$$P(E_T, \Theta) = P(E_T)I(\Theta) \tag{5.4}$$

where $I(\Theta)$ has the functional form[24]

$$I(\Theta) = \frac{1}{4\pi}\left[1 + \beta P_2(\cos\Theta)\right] \tag{5.5}$$

with anisotropy parameter β and second Legendre polynomial, $P_2(a) = {}^1\!/_2(3a^2 - 1)$.

The $P(E_T)$ distribution used to simulate $C_6H_{11} \rightarrow C_6H_{10} + H$ is shown in Figure 5.5, which provides the best simulation to the data collected at $m/z = 82$ ($C_6H_{10}^+$) and $m/z = 81$ ($C_6H_9^+$). Measuring TOF spectra at $m/z = 1$ for the H-atom counter-fragment is infeasible due to the short residence time of H atoms in the ionizer, their small ionization cross-section, and high detector background at this m/z, as well as detection of H-atoms being kinematically disfavored. The bimodal distribution in Figure 5.5 extends up to the available energy of 84 kcal/mol for H-atom loss, and is deconvoluted into a 'fast' and 'slow' feature. For the slow

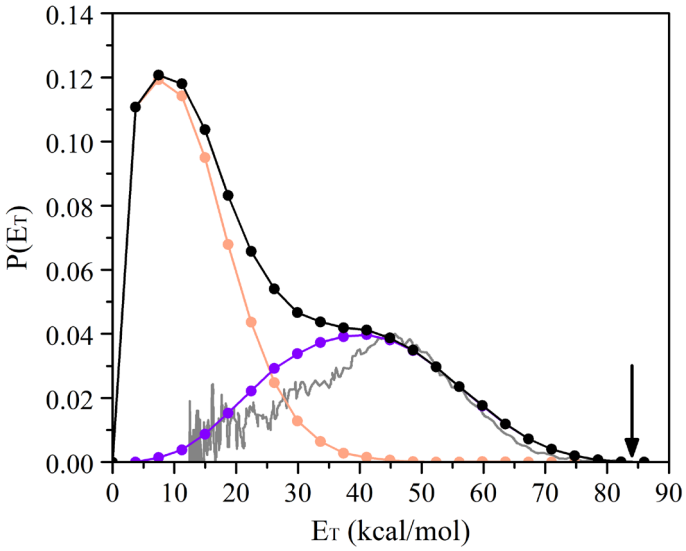

Figure 5.5: Center-of-mass P(E_T) distribution for $C_6H_{11} \rightarrow C_6H_{10} + H$. The black distribution provides the best simulation of the experimental data. This overall distribution is separated into a slow and a fast feature. This P(E_T) produces the orange and purple TOF simulations in Figure 5.3 for 'slow' and 'fast' C_6H_{10} respectively. The gray distribution is the H-atom P(E_T) reported previously.[246] The available energy for cyclohexene formation is indicated by the black arrow.

feature we take $\beta = 0$ for the anisotropy parameter, while for the fast we take $\beta = 0.5$ in accord with previous findings of other alkyl radicals and with previous work on cyclohexyl H-atom loss at the same laser wavelength.[243–246] The $P(E_T)$ distribution reported previously by measuring H-atoms is also shown for comparison.[246]

The $P(E_T)$ used to simulate $C_6H_{11} \rightarrow C_5H_8 + CH_3$ is shown in Figure 5.6, determined using the TOF spectra collected at $m/z = 68$ ($C_5H_8^+$), m/z = m/z ($C_5H_7^+$), and $m/z = 15$ (CH_3^+). We take $\beta = 0$ for this distribution. The distribution extends up to 33 kcal/mol, well below E_{avail} = 71-89 kcal/mol for methyl loss depending on the C_5H_8 isomer formed.

The $P(E_T)$ distribution for $C_6H_{11} \rightarrow C_4H_7 + C_2H_4$ is shown in Figure 5.7, with $\beta = 0$ assumed. This distribution gave the best simulation for TOF spectra at $m/z = 55$ ($C_4H_7^+$), $m/z = 54$ ($C_4H_6^+$), and $m/z = 27$ ($C_2H_3^+$). The parent ion of C_2H_4 cannot be observed at $m/z = 28$ due to high N_2^+ background in the detector, so the daughter ion $m/z = 27$ ($C_2H_3^+$) is used instead. The distribution extends up to 47 kcal/mol, with E_{avail} = 72 kcal/mol for ethene loss. The very weak signal at $m/z = 55$ ($C_4H_7^+$) relative to 54 in Figure 5.3 (see results at $\Theta_{LAB} = 10^o$) is discussed later in this section.

All other TOF spectra could be simulated using a combination of these three $P(E_T)$ distributions. The distributions are compared in Table 5.2 across several key characteristics: the peak of the distribution, the average translational energy $\langle E_T \rangle$, the maximum translational energy E_T^{max}, and the fraction of available energy partitioned into relative product

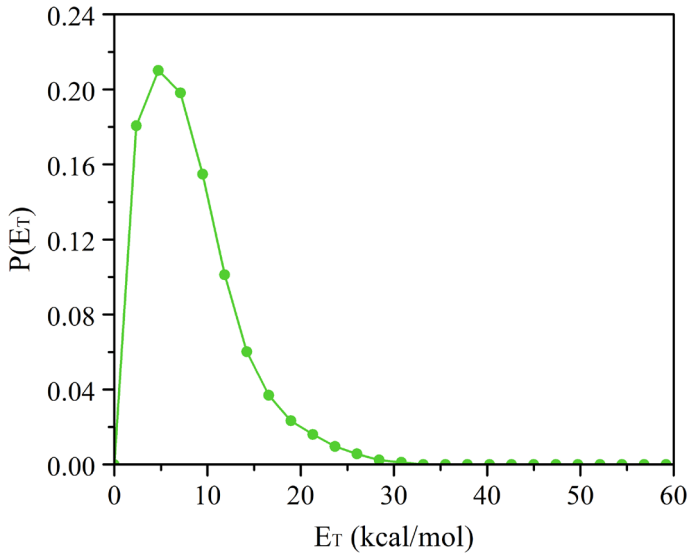

Figure 5.6: Center-of-mass P(E_T) distribution for $C_6H_{11} \rightarrow C_5H_8 + CH_3$, with $\beta = 0$. This P(E_T) produces the green and magenta TOF simulations in Figure 5.3, corresponding to the C_5H_8 and CH_3 fragments respectively.

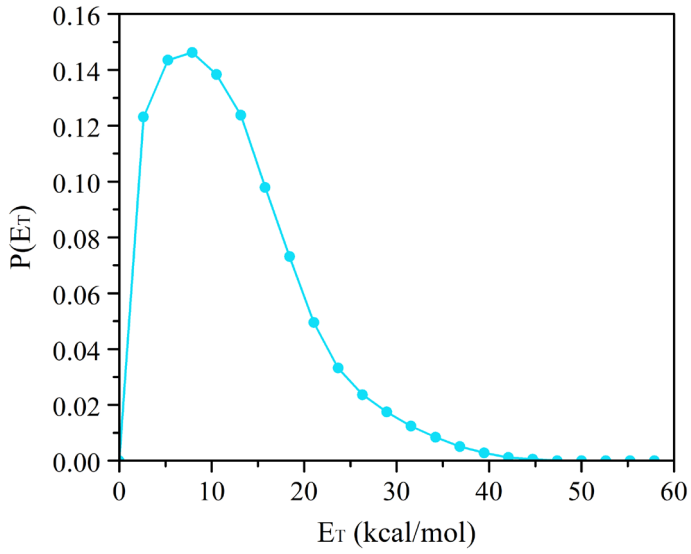

Figure 5.7: Center-of-mass P(E_T) distribution for $C_6H_{11} \rightarrow C_4H_7 + C_2H_4$, with $\beta = 0$. This P(E_T) produces the blue and gold TOF simulations in Figure 5.3, corresponding to the C_4H_7 and C_2H_4 fragments respectively.

Table 5.2: Characteristics of the $P(E_T)$ distributions for cyclohexyl dissociation. All values are in kcal/mol except for $\langle f_T \rangle$, which is a dimensionless quantity ranging from 0 to 1.

Channel	**Peak**	$\langle E_T \rangle$	E_T^{max}	$\langle f_T \rangle$
C_6H_{10} + H				
Slow	7	13	65	0.15
Fast	41	40	84	0.48
C_5H_8 + CH_3	5	8	33	0.10
C_4H_7 + C_2H_4	8	12	47	0.17

translation $\langle f_T \rangle$. The values of E_T^{max} and $\langle f_T \rangle$ presuppose all photoproducts are formed in their ground electronic states.

The branching ratio between pairs of different product channels may be extracted from TOF spectra containing contributions from both channels according to

$$BR\left(\frac{A}{B}\right) = \frac{W_A}{W_B} \times \frac{\sigma_B}{\sigma_A} \times \frac{f_B}{f_A} \tag{5.6}$$

in which W_i is the weighting of the $P(E_T)$ for channel i, σ_i is the ionization cross-section for product i, and f_i is the fraction of product i that dissociatively ionizes to the measured m/z. In this work, the relative ionization cross-sections of different products are estimated according to an empirical scheme,[146] and f_i values are taken from published mass spectra.[148,276,277] Figure 5.3 shows many examples of TOF spectra simulated by using components from multiple dissociation channels which can be used to calculate product branching ratios. These calculations produce the relative product yields shown in Table 5.3, normalized with respect to the slow H-loss channel. The uncertainty in these ratios is determined by varying W_i for each component until agreement between simulation and data becomes unsatisfactory based on simulations falling outside the envelope of experimental data points across the global data set (e.g., see the Supporting Information for discussion of the bimodal H-loss distribution).

Calculated RRKM branching ratios for ground-state statistical dissociation of cyclohexyl radicals are also included in Table 5.3, expressed relative to the amount of H atom loss. Because the RRKM analysis is applied only to the ground-state dissociation pathways, the fast H-loss channel is not included. The only dissociation channel directly accessible to cyclohexyl is H-loss to form cyclohexene, and this is the dominant channel identified in the RRKM analysis. To form any other products, the first step must always be ring-opening to 1-hexen-6-yl, with additional isomerization also usually required. Differentiating between isomer yields, these calculations indicate that cyclohexene accounts for 92% of all ground-state H-loss reactions. All other H-loss channels contribute well below 1% except for 1,5-hexadiene and 4-methyl-1,3-pentadiene, which each account for 3.6% of C_6H_{10}. Within the CH_3-loss

Table 5.3: Experimental and RRKM branching ratios and approximate experimental yields for cyclohexyl photodissociation. All ratios are expressed relative to the yield of the slow H-loss channel.

Channel	**Branching ratio**		**Yield (%)**
	Experimental	**RRKM**	
C_6H_{10} + H			
Total	$1.7^{+1.6}_{-0.4}$	-	66
Slow	1	1	39
Fast	$0.7^{+1.6}_{-0.4}$	-	27
C_5H_8 + CH_3	$0.015^{+0.005}_{-0.005}$	0.0037	1
C_4H_7 + C_2H_4	$0.86^{+0.10}_{-0.07}$	0.80	33
C_4H_6 + C_2H_5	Not observed	0.019	0
C_3H_6 + C_3H_5	Not observed	0.0071	0

channels considered, the predicted yields of 1,3-pentadiene, cyclopentene, and 1,4-pentadiene were 76%, 14%, and 10%, respectively. If cyclohexyl radicals were to undergo ring-opening in the pyrolysis source, the RRKM product branching changes dramatically (see the Supporting Information).

Distinguishing between the C_4H_7 + C_2H_4 and C_4H_6 + C_2H_5 channels is challenging in this experiment. These channels should give parent ions with m/z = 55 and 28 and m/z = 54 and 29, respectively. As described above, while signal levels were favorable for m/z = 54 ($C_4H_6^+$) and m/z = 27 ($C_2H_3^+$), they were very weak for m/z = 55 ($C_4H_7^+$) and undetectable for m/z = 29 ($C_2H_5^+$). The greatest relative ion abundance in the mass spectrum of C_2H_5 is for m/z = 29 ($C_2H_5^+$),[276] and the absence of this signal is a strong indicator that the C_4H_6 + C_2H_5 channel cannot explain the observed data. Hence, we propose that nearly all the signal at these three m/z values is from the C_4H_7 + C_2H_4 channel and that C_4H_7 is produced with sufficient internal energy to dissociate to C_4H_6 in transit to the detector. Arguments in support of this mechanism are as follows.

Unlike other photoproducts in this experiment, the reaction barriers for 1-buten-4-yl are quite low compared to the available energy for the C_4H_7 + C_2H_4 channel. H-loss to form butadiene requires 28 kcal/mol whereas dissociation to C_2H_4 + C_2H_3 requires 34 kcal/mol, with exit barriers of approximately 6 and 5 kcal/mol, respectively.[258,278] The RRKM branching between these two channels is shown as a function of 1-buten-4-yl internal energy in Figure 5.8. The relative yields of these two channels varies greatly over the available energy range. The questions then are how much of the available energy is partitioned into 1-buten-4-yl internal degrees of freedom during dissociation of cyclohexyl radicals, and what is the corresponding dissociation rate?

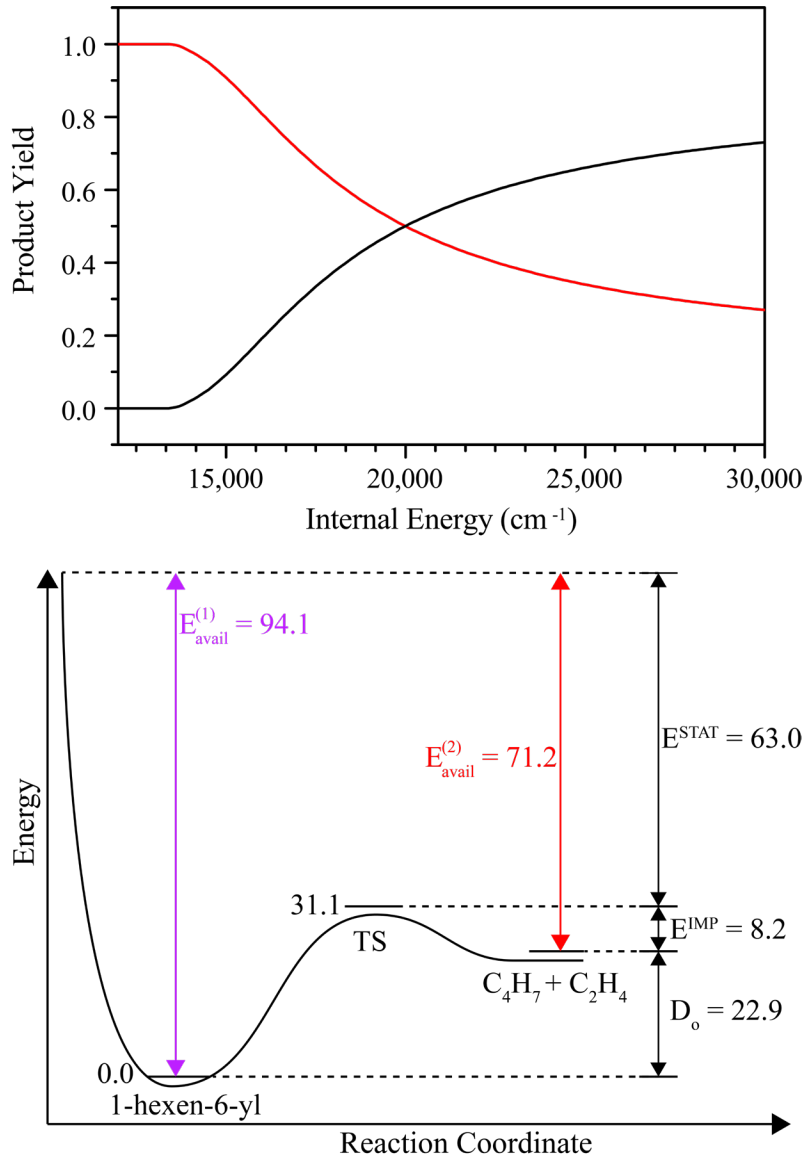

Figure 5.8: Top panel: RRKM product yield of $C_4H_7 \rightarrow C_4H_6 + H$ (red) and $C_4H_7 \rightarrow C_2H_4 + C_2H_3$ (black) as a function of 1-buten-4-yl internal energy (cm^{-1}). Bottom panel: schematic diagram of the 1-hexen-6-yl $\rightarrow C_4H_7 + C_2H_4$ reaction coordinate (energies given in units of kcal/mol).

Ring-opening of photoexcited cyclohexyl radical produces 1-hexen-6-yl with $E_{avail}^{(1)} =$ 94.1 kcal/mol of available energy. These 1-hexen-6-yl radicals may then dissociate over a 31.1 kcal/mol barrier to form 1-buten-4-yl + ethene with $E_{avail}^{(2)} = 71.2$ kcal/mol of energy available for partitioning between the product fragments. Figure 5.8 includes a schematic energy diagram of the 1-hexen-6-yl $\rightarrow$ C_4H_7 + C_2H_4 reaction coordinate. To assess the likelihood of 1-buten-4-yl spontaneous secondary dissociation, we use a model to estimate energy partitioning in the dissociation fragments. The available energy $E_{avail}^{(2)}$ is first split into statistical (E^{STAT}) and nonstatistical (E^{IMP}) reservoirs (see Figure 5.8). The statistical reservoir of 63.0 kcal/mol corresponds to the energy difference between the full available energy and the energy of the transition state located atop the exit barrier (including zero-point correction). The average values for energy partitioning into various product degrees of freedom are determined by applying a simple statistical model relating microcanonical to canonical energy partitioning.[279] In this model, the available energy is partitioned into relative translation, total rotation of both fragments, and vibrations of individual fragments according to

$$\begin{aligned} E_{avail} &= \langle E_T \rangle + \langle E_R \rangle_{tot} + \langle E_V \rangle_1 + \langle E_V \rangle_2 \\ &= k_B T^* + \frac{r-1}{2} k_B T^* + \sum_{i=1}^{s_1} \frac{h\nu_i}{\exp\left[h\nu_i / k_B T^*\right] - 1} + \sum_{j=1}^{s_2} \frac{h\nu_j}{\exp\left[h\nu_j / k_B T^*\right] - 1} \end{aligned} \tag{5.7}$$

In this expression, r is the total number of rotational degrees of freedom for both products, s_1 and s_2 are the number of vibrational modes available to C_4H_7 and C_2H_4 and ν_i and ν_j their frequencies, k_B is the Boltzmann constant, and T^* is the effective product temperature. Evaluating Equation 5.7 as a function of T^* enables a correlation between T^* and E_{avail}. This model assumes equilibrium between the translational, rotational, and vibrational degrees of freedom, subject to constraints ensuring conservation of angular momentum. The translational and rotational degrees of freedom thus take on values $1/2 k_B T^*$ less than their classical equipartition expressions. The vibrational modes are treated quantum mechanically since their energy spacing is significant compared to the available energy. This model has shown excellent agreement for the dissociation of other neutral species, such as styrene $\rightarrow$ benzene + acetylene, with very similar available energy and internal degrees of freedom as 1-hexen-6-yl considered here.[280,281]

The 63.0 kcal/mol of available energy in the statistical reservoir is satisfied for $T^* = 1476$ K in Equation 5.7. The model then predicts $\langle E_T \rangle = 3.0$ kcal/mol of relative fragment motion and a combined value of $\langle E_R \rangle_{tot} = 7.4$ kcal/mol of total external fragment rotations. The value of $\langle E_T \rangle$ from this model is not expected to correspond to the experimental value given in Table 5.2 for two reasons. First, the influence of the exit barrier is not included here, and this barrier is expected to yield faster relative motion of the two fragments. Additionally, a two-step dissociation process leading to the observed photofragment signal would lead to an experimental translational energy distribution which is a convolution of the distributions for

the individual reaction steps. This broadens the experimental translational energy distribution and skews $\langle E_T \rangle$ to higher values.

The model predicts 62% of the statistical reservoir is partitioned into C_4H_7 vibrational modes. The partitioning of the remaining 8.2 kcal/mol in the non-statistical reservoir is subject to the influence of the exit barrier in a non-trivial way. On the basis of the very nonrigid structure of 1-hexen-6-yl and the geometry of the transition state, it is expected that an additional few kcal/mol are partitioned into C_4H_7 vibrations. We take the average internal energy of nascent C_4H_7 to be ∼40 kcal/mol (∼14,000 cm^{-1}). The RRKM analysis for 14,000 cm^{-1} of available energy suggests that, on average, 1-buten-4-yl dissociates to C_4H_6 + H and C_2H_4 + C_2H_3 in a 98:2 ratio and that these reactions only take ∼1 μs to occur completely. Thus, all the C_4H_7 dissociates in transit to the detector, and since nearly all of this dissociation proceeds via statistical H atom loss, the time-of-flight spectrum measured for C_4H_6 will be very similar to that for undissociated C_4H_7. The C_2H_3 from this channel will be formed in amounts likely too small to be distinguished from dissociative ionization of other, more numerous photoproducts.

The $m/z = 54$ ion signal in this experiment is thus associated with 1,3-butadiene from dissociated C_4H_7 that will be formed in essentially equal amounts to C_2H_4. A branching ratio was extracted from the $m/z = 27$ ($C_2H_3^+$) TOF spectra, which contain simulations from both components of the C_4H_7 + C_2H_4 channel. In light of the above, the calculation uses σ_i and f_i values for 1,3-butadiene and ethene. The C_4H_6:C_2H_4 branching ratio of $0.98^{+0.22}_{-0.35}$ is consistent with the same dissociation event ultimately giving rise to both of these fragments.

A similar analysis was done for the C_4H_6 + C_2H_5 channel since secondary H-loss from ethyl could explain the lack of signal at $m/z = 29$. Considering the available energy for this channel, the model predicts that ethyl radicals will have insufficient energy to lose H atoms, even in the unphysical scenario in which the entirety of the exit barrier is partitioned into product internal energy. In fact, C_4H_7 is the only photofragment expected to be formed with sufficient internal energy to undergo secondary dissociation.

5.6 Discussion

This experiment investigates the photochemistry of cyclohexyl radicals at 248 nm to determine the yield of different possible photoproducts and the dissociation mechanisms that produce them. This wavelength corresponds to excitation to the 3p Rydberg state of cyclohexyl and results predominantly in liberation of an H atom. As with ethyl radical, photoexcitation is localized on a different C atom from which H atom loss occurs. Dissociation formally occurs from a C atom adjacent to the radical site to produce cyclohexene, but this process involves a bridged structure with H equidistant from two C atoms. In addition to H-loss, we observe C_5H_8 + CH_3 and C_4H_7 + C_2H_4 channels, with C_4H_7 further decomposing to C_4H_6 + H.

The excited-state mechanism observed here is presumably similar to that extensively characterized for H atom loss from the ethyl radical excited to its 3s and 3p Rydberg states

to form H + C_2H_4.[238–241] In both species, H atom loss does not occur from the radical center, as this would lead to CH_3CH + H from ethyl and a similar high-energy product here (note that there is evidence for CH_3CH from ethyl at higher excitation energies than are relevant here[240,241]). Excitation of ethyl to the 3s state leads to an H-bridged structure with C_{2v} symmetry that is repulsive along the coordinate for dissociation of the bridged H atom,[282] and passage through a conical intersection en route to dissociation leads to H + ground-state C_2H_4.[240,241] Branching at this conical intersection is found by experiment to favor the slow H atom loss channel. Accessing other curve crossings requires energies greater than are relevant here.[240,241,283,284] The observation of very similar kinetic energy release into H atoms formed from an array of alkyl radicals suggests that near the excitation threshold crossing always occurs through this particular H-bridged conical intersection with the ground state.[285] Excitation to the 3p state of ethyl leads to internal conversion to the 3s state, followed by the same dynamical pathway seen following 3s excitation.[233,240,241,284] The general features for ethyl have also been observed in the photodissociation of other alkyl radicals.

For cyclohexyl excited to the 3p Rydberg state, the dominant dissociation channel is H atom loss, yielding a bimodal photofragment translational energy distribution very similar to all other alkyl radicals in the literature, with a branching ratio of ∼0.7:1 for the fast:slow components of the distribution. There is good agreement between the fast component in the translational energy distribution measured herein for C_6H_{10} and that reported previously by using H atom Rydberg tagging, but that H atom study did not show the slow component of the distribution.[246] It is possible the slow component was obscured by the considerable noise evident in the H atom data or an artifact of the high-n Rydberg tagging detection scheme. Follow-up experiments on cyclohexyl in the Zhang group have produced some evidence of a bimodal distribution including the slow component,[247] in contrast to their earlier study.

As with the ethyl radical, an H-bridged geometry of cyclohexyl such as shown in Figure 5.4b is presumably responsible for the impulsive cleavage leading to the fast, nonstatistical H-loss channel. This pathway partitions an average of 48% of available energy into relative product translation and extends up to the maximum available energy, accordant with observations of all other alkyl radicals to date. Simulation of TOF data used an anisotropy parameter $\beta > 0$, consistent with a parallel electronic transition and a dissociation rate faster than the rotational period of cyclohexyl. By analogy with the dynamics of 3p photoexcited ethyl radicals, we propose that the initially prepared 3p state internally converts to the 3s state, where prompt recoil and dissociation to ground-state H + C_6H_{10} products occur through the H-bridged conical intersection. In the case of cyclohexyl this occurs in ∼27% of the excited radicals, and this mechanism leads exclusively to cyclohexene as the C_6H_{10} photofragment.

The slow H-loss pathway partitions an average of only 15% of available energy into relative product translation, peaking at low translational energy in line with expectations for statistical dissociation. This channel is thus assigned to statistical dissociation of cyclohexyl radicals, and it is responsible for the greatest fraction of total dissociation, ∼39%. It arises by population of the ground-state well of cyclohexyl during passage through the conical intersection, followed by intramolecular vibrational energy redistribution. While the potential energy diagrams show nine H atom loss pathways accessible through isomerization, RRKM

calculations suggest cyclohexene is the only non-negligible C_6H_{10} isomer, accounting for 92% of C_6H_{10} photoproduct formed following internal conversion.

The presence of ground-state statistical H atom loss suggests that several other pathways known on the ground state should also be operative, and this is consistent with our observation of channels other than H atom loss. We find production of C_4H_7 + C_2H_4 and C_5H_8 + CH_3 with generally slow translational energy distributions consistent with statistical dissociation over exit barriers. Assigning these channels to ground-state dissociation is further supported by experimental product branching ratios in good agreement with statistical RRKM predictions. Both of these channels begin with ring-opening of cyclohexyl to 1-hexen-6-yl, which can dissociate over a barrier to 1-buten-4-yl + ethene. Successive internal H abstractions by 1-hexen-6-yl lead first to 1-hexen-3-yl and then to 2-hexen-4-yl, which dissociates over a barrier to 1,3-pentadiene + CH_3. Isomers of C_5H_8 other than 1,3-pentadiene contribute individually to the yield in this channel only modestly as they require recyclization of 1-hexen-6-yl to the cyclopentylmethyl radical followed by multiple isomerization reactions. The 1-buten-4-yl (C_4H_7) fragment further undergoes spontaneous secondary dissociation via H atom loss to form 1,3-butadiene, as discussed in Section 5.5.

The relevant photodissociation reactions of the cyclohexyl radical excited to the 3p Rydberg state are summarized pictorially in Figure 5.9 as a simplified potential energy diagram. Despite the large size and cyclic structure of cyclohexyl, this radical appears to follow essentially the same mechanisms described for ethyl photodissociation and observed for the other alkyl radicals: passage through the conical intersection between the Rydberg 3s and ground states leads to a significant number of impulsive H-loss dissociation events, with the remaining radicals dissociating from the hot ground state. The major difference here is that ground-state cyclohexyl radicals can ring-open, and can access a variety of product channels not available to smaller radicals. Because cyclization does not affect the Rydberg states of the radical significantly and introduces no lower-lying valence states, the ultraviolet photochemistry in other cycloalkyl radicals should proceed similarly to cyclohexyl and the alkyl radicals in general.

5.7 Conclusions

Photoexcitation of cyclohexyl radical to the 3p Rydberg state at 248 nm leads to both excited-state and ground-state dissociation dynamics. Approximately 27% of radicals lose H atoms to form cyclohexene via a prompt, impulsive mechanism, likely following transfer from the 3p to the 3s Rydberg state and then passing through a conical intersection. The remaining 73% of radicals internally convert and dissociate with rates governed by statistical energy partitioning. The predominant channel remains H-loss to form cyclohexene (∼36%), with other H-loss channels taken together representing ∼3%. Dissociation to 1-buten-4-yl + ethene is an important ground-state channel at ∼33% of dissociation, and the internally hot C_4H_7 fragment loses another H atom forming 1,3-butadiene. The final ∼1% of experimentally observed ground-state dissociation occurs via the C_5H_8 + CH_3 channel, with 1,3-pentadiene

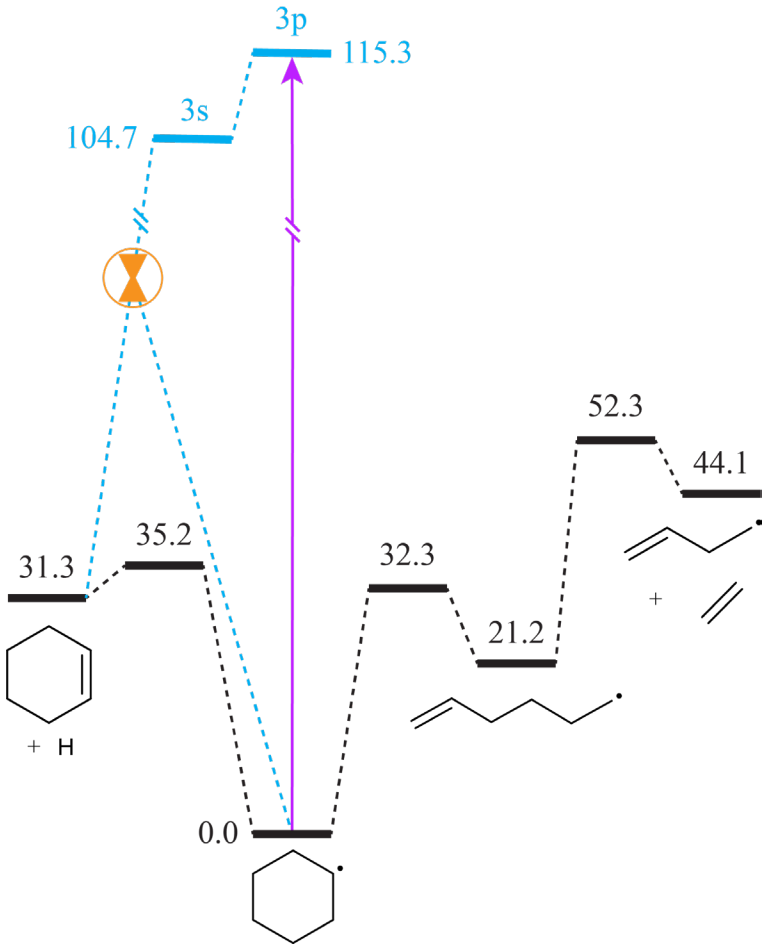

Figure 5.9: Simplified potential energy diagram highlighting the major photodissociation reactions undergone by cyclohexyl radicals excited to their 3p Rydberg state. Points on the ground electronic state are shown in black while excited states are blue. In yellow is an arbitrarily positioned representation of the conical intersection connecting the 3s Rydberg state to the ground state.

as the predominant isomer. The branching to these channels is in excellent agreement with RRKM calculations, which also predict C_4H_6 + C_2H_5 and C_3H_6 + C_3H_5 channels of comparable importance to methyl loss. If these latter two channels are active, their signal levels were too low to be detected because of a combination of low yield and unfavorable kinematics. Cyclohexyl is the largest alkyl radical and first cycloalkyl radical studied in this manner to date yet seems to display essentially the same dissociation dynamics observed for all other smaller alkyl radicals.

5.8 Supporting Information

Multi-component simulations of C_6H_{10} TOF spectra

Representative TOF spectra collected for $m/z = 81$ ($C_6H_9^+$) are shown in Figure 5.10, and several unique simulations to this data are included. If only the 'fast' component is included (purple lines) it is not possible to adequately simulate ion signal at long arrival times. In order to simulate these TOF spectra it is necessary to include a 'slow' component in the distribution. The simulated spectra are weakly dependent on the amount of the slow component under the present experimental conditions. The shaded areas display the range of acceptable simulations to the global dataset, corresponding to a slow component weighting of 0.30-0.75 of the total simulation. The best agreement between experimental and simulated TOF data is found when 0.6 is used as the slow-component weighting (black lines).

RRKM branching ratios for cyclohexyl and 1-hexen-6-yl radicals

The RRKM product branching was evaluated as a function of available energy for cyclohexyl radical, as well as 1-hexen-6-yl which could potentially be formed by ring-opening of cyclohexyl radical inside the pyrolysis source. The relative yields of different product channels for these two species are compared in Figure 5.11. The available energy for absorption of a single 248 nm photon is 115.3 kcal/mol (40,327 cm^{-1}) assuming radicals internally convert to their ground electronic states.

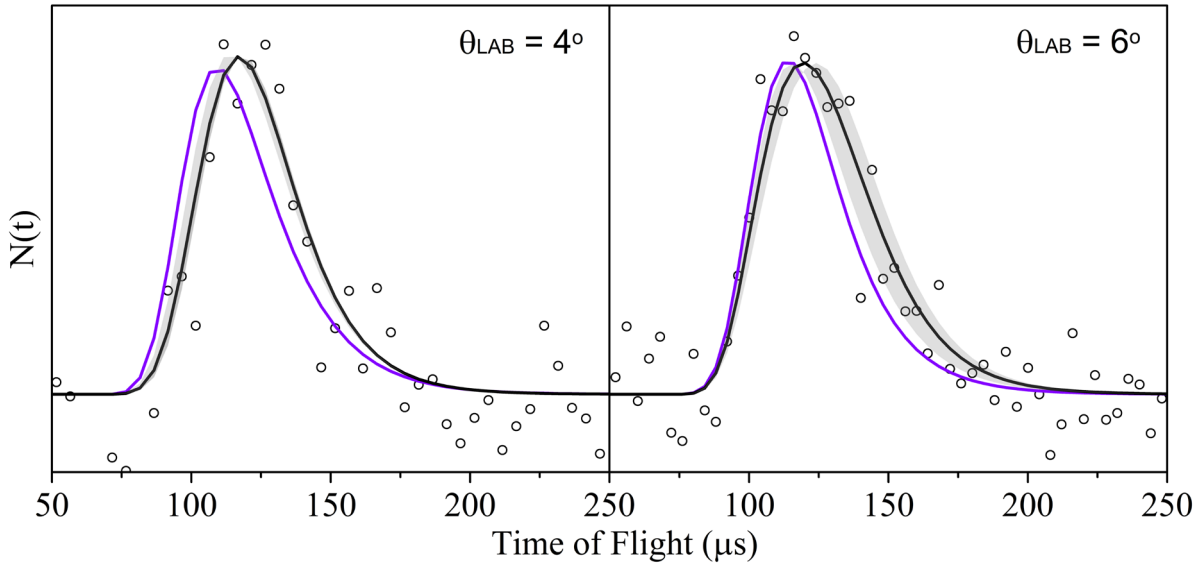

Figure 5.10: TOF spectra of $m/z = 81$ ($C_6H_9^+$) showing different simulations achieved by varying the weighting of the fast and slow components of the $P(E_T)$.

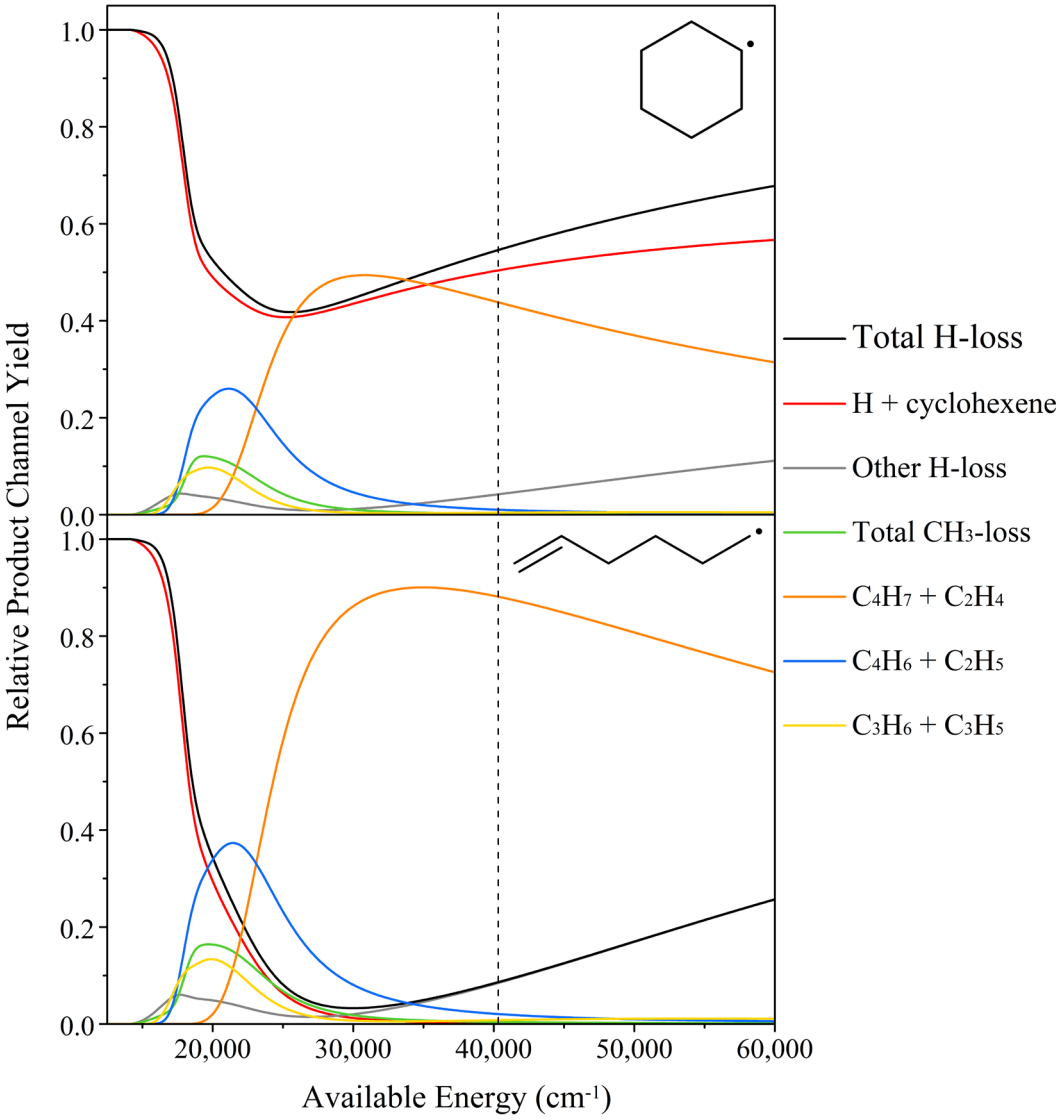

Figure 5.11: RRKM product branching as a function of available energy starting from cyclohexyl radical (top) and 1-hexen-6-yl radical (bottom). The vertical dashed line shows the energy contained in a single 248 nm photon.

For cyclohexyl radicals, H-atom loss is almost always the dominant channel. Of the 9 different H-loss pathways considered, cyclohexene represents the overwhelming majority of this channel over the entire range of energies. While the $C_4H_7 + C_2H_4$ channel accounts for slightly less of overall dissociation for the photon energy used in the experiment, it actually accounts for the greatest fraction of dissociation from ∼26,000-34,000 cm^{-1}. This channel peaks in importance at 30,800 cm^{-1} with 49% of total dissociation and then gradually decreases for higher energies. The other channels all peak in importance at around 20,000 cm^{-1} before decreasing to very low percentage yields. The maximum predicted yields of $C_5H_8 + CH_3$, $C_4H_6 + C_2H_5$, and $C_3H_6 + C_3H_5$ are about 12%, 26% and 10% respectively.

If 1-hexen-6-yl were formed instead, the RRKM product branching differs dramatically compared to cyclohexyl radicals. Once the available energy is high enough to make other product channels accessible, H-atom loss channels decrease enormously in importance, falling to a low of only ∼3% at 30,000 cm^{-1}. For much higher available energies their relative importance starts to increase again, with only 1,5-hexadiene and 4-methyl-1,3-pentadiene isomers carrying any real importance. The $C_5H_8 + CH_3$, $C_4H_6 + C_2H_5$, and $C_3H_6 + C_3H_5$ channels again achieve peak yields for ∼20,000 cm^{-1} before decreasing to negligible levels. Maximum yields for these channels are in this case about 16%, 37% and 13% respectively. Of particular importance to this experiment is the very large branching to $C_4H_7 + C_2H_4$, responsible for the greatest yield of any channel over almost the full energy range. At the available energy relevant to this experiment, the theoretical $(C_4H_7 + C_2H_4)/(C_6H_{10} + H)$ channel ratio is 10.2, compared to the values of 0.80 for cyclohexyl RRKM and $0.86^{+0.10}_{-0.07}$ found experimentally.

Extended potential energy diagrams

Isomerization and dissociation channels not previously considered for cyclohexyl radical were calculated using DFT at the ωB97X-D/aug-cc-PVTZ level of theory. These calculations produced the W8-W10 minima and TS19-TS36 transition states shown in Figures 5.12-5.13. Energies are reported in units of kcal/mol relative to cyclohexyl radical, including zero-point corrections, and ring-opening of cyclohexyl is the first step required to access all isomers in these diagrams. Where these are connected to parts of the potential energy diagram from Gong et al.,[258] the nomenclature of W1-W7 is used. See Gong et al. for connectivity amongst W1-W7 via TS1-TS18, which are not reproduced here.

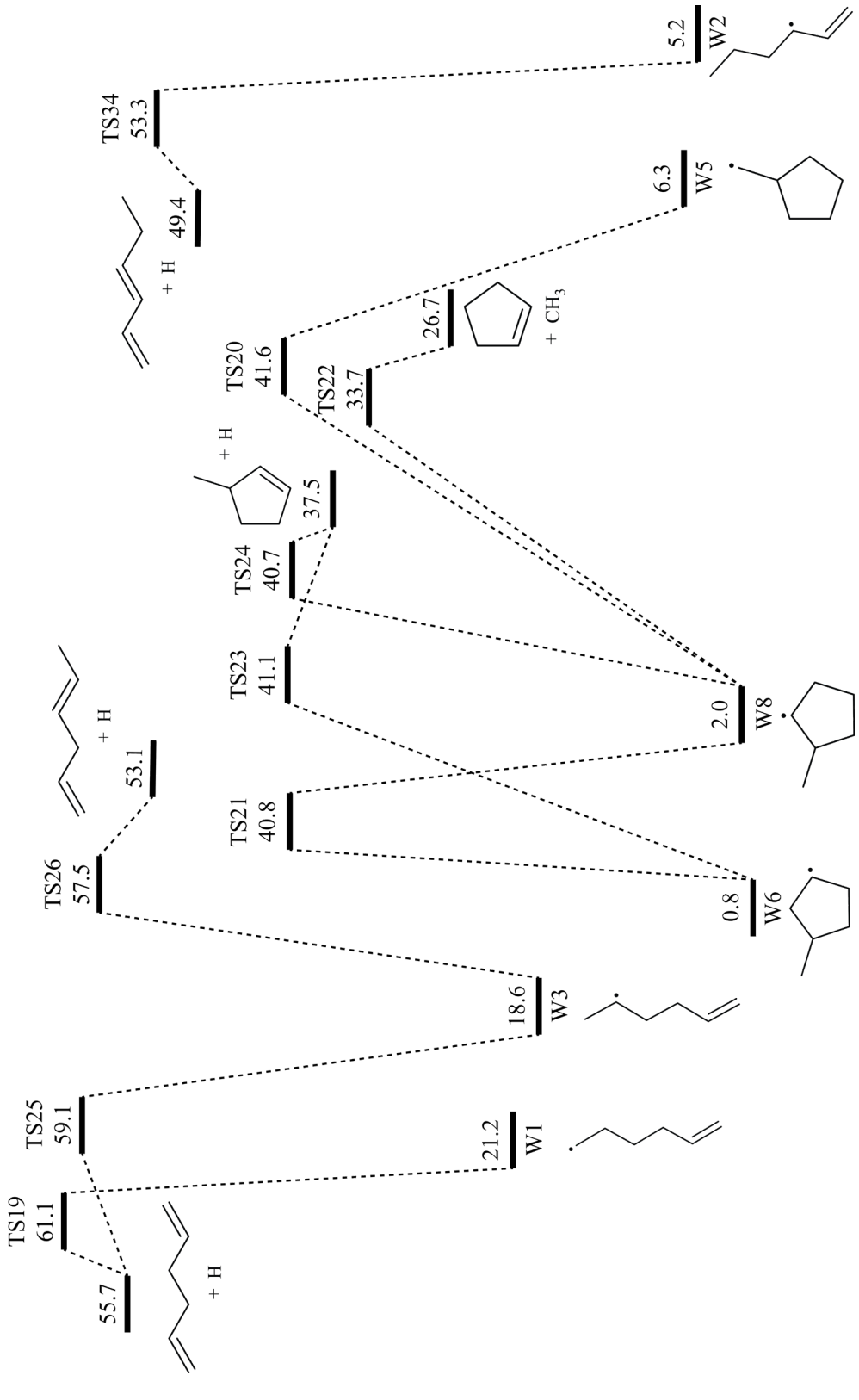

Figure 5.12: Extended potential energy diagram showing additional isomerization and dissociation pathways available to ground-state C_6H_{11} radicals (part 1).

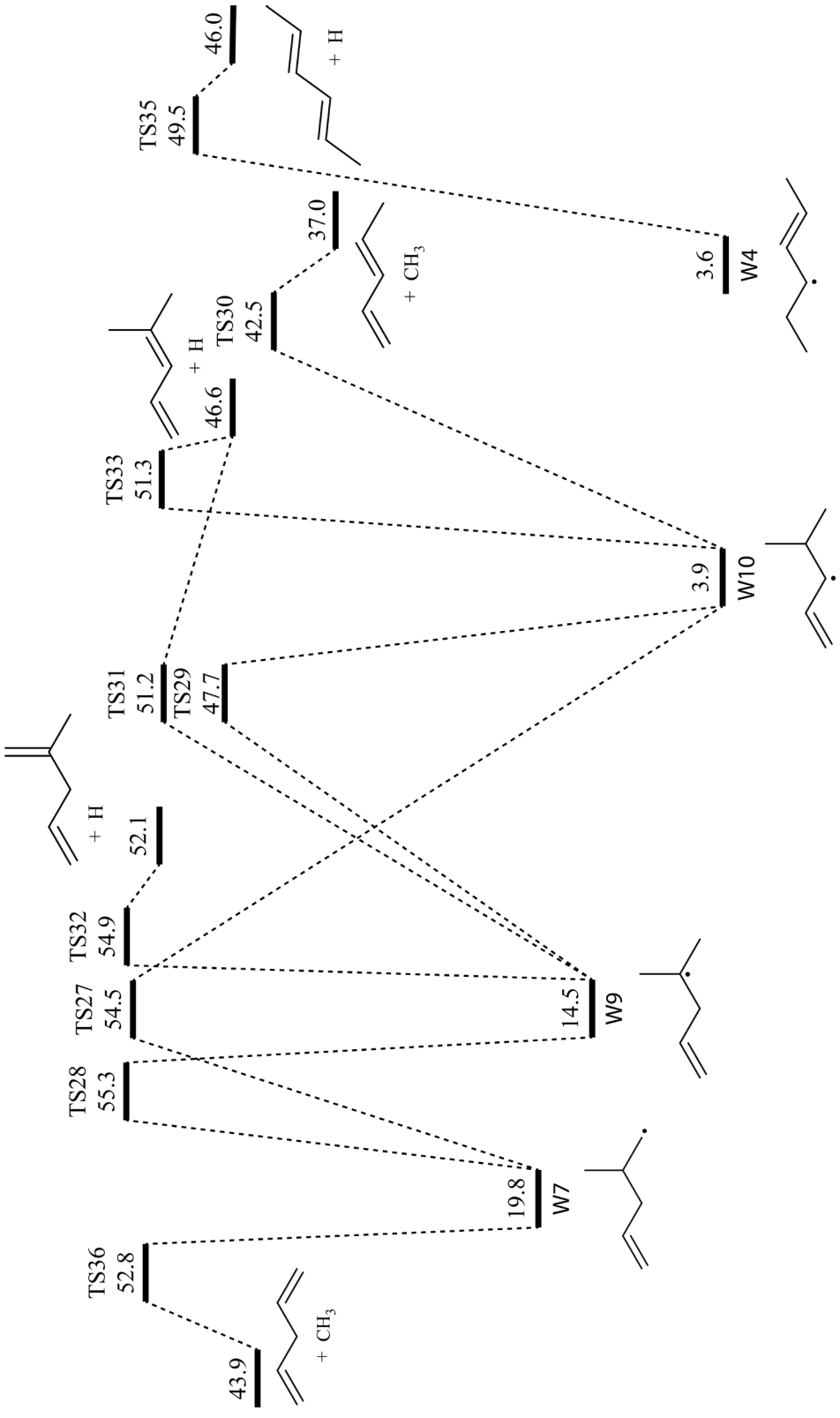

Figure 5.13: Extended potential energy diagram showing additional isomerization and dissociation pathways available to ground-state C_6H_{11} radicals (part 2).

Stationary point geometries and vibrational frequencies from DFT calculations

The results of the DFT calculations for species relevant to this work are included below. Frequencies are in units of cm^{-1} and the molecular geometries use units of Å.

Minima:

W8 (1-methylcyclopenten-2-yl // 1-CH_3-cC_5H_8-2):

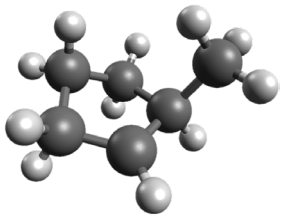

Frequencies:
118, 212, 244, 302, 374, 436, 591, 710, 797, 850, 890, 907, 934, 980, 1003, 1028, 1056, 1059, 1100, 1187, 1211, 1251, 1292, 1312, 1337, 1337, 1362, 1376, 1410, 1476, 1494, 1500, 1506, 1515, 2970, 3021, 3038, 3053, 3056, 3066, 3104, 3111, 3117, 3120, 3210

	Geometry		
C	1.2213950	−0.7715810	0.4564670
C	1.4806680	0.7117910	0.1497860
C	−0.8239150	0.1041870	−0.5268730
H	2.1032640	−1.3964570	0.3230210
H	0.8975820	−0.8800710	1.4934290
H	2.2158480	0.8097340	−0.6616870
H	−1.3009930	0.2097090	−1.5064090
C	0.0775410	−1.1462480	−0.4916580
H	−0.4599920	−2.0409470	−0.1769710
H	0.4784760	−1.3364690	−1.4894080
C	−1.9421290	0.0525040	0.5255760
H	−2.6406300	−0.7570150	0.3061240
H	−1.5303670	−0.1129330	1.5226010
H	−2.5010190	0.9883950	0.5472250
C	0.1443950	1.2154680	−0.2763960
H	1.8966710	1.2577120	0.9999610
H	−0.1065730	2.2616130	−0.3793070

W9 (4-methylpent-1-en-4-yl // 4-CH_3-1-C_5H_8-4):

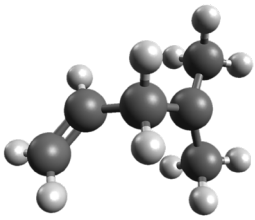

Frequencies:
51, 82, 114, 121, 189, 346, 367, 405, 458, 656, 792, 914, 927, 946, 962, 995, 1015, 1044, 1056, 1094, 1220, 1282, 1322, 1334, 1341, 1406, 1419, 1456, 1473, 1477, 1482, 1491, 1498, 1724, 2963, 2975, 3026, 3060, 3061, 3075, 3107, 3109, 3143, 3156, 3234

	Geometry		
C	0.3372320	−0.4030790	0.8560240
H	0.1922130	−1.3672400	1.3518970
H	0.6905030	0.3059190	1.6096170
C	−1.0843510	1.4971710	−0.1162560
H	−2.1292980	1.8023910	−0.1953230
H	−0.5861740	2.1525380	0.6006740
H	−0.6200040	1.6913310	−1.0937840
C	1.3960000	−0.5505250	−0.2071640
H	1.2103920	−1.3145530	−0.9563680
C	2.4812750	0.2013620	−0.3055130
H	2.6970520	0.9765320	0.4208010
H	3.1928000	0.0675930	−1.1093270
C	−0.9619550	0.0656330	0.2733140
H	−1.5796240	−1.1798320	−1.3732680
C	−1.8800650	−0.9303640	−0.3446010
H	−2.9011370	−0.5488920	−0.4054790
H	−1.8955360	−1.8669750	0.2157390

W10 (4-methylpent-1-en-3-yl // 4-CH_3-1-C_5H_8-3):

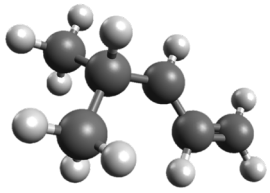

Frequencies:
84, 163, 209, 245, 295, 348, 406, 432, 549, 582, 775, 812, 827, 930, 945, 978, 1008, 1038, 1091, 1143, 1198, 1222, 1303, 1325, 1349, 1374, 1407, 1427, 1494, 1498, 1510, 1510, 1520, 1533, 2996, 3040, 3044, 3113, 3117, 3119, 3123, 3141, 3157, 3169, 3257

	Geometry		
C	0.4207980	−0.4717700	−0.3522140
H	−1.3222960	−0.1302480	−1.4683120
H	0.6272300	−1.4858840	−0.6838890
C	−1.2725350	1.3803100	0.0348010
H	−1.0073590	1.5130400	1.0856570
H	−0.7001600	2.0983190	−0.5528760
H	−2.3292380	1.6252390	−0.0734590
C	1.4857750	0.2823130	0.0929230
H	1.2923940	1.2953660	0.4293210
C	2.7900470	−0.1620010	0.1414140
H	3.0509680	−1.1622910	−0.1792190
H	3.5865790	0.4728980	0.5000650
C	−1.0155950	−0.0523800	−0.4175540
H	−2.9454330	−0.7999340	0.2506730
C	−1.8877330	−1.0381310	0.3712050
H	−1.6466380	−0.9934240	1.4347010
H	−1.7305900	−2.0631360	0.0338860

Transition States:

TS19:

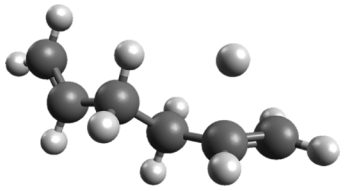

Frequencies:
718*i*, 69, 87, 111, 197, 350, 379, 419, 463, 477, 614, 662, 790, 932, 938, 957, 966, 974, 1042, 1046, 1064, 1104, 1183, 1253, 1283, 1313, 1323, 1340, 1380, 1460, 1462, 1481, 1495, 1653, 1736, 3027, 3034, 3080, 3098, 3139, 3149, 3152, 3156, 3237, 3247

Geometry			
C	2.9456150	−0.2610330	0.4651680
C	1.9687420	−0.0149680	−0.3933920
H	2.8468440	−0.0169230	1.5164480
H	3.8775110	−0.7100810	0.1491860
H	2.1080780	−0.2780590	−1.4388110
C	0.6480260	0.5940920	−0.0414940
C	−0.5214640	−0.3447560	−0.3516730
H	0.5130440	1.5206190	−0.6084620
H	0.6296580	0.8669390	1.0150590
C	−1.8798850	0.2717080	−0.1831380
H	−0.4356520	−0.6682790	−1.3946510
H	−0.4434250	−1.2459690	0.2589850
C	−2.9488390	−0.3823690	0.2909120
H	−1.5557040	1.4198660	1.4263970
H	−2.0278440	1.2352790	−0.6614470
H	−3.9282820	0.0747670	0.3030960
H	−2.8573950	−1.3742020	0.7159020

TS20:

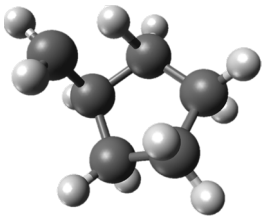

Frequencies:
2116*i*, 172, 245, 376, 387, 569, 587, 676, 819, 848, 875, 896, 909, 929, 947, 981, 1004, 1035, 1083, 1125, 1177, 1211, 1214, 1275, 1283, 1319, 1341, 1345, 1354, 1366, 1430, 1488, 1498, 1515, 1809, 3011, 3052, 3060, 3098, 3102, 3105, 3111, 3120, 3156, 3206

Geometry			
C	1.2658090	−0.5915570	0.5029200
C	1.2825410	0.8801690	0.0747150
C	−0.8582740	−0.1688450	−0.5914940
H	2.2447580	−1.0640030	0.4388090
H	0.9324550	−0.6688560	1.5398420
H	1.9181910	1.0007560	−0.8102670
H	−1.3791510	−0.2382390	−1.5434970
C	0.2332810	−1.2315610	−0.4329200
H	−0.1551550	−2.1776970	−0.0556800
H	0.6940350	−1.4280180	−1.4036040
C	−1.7794450	−0.0115270	0.6122880
H	−1.6760250	−0.7183930	1.4311360
H	−0.9964710	1.1292750	0.8095870
H	−2.7928640	0.3215460	0.4162290
C	−0.1537670	1.1658160	−0.2956270
H	1.6734220	1.5465470	0.8428310
H	−0.4040650	2.0421180	−0.8846790

TS21:

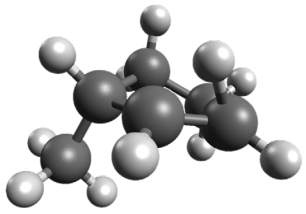

Frequencies:
1887*i*, 166, 233, 256, 371, 412, 578, 668, 689, 791, 813, 879, 909, 941, 970, 998, 1042, 1051, 1110, 1115, 1194, 1214, 1265, 1287, 1303, 1320, 1346, 1361, 1376, 1411, 1492, 1499, 1508, 1512, 2213, 3006, 3038, 3053, 3066, 3095, 3110, 3114, 3118, 3198, 3215

	Geometry		
C	−1.2689550	−0.7429820	−0.4441480
C	−1.3775480	0.7434730	−0.2602180
C	0.8218970	0.0618190	0.5417950
H	−2.1947000	−1.2839000	−0.2496360
H	−0.9769410	−0.9684480	−1.4765640
H	−1.2327290	1.0944770	0.9814950
H	1.3560210	0.1091320	1.4923430
C	−0.1418230	−1.1415710	0.5231270
H	0.3562840	−2.0655840	0.2321330
H	−0.5581240	−1.2899080	1.5216750
C	1.8531700	−0.0121730	−0.5886240
H	2.5010930	−0.8819840	−0.4644020
H	1.3630330	−0.0899710	−1.5607330
H	2.4816750	0.8787210	−0.6040620
C	−0.1048330	1.2343180	0.3511340
H	−2.0201070	1.3862960	−0.8430050
H	0.2330510	2.2538640	0.2323620

TS22:

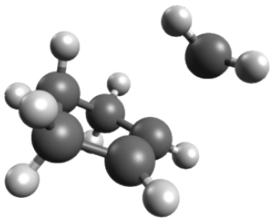

Frequencies:
516*i*, 114, 135, 156, 225, 381, 508, 533, 619, 726, 782, 819, 844, 893, 921, 932, 956, 981, 1047, 1066, 1116, 1150, 1229, 1244, 1317, 1332, 1337, 1385, 1424, 1429, 1487, 1497, 1516, 1545, 3019, 3035, 3063, 3076, 3100, 3105, 3124, 3200, 3220, 3258, 3265

	Geometry		
C	1.2658090	−0.5915570	0.5029200
C	1.2825410	0.8801690	0.0747150
C	−0.8582740	−0.1688450	−0.5914940
H	2.2447580	−1.0640030	0.4388090
H	0.9324550	−0.6688560	1.5398420
H	1.9181910	1.0007560	−0.8102670
H	−1.3791510	−0.2382390	−1.5434970
C	0.2332810	−1.2315610	−0.4329200
H	−0.1551550	−2.1776970	−0.0556800
H	0.6940350	−1.4280180	−1.4036040
C	−1.7794450	−0.0115270	0.6122880
H	−1.6760250	−0.7183930	1.4311360
H	−0.9964710	1.1292750	0.8095870
H	−2.7928640	0.3215460	0.4162290
C	−0.1537670	1.1658160	−0.2956270
H	1.6734220	1.5465470	0.8428310
H	−0.4040650	2.0421180	−0.8846790

TS23:

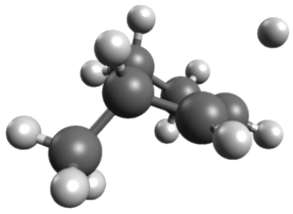

Frequencies:
561*i*, 122, 218, 248, 318, 359, 375, 493, 683, 747, 792, 808, 878, 915, 956, 976, 994, 1005, 1063, 1101, 1123, 1137, 1207, 1239, 1313, 1326, 1338, 1358, 1391, 1415, 1488, 1500, 1505, 1508, 1633, 3039, 3042, 3051, 3071, 3105, 3114, 3118, 3121, 3198, 3221

Geometry			
C	−1.2793310	−0.7461690	−0.4668900
C	−1.2999640	0.7522540	−0.3010190
C	0.8062250	0.0782570	0.5314940
H	−2.2166350	−1.2226660	−0.1835860
H	−1.0970100	−0.9965540	−1.5161610
H	−2.4225830	0.7942320	1.4162040
H	1.2095030	0.1868490	1.5409460
C	−0.1066990	−1.1642390	0.4360560
H	0.4244230	−2.0402830	0.0652370
H	−0.4931070	−1.4047250	1.4270000
C	1.9799860	0.0420590	−0.4514080
H	2.6647460	−0.7703480	−0.2051490
H	1.6228400	−0.1103540	−1.4715910
H	2.5421280	0.9764660	−0.4303280
C	−0.1449190	1.1985550	0.2064090
H	−2.0747000	1.3821080	−0.7147240
H	0.1086140	2.2409770	0.3442930

TS24:

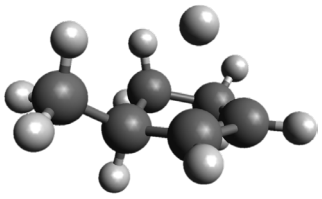

Frequencies:
526*i*, 143, 235, 241, 313, 364, 407, 523, 585, 754, 764, 835, 871, 923, 956, 975, 989, 1011, 1080, 1115, 1127, 1151, 1214, 1239, 1309, 1325, 1340, 1354, 1402, 1418, 1485, 1500, 1502, 1506, 1631, 3000, 3027, 3040, 3055, 3086, 3114, 3116, 3119, 3198, 3221

Geometry			
C	−1.6043440	−0.6403720	0.0292830
C	−1.3964030	0.8471430	0.0281000
C	0.7287330	−0.0615900	−0.4332790
H	−2.2391720	−0.9809280	0.8484090
H	−2.0965870	−0.9515270	−0.8982760
H	−2.1985550	1.5600250	0.1571370
C	−0.1678840	−1.1840580	0.1186330
H	−0.0327850	−2.1288760	−0.4056610
H	0.0905520	−1.3453070	1.1678380
C	−0.1108710	1.1656700	−0.1641350
H	0.2616950	2.1711050	−0.3053110
H	0.3753610	1.4808400	1.8397900
C	2.1397960	−0.0458330	0.1343460
H	2.6674530	−0.9672010	−0.1158780
H	2.7173740	0.7895170	−0.2636030
H	2.1147040	0.0506070	1.2210860
H	0.8058030	−0.1640070	−1.5232180

TS25:

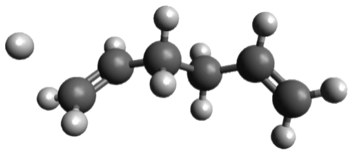

Frequencies:
540*i*, 66, 87, 102, 171, 251, 304, 375, 430, 449, 652, 703, 791, 944, 960, 966, 972, 979, 1030, 1045, 1048, 1101, 1189, 1255, 1280, 1316, 1329, 1339, 1376, 1458, 1462, 1488, 1500, 1679, 1736, 3028, 3035, 3080, 3098, 3141, 3147, 3152, 3155, 3237, 3244

	Geometry		
C	1.8247860	−0.3279610	−0.2256810
H	2.0027920	−1.1961040	−0.8538160
C	0.4987540	−0.2705970	0.4582030
H	0.4321300	0.6284450	1.0734290
H	0.4087670	−1.1258660	1.1363190
C	−0.6742240	−0.3050480	−0.5325190
H	−0.5750300	−1.1955060	−1.1610780
H	−0.6176770	0.5598950	−1.1959850
C	−1.9999650	−0.3333810	0.1604810
H	−2.1730570	−1.1807580	0.8185950
C	−2.9414670	0.5890460	0.0401850
H	−2.8074210	1.4514280	−0.6024370
H	−3.8785710	0.5147100	0.5750850
C	2.7899140	0.5846980	−0.0984780
H	3.7150870	0.5081180	−0.6524990
H	2.6337350	1.4897230	0.4756720
H	3.8724500	−0.0746260	1.5735750

TS26:

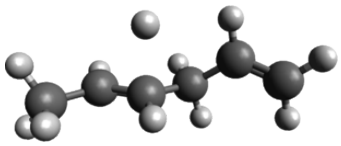

Frequencies:
630*i*, 61, 76, 157, 175, 261, 345, 381, 405, 450, 506, 677, 791, 897, 945, 958, 971, 1016, 1039, 1067, 1079, 1119, 1168, 1255, 1300, 1324, 1331, 1370, 1420, 1458, 1479, 1482, 1493, 1686, 1734, 3035, 3037, 3079, 3094, 3126, 3145, 3148, 3155, 3160, 3236

	Geometry		
C	−1.7395010	0.3633710	0.1582930
H	−1.8102920	1.2552740	0.7742740
C	−0.5246380	−0.0592390	−0.2180600
H	−0.4478900	−0.9102360	−0.8884830
H	−0.3738020	−1.5073850	1.1935890
C	0.7474360	0.7147280	0.0090540
H	0.5660920	1.4824550	0.7655210
H	1.0042730	1.2348400	−0.9183260
C	1.9128160	−0.1352410	0.4214330
H	1.8123120	−0.6437690	1.3750460
C	3.0121430	−0.3048890	−0.2954520
H	3.1423230	0.1814940	−1.2554140
H	3.8208720	−0.9339980	0.0508630
C	−3.0157510	−0.3431230	−0.1478360
H	−3.7198120	0.3201950	−0.6542390
H	−2.8478920	−1.2146080	−0.7795510
H	−3.5012170	−0.6779030	0.7721310

TS27:

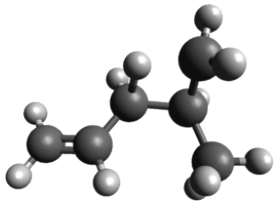

Frequencies:
2148*i*, 83, 112, 209, 289, 341, 372, 410, 498, 624, 657, 826, 884, 911, 915, 929, 947, 1007, 1025, 1057, 1132, 1198, 1219, 1277, 1305, 1330, 1342, 1376, 1419, 1435, 1471, 1505, 1510, 1662, 1796, 3043, 3080, 3114, 3115, 3123, 3131, 3150, 3171, 3223, 3243

	Geometry		
C	−0.3321180	−0.5409060	0.3182710
H	−0.6199500	−1.2711570	1.0705080
H	0.2195700	−1.3416170	−0.6077650
C	1.3892180	1.3710310	−0.0048240
H	1.1105580	1.4924960	−1.0534260
H	0.8397380	2.1112070	0.5775130
H	2.4531720	1.5933430	0.0785910
C	−1.4208560	0.2758780	−0.1953470
H	−1.1505550	1.1637200	−0.7564870
C	−2.7173900	−0.0173800	−0.0624110
H	−3.0467890	−0.8908820	0.4872940
H	−3.4824240	0.6093920	−0.4986350
C	1.1104100	−0.0406700	0.4814690
H	1.4590830	−0.1428450	1.5086390
C	1.6489750	−1.1275810	−0.4411800
H	2.0865310	−0.8202590	−1.3854760
H	2.0616400	−2.0256360	0.0033720

TS28:

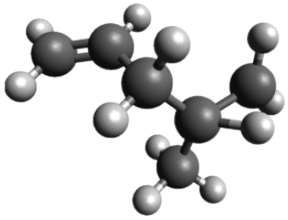

Frequencies:
1861*i*, 82, 87, 191, 209, 344, 365, 405, 433, 488, 662, 723, 808, 917, 938, 962, 963, 1022, 1043, 1057, 1104, 1223, 1243, 1311, 1327, 1342, 1353, 1423, 1436, 1460, 1480, 1491, 1498, 1728, 2225, 3005, 3030, 3079, 3082, 3117, 3143, 3155, 3159, 3234, 3273

	Geometry		
C	−1.8353390	−0.9786130	−0.4087610
H	−1.5336350	−2.0156290	−0.4090580
H	−2.5907440	−0.6508380	−1.1070720
C	0.3415650	−0.4296850	0.8231220
H	0.2212020	−1.4236710	1.2649020
H	0.6751840	0.2404370	1.6184370
C	−1.1368790	1.4653110	−0.1245850
H	−0.7329990	2.1345100	0.6359900
H	−0.6072170	1.6699810	−1.0626440
H	−2.1858020	1.7210000	−0.2808740
C	1.3861400	−0.4888470	−0.2559590
H	1.1646710	−1.1508760	−1.0879810
C	2.5011830	0.2244410	−0.2723700
H	2.7496910	0.9013410	0.5370610
H	3.2059650	0.1556740	−1.0901520
C	−0.9803150	0.0306340	0.2692800
H	−2.0244430	−0.5213720	0.7970320

TS29:

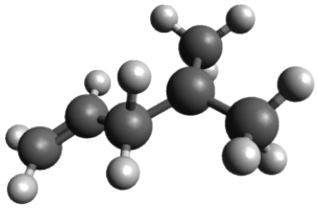

Frequencies:
1878*i*, 125, 160, 172, 205, 232, 347, 364, 407, 515, 610, 793, 819, 871, 949, 977, 999, 1019, 1052, 1090, 1167, 1237, 1285, 1318, 1330, 1374, 1417, 1431, 1482, 1484, 1491, 1498, 1509, 1640, 2193, 2980, 2986, 3070, 3073, 3116, 3119, 3153, 3165, 3171, 3249

Geometry			
C	0.3935980	−0.5249220	−0.1675080
H	−0.2321920	−0.3230450	−1.2386240
H	0.4994690	−1.6000350	−0.0766850
C	−1.2526700	1.4373400	0.0323400
H	−1.0464420	1.7430690	1.0672880
H	−0.6153180	2.0493820	−0.6084550
H	−2.2887340	1.6897780	−0.1914250
C	1.5747640	0.2750170	0.0138690
H	1.4399480	1.3498710	0.0717500
C	2.8238240	−0.2109090	0.1104220
H	3.0236640	−1.2743670	0.0650250
H	3.6699810	0.4472440	0.2430700
C	−1.0057380	−0.0218650	−0.1546510
H	−3.0528140	−0.6734320	−0.2349780
C	−2.0888200	−1.0025280	0.1539780
H	−2.1954450	−1.1355080	1.2389430
H	−1.8718670	−1.9857550	−0.2666050

TS30:

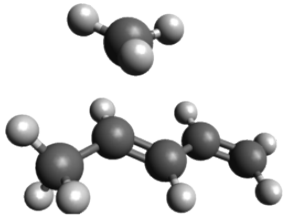

Frequencies:
455*i*, 91, 102, 145, 181, 207, 238, 289, 443, 468, 493, 513, 648, 778, 854, 918, 931, 966, 994, 1043, 1051, 1106, 1211, 1299, 1309, 1335, 1417, 1421, 1424, 1457, 1490, 1499, 1599, 1664, 3042, 3105, 3106, 3133, 3144, 3150, 3157, 3164, 3247, 3267, 3276

Geometry			
C	0.422670	−0.502893	0.182671
H	0.493227	−0.965899	1.162860
H	−1.950338	−1.313123	1.153408
C	−1.475005	1.779176	0.198270
H	−1.705892	1.590027	1.236279
H	−0.575083	2.336412	−0.014534
H	−2.306556	1.892788	−0.483220
C	1.633239	0.040239	−0.376947
H	1.545496	0.506915	−1.354110
C	2.829018	0.008632	0.218073
H	2.960134	−0.446493	1.192295
H	3.705582	0.430542	−0.252554
C	−0.793756	−0.401750	−0.411196
H	−0.829650	−0.040115	−1.433048
C	−2.005075	−1.137839	0.079027
H	−2.924576	−0.594492	−0.132173
H	−2.078891	−2.109950	−0.414598

TS31:

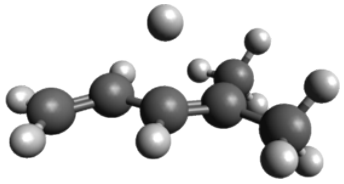

Frequencies:
715*i*, 86, 108, 147, 191, 227, 297, 357, 375, 444, 511, 541, 700, 834, 928, 960, 965, 978, 1012, 1043, 1088, 1100, 1175, 1251, 1337, 1373, 1421, 1425, 1458, 1473, 1485, 1494, 1500, 1648, 1723, 3029, 3035, 3083, 3087, 3136, 3152, 3156, 3157, 3189, 3246

	Geometry		
C	−0.3547570	−0.4846330	0.0458930
H	−0.2967220	−0.8535700	1.9691110
H	−0.5130390	−1.5526840	−0.0629160
C	2.0597820	−0.9974040	−0.1096220
H	2.7043150	−0.8758620	0.7658890
H	1.7206130	−2.0310730	−0.1411670
H	2.6826970	−0.8081830	−0.9872120
C	−1.5712810	0.3249410	0.0214140
H	−1.4698010	1.3974380	0.1316140
C	−2.7871440	−0.1882600	−0.1309510
H	−2.9408110	−1.2557770	−0.2337120
H	−3.6657310	0.4408620	−0.1528920
C	0.9179080	−0.0325700	−0.0506260
H	0.4695480	2.0942020	−0.0337380
C	1.3117740	1.4092990	0.0002130
H	1.9784890	1.6486490	−0.8311760
H	1.8727560	1.6077610	0.9182690

TS32:

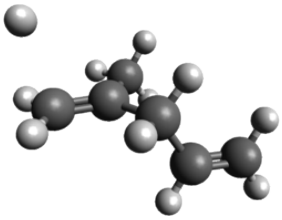

Frequencies:
443*i*, 54, 88, 162, 178, 220, 262, 372, 402, 471, 534, 661, 774, 857, 918, 953, 955, 971, 1003, 1033, 1052, 1070, 1137, 1241, 1309, 1331, 1338, 1418, 1450, 1460, 1478, 1487, 1502, 1691, 1733, 3036, 3039, 3090, 3097, 3140, 3146, 3154, 3159, 3237, 3240

	Geometry		
C	0.2869820	−0.6611060	0.5472150
H	0.0928800	−1.7286120	0.6685940
H	0.5169770	−0.2549640	1.5365080
C	−0.9365270	1.5060870	−0.0114310
H	−0.8302510	1.8954730	1.0047210
H	−0.0819980	1.8769410	−0.5804530
H	−1.8488830	1.9137800	−0.4421450
C	1.4749480	−0.4696190	−0.3526590
H	1.3808540	−0.8931220	−1.3481170
C	2.5831200	0.1735360	−0.0219100
H	2.7089460	0.6129040	0.9608040
H	3.4042830	0.2795770	−0.7178460
C	−0.9526070	0.0096370	0.0089280
H	−2.8849430	−0.2199640	−0.8121480
C	−2.0116720	−0.7000690	−0.3908020
H	−3.1269780	−0.8507330	1.4465360
H	−1.9963500	−1.7820720	−0.3924900

TS33:

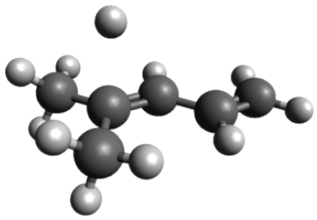

Frequencies:
660*i*, 119, 138, 185, 218, 238, 354, 370, 418, 450, 484, 544, 678, 830, 901, 956, 967, 980, 1014, 1040, 1091, 1095, 1178, 1250, 1336, 1372, 1421, 1428, 1460, 1476, 1489, 1497, 1509, 1651, 1692, 3037, 3044, 3102, 3108, 3140, 3152, 3155, 3158, 3185, 3247

	Geometry		
C	−0.3820740	−0.4971470	−0.0058790
H	0.8892030	−0.0805270	2.0780550
H	−0.5349700	−1.5720240	−0.0051580
C	1.2779260	1.4007820	−0.0691400
H	1.5659430	1.6301910	−1.0986910
H	0.4789090	2.0784470	0.2185080
H	2.1413640	1.6100400	0.5620420
C	−1.5865830	0.3037400	−0.0142260
H	−1.4828040	1.3820430	−0.0029630
C	−2.8135580	−0.2168490	−0.0385100
H	−2.9707720	−1.2886640	−0.0516420
H	−3.6931930	0.4110580	−0.0481250
C	0.8933410	−0.0488970	0.0327410
H	2.8256310	−0.7944570	0.6194890
C	2.0402080	−1.0113820	−0.1048610
H	2.4834940	−0.9139130	−1.0998990
H	1.7216350	−2.0436660	0.0276320

TS34:

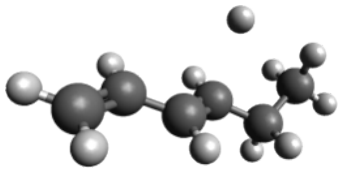

Frequencies:
556*i*, 65, 129, 165, 199, 260, 293, 382, 414, 447, 524, 663, 782, 890, 923, 954, 964, 992, 1051, 1056, 1100, 1133, 1217, 1276, 1307, 1327, 1339, 1375, 1420, 1463, 1482, 1501, 1506, 1661, 1705, 3028, 3048, 3083, 3121, 3128, 3142, 3149, 3154, 3163, 3247

	Geometry		
C	−3.1778180	−0.1168240	0.1801730
H	−3.2713640	−1.0938250	0.6387020
H	−4.0892420	0.4394270	0.0129600
C	−1.9892090	0.3745950	−0.1635050
H	−1.9312180	1.3583920	−0.6187550
C	−0.7340840	−0.3210470	0.0331190
H	−0.7828830	−1.2982810	0.5051430
C	1.7583050	−0.5685940	−0.2202900
H	1.9783580	−0.9606250	−1.2188280
H	1.6342970	−1.4364660	0.4297830
C	2.9441020	0.2726950	0.2412670
H	2.8014210	0.6193680	1.2647820
H	3.8678250	−0.3039830	0.1992080
H	3.0683120	1.1524040	−0.3920350
C	0.4645010	0.1821850	−0.3061870
H	0.6328390	1.4474360	1.4142190
H	0.4968700	1.1381020	−0.8226330

TS35:

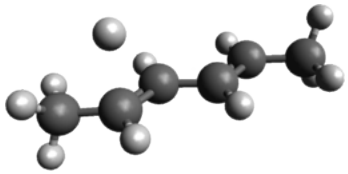

Frequencies:
559*i*, 100, 144, 153, 184, 209, 318, 331, 349, 364, 448, 554, 793, 887, 945, 946, 979, 1033, 1067, 1074, 1102, 1122, 1205, 1274, 1327, 1346, 1367, 1419, 1423, 1484, 1485, 1495, 1500, 1675, 1732, 3037, 3042, 3093, 3105, 3124, 3130, 3142, 3146, 3151, 3158

	Geometry		
C	0.6219900	−0.3045570	0.0326900
H	0.6820060	−1.3639210	0.2669080
C	−0.7040240	0.2649350	−0.0810700
H	−0.7624630	1.3275110	−0.3017580
C	−1.8310050	−0.4303700	0.0714030
H	−1.7582110	−1.4913000	0.2947790
C	3.1309420	−0.2038810	−0.0853010
H	3.5533380	−0.2142900	−1.0928900
H	3.8094920	0.3736860	0.5421720
H	3.1107430	−1.2287250	0.2838780
C	−3.2081140	0.1327430	−0.0413930
H	−3.7731500	−0.3709710	−0.8288220
H	−3.7655370	−0.0110340	0.8868010
H	−3.1864040	1.1988870	−0.2649350
C	1.7601260	0.3954060	−0.1041780
H	1.7798010	1.2137550	1.8499420
H	1.6908960	1.4407490	−0.3889880

TS36:

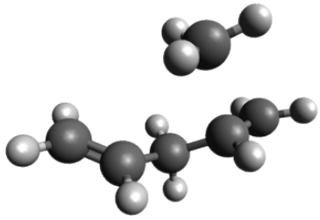

Frequencies:
510*i*, 67, 93, 128, 187, 250, 290, 420, 447, 527, 536, 566, 635, 834, 860, 900, 929, 967, 987, 998, 1046, 1079, 1192, 1254, 1291, 1313, 1341, 1419, 1425, 1444, 1463, 1478, 1585, 1739, 3020, 3085, 3103, 3140, 3150, 3152, 3160, 3237, 3244, 3264, 3268

	Geometry		
C	0.2228180	−0.9513710	0.1302150
H	0.2288480	−2.0124830	−0.1439100
H	0.2388250	−0.9130670	1.2209900
C	−0.7164020	1.8416200	0.0787220
H	−1.6995070	2.2508950	−0.1019260
H	−0.4094120	1.7536230	1.1112190
H	0.0590690	2.0905120	−0.6322830
C	1.4632530	−0.3265530	−0.4283800
H	1.4996810	−0.2364510	−1.5108970
C	2.4955690	0.0905960	0.2858660
H	2.4979560	0.0231300	1.3675220
H	3.3733930	0.5145000	−0.1825080
C	−1.0734600	−0.3693240	−0.3879800
H	−1.0770260	−0.0801210	−1.4332590
C	−2.2601180	−0.6204510	0.2125650
H	−3.1947890	−0.3391620	−0.2514440
H	−2.3070050	−1.0384710	1.2104510

Polyatomic Products:

1,3-hexadiene:

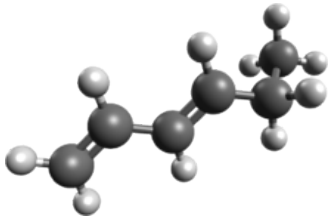

Frequencies:
68, 156, 173, 194, 263,
388, 455, 508, 672, 792,
892, 922, 953, 961, 997,
1044, 1055, 1101, 1134,
1217, 1276, 1313, 1336,
1344, 1370, 1416, 1464,
1490, 1503, 1511, 1696,
1758, 3036, 3047, 3083,
3120, 3127, 3135, 3143,
3151, 3160, 3245

	Geometry		
C	3.1098720	−0.1561450	0.2681730
H	3.1725600	−1.2016060	0.5453720
H	4.0306870	0.4099100	0.2665590
C	1.9485910	0.4040060	−0.0557690
H	1.9225540	1.4545710	−0.3288770
C	0.6746270	−0.2990390	−0.0733000
H	0.6947970	−1.3509990	0.1993660
C	−0.4842300	0.2675040	−0.4003420
H	−0.4907880	1.3223660	−0.6665270
C	−1.8101520	−0.4221710	−0.4161230
H	−1.6778950	−1.4771150	−0.1690640
H	−2.2205880	−0.3850290	−1.4294640
C	−2.8113790	0.2186070	0.5458070
H	−2.9626850	1.2724130	0.3070470
H	−3.7793340	−0.2793910	0.4912310
H	−2.4532840	0.1583070	1.5736770

1,4-hexadiene:

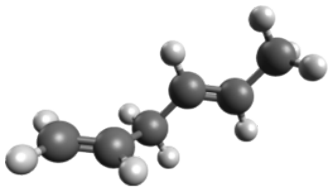

Frequencies:
73, 87, 178, 212, 282, 375,
398, 515, 674, 800, 894,
945, 958, 969, 1014, 1045,
1080, 1085, 1108, 1171,
1252, 1307, 1332, 1344,
1363, 1422, 1459, 1482,
1486, 1499, 1730, 1766,
3036, 3040, 3080, 3097,
3122, 3140, 3144, 3145,
3157, 3236

	Geometry		
C	2.9624200	−0.4343690	−0.1140180
H	3.2333760	−0.0346070	−1.0843800
H	3.6780010	−1.0879590	0.3663120
C	1.8074990	−0.1325410	0.4577510
H	1.5660700	−0.5568680	1.4277420
C	0.7541730	0.7545010	−0.1420410
H	0.5679790	1.6015650	0.5234600
H	1.1248800	1.1599610	−1.0870920
C	−0.5346670	0.0175850	−0.3722070
H	−0.4829030	−0.8207620	−1.0622950
C	−1.6892530	0.3048810	0.2109160
H	−1.7278380	1.1415600	0.9040920
C	−2.9708590	−0.4329900	−0.0082220
H	−3.3496930	−0.8451280	0.9293000
H	−3.7440470	0.2331840	−0.3964980
H	−2.8417000	−1.2533450	−0.7137230

1,5-hexadiene:

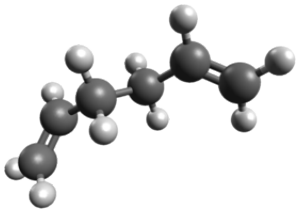

Frequencies:
73, 92, 109, 220, 355, 424, 446, 641, 674, 792, 944, 958, 964, 970, 973, 1043, 1047, 1049, 1102, 1190, 1255, 1282, 1319, 1335, 1341, 1378, 1460, 1463, 1489, 1501, 1734, 1737, 3029, 3034, 3078, 3096, 3141, 3141, 3152, 3152, 3236, 3236

Geometry			
C	−0.4416570	2.8181460	0.5939880
H	0.1870670	2.7547410	1.4745240
H	−1.0820430	3.6855640	0.5078530
C	−0.4219260	1.8760540	−0.3355860
H	−1.0712870	1.9767460	−1.2013240
C	0.4219260	0.6414050	−0.2928910
H	1.0832340	0.6248780	−1.1649280
H	1.0625840	0.6558820	0.5908110
C	−0.4219260	−0.6414050	−0.2928910
H	−1.0832340	−0.6248780	−1.1649280
H	−1.0625840	−0.6558820	0.5908110
C	0.4219260	−1.8760540	−0.3355860
H	1.0712870	−1.9767460	−1.2013240
C	0.4416570	−2.8181460	0.5939880
H	−0.1870670	−2.7547410	1.4745240
H	1.0820430	−3.6855640	0.5078530

2,4-hexadiene:

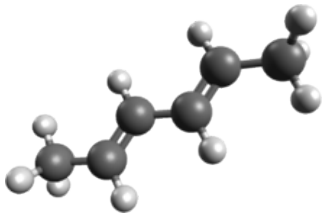

Frequencies:
102, 145, 169, 194, 244, 342, 344, 440, 555, 783, 885, 944, 948, 983, 1036, 1075, 1077, 1103, 1121, 1203, 1276, 1337, 1350, 1368, 1418, 1423, 1484, 1484, 1495, 1500, 1723, 1769, 3036, 3037, 3092, 3092, 3121, 3121, 3138, 3142, 3147, 3150

Geometry			
C	−1.7907280	−0.4294360	−0.0000030
H	−1.7138790	−1.5134620	−0.0000010
C	−0.6685990	0.2860870	−0.0000020
H	−0.7329250	1.3713240	−0.0000030
C	0.6685990	−0.2860870	0.0000020
H	0.7329250	−1.3713240	0.0000030
C	1.7907280	0.4294360	0.0000030
H	1.7138790	1.5134620	0.0000010
C	−3.1712760	0.1392000	−0.0000060
H	−3.7319520	−0.1928290	−0.8766310
H	−3.7319550	−0.1928260	0.8766180
H	−3.1532100	1.2287930	−0.0000080
C	3.1712760	−0.1392000	0.0000060
H	3.7319550	0.1928260	−0.8766180
H	3.7319520	0.1928290	0.8766310
H	3.1532100	−1.2287930	0.0000080

3-methylcyclopentene:

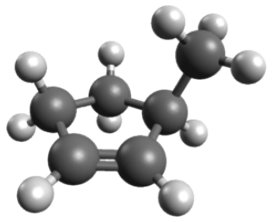

Frequencies:
107, 251, 273, 356, 487,
691, 727, 778, 807, 873,
915, 960, 977, 996, 1010,
1067, 1109, 1128, 1141,
1210, 1244, 1310, 1325,
1339, 1360, 1393, 1414,
1490, 1500, 1505, 1512,
1710, 3037, 3039, 3049,
3070, 3086, 3112, 3115,
3118, 3190, 3217

Geometry			
C	1.4187270	−0.6232910	0.3691930
C	1.2976600	0.8640580	0.1753070
C	0.1164590	1.2055270	−0.3179900
C	−0.7895550	0.0160980	−0.5176590
H	2.3568660	−1.0241220	−0.0167270
H	1.3892920	−0.8723000	1.4341140
H	2.0807820	1.5586030	0.4475030
H	−0.2085630	2.2206970	−0.5048170
H	−1.2464180	0.0325600	−1.5096980
C	0.1936670	−1.1699180	−0.3903920
H	−0.2606100	−2.0278150	0.1047770
H	0.5027460	−1.4933210	−1.3845070
C	−1.9097500	−0.0140820	0.5241440
H	−2.5225590	0.8869320	0.4719160
H	−2.5616040	−0.8752110	0.3704690
H	−1.4931720	−0.0763770	1.5313520

4-methyl-1,3-pentadiene:

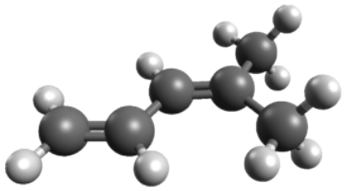

Frequencies:
107, 127, 177, 211, 247,
367, 446 459, 533, 687,
834, 905, 955, 966, 980,
1013, 1044, 1093, 1110,
1176, 1251, 1334, 1375,
1422, 1429, 1464, 1476,
1490, 1497, 1503, 1691,
1757, 3031, 3039, 3084,
3089, 3133, 3146, 3151,
3154, 3181, 3244

Geometry			
C	−2.0547130	−1.0147570	−0.0000030
H	−2.6885670	−0.8574080	−0.8765660
H	−2.6885590	−0.8574220	0.8765690
C	−0.9035720	−0.0523600	0.0000000
C	0.3580960	−0.4941820	−0.0000010
H	0.5156960	−1.5689650	−0.0000040
H	−1.7200780	−2.0506420	−0.0000130
C	−1.3064910	1.3923570	0.0000030
H	−0.4656210	2.0800570	0.0000190
H	−1.9220550	1.6104180	−0.8761510
H	−1.9220800	1.6104080	0.8761420
C	1.5732810	0.3055000	0.0000020
H	1.4736410	1.3844790	0.0000060
C	2.7975900	−0.2156110	−0.0000010
H	2.9542290	−1.2877710	−0.0000060
H	3.6782490	0.4111680	0.0000010

2-methyl-1,4-pentadiene:

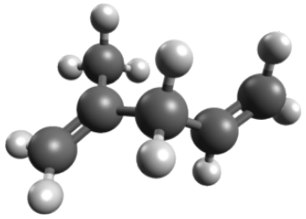

Frequencies:
61, 89, 184, 233, 372, 401, 471, 521, 657, 731, 855, 918, 945, 953, 969, 1001, 1035, 1053, 1075, 1141, 1243, 1308, 1329, 1338, 1419, 1455, 1461, 1480, 1488, 1503, 1729, 1746, 3038, 3041, 3089, 3098, 3137, 3145, 3149, 3157, 3232, 3236

Geometry			
C	−2.0585670	−0.7954300	−0.2513910
H	−2.0227040	−1.8742020	−0.1661870
H	−2.9765110	−0.3610250	−0.6263730
C	−1.0240790	−0.0389740	0.0920590
C	0.2630110	−0.6422900	0.6054320
H	0.1115260	−1.7088870	0.7835660
H	0.5247280	−0.1831950	1.5629400
C	−1.0479380	1.4570880	−0.0096290
H	−0.8827230	1.9082480	0.9719670
H	−0.2449890	1.8136260	−0.6575490
H	−1.9975720	1.8183360	−0.3998300
C	1.4019350	−0.4573910	−0.3563930
H	1.2709330	−0.9212690	−1.3295660
C	2.5082350	0.2239140	−0.1048440
H	2.6693640	0.7047900	0.8530280
H	3.2923740	0.3220760	−0.8433950

Cyclopentene:

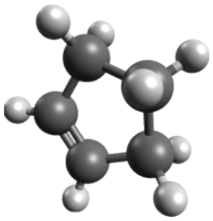

Frequencies:
147, 398, 618, 723, 790, 832, 903, 920, 928, 986, 994, 1053, 1078, 1135, 1167, 1238, 1243, 1319, 1334, 1342, 1392, 1490, 1497, 1518, 1709, 3034, 3035, 3068, 3086, 3091, 3125, 3195, 3221

Geometry			
C	−0.2667570	−1.1977950	0.0000000
C	0.0687450	−0.3269130	1.2276530
C	0.0687450	1.0682540	−0.6625740
H	0.2649240	−2.1475950	0.0000000
H	−1.3338450	−1.4217870	0.0000000
H	1.0530970	−0.5677540	1.6409340
H	0.1061580	1.9539880	−1.2818930
C	0.0687450	−0.3269130	−1.2276530
H	−0.6494610	−0.4562010	−2.0383180
H	1.0530970	−0.5677540	−1.6409340
C	0.0687450	1.0682540	0.6625740
H	−0.6494610	−0.4562010	2.0383180
H	0.1061580	1.9539880	1.2818930
C	−0.2667570	−1.1977950	0.0000000

1,4-pentadiene:

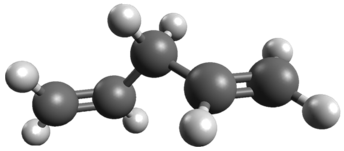

Frequencies:
85, 100, 304, 381, 463,
623, 691, 907, 926, 969,
971, 979, 1042, 1048,
1097, 1182, 1273, 1313,
1332, 1340, 1457, 1463,
1484, 1725, 1739, 3039,
3084, 3146, 3146, 3159,
3159, 3237, 3237

Geometry			
C	0.0000000	2.3582730	−0.1824440
H	−0.8384300	2.6271060	0.4495880
H	0.4053820	3.1334380	−0.8185460
C	0.5069910	1.1358430	−0.1728900
H	1.3434320	0.9001500	−0.8237870
C	0.0000000	0.0000000	0.6694360
H	0.8019900	−0.3644220	1.3164400
H	−0.8019900	0.3644220	1.3164400
C	−0.5069910	−1.1358430	−0.1728900
H	−1.3434320	−0.9001500	−0.8237870
C	0.0000000	−2.3582730	−0.1824440
H	0.8384300	−2.6271060	0.4495880
H	−0.4053820	−3.1334380	−0.8185460
C	0.0000000	2.3582730	−0.1824440

Methyl:

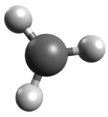

Frequencies:
528, 1409, 1410, 3122,
3303, 3303

Geometry			
C	0.0000080	−0.0000120	0.0000000
H	−0.2031130	1.0589480	−0.0000010
H	−0.8155910	−0.7053130	−0.0000010
H	1.0186590	−0.3535640	−0.0000010

Part III

Dynamics at Liquid Surfaces

Chapter 6

Evaporation at the Liquid-Vacuum Interface

Abstract

Evaporation studies on volatile liquid dodecane and water jets have been conducted, comparing the dynamical information accessible for both cylindrical and flat jets with respect to the evaporation process. Dodecane is found to be of sufficiently low volatility to produce measured distributions with generally good agreement with expectations based on the physical processes at play for evaporation from liquid surfaces, and represents a promising model hydrocarbon system for future experiments. Experiments on neat water jets find that the vapor-phase collision number during evaporation is extensive, leading to severe distortions in arrival time and angular distributions which can erase signatures of the fundamental distributions governing evaporation. Further experimental improvements are needed to construct conditions as conducive as possible to measuring these properties for the very volatile water jets, and to make them more accessible for scattering experiments. A major result of this work is the discovery that the beam skimmers relied upon heavily to suppress vapor-phase collisions in other liquid jet experiments must be so small and positioned so close to the surface to have any effect that they influence the measured distributions substantially. Under the experimental conditions explored here, this all but precludes their utility for flat jet experiments. With careful design considerations, liquid flat jets demonstrate significant promise for future evaporation and scattering studies into both reactive and non-reactive dynamics taking place at the surfaces of volatile liquids.

6.1 Introduction

Liquid evaporation studies have provided tremendous insight into the chemical and physical interactions taking place at the liquid-vapor and liquid-vacuum interface. Early work took both a fundamental and a practical interest in the rate at which evaporation occurred from a liquid surface, and the ability of impurities to retard this process. Langmuir conducted early experiments on this topic using monolayers of impurities on the surface of water,[286] confirming the pronounced effects observed by contemporaries which these impurities had on evaporation rates.[287,288] The matter of whether liquids always evaporated at their maximum thermodynamic rates (given by the Hertz-Knudsen-Langmuir relation) was subsequently addressed by Hickman with the development of the falling stream tensimeter.[289,290] Results for low vapor pressure liquids on the tensimeter indicated that when great care is taken to prepare clean fluid surfaces the evaporation coefficient ε has a unity value, i.e. evaporation proceeds at the maximal rate prescribed by thermodynamics. Yet a wide range of ε values continued to be reported for volatile liquids. Using his tensimeter, Hickman reported $\varepsilon = 0.243$ for water,[291] with others findings values between 10^{-3} and 1.[292] More recent experiments on diminutive water droplets by Saykally and coworkers find a value of 0.62 ± 0.09 for ε.[50]

In some cases the culprit behind the wide range of ε values is erroneous measurement technique or a failure to prepare a surface free of impurities. More fundamentally, molecular collisions during the evaporation of volatile liquids can decrease the number of particles which permanently escape the surface, leading to an under-counting of the evaporative flux. Additionally, rapid evaporation of volatile species leads to localized cooling of the liquid interfacial layer, and sustained vaporization then relies on the rate at which heat can transfer to the surface. Combined quantum and statistical mechanical approaches using statistical rate theory[293,294] have deepened our understanding of evaporation dynamics by accounting for the coupling that must exist to promote a transition across a phase boundary, and provided explicit expressions for the evaporation and condensation coefficients in terms of this coupling.[295] The theory results in impeccable agreement with experimental data on the vaporization behavior of several liquids, including accurately describing the interfacial temperature inversion and interfacial temperature discontinuity.

While the evaporation coefficient parameterizes the total evaporative flux, it does not contain any information about the velocity and internal state distribution of particles that escape the surface. Specifically, the speed, angular, and internal energy distributions of evaporating particles collectively provide detailed insight into the evaporation process.[38] In a liquid-vapor system under thermal equilibrium there are three distinct mechanisms through which particles may depart from the liquid surface: elastic scattering of incident gas particles, inelastic scattering of incident gas (by exciting surface modes), and thermal desorption. A substantial body of work spanning well over a century has sought to characterize the angular, speed, and internal energy distributions of evaporating molecules, under both equilibrium and non-equilibrium conditions, to construct a detailed description of the evaporation process.

Volatile liquids became truly accessible with the advent of liquid microjets, for which collisions can be suppressed if the jet diameter is smaller than the vapor-phase mean free

path.[49] Using diminutive, 5 μm liquid water microjets, it was found that placing a conical molecular beam skimmer close to the liquid surface adjusts the vapor-phase expansion geometry, leading to a faster decay in gas density with distance from the surface along with a correspondingly lower collision number. It was posited that the use of a beam skimmer is thus essential in exposing the bare surface of volatile liquids, and a large number of research groups rely on this technique for various (mostly spectroscopic) liquid jet experiments.

Particular interest has been given to helium evaporation from both protic and hydrocarbon liquids.[296–298] Translational energy distributions for evaporating He atoms were found to exceed the flux-weighted value of $2RT$ expected for thermal desorption processes. This has been attributed to collisions with liquid molecules within the interfacial layer imparting significant excess kinetic energy to the helium atoms as they are ejected from the surface. The manifestation of these effects are governed by the interplay between solute particle mass and interaction potential with the liquid molecules.[299] Simulations of these interactions for various atoms and small molecules find that helium should evaporate from water with a super-Maxwellian speed distribution as observed experimentally. In contrast, H_2 is expected to display sub-Maxwellian evaporation dynamics, which has also been experimentally verified using a variety of liquids.[300] Simulations of He and Ar evaporating from dodecane find similar results, with superthermal He evaporation and essentially thermal Ar evaporation.[301]

Work on larger molecular liquids such as highly concentrated formic and acetic acid has found that single molecules of the acid evaporate with Maxwellian distributions, while the acid dimers are strongly super-Maxwellian.[302] For the dimers, fit temperatures were on the order of $\sim$100 K greater than the liquid temperature for $(CH_3COOH)_2$. A model based on surface tension was put forth: dimers existing in pockets in the fluctuating liquid surface are accelerated away from the surface as surface tension counteracts the curvature of the liquid depression. This mechanism occurs specifically for dimers because their mutual hydrogen-bonding shields the acid functional groups from the rest of the surface, and the pair interacts with the rest of the liquid as if it were hydrophobic.

The internal state distribution of benzene molecules evaporating from mixtures of water and ethanol has also been studied previously.[303] From these experiments it was possible to estimate the vapor-phase collision number and the collisional cooling undergone by the rotational degrees of freedom for benzene, as well as for various high- and low-frequency vibrational modes. A recent study employed laser-induced fluorescence to measure the rotational and spin-orbit distributions of NO molecules evaporating from 4-5 μm water microjets.[304] It was found that the internal quantum-state distributions of NO were well-fit by Boltzmann distributions, but for temperatures significantly colder than the liquid jet temperature. The results of this experiment implied that even small collision probabilities such as those existing for the NO-H_2O pair can still produce large effects on the distributions describing evaporating species.

Evaporation is also actively being studied with a focus on better understanding the formation, growth, and chemistry of aerosol particles in the atmosphere.[305,306] Given the pivotal role of evaporation dynamics to the atmospheric fate of these particles, it is important to characterize the evaporation of molecules from both aqueous and organic surfaces.

Evaporation studies also isolate one of the major channels encountered in scattering experiments (trapping-desorption), and a detailed understanding of how these phenomena manifest themselves in liquid-vacuum time-of-flight experiments will be key to successful scattering experiments. The goal of this work is to extend the capabilities of evaporation and scattering experiments to the surfaces of volatile liquid flat jets, which will allow for both the speed and angular distributions of evaporating molecules to be determined.

6.2 Experimental

The evaporation of neat liquid water and *n*-dodecane and of dissolved gases in these solvents was carried out on the modified crossed molecular beam apparatus with a rotatable detector as described previously.[11] Liquid jets were introduced into the vacuum chamber by using an Agilent 1260 Infinity II high-performance liquid chromatography (HPLC) pump to force pressurized liquid through micrometer-scale channels of a glass microfluidics chip.[97] By using the single central or the convergent outer channels of this nozzle it is possible to create either cylindrical microjets (∼28 μm diameter) or flat jets with dimensions of a few millimeters. Typical liquid pressures were 25-50 bar with flow rates of 0.5 mL/min for cylindrical jets and 2.5-3.5 mL/min for flat jets.

To reduce the vapor pressure of the volatile liquids studied here, they are first pre-cooled by a counter-current heat-exchanger before entering the liquid jet nozzle. Water is typically cooled to 1-2 °C (P_{vap} = 5 Torr) while dodecane is cooled to about -6 °C (P_{vap} = 7 mTorr). Cold liquid then emanates into the vacuum chamber where it undergoes further cooling through evaporation. The liquid jet exits the vacuum chamber through a conical beryllium copper catcher with a small internal diameter.[307] Liquid removed by the catcher flows into a differentially pumped collection reservoir held at ∼ 0.2-2 Torr. For cylindrical jets the liquid is captured after travelling several millimeters, while flat jets are caught at the narrow node where the fluid sheet recombines under the action of surface tension. The catcher is heated to 10-15 °C when using water jets to prevent freezing of the liquid inside the catcher. A 1 m^2 liquid nitrogen-cooled copper coldshield reduces the ambient chamber pressure to 4–12 × 10^{-6} Torr during operation of the liquid jets, resulting in a mean free path on the order of several meters.

To study the evaporation of dissolved gases, the liquids are degassed by using a vacuum pump to evacuate the headspace of the HPLC liquid bottle while immersed in an ultrasonication bath. After degassing, a flow of the desired gas is bubbled through the liquid to saturate it. Once gas has bubbled through the liquid for a few minutes the vacuum pumping ceases. The continuous, slow stream of analyte gas bubbling through the liquid prevents the diffusion of air back into the headspace of the liquid bottle. For the noble gases He through Ar, saturated mole fractions of dissolved gas in 0 °C water vary between ∼10^{-5}–10^{-4}.[308] Extrapolation down to -6 °C of experimental solubility data for these gases in dodecane gives mole fractions between ∼10^{-4}–10^{-3}.[309]

To assess the effect of collisions during evaporation on the velocity and angular distributions

of the desorbing particles, various conical molecular beam skimmers with diameters varying between 0.2-1 mm are installed between the chopper wheel and the liquid jet. The skimmer changes the collision frequency of evaporating molecules from a $1/d$ to a $1/d^2$ dependence on distance d from the liquid surface. The resulting TOF spectra for these skimmers at several distances from the surface can then be compared to data collected without a skimmer.

Detection of evaporating particles occurs in the plane defined by the detector rotation and perpendicular to the jet flow axis. Cations created by an electron impact ionizer nested within three differentially pumped regions and operated at 80 eV were mass selected using a quadrupole filter and detected with a Daly style ion detector.[85,135] The velocity distribution of evaporating particles was characterized using a slotted spinning chopper wheel inserted between the liquid jet and the detector aperture to produce a narrow pulse of gas traveling towards the detector. A multichannel scalar collected and binned the ion signal as a function of arrival time, producing time-of-flight (TOF) spectra. The TOF spectra were collected as a function of detector angle θ relative to the surface normal.

6.3 Results

The mass spectra resulting from the presence of dodecane and water liquid jets in the main chamber are shown in Figure 6.1. The extreme volatility of water leads to such incredibly large ion signal at $m/z = 18$ (H_2O^+) that problems can arise from detector saturation. In the face of such an enormity of signal, the low natural abundance of deuterium and ^{17}O makes $HDO/H_2{}^{17}O$ at $m/z = 19$, and even $m/z = 20$ for heavier isotopologues, very suitable targets for routine measurements. These m/z values also benefit from a lack of any significant background within the ionization chamber. Alternatively, the ionizer emission current could be lowered to decrease ion counts to manageable levels. Dodecane is much less volatile and its entire mass spectrum is accessible for experiments. The two most commonly used ions are $m/z = 170$ ($C_{12}H_{26}^+$) and $m/z = 57$ ($C_4H_9^+$), being the molecular ion and the most intense daughter ion at 80 eV ionization energy respectively. For evaporation experiments, the solute species must be chosen so that it does not coincide with any daughter ions formed by dissociative ionization of the liquid molecule. Given the enormous signal from many jets this can sometimes be more difficult than one might expect. For different data the detected species is specified in each case, and may be evaporating molecules of the liquid from which the jet is formed, or some other species dissolved into the liquid jet.

In order to characterize the time-of-flight distribution of particles evaporating from jets the chopper wheel is used to define time $t = 0$ for a narrow gas pulse and initiate data acquisition in the multichannel scalar. The TOF spectra collected for a 28 μm diameter dodecane cylindrical jet at two different detector angles are shown in Figure 6.2. The spectra agree very well with simulations of a Maxwellian speed distribution corresponding to the temperature of the jet. Deviations on the slow edge of the peaks are caused by gas-phase collisions between dodecane molecules during evaporation and in transit to the detector, discussed further in the Analysis section. The residual remaining after subtracting the two

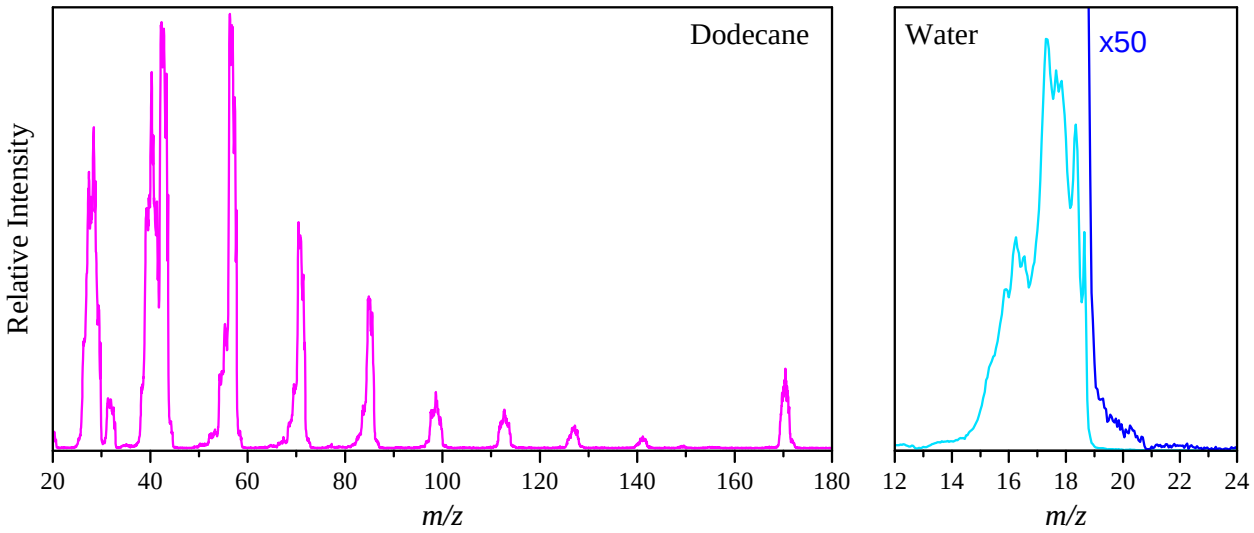

Figure 6.1: Mass spectra obtained when the detector is exposed to dodecane and water flat jets. A 50x multiplication of the water spectrum is shown to highlight the substantial ion signal at $m/z = 19$, and even at $m/z = 20$, from naturally abundant heavy isotopes.

experimental curves from one another is a flat spectrum containing only noise. The essentially identical curves at the two detector angles are unsurprising given the cylindrical symmetry of the jet, underscoring the fundamental lack of angular information that can be gleaned from cylindrical jet studies. Figure 6.3 shows a comparison of TOF spectra collected for dodecane and cylindrical water jets in our lab to cylindrical jet data for each liquid produced in the Nathanson group using jets with comparable diameters.[310,311] The data collected here are very similar to these previously collected spectra, with water showing worse agreement with the Maxwellian simulation than dodecane owing to a greater number of collisions due to its much higher vapor pressure.

Equivalent data taken using water and dodecane flat jets is shown in Figures 6.4 and 6.5, collected at $m/z = 170$ and $m/z = 19$ respectively. Flat jets evaporation data is shown for several detector angles relative to the jet surface normal. For dodecane measured along the jet surface normal (i.e. $\theta = 0^o$) the TOF spectra show moderate distortion from the Maxwellian simulations, especially on the slow edge of the spectrum. The data are also peaked at slightly shorter arrival times of $\sim$680 μs as compared to the simulation, which peaks at 734 μs. In general, the time-of-flight distribution is found to slow down, broaden, and better agree with the Maxwellian simulations as the detector is rotated to larger angles. The measured evaporation flux also decreases at larger angles, reflected in the relative peak heights displayed in Figure 6.4. The 90^o spectrum corresponds to the detector viewing the cylindrical rim of the jet, and the measured distribution is substantially slower than the Maxwellian simulation, by about 100 μs ($\sim$830 μs vs. 734 μs). The 90^o flat jet spectrum is thus also much slower than the data for the 28 μs cylindrical jet, which agrees very well with the Maxwellian simulation.

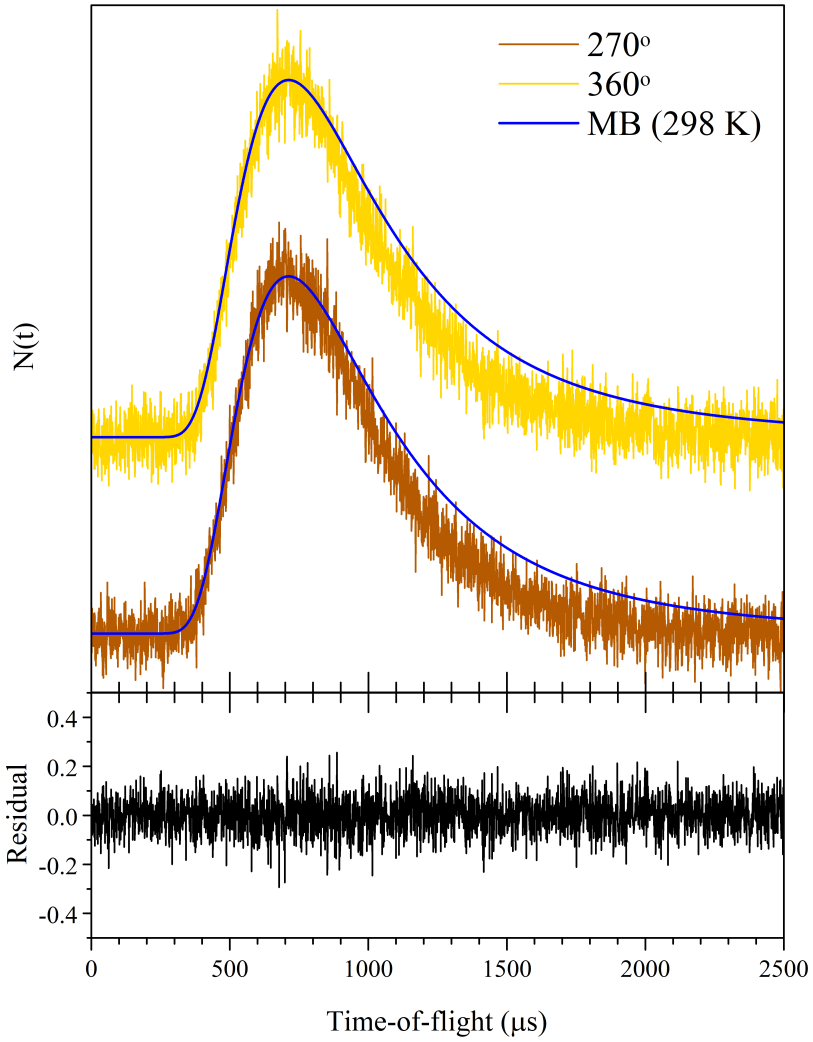

Figure 6.2: Top: evaporation of dodecane measured at $m/z = 170$ ($C_{12}H_{26}^{+}$) at two detector angles. The two curve are offset from one another for viewing clarity. Also shown is a simulation for Maxwellian evaporation at 298 K. Bottom: residual after subtraction of the two experimental curves.

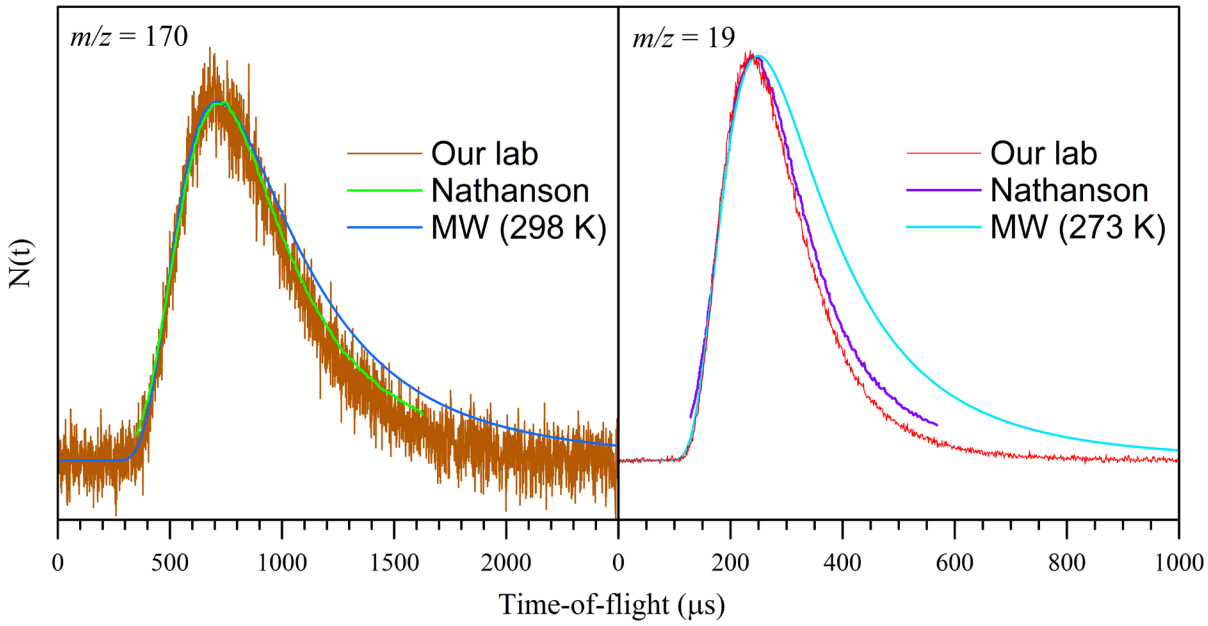

Figure 6.3: Left panel: comparison between a 28 μm dodecane cylindrical microjet in our lab and a similar 40 μm jet produced by the Nathanson group.[310] Right panel: comparison between a 28 μm water cylindrical microjet in our lab and a similar 35 μm jet produced by the Nathanson group.[311] The blue curves in each spectrum correspond to Maxwellian simulations. Note the shorter timescale in the water evaporation data.

As was the case for the cylindrical jets, measurements of evaporation from water flat jets (Figure 6.5) contain greater distortions from the Maxwellian simulations than dodecane jets do due to the much higher vapor pressure. In fact for all evaporation angles the data were peaked at noticeably faster arrival times than the simulations, and their arrival time distribution was significantly narrower. For example, the TOF spectrum for evaporation along the surface normal is peaked at 191 μs and has a FWHM of $\sim$100 μs, compared to the 246 μs and 230 μs respectively for the Maxwellian simulation. Even the spectrum collected for the jet rim at 90^o is significantly faster than the simulation in the case of water evaporation.

Other than the liquid itself, the evaporation of other species can be measured by dissolving them into the liquid before it forms a jet. Evaporation experiments were thus carried out using noble gases dissolved in the liquids. Neon was chosen for dodecane, whose mass spectrum contains no ion signal at $m/z = 20$ where Ne^+ is detected. Heavy isotopes contained in water produce non-negligible ion signal at $m/z = 20$ (see Figure 6.1), so argon was chosen instead, detected as Ar^+ at $m/z = 40$ free from background contributions.

Select spectra for neon evaporation from dodecane and for argon evaporation from water are shown in Figures 6.6 ($m/z = 20$) and 6.7 ($m/z = 40$) respectively, at angles of 2^o, 45^o, and 90^o with respect to the surface normal. Although suffering from poor signal-to-noise ratios, the spectra overall for neon evaporating from dodecane agree quite well with

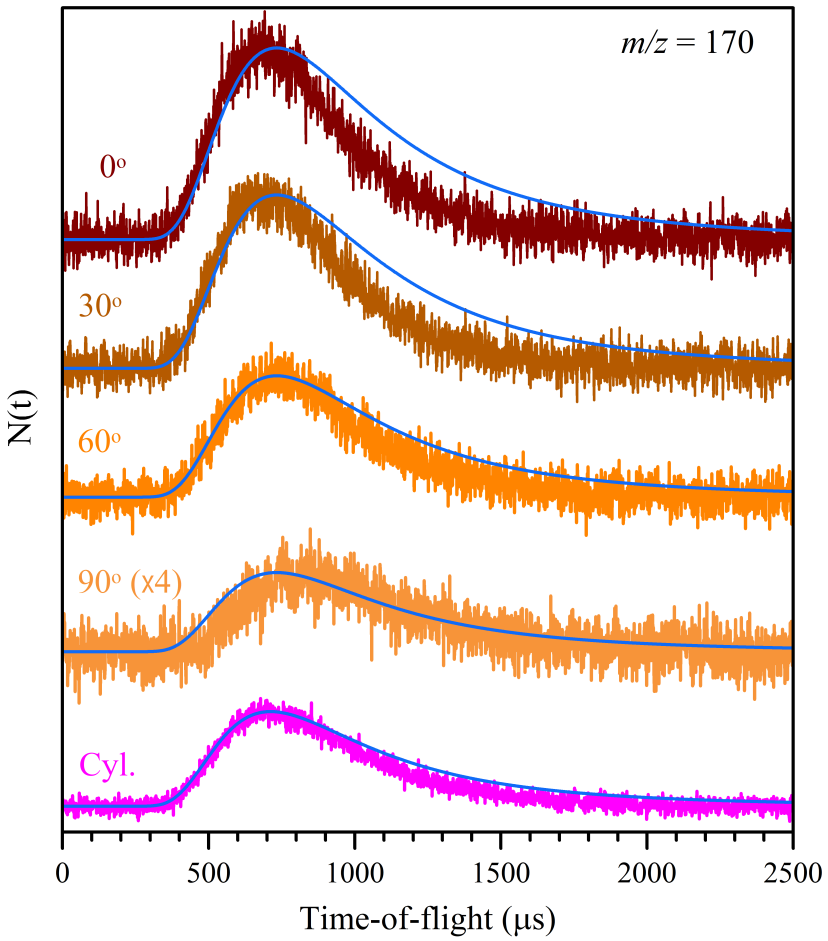

Figure 6.4: TOF spectra collected at various angles for $m/z = 170$ for evaporation of dodecane from a flat jet of neat liquid dodecane. The blue curves are Maxwellian TOF simulations corresponding to the measured liquid temperature.

Maxwellian simulations. For argon evaporating from water flat jets, significant distortions are still observed. In fact, argon TOF spectra have worse disagreement with their Maxwellian simulations than was exhibited for water, which is considered further in the Analysis section.

In the example TOF spectra shown in Figures 6.4-6.7, the peak heights (and integrated ion counts) of the arrival time distributions are observed to depend on the angle at which the spectra are collected relative to the surface normal. Unlike the cylindrical jets, there is clearly an underlying angular distribution present in the flat jet evaporation data. Figure 6.8 shows the angular distributions measured for evaporation from liquid flat jets of water and dodecane. The angular distribution for dodecane evaporation from the dodecane jet have a characteristic $\cos\theta$ shape. The data for evaporation of neon dissolved into the dodecane jet also agree very well with the cosine distribution.

For data collected from the water flat jet, as was the case for the time-of-flight distributions,

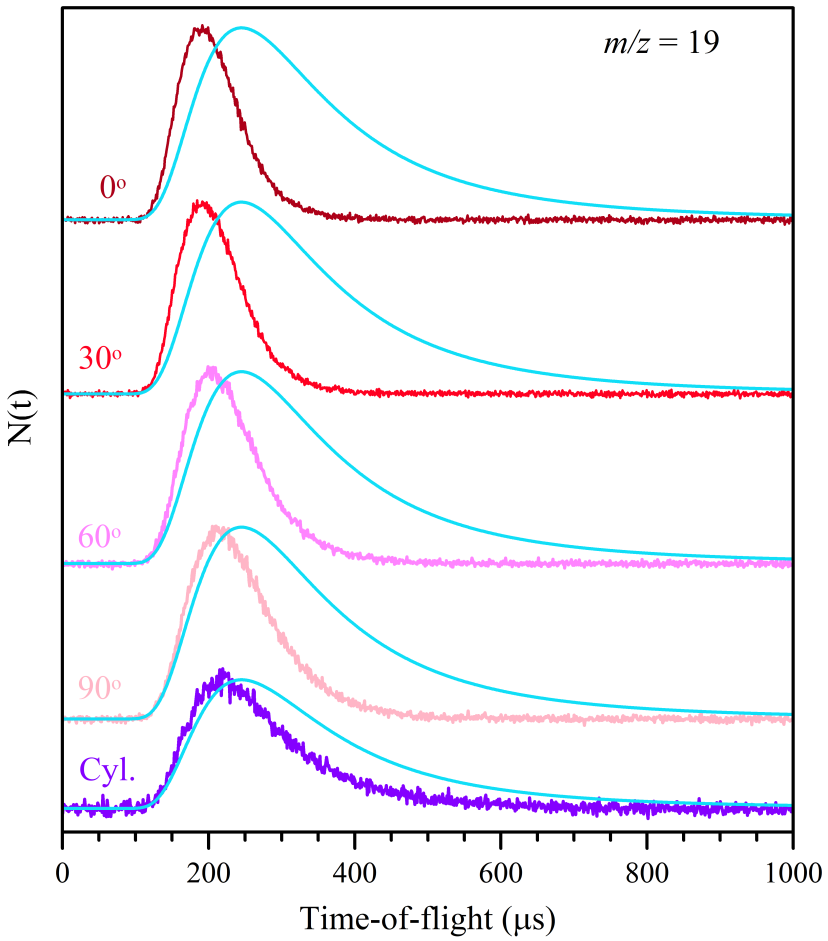

Figure 6.5: TOF spectra collected at various angles for $m/z = 19$ for evaporation of water from a flat jet of neat liquid water. The light blue curves are Maxwellian TOF simulations corresponding to the measured liquid temperature.

the angular distributions also display distortions from the expected signal dependence. This problem is particularly bad for water, which hardly resembles a cosine distribution. The data for argon evaporation from water do display a generally cosine shape. Of particular note, the measured signal for large angles drops off much slower than expected relative to the points measured at angles closer to normal, and becomes angle-independent as 90^0 is approached. This feature is observed for all flat jets, and is discussed in more detail in the Analysis section.

As mentioned in the Experimental section, precedent on other liquid jet experiments extols the use of beam skimmers to suppress vapor-phase collisions. The effect of various skimmers on the evaporation TOF distributions is shown in Figure 6.9. Skimmers of various sizes were tested at many different distances from the jet surface (not shown). To have a significant effect on the data, these skimmers must typically be placed no farther than

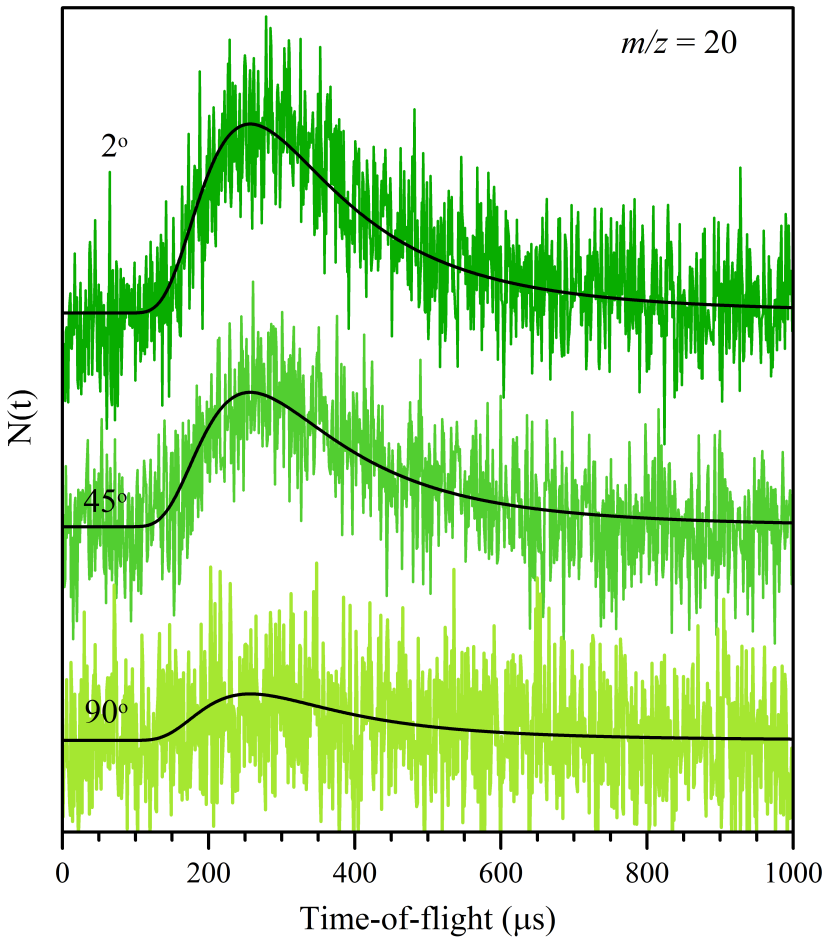

Figure 6.6: TOF spectra collected at various angles for $m/z = 20$ for evaporation of neon from a flat jet of liquid dodecane. The black curves are Maxwellian TOF simulations.

∼1-2 mm from the surface of the liquid, and generally much closer to significantly affect the TOF spectra. Greater effects are seen for closer skimmer distances, which were tested down to as low as ∼150-200 μm above the liquid.

Insertion of the skimmer clearly results in the arrival time distributions slowing down and broadening, coming into better agreement with the Maxwellian simulations. The modification to the spectrum is observed to be more pronounced when smaller skimmers are used. Data collected using a 0.5 mm skimmer (not shown) gives intermediate results between those for 1 mm and for 0.2 mm skimmers. Even in the most extreme case, the effect on the water spectrum only shifts the distribution about halfway toward the Maxwellian simulation. In contrast, the argon TOF spectra do shift fully on top of the Maxwellian simulations when the 0.2 mm skimmer is used for data collection. These modifications come at the expense of a significant increase in data acquisition times and decrease in signal-to-noise ratios, clearly evident in the TOF spectra.

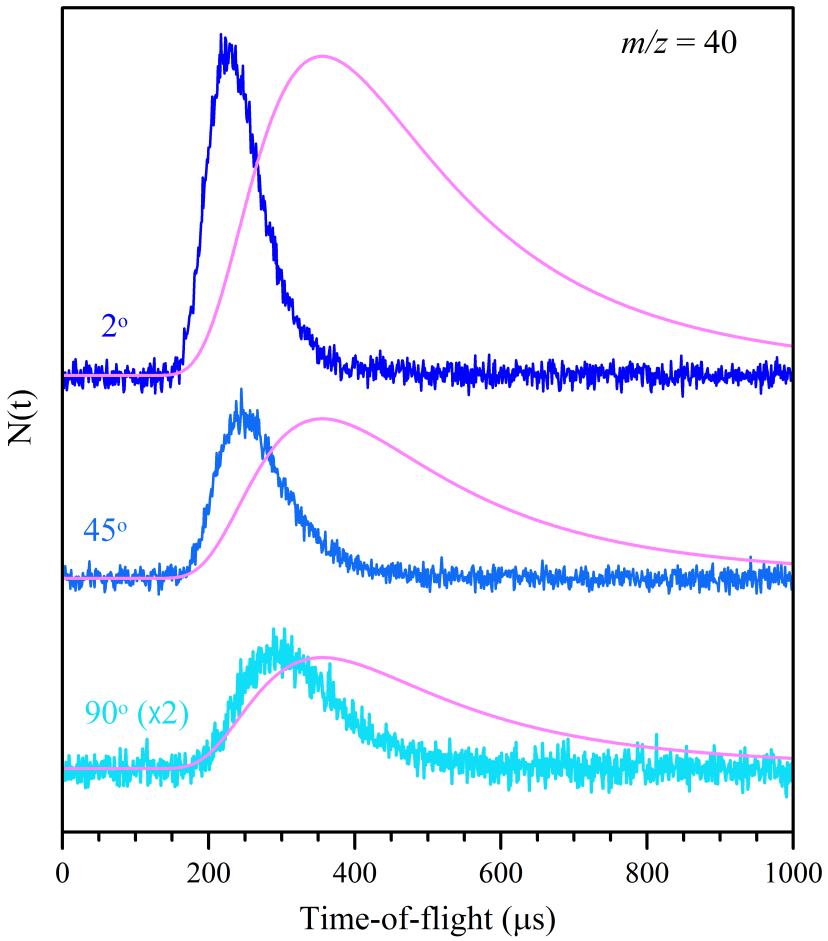

Figure 6.7: TOF spectra collected at various angles for $m/z = 40$ for evaporation of argon from a flat jet of liquid water. The pink curves are Maxwellian TOF simulations.

When using a skimmer, the angular distributions (not shown) also agree very well with cosine distributions. However, this is actually contrary to expectations when a skimmer is used. A cosine angular distribution with the skimmers inserted is indicative of the skimmer influencing the data in an undesired way (this important point is discussed in greater detail in the Analysis section). To confirm this, the effect on the TOF spectra of heating the skimmer was investigated (Figure 6.10).

When the skimmer is heated from $\sim 25^o$C to $\sim 50^o$C, the grey spectrum in Figure 6.10 shifts to faster arrival times by about 5-10 μs, shown in the yellow spectrum. Also shown are Maxwellian simulations for these two spectra. For the heated skimmer the best fit Maxwellian distribution corresponds to a temperature of $\sim 15^o$C hotter than the unheated case. When heating is turned off and the skimmer allowed to return to ambient temperature, the TOF spectrum shifts back to its original shape. This is a sizeable effect, indicating that the beam skimmer is substantially altering the measured TOF distributions and creating significant

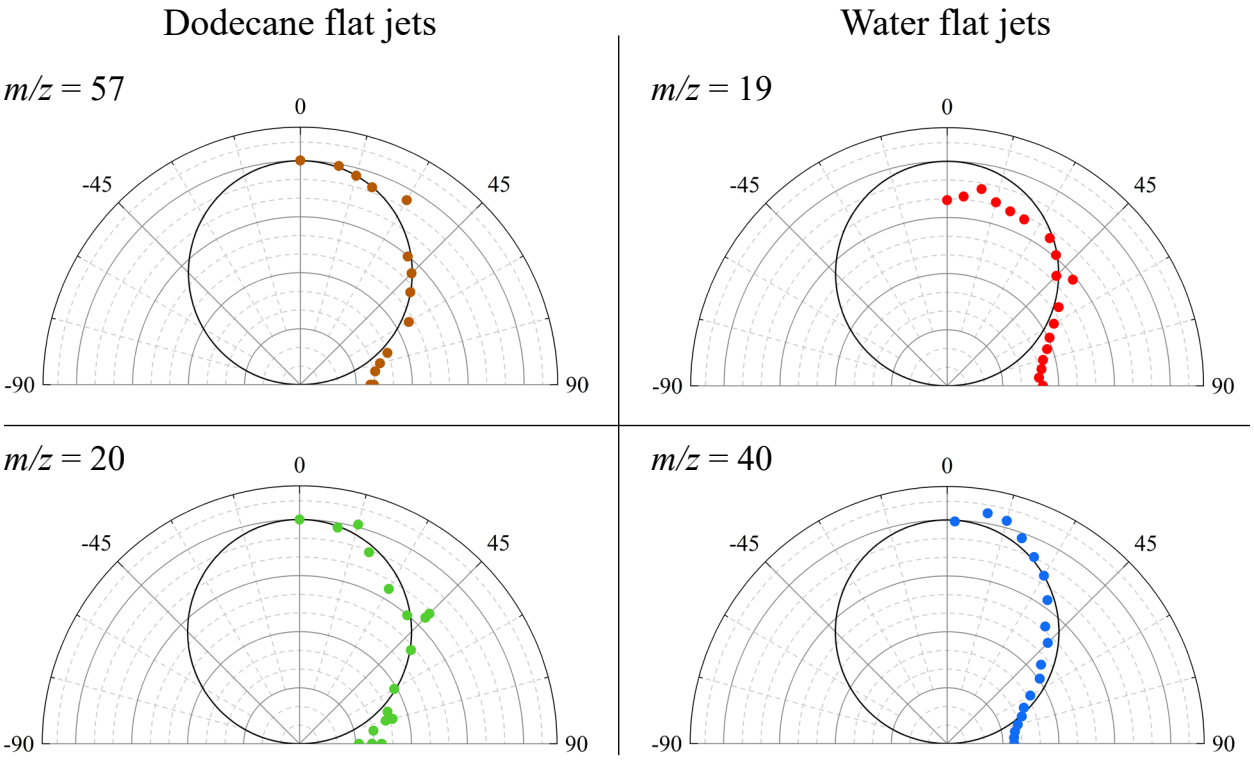

Figure 6.8: Evaporation angular distributions from dodecane and water flat jets. For the dodecane jets, measurements of dodecane and dissolved neon are shown at $m/z = 57$ (brown) and $m/z = 20$ (green) respectively. For the water jets, measurements of water and dissolved argon are shown at $m/z = 19$ (red) and $m/z = 40$ (blue) respectively. The horizontal axis represents the flat jet surface, and the black circles are $\cos\theta$ distributions.

doubt as to the origin of TOF signal collected using the skimmer. Either the entire distribution undergoes partial thermalization with the skimmer to an intermediate temperature, or the distribution contains inseparable contributions from unperturbed and thermalized particles. Since beam skimmers are designed specifically to introduce minimal disturbances to gas flows, the strong dependence of the TOF spectra on the skimmer temperature even at $\theta = 0^o$ is worrying.

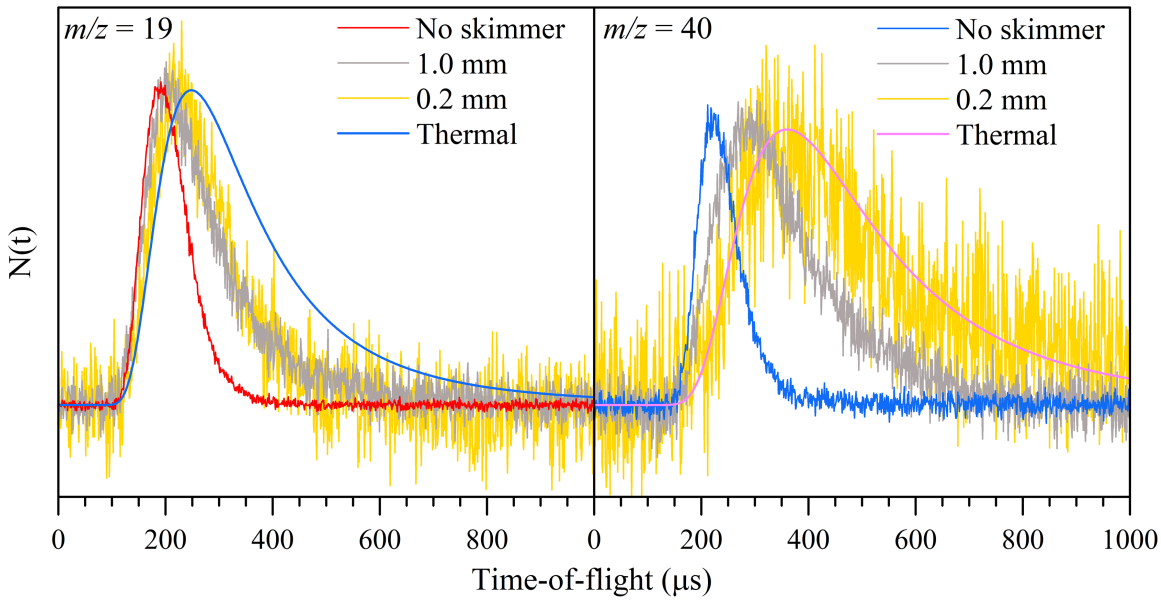

Figure 6.9: Comparison of TOF spectra for H_2O (left) and Ar (right) evaporating from water flat jets ($\theta = 0^o$) and measured using no skimmer, a 1.0 mm skimmer, and a 0.2 mm skimmer.

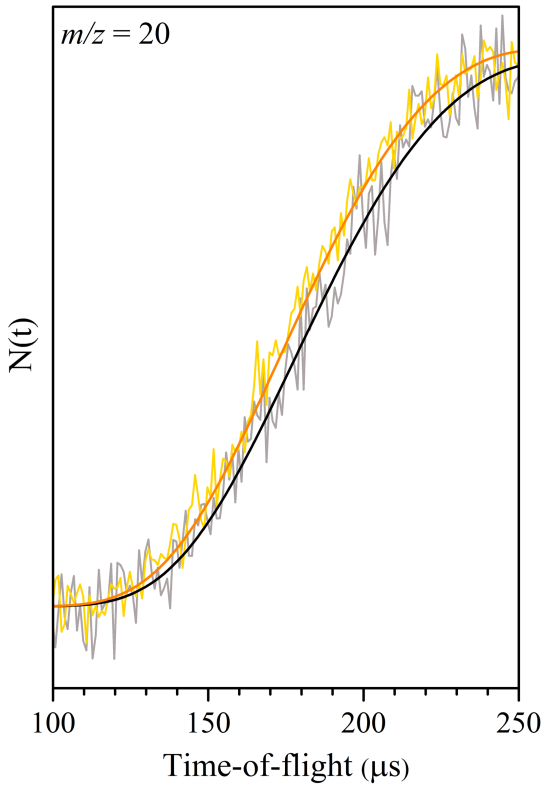

Figure 6.10: Effect of heating the detector beam skimmer on the measured TOF spectrum for Ne evaporating from a dodecane flat jet ($\theta = 0^o$).

6.4 Analysis

Particles evaporating from a liquid are expected to have a Maxwellian velocity distribution with a temperature matching the surface temperature, T_s. Using a Maxwellian distribution for evaporative flux, the experimental time-of-flight distribution has the form

$$N(t) = C\ \frac{L^3}{t^4}\ \exp\left[-\frac{m}{2k_B T_s}\frac{L^2}{t^2}\right] \tag{6.1}$$

where C is a normalization constant, L is the flight length, m is the particle mass, and k_B is Boltzmann's constant. A distribution of particles described by Equation 6.1 has a mean energy of $2k_BT$ rather than $^3/_2 k_BT$. For evaporation from a cylindrically symmetric surface such as a cylindrical microjet, the signal intensity will be uniform across all laboratory angles for a detector rotating about the flow axis of the jet. In the case of evaporation from the planar surface of a flat jet, the evaporative flux is weighted by $\cos\theta$ for the angle θ relative to the surface normal.

The TOF spectra shown in Figures 6.2-6.7 are compared to distributions generated from Equation 6.1, and the angular distributions obtained for evaporation from flat jets are compared to the expected $\cos\theta$ distribution. When comparing experimental TOF spectra to simulations based on Maxwellian evaporation it is helpful to attempt to quantify the number of collisions taking place during desorption, since collisions during evaporation are known to lead to acceleration of the colliding particles. For a cylindrical jet of finite length L_{jet} the collision number is around[312]

$$N_{coll}^{cyl} \approx \frac{r_{cyl}}{\lambda_o}\ \ln\left(\frac{d}{r_{cyl}}\frac{L_{jet}+\sqrt{r_{cyl}^2+L_{jet}^2}}{L_{jet}+\sqrt{d^2+L_{jet}^2}}\right) \tag{6.2}$$

for mean free path λ_o, radius r_{cyl} and travel distance d over which collisions can occur. The reference mean free path is $\lambda_o = (c\sigma n_{vap}/2)^{-1}$ where $c = \langle v_{rel}/v\rangle$ is the ratio of the relative and the gas velocities, and is estimated as $c \approx 0.75$ for collisions between evaporating particles,[52,313] σ is the effective collision cross-section, and $n_{vap}/2$ is half the equilibrium vapor density, since evaporating molecules are pumped away. For the flat jet, approximating the sheet geometry as being circular gives the collision number according to[314]

$$N_{coll}^{circ} \approx \frac{r_{circle}}{\lambda_o}\ \left[1+\frac{d}{r_{circle}}-\left(1+\left(\frac{d}{r_{circle}}\right)^2\right)^{1/2}\right] \tag{6.3}$$

for circular radius r_{circle}. Equations 6.2 and 6.3 are not rigorously accurate descriptions, but they have been found by others to be very helpful in giving a sense of the true collision number.[52] In each case, d is approximated as the separation between the surface and the chopper wheel mounted in front of the detector. The fraction of particles expected to traverse

Table 6.1: Estimates of collision numbers for the experimental data shown in the Results section for the relevant pairs of gas particles. Some quantities differ between entries due to different liquid temperatures (e.g. flat jets are usually run much colder than cylindrical ones).

Figure	**Jet**	**Collision Pair**	σ **(Å²)**	λ_o **(μm)**	$\mathbf{N_{coll}}$	$\mathbf{f_{nc}}$
6.2	$C_{12}H_{26}$ cyl.	$C_{12}H_{26}$–$C_{12}H_{26}$	∼250	254	0.25-0.35	0.70-0.78
6.3	H_2O cyl.	H_2O–H_2O	30	60	1.0-1.5	0.22-0.37
6.4	$C_{12}H_{26}$ flat	$C_{12}H_{26}$–$C_{12}H_{26}$	∼250	1213	0.58-1.2	0.30-0.56
6.5	H_2O flat	H_2O–H_2O	30	68	10-20	$<10^{-4}$
6.6	$C_{12}H_{26}$ flat	Ne–$C_{12}H_{26}$	∼110	4520	0.16-0.32	0.73-0.85
6.7	H_2O flat	Ar–H_2O	<30	110	9-15	$<10^{-4}$

this distance without undergoing a collision is then given by the Beer-Lambert relation as $e^{-N_{coll}}$.

Using Equations 6.2 and 6.3 and the Beer-Lambert relation, the collision number, N_{coll}, and fraction of particles that do not undergo collisions during evaporation, f_{nc}, are estimated for each of the experimental data shown in the Results section and collected in Table 6.1. These estimations rely on the mean free path, λ_o, which depends on the effective collision cross-section for relevant gas pairs in each experiment. These cross-sections are either acquired from the existing literature or estimated based on these values. The resulting expected values of N_{coll} are consistent with the evaporation measurements shown in Figures 6.2-6.7. The average N_{coll} for the dodecane jets are ≤ 1 in virtually all cases, and these spectra almost universally demonstrate very good agreement with the Maxwellian and cosine distributions. In contrast, the liquid water jet data which were observed to deviate significantly from the expected distributions have very high collision numbers, and virtually no particles will arrive at the detector unperturbed.

Previous studies have shown that the effect of vapor-phase collisions between evaporating particles above the jet surface results overall in an acceleration of the particles in a manner analogous to how a supersonic molecular beam forms.[52,314] Under these conditions, it is expected that the data will be well simulated by the velocity distribution for a supersonic molecular beam with average flow velocity v_{SS} and temperature T_{SS}:[314]

$$f(v) \propto v^2 \exp\left(\frac{-m(v - v_{SS})^2}{2RT_{SS}}\right) \tag{6.4}$$

Fits of this expression to the water evaporation data collected at 0^o are shown in Figure 6.11. For the water TOF spectrum collected at $m/z = 19$, the spectrum is best fit with $v_{SS} \approx 795$ m/s and $T_{SS} \approx 87$ K. In the case of the argon spectrum collected at $m/z = 40$ we find very similar fit parameters, $v_{SS} \approx 735$ m/s and $T_{SS} \approx 80$ K. The speed ratio,

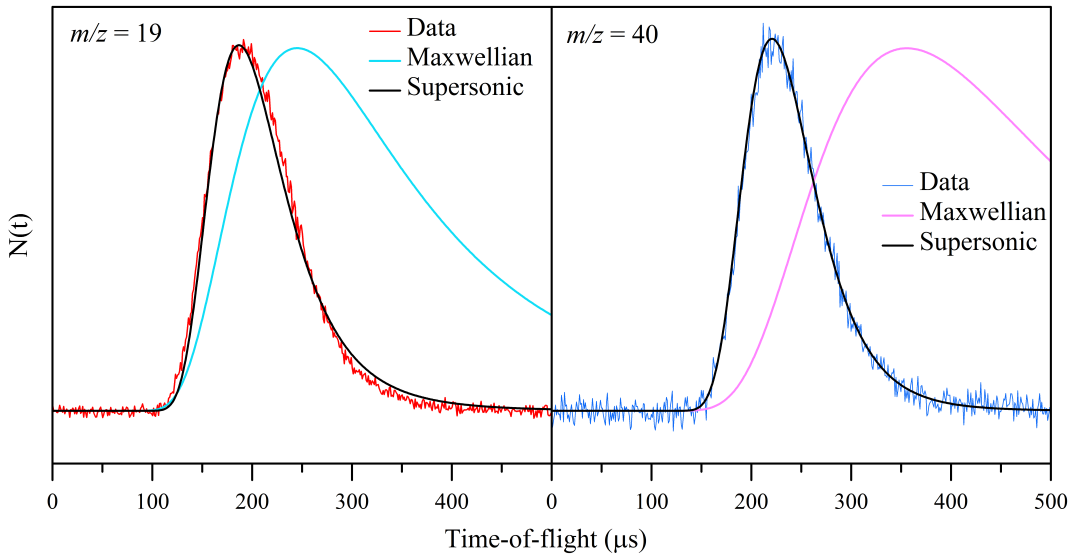

Figure 6.11: Evaporation of water (left) and argon (right) from flat water jets. Thermal distributions corresponding to the liquid temperature are compared to best fits to the data using supersonic velocity distributions.

$S = {}^{mv_{SS}^2}/_{2RT_{SS}}$, is approximately 8.3 and 16.2 for water and argon respectively. The fit to the $m/z = 19$ data is quite good, while the $m/z = 40$ spectrum is matched essentially perfectly within the experimental signal-to-noise.

The angular distributions also differ from the $\cos\theta$ expectations in important ways. For water evaporation, the angular distribution is distorted heavily, and it is not clear what the correct way to normalize the data is. The assumption that intensity should be greatest at 0^o can reasonably be called into question given the appearance of these data. The data were scaled such that the higher angle data points approach the circle before once again deviating at very large angles (see below). Although the argon evaporating from water has a heavily modified arrival time distribution, its angular distribution maintains surprisingly good agreement with a cosine distribution.

Insertion of a skimmer was found to create good agreement between the angular distributions and model cosine distributions. The schematic in Figure 6.12a demonstrates why this should not be the case. While the evaporating flux does indeed change as $\cos\theta$, the viewing area increases with θ as $1/\cos\theta$. The resulting distribution then goes as

$$f(v,\theta) \propto \frac{\cos\theta}{\cos\theta} f(v) = f(v) \tag{6.5}$$

and the signal intensity will be angle-independent until the viewing area exceeds the jet size.

All of the angular distributions in Figure 6.8 demonstrate deviations from cosine for large angles, where the distribution becomes approximately angular-independent. This is an

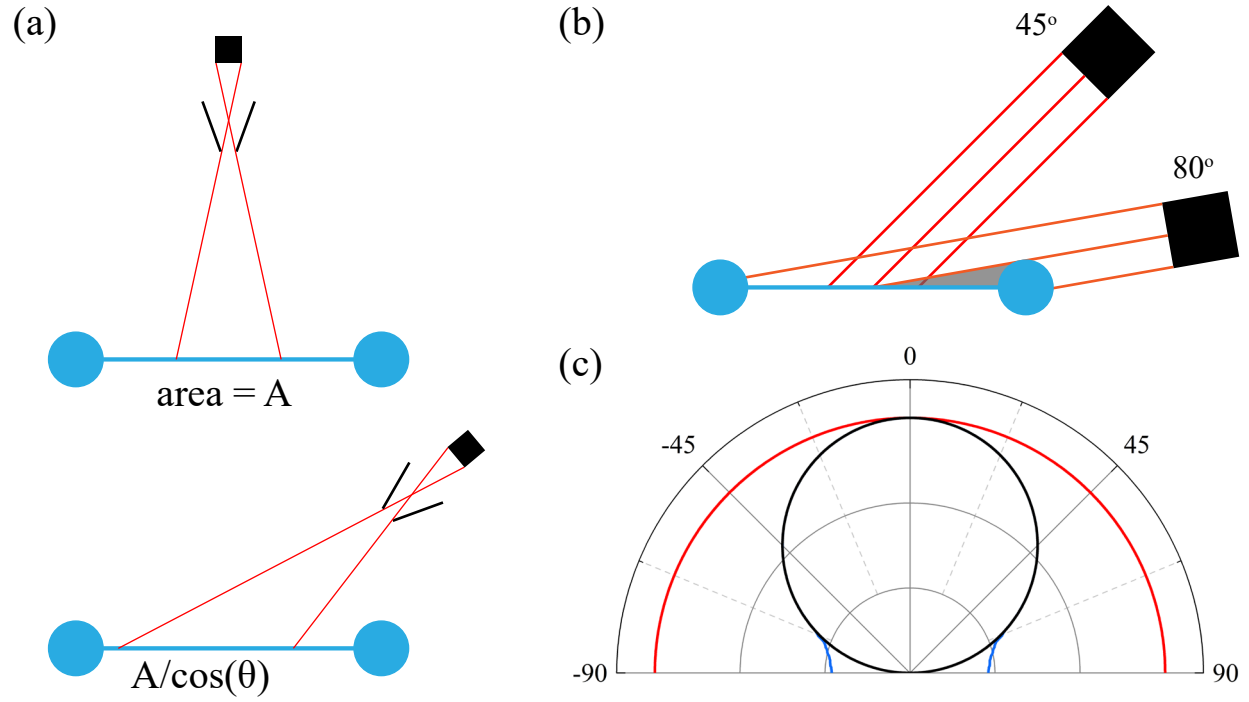

Figure 6.12: (a) Schematic showing how the area probed by a well-collimated apparatus using a detector skimmer depends on the surface viewing angle. (b) Schematic showing the effects of the jet rim thickness on large angle spectra. The grey shaded area cannot be measured in the 80^o case. These schematics are not shown to scale, and are constructed to highlight different features of the experiment that cannot be visually distinguished in a true scale model. (c) Model angular distributions for cosine emission from a surface with no detector skimmer (black), with a detector skimmer inserted (red), and for a surface bounded by cylindrical rims (blue).

artefact of the thick, cylindrical rims bounding the flat jets, which for large angles begin to obscure the view of the flat jet surface and the angular-dependence shifts to the isotropic distribution for a cylindrical surface (see Figure 6.12b). The exact position of this deviation depends on the particular jet size and geometry, but in general it starts at $\sim 70^o$ and the flat sheet is essentially fully obscured by about 82-85^o.

The effects of these experimental features on the expected angular distribution are demonstrated in Figure 6.12c. For the case of no detector skimmer, the black curve is the expected cosine distribution for emission from a surface. When a skimmer is inserted, the angular distribution becomes isotropic, shown by the red curve. For the realistic case here, increasing the detector angle eventually leads to a transition from viewing the flat sheet to viewing the cylindrical rim, which produces fewer particles than the flat sheet. To determine how much this signal should decrease, it is necessary to know in detail how the specific shape of the entire jet affects the gas density throughout the vacuum chamber. The flow dynamics

of gas leaving the jet as a whole are non-trivial to describe, and estimating the amount of signal decrease expected in this case is thus challenging. Since the collision number is directly proportional to the local gas density integrated along the flight path to the detector, it should serve as a good proxy for this quantity. As a first approximation, the ratio $N_{coll}^{cyl}/N_{coll}^{circ}$ takes on a limiting value of ∼0.31 when computed in the far-field. The expectation then is that for large angles the angular distribution will deviate from cosine and take on a value of $I_{\theta=90^o}^{evap} \approx 0.31 I_{\theta=0^o}^{evap}$ for the signal intensity. Allowing for the transition from viewing the flat sheet to viewing the cylindrical rims at large angles for a model our typical experimental geometry results in the blue curve in Figure 6.12c, which follows the black $\cos\theta$ curve until large angles. This distribution agrees strikingly well the the measured experimental data, which deviate from the cosine shape at about the same angle as this model, and for which the signal drops to a very similar value of 0.32 ± 0.03 relative to the $\theta = 0^o$ measurements across the datasets showcased in this chapter.

6.5 Discussion

Evaporation dynamics have been measured for both cylindrical and flat jets of the volatile liquids dodecane and water, for which the arrival time and angular distributions were determined. For dodecane experiments the arrival time and angular distributions agree very well with expectations for thermal desorption. In contrast, when water jets are used the significant vapor pressure leads to severe distortions in the arrival time distribution, but species with smaller collision cross-sections than the H_2O-H_2O pair appear to maintain signatures of their desorption angular distribution.

The data collected for cylindrical jets are found to agree very well with previous measurements taken on comparable jets in other research groups.[300,310,311] As expected for a cylindrically symmetric jet, the underlying angular distribution of desorbing particles cannot be measured from such surfaces. The very good agreement of the data with simulated Maxwellian speed distributions corresponding to the measured liquid jet temperatures suggest that for jets of volatile liquids ∼30 μm in diameter the collision numbers are not very large, in agreement with collision models, and there is no particular reason to believe that the underlying angular distribution should not be cosine.

To verify this, and to assess the feasibility of evaporation and scattering experiments from liquid flat jets placed in a high-vacuum environment, various evaporation measurements from volatile flat jets were undertaken. For water and dodecane jets both the neat liquids as well as dissolved noble gases were measured. Dodecane experiments were very successful, and dodecane has proven to be an accessible and convenient flat jet system to operate. Although effective collision cross-sections with all gases are much larger for dodecane owing to its large molecular size, the low vapor pressures achievable with this solvent appear to be sufficient to mostly compensate for this. Data for both dodecane and dissolved neon show generally good agreement with Maxwellian time-of-flight simulations and with cosine angular distributions. The fact that even the dodecane TOF spectra, subject to the influence

of dodecane-dodecane collisions and the large cross-section for this scattering pair, do not show extreme perturbations bodes well for evaporation and scattering experiments on a large variety of both non-reactive and reactive systems using atoms and small molecules. In comparison to lighter species dissolved in the dodecane, or for future experiments involving supersonic beam scattering, the dodecane peaks are slow and broad enough that they should be readily distinguishable in any time-of-flight spectra.

Water flat jets are much more difficult to operate, since their high vapor pressure leads to extensive evaporative cooling, resulting in a tendency to freeze when the liquid jet is perturbed. Despite the substantial vapor load they introduce, careful considerations regarding vacuum pumping and liquid pre-cooling allow for the attainment of high-vacuum conditions where the ambient mean free path is large relative to the apparatus components. Nevertheless, collisions above the surface of the liquid flat jets between pairs of evaporating particles are extensive, and in extreme cases lead to enormous changes in both the arrival time and angular distributions.

Previous indications from experiments using cylindrical microjets and wetted wheels of volatile liquids that these collisions result in a supersonic expansion-type acceleration of the gas flow are confirmed in the water jet measurements herein. The smaller Ar-H_2O cross-section compared to H_2O-H_2O has allowed experiments using water cylindrical microjets to better fit the argon TOF spectrum to a Maxwellian distribution, forming the basis for argon thermometry measurements of the jet temperature.[52,314] However, the argon data collected here actually disagree with their Maxwellian simulations more so than do the water spectra. Argon atoms experiencing the high collision numbers in our measurements take on a supersonic speed distribution characterized by a flow velocity and "beam" temperature very close to those of the much lighter water molecules in which they are effectively seeded.

Although desorbing particles intrinsically have a directional preference already favoring the surface normal direction, it is hard to imagine that a mere 10-30 collisions for H_2O-H_2O and Ar-H_2O could result in such a significant acceleration of the speed distribution. This calls into question the validity of the $\sim$30 Å^2 effective cross-section used to model collision numbers for these gas pairs. The much larger H_2O-H_2O cross-section of 320 Å^2 determined by crossed molecular beams scattering would lead instead to $\sim$300 collisions during evaporation,[315] which would seem to be qualitatively more in line with the measured TOF spectra.

Yet the underlying cosine angular distribution for argon seems to be surprisingly well-preserved despite the distortion of its arrival time distribution. The angular distribution for argon is perhaps slightly stretched vertically relative to the liquid surface. Since particles traveling along the surface normal vector should be more numerous than those traveling at other angle relative to the surface, this effect on the distribution would be at least consistent with a picture where collisions are more likely on average to transfer momentum along the surface normal vector. The heavier distortion to the water angular distribution makes it hard to definitively validate this, since it is not at all clear how the distribution should be scaled in the angular plots.

At least some preservation of the angular distributions for the water jet data has important implications for future evaporation and scattering experiments. For example, a major

dynamical pathway observed in scattering from other liquid surfaces is trapping-desorption, where an incident particle is accommodated by the surface, thermalizes with it, and then evaporates.[316] For complete thermalization the particle will lose all memory of its initial state and desorb according to a cosine distribution. However, partial thermalization processes retain some information of the initial state of the particle. It is possible that using the arrival time and angular distributions in concert will enable features of these distributions to be correlated to identify instances of partial thermalization.

Regardless of the volatility of the solvent, the geometry of flat jets involve the presence of bounding cylindrical rims that obscure the jet surface at very large angles. Although a geometric model has succeeded in rationalizing the influence this has on the angular distributions, large angles fundamentally contain contributions from both flat and cylindrical surfaces that will likely be impossible to disentangle. Future scattering experiments at these extreme angles are thus also unlikely to be successful. Nevertheless, for large flat jets of a few millimeters in size this does not become a significant problem until about $75 - 80^o$, providing a very large range over which to assess features of the angular distributions for interactions at the surfaces of flat jets.

An outstanding question from these studies is the cause of the very slow TOF spectra collected at $\theta = 90^o$. In the absence of extensive vapor-phase collisions, evaporation studies almost universally show arrival time distributions peaked significantly more slowly than expected (e.g. see Figure 6.4 for a clear example), often to a significant degree. Best fit Maxwellian simulations to these slower peaks usually result in temperatures in the range of about 230-260 K, which does not correspond to a realistic temperature for any object in the vacuum chamber. Since the flat jet rims are essentially just very large-diameter cylindrical jets, it is not clear why diminutive cylindrical jets give very good agreement with Maxwellian simulations at the liquid temperature while flat jet rims do not. The only major difference expected between the flat jet rim and the 30 μm cylindrical jet is a higher collision number for the former. Based on measurements for $\theta < 90^o$ this would be expected to have the opposite effect on the TOF spectra from what is observed. Experiments are currently being undertaken to explore this effect in greater detail, and to determine whether it is a true dynamical effect of the jet rims or rather is caused by some aspect of the experimental geometry.

6.6 Conclusions

The arrival time and angular distributions have been measured for evaporation from cylindrical and flat jets of the volatile liquids dodecane and water. Evaporation measurements were collected for both the neat liquid as well as for noble gases dissolved into the liquids. The dodecane vapor pressure is just low enough to allow a significant fraction of particles to evaporate without undergoing vapor-phase collisions above the surface. For neat water, the vapor pressure is so high that all data were substantially distorted compared to Maxwellian expectations, and are described much better by the expression for a supersonic expansion than that for thermal desorption. The conventional wisdom of placing beam skimmers very close to

the liquid jet surface to suppress vapor-phase collisions is shown to be incorrect for jets of the size considered here, where the very high vapor density of molecules such as water overwhelm the skimmer and erase dynamical signatures of the liquid surface. Particles evaporating from all flat jets here undergo at least a moderate number of collisions. Importantly, it was found in the case of argon evaporating from water flat jets that significant distortions can exist in the arrival time distribution while still preserving the underlying angular distribution. This has important implications for future measurements of evaporation and for trapping-desorption pathways in scattering experiments. However, the data collected for water itself show that at some point the underlying angular distribution for emission is destroyed if the vapor-phase collisions are numerous enough.

Chapter 7

Scattering at the Liquid-Vacuum Interface

Abstract

The primary goal of the liquid jet modifications to Machine B is to enable scattering experiments at the liquid-vacuum interface. This has been a monumental task for the volatile liquids of interest to our laboratory. While still in their infancy at the time of writing, this chapter discusses the progress made towards this goal to date. The scattering apparatus was first tested using a solid section of a Si (100) wafer for various incident energies, with higher collision energies leading to more pronounced specular peaks in the angular distribution. A preliminary time-of-flight spectrum for scattering of a supersonic helium beam from the surface of a neat water flat jet has provided the first hints at the feasibility of this challenging experiment.

7.1 Introduction

Atomic and molecular scattering experiments from liquid surfaces have historically been hampered by the many challenges associated with preparing samples of many interesting liquids inside a high-vacuum environment. Over several decades of technological innovations, such experiments are finally becoming routinely accessible for a broad range of interesting liquid targets. The work taking place today on scattering from aqueous and organic surfaces is building our understanding of the fundamental physical and chemical dynamics taking place during gas-liquid collisions in terms of the scattering mechanisms, energy transfer, and reactivity. It is also enabling detailed, quantum state-resolved experiments on chemical reactions governing the fate of aerosol particles in the atmosphere, and for liquid films which form naturally over objects.

The early literature on liquid surface scattering is extremely sparse. In what is very likely the first experiment of its kind, effusive beams of Ar and N_2 were found to produce angular patterns of a diffuse character from molten gallium and indium metal surfaces.[317] Many years later, the low-volatility polyol molecule glycerol was subject to collisions of atomic argon beams at thermal and hyperthermal energies.[318] The former resulted in cosine angular emission, while the high-energy beam showed a pronounced specular peak in the angular distribution. Around the same time, energy and angular resolved scattering experiments of ^{3}He and ^{4}He from 30 mK liquid ^{4}He surfaces found the van der Waals potential outside the liquid surface dominated the scattering dynamics, which depended only on the perpendicular momentum during surface collisions.[319,320]

Energy transfer during collisions between various gas-liquid pairs has been broadly studied previously. Atomic and molecular collisions with perfluoropolyether (PFPE) and the large hydrocarbon squalane ($C_{30}H_{62}$) find the degree of energy transfer to the surface increases as the effective surface mass decreases, and the lighter CH_3 groups of squalane extract energy more efficiently from the incident gas particles than the CF_3 surface of PFPE, resulting in higher trapping probabilities.[321] Scattering into larger deflection angles also imparts energy to the surface more effectively than for grazing collisions.[322] Similar results were found for I_2 colliding with these same liquids.[323] Increasing liquid temperatures were also found to increase trapping probabilities, attributed to roughening of the surface, leading to a greater likelihood of multiple collisions occurring, each of which has the potential to trap the gas particle.[34]

The development of wetted wheels by Fenn,[48] and later liquid microjets by Faubel,[49] allowed liquids with higher vapor pressures, including pure liquid water and small hydrocarbons, to be studied.[324] Azeotropic (98.5 %) sulfuric acid represented a productive target for studying the uptake and reactive scattering of neutral acids and organic small molecules.[325,326] The sticking and reaction probability follow the expected trends when inspecting the basicity of the projectile and considering its susceptibility to protonation by H_2SO_4. A recent reactive scattering study of OD radical at squalane (an alkane) and squalene (an alkene) surfaces showed differences in energy-dependent reactivity with important implications for modeling similar reactions in atmospheric chemistry.[327] Lower collision energies with the alkene surface

yielded more H-abstraction, while the equivalent reaction with the alkane was found to be independent of collision energy.

This chapter covers the preliminary surface scattering experiments conducted in our lab. The scattering capabilities of our apparatus are subjected to an initial test using a section of a silicon (100) wafer. A helium supersonic atomic beam is then directed at the surface of a flat jet of pure liquid water and the scattered signal measured. While still in their early infancy, these initial results appear to be promising regarding the feasibility of future liquid flat jet scattering experiments.

7.2 Experimental

Scattering experiments were undertaken using the modified crossed molecular beam apparatus with a rotatable detector as described previously.[11] Scattering targets were the surface of a section of Si (100) wafer and a neat liquid water flat jet. Liquid flat jets were produced by pressurizing the liquid using an Agilent 1260 Infinity II high-performance liquid chromatography (HPLC) pump and directing it through micrometer-scale channels within a glass microfluidics chip[97] mounted in the vacuum chamber. Liquid pressures were typically 25-50 bar corresponding to flow rates 2.5-3.5 mL/min for flat jets.

To make scattering experiments feasible, it is crucial to reduce the vapor pressure of volatile liquids as much as possible. Liquids are first pre-cooled by a counter-current heat-exchanger spanning the vacuum chamber wall before entering the liquid jet nozzle. Water is typically cooled to 1-2 °C ($P_{vap} \approx 5$ Torr). Further cooling then takes place via evaporation once the liquid jet is exposed to the vacuum environment in the scattering chamber. A conical beryllium copper catcher[307] with a narrow through-hole is used to collect the flat jet at the node where the fluid sheet recombines. This liquid drains into a differentially pumped reservoir held at $\sim$ 0.2-2 Torr. The catcher is heated when using water jets to prevent freezing of supercooled liquid inside the catcher. With typical water flat jets, the catcher is able to maintain a temperature of 10-15 °C and is able to maintain water in the liquid state. A 1 m^2 liquid nitrogen-cooled copper coldshield reduces the ambient pressure in the scattering chamber to 4–12 $\times$ 10^{-6} Torr during operation of the liquid jets, resulting in a nominal mean free path on the order of several meters. In reality a large pressure gradient will necessarily be established across the chamber, since pressure must vary smoothly from the vacuum level measured by the ion gauge to the vapor pressure of the liquid just above its surface.

A supersonic atomic He beam is produced using a piezoelectric pulsed valve. In these experiments, the stagnation region behind the valve is filled with helium gas at a pressure of 1-4 bar. The atomic beam is collimated by a pair of 0.5–1 mm conical beam skimmers before entering the main scattering chamber. Particles in the beam impinge onto the liquid jet and can either stick to or scatter from the surface. For liquid flat jets having flow velocities of 10's of meters per second, particles which stick must desorb within about 5-50 μs or they will be carried out of view of the detector.

Detection of scattered particles occurs in the plane defined by the detector rotation and perpendicular to the jet flow axis. Cations are produced using an electron impact ionizer nested within three differentially pumped regions and operated at 80 eV.[135] Ions are mass selected using a quadrupole filter and detected with a Daly style ion detector.[85] The velocity distribution of the incident and scattered particles was characterized using a slotted spinning chopper wheel inserted between the scattering target and the detector aperture. Incident He beams had a velocity of 1760 m/s with speed ratios, defined as the beam velocity divided by the spread in velocities, of 15-20. A multichannel scalar collected and binned the ion signal as a function of arrival time, producing time-of-flight (TOF) spectra. The TOF spectra were collected as a function of detector angle θ relative to the surface normal.

7.3 Results

The scattering configuration was tested by inserting the Si (100) wafer section into the liquid jet chip holder. The silicon was exposed to supersonic beams of pure Ar, Ar (10 %) seeded in He, and N_2 (10 %) seeded in He. This resulted in scattered signal collected for $m/z = 4$ (He^+), $m/z = 28$ (N_2^+), and $m/z = 40$ (Ar^+) across a range of scattering angles. The comparison of the pure Ar beam and the Ar seeded in He allow us to compare "low" and "high" collision energies with the surface. The TOF spectra for the slow Ar beam are dominated by broad and slow peaks, and the angular distribution agrees well with a cosine distribution. For faster particles seeded in He beams, the angular distribution has a pronounced peak at the specular angle, as expected for recoil from a smooth and rigid surface.[39,328]

The high vapor pressure of water makes scattering experiments from these flat jets a significant challenge. Preliminary evidence confirming the feasibility of this type of experiment is shown in Figure 7.1, where a supersonic beam of He atoms scattered from a liquid water flat jet. The He atoms were incident onto the jet with $\theta_{inc} = 60^o$ with respect to the surface normal, and were measured at the corresponding specular angle. The center-of-mass collision energy in this case was 0.71 kcal/mol based on the incident kinetic energy of the He atoms and the assumption of a surface which is stationary with respect to the collision timescale. The incident beam profile is peaked at 117 μs and is fairly narrow, with a speed ratio of ~10 leading to a FWHM of ~20 μs. The scattered signal has an essentially identical rise time to the incident beam, but is greatly broadened. The scattered peak is centered around an arrival time of about 130 μs, with a FWHM of ~40 μs. If the profile of the incident beam is subtracted off, the remaining signal can be approximated by a gaussian profile centered at 140 μs arrival time. The poor signal-to-noise ratio in this spectrum makes it difficult to perform a more sophisticated analysis.

If the measured spectrum only contains the two contributions described above, they occur in roughly equal proportions. A 140 μs peak arrival time corresponds to a helium atom speed of ~1500 m/s. With an incident translational energy of 0.71 kcal/mol for the He beam, the slower scattered signal corresponds to about 0.17 kcal/mol transferred to the surface, corresponding to a fractional energy transfer $\Delta E/E_{inc}$ of about 24 %.

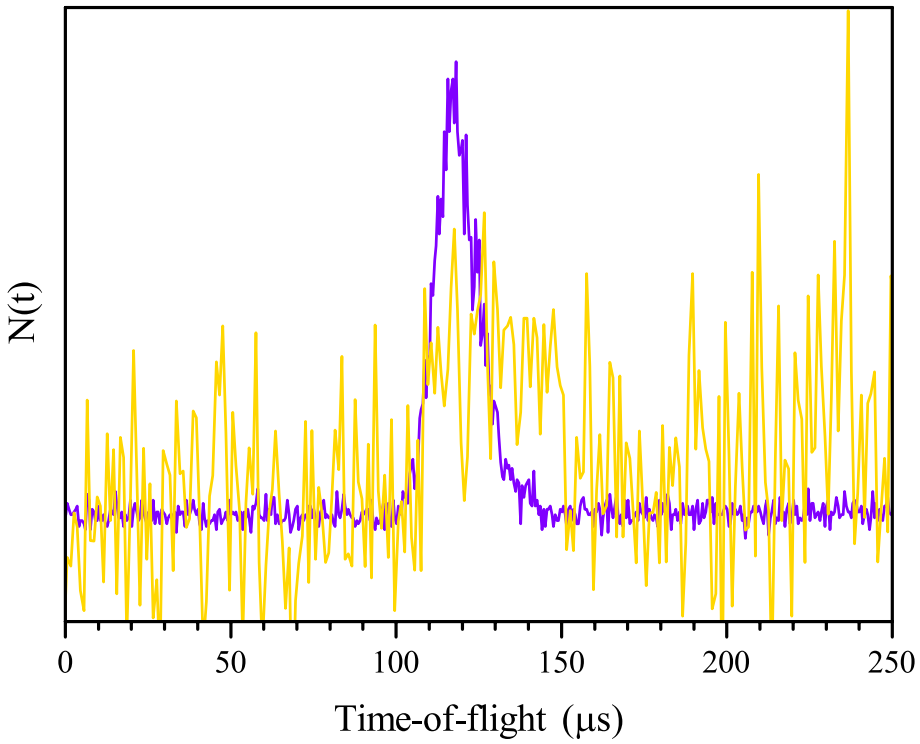

Figure 7.1: Specular scattering of supersonic He atoms incident at $\theta_{inc} = 60^o$ from a flat jet of neat H_2O, collected at $\theta_{scat} = 60^o$. The purple trace is the profile of the incident beam admitted into the detector by the chopper wheel, while the yellow is the scattered signal when the jet is inserted into the beam path. Relative signal intensities are not to scale.

7.4 Analysis

In the limiting case of perfectly elastic scattering, the arrival time distribution for scattered signal should match the profile of the incident molecular beam, described by

$$N(t) \propto \left(\frac{L}{t}\right)^2 \exp\left[-S^2\left(\frac{L/t - V_o}{V_o}\right)^2\right] \tag{7.1}$$

for speed ratio S and beam flow velocity V_o. In the other limiting case, corresponding to surface accommodation, complete thermalization, and subsequent desorption, the flux-weighted Maxwellian distribution is instead expected

$$N(t) \propto \frac{L^3}{t^4} \exp\left[-\frac{m}{2k_B T_s}\frac{L^2}{t^2}\right] \tag{7.2}$$

for mass m, surface temperature T_s, and where k_B is Boltzmann's constant. It is often more likely for the scattering dynamics to occur somewhere in between these two extremes when the scattering is inelastic and the surface responds to the collision in a compliant and thus

dissipative manner. Intermediate distributions can always be described analytically using a sum of gaussian functions, although in general there is no fundamental dynamical information contained within the individual contributions.

For scattering from flat surfaces it is also possible to collect the angular distribution of the scattered particles. Desorption following surface trapping and thermalization is fundamentally equivalent to evaporation, and should be described by a $\cos\theta$ angular distribution with respect to the surface normal vector.[38,39] The specular, impulsive scattering mechanism is often taken to be a rotated and stretched cosine distribution of the form $\cos^n(\theta - \theta_s)$, where the distribution is vertically stretched according to the power n and rotated away from the surface normal by angle θ_s.

7.5 Discussion

Scattering from a silicon wafer provided a good test-case to validate the configuration of the instrument and the data analysis. The data from this system for various gas projectiles was in line with previous results of non-reactive scattering from solid surfaces. Very low collision energies lead to slow TOF spectra and broad, cosine angular distributions due to trapping and thermalization with the surface. For higher collision energies, the TOF spectra are instead dominated by fast peaks and angular distributions skewed and narrowed along the specular angle. These findings are in line with the transition from trapping-desorption to impulsive-type scattering expected for increasing collision energy, and with prior measurements for O_2 and N_2 scattering from Si (100).[329,330]

For the liquid water flat jet, scattering signal was observed for a supersonic He beam impinging on the jet surface. Unfortunately, the spectrum is of quite low quality, precluding a detailed analysis of the TOF features. This is likely in part due to collisions with the vapor cloud surrounding the jet, and in part due to technical limitations in the jet operation. The slow part of the TOF distribution can be described as arising from He atoms that transfer 24 % of their kinetic energy into the surface during the collision, broadly in line with findings for other liquid surface scattering experiments and calculations.[40,310,331]

Experiments are ongoing in the lab to ensure the jet is formed as close to 273 K as possible, and to test the results when the gas projectile is varied. Heavier particles will be less perturbed by collisions with the vapor cloud surrounding the jet, although they will also have larger cross-sections in general. However, evaporation experiments detailed in Chapter 6 indicate that even for the small argon atoms evaporating from water the collision number is possibly already on the order of several hundred. Promising candidates to explore include Ne, NO, and SF_6, with respective masses of 20, 30, and 146 amu. Similar experiments using liquid dodecane flat jets are also ongoing in the laboratory.

7.6 Conclusions

Scattering of He, Ar and N_2 from a silicon wafer demonstrated the capabilities of the scattering configuration of Machine B, and provided spectra which were useful in exploring data analysis techniques. Subsequent exposure of a pure water flat jet to a He beam produced a scattered TOF spectrum consistent with an average of $\sim$24 % kinetic energy transfer to the surface during approximately half of the total number of collisions probed in the TOF spectrum. It is felt that the modest scattered TOF spectrum collected for He colliding with a the surface of a pure liquid water flat jet represents a triumph of the last few years of effort. The door to the exciting future of molecular beam scattering from volatile liquid surfaces finally appears to be ajar.

Chapter 8

Prospective Roadmap for Liquid Jet Experiments

Abstract

This section reflects on the state of liquid jet evaporation and scattering experiments conducted thus far, considering the outstanding experimental challenges and suggesting possible ways to resolve them. The potential application of this apparatus to study more complex experiments at the surfaces of water and volatile organic liquids is described, ranging from fundamental chemical dynamics studies to reactions with relevance to heterogeneous atmospheric chemistry.

8.1 Current Challenges of Liquid Jet Experiments

An unresolved question involves the degree of cooling undergone by jets of very volatile liquids such as water. The flat liquid sheet has a large surface area to volume ratio and thus cools substantially while exposed to vacuum. The bounding rims contain a much greater proportion of the liquid, and cool at a slower rate because of their geometry and smaller surface area to volume ratio – they are essentially a pair of large cylindrical jets. Figure 1.7 demonstrates that for very volatile liquids the evaporative cooling is initially substantial, but then slows down as the liquid cools and the vapor pressure decreases. Although the first liquid sheet is about twice as big as the second one, it may be necessary to perform scattering experiments for particularly volatile liquids such as water by using the second sheet. The hope here rests on a twofold implication of cooling taking place within the first sheet. A large first sheet with a big surface area will facilitate a greater degree of cooling, dropping the temperature (and therefore the vapor pressure) as much as possible; a subtle factor in this cooling is that the jet cools specifically by evaporating. Hence, probing the first sheet may come with the challenge that the jet is actively cooling by shedding large numbers of molecules in the direct vicinity of the molecular beam target. Scattering from the second leaf potentially resolves both of these issues: if the evaporative cooling is sufficient in the first sheet then the liquid will form a second sheet at a very cold temperature with a correspondingly low vapor pressure; additionally, because alternating liquid sheets are oriented orthogonally with respect to one another, the cooling takes plane orthogonal to the second sheet being probed, and situated vertically above it. It is hoped that the scattering target is thus shielded from the large evaporative flux issued by the initial cooling of the first sheet.

Another issue with scattering experiments is the broad temporal profile of molecular beams produced using the current valve. Most of the beam is not being collected by the chopper wheel and is at best wasted, at worst actively complicating the collected TOF specta with large background signals. This is not a significant problem for photodissociation experiments since the undissociated beam simply passes by the detector, but with the liquid jet the entire beam will strike and recoil from it. This problem could be solved by using a valve that produces much narrower gas pulses, such as an Even-Lavie valve or the Amsterdam Piezovalve cantilever piezovalve capable of producing intense gas pulses with temporal profiles as short as 7 μs FWHM, and with speed ratios in excess of 100.[332,333] However, this is still not really ideal for the experimental geometry utilized for beam-jet scattering experiments since in general inelastic collisions with the surface should be commonplace. Characterization of the scattered velocity distribution requires a velocity selector to be inserted between the jet and detector, as currently implemented with the chopper wheel. Since this scattered velocity distribution is not known *a priori*, even for a narrow incident gas pulse it will be necessary to scan the time delay between the pulsed valve and chopper to collect the full scattered velocity distribution piecewise. This would be particularly burdensome for low signal-to-noise experiments or when the scattered velocity distribution is very broad.

A better solution may be to expose the liquid jet to a continuous molecular beam so that

the particle density impinging on the jet is no longer time-dependent. Every pass of the chopper slot in front of the detector would then admit a pulse of gas containing the entirety of the scattered distribution. The use of a pseudorandom chopper wheel and cross-correlation data deconvolution techniques[334,335] may also help with these experiments by allowing very high transmission through the wheel for many potentially low-signal reactive scattering experiments. This virtue has long been recognized for many gas-surface scattering and desorption experiments for solid surfaces, noted to suffer from low signal-to-noise ratios.[336]

Operation of a continuous molecular beam increases the gas load into the source chamber substantially, requiring modifications to the current chamber configuration to be feasible. At the least, an additional stage of differential pumping would probably need to be added between the pulsed valve and scattering chamber to prevent large main chamber background pressures of analyte species entrained in the beam. The positioning of the beam skimmers should also be re-evaluated to ensure the more prominent shock-wave structures formed at the higher source chamber pressure are not impeding the molecular beam, and that the skimmers are correctly sampling gas from within the 'zone-of-silence' region of the expansion.[10]

8.2 Future Evaporation Studies

The evaporation studies on Machine B have been a fairly fruitful endeavor that has allowed iterating on the design and capabilities of the apparatus for optimizing experiments with volatile liquid flat jets. There remain some unexplained features in the evaporation data which should be investigated further. There are also some interesting systems from which this experiment might provide some novel contributions to the scientific community.

The origin of the very cold arrival time distributions measured from the cylindrical rims of the jet are currently an unexplained phenomenon. In particular, one would expect that very narrow liquid jets should cool faster than larger ones, which require greater amounts of diffusive transport to sustain cooling. It is thus puzzling that the very narrow cylindrical jets agree well with Maxwellian simulations while the spectra from the flat jet rims are much colder. Perhaps the flow dynamics of the larger jets are such that the outer portions of the rim cool substantially while a much warmer inner core is maintained due to diffusive heat transfer limitations, as proposed for diminutive water droplets.[50] However, we currently have no definitive experimental or modeling evidence for this occurring in the flat jets. This also fails to explain such an observation for dodecane flat jets which undergo negligible cooling.

The moderate volatility of dodecane is sufficient to introduce large distortions to the arrival time distributions in some cases, and it would be helpful to benchmark various features of the data against an even less volatile system. At the time of writing a large volume of the sesquiterpene molecule farnesene ($C_{15}H_{24}$) has been delivered, having a vapor pressure of $\sim$1.5 mTorr at 298 K,[337] and which can be cooled down to 183 K before freezing to lower the vapor pressure even further.[338] It's viscosity is comparable to that of dodecane,[338,339] and should easily afford flat jets of farnesene with widely tunable vapor pressure. Evaporation studies

using farnesene should be illuminating with regards to the anomalous features exhibited in flat jet data collected to date.

The case of sub-Maxwellian and super-Maxwellian evaporation for very light gases is also interesting to explore using flat jets. Of particular interest would be a comparison of the evaporation dynamics of H_2, D_2, and He from water and dodecane. The evaporation model of Kann and Skinner relates the evaporation energy to the mass and interaction potential of the solute with the liquid.[299] Deviations from the flux-weighted value of $2RT$ are only expected for very light gases such as hydrogen and helium, and for heavy particles with small interaction potentials (which do not exist). This model predicts He atoms to exceed $2RT$ by a factor of 1.1-1.2, while 0.7-0.8 is the predicted factor for H_2 molecules, and both of which have been confirmed experimentally.[296–298,300] It would be interesting to extend this study to D_2, predicted to have a relative energy factor of $\sim$0.9 based on having the same mass as He and the same interaction potential as H_2. A similar experiment for ^{3}He would expect to find a relative factor of 1.0-1.1 based on this model, closer to Maxwellian than ^{4}He.

Finally, it would be worthwhile to investigate the evaporation dynamics of the NO molecule from the flat jets. During evaporation from 4-5 μm diameter water jets, laser-induced fluorescence measurements found the internal quantum state distribution of NO to be well described by thermal expectations, but for temperature significantly colder than the liquid, attributed to a combination of evaporative cooling and vapor-phase collisional cooling.[304] A model of the rotational temperature provided a best fit to the measured data for a very small effective collision cross-section for the NO-H_2O pair of only 13 Å^2. It would be advantageous to conduct experiments with a molecular system exhibiting such a small cross-section, and to observe whether the translational energy distribution is similarly supercooled.

8.3 Fundamental Reactive Scattering Studies

Aside from noble gas scattering experiments, it would also be interesting to study non-reactive scattering of molecules with more varied chemical interactions with water and dodecane, such as NH_3, CH_3OH, or CO_2. However, the ultimate goal of the flat jet experiment is to probe reactive scattering at the liquid interface.

As a former denizen of the Neumark group, I would be remiss in failing to champion the importance of studying the F + H_2O reaction at the surface of a water jet. The strong affinity of F radicals for H atoms imply that this reaction should proceed readily, forming the weak acid HF. The likelihood of HF desorption as a function of the collision energy, and how this varies for water compared to dodecane, is worth investigating. The equivalent H-abstraction reaction by OH radical does have important implications for atmospheric chemistry, and is discussed in the following section.

An interesting experiment from a fundamental perspective would probe whether collisions with a liquid surface are able to facilitate isomerization in an organic molecule such as 1-methylcyclobutene. Collisions of 1-methylcyclobutene with hot silica surfaces experienced

sufficient energy transfer to activate isomerization to isoprene.[340] While highly unlikely that the collision of a supersonic beam with an essentially ambient-temperature, compliant liquid surface would provide enough energy to induce this isomerization, it is intriguing to consider that the interaction dynamics at water surfaces may stabilize the transition state sufficiently to permit isoprene formation. Several examples of this type of catalytic behavior are described in the following sections.

8.4 Oxidation of Unsaturated Hydrocarbons

Terrestrial plants release a colossal variety hydrocarbon molecules into the atmosphere in huge abundance, which ultimately partake it both gas-phase and heterogeneous chemical reactions. Many of these molecules have unsaturated or otherwise functionalized carbon backbones. The most prominent example is the atmospherically relevant C_5H_8 isomer isoprene, and the (greatly) extended class of terpenoids derived from it, emitted by plants in large abundance.[341] Myriad alcohols and other oxygenated moieties are similarly admitted into the atmosphere.

Hydroxyl radical (OH) is produced throughout the upper troposhere where ozone photolysis liberates O atoms which in turn abstract H atoms from water, forming two OH radicals.[342] Although OH is only found in mixing ratios below the part per trillion level, this low abundance is precisely because their pronounced reactivity means that the majority of total atmospheric oxidation chemistry can be attributed to OH radicals. They are responsible for initiating many reactions of atmospheric hydrocarbons via abstraction of an H-atom or addition to alkene double bonds, typically leaving behind reactive radical species in both cases.

A very simple experiment would study the reaction of gas-phase OH with a liquid dodecane jet. The OH radical is readily afforded by ultraviolet photolysis of nitrous acid, HONO. Since the O–N bond in HONO is much weaker (49 kcal/mol bond energy)[343,344] than other bonds within this molecule, pyrolysis of HONO may be well-suited to yield large amounts of OH radical. The H_2O product of this abstraction reaction does not suffer from signal contamination at $m/z = 18$ since dodecane does not produce ion signal at this m/z during dissociative ionization. This could be compared to the dynamics of the same reaction with jets of water containing dodecane or other hydrocarbon species. Since H_2O is the product of the abstraction reaction, this experiment would almost certainly need to be conducted with OD radicals, producing HDO signal at $m/z = 19$ where the background from the liquid jet would be more manageable (though, as demonstrated herein, still very large). If the abstraction reaction occurs on the impulsive scattering timescale it will be much easier to observe, since the arrival time of the reactive scattering events will be shorter than the thermal evaporation signal due to the jet.

Another major oxidant in the atmosphere is ozone (O_3), for which the ozonolysis reaction with alkenes cleaves the double bond site and yields a ketone/aldehyde and a zwitterionic carbonyl oxide (the Criegee intermediate).[345,346] As an example, consider ozonolysis of the

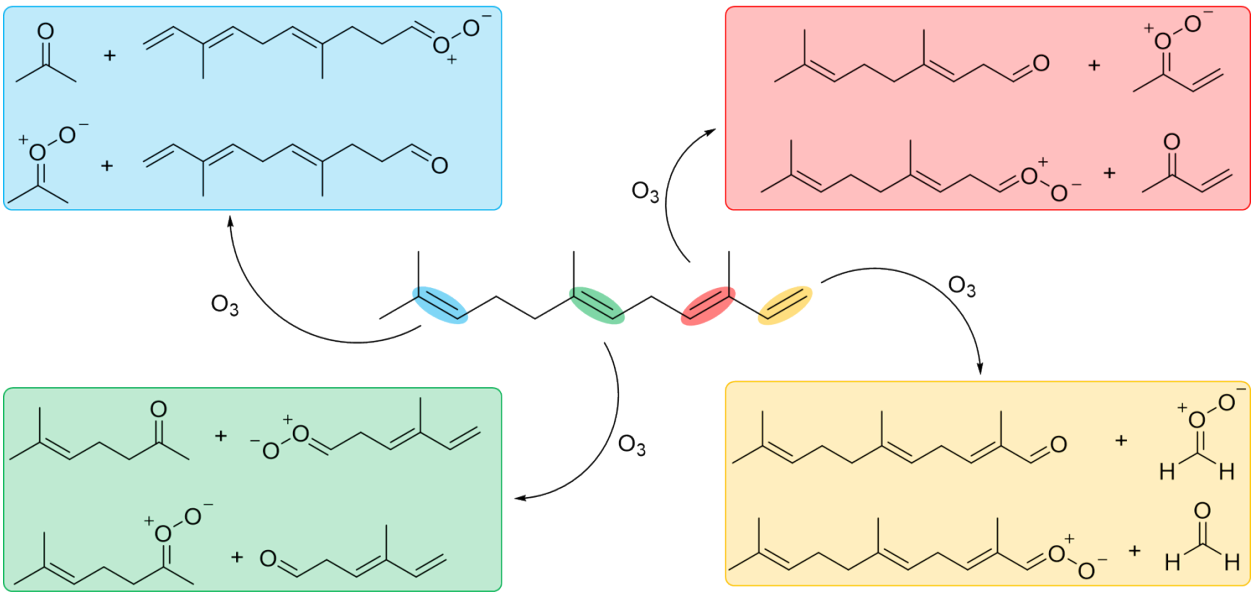

Figure 8.1: Possible products of the ozonolysis of farnesene. Two product pairs are possible for each double bond depending on how bond cleavage of the secondary ozonide intermediate proceeds.

sesquiterpene molecule farnesene, $C_{15}H_{24}$, discussed above and containing 4 carbon-carbon double bonds. The 16 possible ozonolysis products for farnesene are shown in Figure 8.1. These products have different parent m/z values, and the product channel branching may be measured by using low-energy electron ionization to suppress dissociative ionization. Such an experiment would represent a prototypical study of the dynamics of a fundamental atmospheric reaction taking place heterogeneously at the surface of an organic liquid. This reaction could also be used to probe the orientational population farnesene adopts at the liquid-vacuum interface for comparison with molecular dynamics simulations. The scattered signal of ozonolysis products will generally be proportional to a site-specific rate constant and the effective surface coverage of the different unsaturated sites. If the relative rate constants can be estimated using a statistical or quantum mechanical treatment then the scattered intensity distribution of different m/z values will carry information about the surface orientational distribution imprinted upon it.

8.5 Neutral Bond Hydration Reactions

A promising class of experiments amenable to study using Machine B is the neutral hydration of unsaturated bonds through vicinal addition of water. Good initial candidates for such an experiment are inorganic acid anhydrides relevant for atmospheric chemistry, such as the important gas sulfur trioxide, SO_3. The reaction of SO_3 with water in the

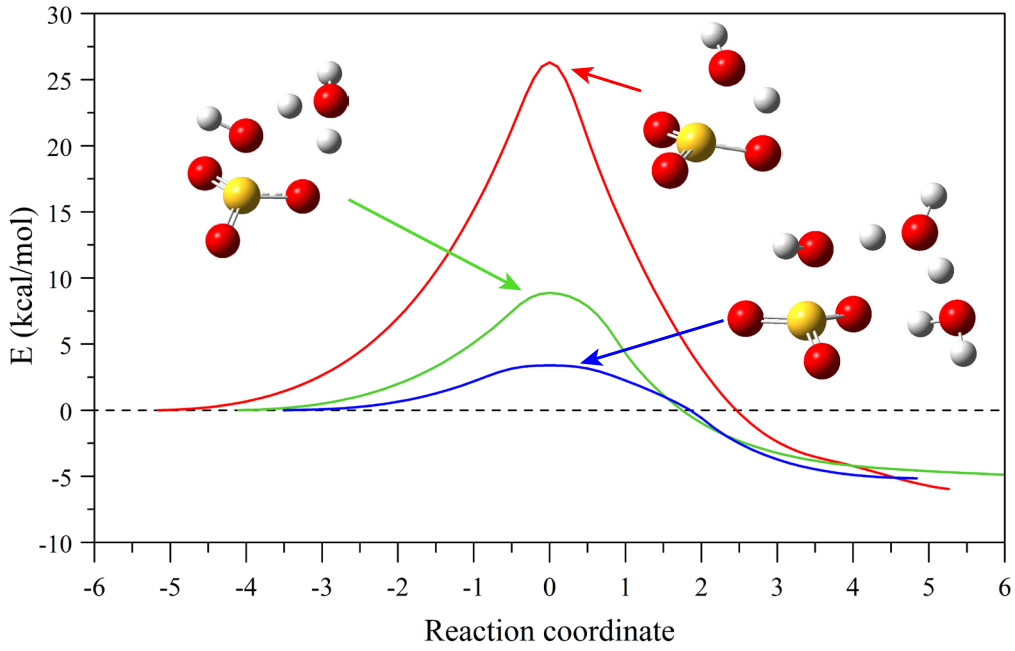

Figure 8.2: Intrinsic reaction coordinate for SO_3 + H_2O (red), SO_3 + $2H_2O$ (green), and SO_3 + $3H_2O$ (blue). Energies are shown relative to those of separated reactants (dashed line). Also shown are the transition state structures for each hydration reaction.

atmosphere leads to H_2SO_4, implicated as a leading cause of acidified aerosol particles and acid rain. An appealing feature of this reaction is that the reaction barrier for the bimolecular SO_3 + H_2O reaction is very high, at about ∼28 kcal/mol, whereas additional waters play a catalytic role on the reaction, lowering the reaction barrier substantially. Catalysis occurs through a concerted, synchronous H-transfer mechanism, where water molecules mediate the simultaneous transfer of H-atoms around the cyclic transition state. Figure 8.2 shows the intrinsic reaction coordinate for SO_3 + nH_2O → H_2SO_4 + (n-1)H_2O (n = 1-3) reactions, calculated at the B3LYP/6-31G+(d,p) level of theory. When two water molecules react with SO_3 the reaction barrier falls to 8.9 kcal/mol, while for three water molecules it is only 3.4 kcal/mol. These values agree well with previous calculations for the SO_3-H_2O system.[347]

Since the bimolecular SO_3 + H_2O reaction has such a large barrier it is very unlikely that any H_2SO_4 signal observed in an SO_3 scattering experiment could be attributed to gas-phase collisions. The detection of H_2SO_4 should then be an unambiguous probe of the hydration reaction occurring at the water-vacuum interface. A further practical benefit of such an experiment is that the product mass will be detected at m/z = M + 18 relative to the reactant species (m/z = 98 for $H_2SO_4^+$ vs. m/z = 80 for SO_3^+), producing TOF spectra free from the influence of daughter ions or of heavier isotopes. A similar situation prevails for N_2O_5 + H_2O → $2HNO_3$,[348] and may also be expected for N_2O_3 + H_2O → 2HONO.

Although one might expect a strong acid such as H_2SO_4 to dissociate completely in an aqueous environment, there is lengthy precedent for undissociated and neutral nitric acid,

HNO_3, existing at the surface of liquid water (see Ref. [349] and references therein), for which the molecular state represents a a sizeable fraction of nitric acid at the air-water interface. Moreover, its chemical and photochemical rate constants are enhanced, in some cases by orders of magnitude. Scattering experiments of HCl and DCl from cold, salty water also measure emission of neutral HCl and DCl from the liquid surface.[314] A similar enhancement by 2-3 orders of magnitude in the reaction rate between Criegee intermediates and water to form hydroxyalkyl hydroperoxide species at the air-water interface has been recently predicted.[350] The literature abounds with other examples of catalytic activity of water and reaction rate enhancements at liquid surfaces.

An interesting but somewhat esoteric reaction between *o*-benzyne and water to produce phenol could also be studied. A molecular beam of *o*-benzyne can be produced from the pyrolysis of benzoyl chloride, then react at the surface of a water jet according to

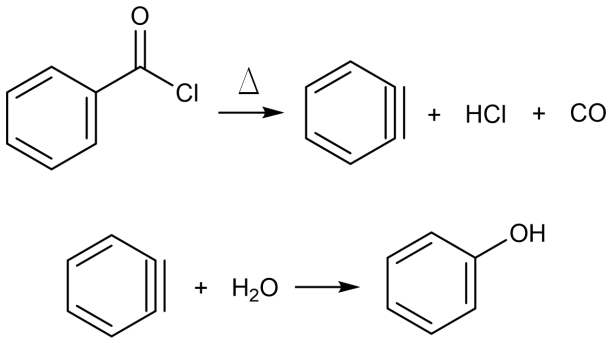

This reaction requires overcoming a substantial 15.2 kcal/mol energy barrier and is exothermic by 71.2 kcal/mol.[351] As in the case of SO_3, this barrier is too large to overcome for the bimolecular reaction in typical molecular beams. Catalytic stabilization of the transition state by water should lower this barrier significantly.

8.6 Conclusions

This chapter has described the major challenges currently facing liquid flat jet experiments, and the potential benefits of various improvements in the instrumentation and its configuration. A survey of candidate systems for scattering studies is laid out in rather broad strokes. The combined capabilities for measuring incident energy- and angular-resolved time-of-flight spectra for scattering from flat jets opens up many avenues for meaningful contribution to the field of chemical dynamics. It is the authors opinion that oxidation reactions of hydrocarbon jets and hydration reactions of acid anhydrides at the surface of water jets represent the most promising reactive scattering systems for immediate study, based on a combination of technical considerations and relevance to atmospheric chemistry.

Bibliography

[1] Boyle, R., *The Sceptical Chymist*; J. Cadwell, London: 1661.

[2] Dunoyer, L. "Sur la réalisation d'un rayonnement matériel d'origine purement thermique. Cinétique expérimentale" [On the realization of a material radiation of purely thermal origin. Experimental kinetics]. *Le Radium* **1911**, *8*, 142–146.

[3] Kallmann, H.; Reiche, F. "Über den Durchgang bewegter Moleküle durch inhomogene Kraftfelder" [On the passage of moving molecules through inhomogeneous force fields]. *Z. Phys.* **1921**, *6*, 352–375.

[4] Gerlach, W.; Stern, O. "Der experimentelle nachweis der richtungsquantelung im magnetfeld" [The experimental proof of directional quantization in the magnetic field]. *Z. Phys.* **1922**, *9*, 349–352.

[5] Van de Meerakker, S. Y.; Bethlem, H. L.; Vanhaecke, N.; Meijer, G. "Manipulation and control of molecular beams". *Chem. Rev.* **2012**, *112*, 4828–4878.

[6] Gordon, J. P.; Zeiger, H. J.; Townes, C. H. "Molecular microwave oscillator and new hyperfine structure in the microwave spectrum of NH_3". *Phys. Rev.* **1954**, *95*, 282.

[7] Gordon, J. P.; Zeiger, H. J.; Townes, C. H. "The maser – new type of microwave amplifier, frequency standard, and spectrometer". *Phys. Rev.* **1955**, *99*, 1264.

[8] Hostettler, H. U.; Bernstein, R. B. "Improved slotted disk type velocity selector for molecular beams". *Rev. Sci. Instrum.* **1960**, *31*, 872–877.

[9] Anderson, J.; Fenn, J. "Velocity distributions in molecular beams from nozzle sources". *Phys. Fluids* **1965**, *8*, 780–787.

[10] Scoles, G., *Atomic and molecular beam methods*; Oxford University Press: 1988.

[11] Lee, Y.; McDonald, J.; LeBreton, P.; Herschbach, D. "Molecular beam reactive scattering apparatus with electron bombardment detector". *Rev. Sci. Instrum.* **1969**, *40*, 1402–1408.

[12] Ohshima, Y.; Endo, Y. "Structure of C_3S studied by pulsed-discharge-nozzle Fourier-transform microwave spectroscopy". *J. Mol. Spectrosc.* **1992**, *153*, 627–634.

[13] Monts, D.; Dietz, T.; Duncan, M.; Smalley, R. "New vibronic bands of CH_2 observed in a pulsed supersonic jet". *Chem. Phys.* **1980**, *45*, 133–139.

[14] Kohn, D. W.; Clauberg, H.; Chen, P. "Flash pyrolysis nozzle for generation of radicals in a supersonic jet expansion". *Rev. Sci. Instrum.* **1992**, *63*, 4003–4005.

[15] Demtröder, W., *Molecular Physics: Theoretical Principles and Experimental Methods*; John Wiley & Sons, Weinheim: 2008.

[16] Harris, D. C.; Bertolucci, M. D., *Symmetry and Spectroscopy: An Introduction to Vibrational and Electronic Spectroscopy*; Dover, New York: 1989.

[17] Bright, F. V. "Modern molecular fluorescence spectroscopy". *Appl. Spectrosc.* **1995**, *49*, 14A–19A.

[18] Oref, I.; Tardy, D. "Energy transfer in highly excited large polyatomic molecules". *Chem. Rev.* **1990**, *90*, 1407–1445.

[19] Von Neumann, J.; Wigner, E. P. "Über das Verhalten von Eigenwerten bei adiabatischen Prozessen" [On the behavior of eigenvalues in adiabatic processes]. *Phys. Z.* **1929**, *30*, 467–470.

[20] Domcke, W.; Yarkony, D. R. "Role of conical intersections in molecular spectroscopy and photoinduced chemical dynamics". *Ann. Rev. Phys. Chem.* **2012**, *63*, 325–352.

[21] Uzer, T.; Miller, W. "Theories of intramolecular vibrational energy transfer". *Phys. Rep.* **1991**, *199*, 73–146.

[22] Nesbitt, D. J.; Field, R. W. "Vibrational energy flow in highly excited molecules: Role of intramolecular vibrational redistribution". *J. Phys. Chem.* **1996**, *100*, 12735–12756.

[23] Zhao, X. "Photodissociation of cyclic compounds in a molecular beam"., Ph.D. Thesis, University of California, Berkeley, 1989.

[24] Zare, R. N. "Photoejection dynamics". *Mol. Photochem.* **1972**, *4*, 1–37.

[25] Zhao, X.; Nathanson, G. M.; Lee, Y. T. "Modeling simulation of secondary processes in photofragment-translational spectroscopy". *Acta Phys.-Chim. Sin.* **1992**, *8*, 70–81.

[26] Molina, M. J.; Tso, T.-L.; Molina, L. T.; Wang, F. C.-Y. "Antarctic stratospheric chemistry of chlorine nitrate, hydrogen chloride, and ice: release of active chlorine". *Science* **1987**, *238*, 1253–1257.

[27] Weber, M.; Coldewey-Egbers, M.; Fioletov, V. E.; Frith, S. M.; Wild, J. D.; Burrows, J. P.; Long, C. S.; Loyola, D. "Total ozone trends from 1979 to 2016 derived from five merged observational datasets – the emergence into ozone recovery". *Atmos. Chem. Phys.* **2018**, *18*, 2097–2117.

[28] Wang, J.; Cieplak, P.; Kollman, P. A. "How well does a restrained electrostatic potential (RESP) model perform in calculating conformational energies of organic and biological molecules?" *J. Comput. Chem.* **2000**, *21*, 1049–1074.

[29] Shao, Y.; Gan, Z.; Epifanovsky, E.; Gilbert, A. T.; Wormit, M.; Kussmann, J.; Lange, A. W.; Behn, A.; Deng, J.; Feng, X., et al. "Advances in molecular quantum chemistry contained in the Q-Chem 4 program package". *Mol. Phys.* **2015**, *113*, 184–215.

[30] Gibbs, J. W. "On the equilibrium of heterogeneous substances". *Am. J. Sci.* **1878**, *16*, 441.

[31] Butt, H.-J.; Graf, K.; Kappl, M. In *Physics and Chemistry of Interfaces*; Wiley-VCH Verlag GmbH & Co. KGaA, Weinheim: 2003; Chapter "Thermodynamics of interfaces".

[32] Willard, A. P.; Chandler, D. "Instantaneous liquid interfaces". *J. Phys. Chem. B* **2010**, *114*, 1954–1958.

[33] King, M. E.; Saecker, M. E.; Nathanson, G. M. "The thermal roughening of liquid surfaces and its effect on gas–liquid collisions". *J. Chem. Phys.* **1994**, *101*, 2539–2547.

[34] King, M. E.; Fiehrer, K. M.; Nathanson, G. M.; Minton, T. K. "Effects of thermal roughening on the angular distributions of trapping and scattering in gas–liquid collisions". *J. Phys. Chem. A* **1997**, *101*, 6556–6561.

[35] Chang, T.-M.; Dang, L. X. "Liquid-vapor interface of methanol-water mixtures: a molecular dynamics study". *J. Phys. Chem. B* **2005**, *109*, 5759–5765.

[36] Donaldson, D.; Vaida, V. "The influence of organic films at the air – aqueous boundary on atmospheric processes". *Chem. Rev.* **2006**, *106*, 1445–1461.

[37] Gantt, B.; Meskhidze, N. "The physical and chemical characteristics of marine primary organic aerosol: a review". *Atmos. Chem. Phys.* **2013**, *13*, 3979–3996.

[38] Comsa, G.; David, R. "Dynamical parameters of desorbing molecules". *Surf. Sci. Rep.* **1985**, *5*, 145–198.

[39] Goodman, F. O., *Dynamics of Gas-Surface Scattering*; Academic Press, New York: 1976.

[40] Saecker, M. E.; Nathanson, G. M. "Collisions of protic and aprotic gases with hydrogen bonding and hydrocarbon liquids". *J. Chem. Phys.* **1993**, *99*, 7056–7075.

[41] Dupuy, R.; Richter, C.; Winter, B.; Meijer, G.; Schlögl, R.; Bluhm, H. "Core level photoelectron spectroscopy of heterogeneous reactions at liquid–vapor interfaces: current status, challenges, and prospects". *J. Chem. Phys.* **2021**, *154*, 060901.

[42] Baule, B. "Theoretische Behandlung der Erscheinungen in verdünnten Gasen" [Theoretical treatment of phenomena in rarefied gases]. *Ann. Physik* **1914**, *349*, 145–176.

[43] Alexander, W. A.; Zhang, J.; Murray, V. J.; Nathanson, G. M.; Minton, T. K. "Kinematics and dynamics of atomic-beam scattering on liquid and self-assembled monolayer surfaces". *Faraday Discuss.* **2012**, *157*, 355–374.

[44] Cardillo, M. J. "Gas-surface interactions studied with molecular beam techniques". *Ann. Rev. Phys. Chem.* **1981**, *32*, 331–357.

[45] Tesa-Serrate, M. A.; Marshall, B. C.; Smoll Jr, E. J.; Purcell, S. M.; Costen, M. L.; Slattery, J. M.; Minton, T. K.; McKendrick, K. G. "Ionic liquid–vacuum interfaces probed by reactive atom scattering: influence of alkyl chain length and anion volume". *J. Phys. Chem. C* **2015**, *119*, 5491–5505.

[46] Zutz, A.; Nesbitt, D. J. "Angle-resolved molecular beam scattering of NO at the gas-liquid interface". *J. Chem. Phys.* **2017**, *147*, 054704.

[47] Zutz, A.; Peterson, K. A.; Nesbitt, D. J. "Nonadiabatic dynamics at the gas–molten metal interface: State-to-state resolved scattering of NO from hot gallium (600–1000 K)". *J. Phys. Chem. C* **2020**.

[48] Lednovich, S. L.; Fenn, J. B. "Absolute evaporation rates for some polar and nonpolar liquids". *AIChE J.* **1977**, *23*, 454–459.

[49] Faubel, M.; Schlemmer, S.; Toennies, J. "A molecular beam study of the evaporation of water from a liquid jet". *Z. Phys. D: Atom. Mol. Cl.* **1988**, *10*, 269–277.

[50] Smith, J. D.; Cappa, C. D.; Drisdell, W. S.; Cohen, R. C.; Saykally, R. J. "Raman thermometry measurements of free evaporation from liquid water droplets". *J. Am. Chem. Soc.* **2006**, *128*, 12892–12898.

[51] Daniel DePonte, Private communication.

[52] Faust, J. A.; Nathanson, G. M. "Microjets and coated wheels: versatile tools for exploring collisions and reactions at gas–liquid interfaces". *Chem. Soc. Rev.* **2016**, *45*, 3609–3620.

[53] Savart, F. "Mémoire sur le choc de deux veines liquides animeés de mouvements directement opposés [Dissertation on the shock of two liquid veins animated by directly opposite movement]". *Ann. Chim. Phys.* **1833**, *55*, 257–310.

[54] Runge, P.; Rosenberg, R. "Unconfined flowing-dye films for CW dye lasers". *IEEE J. Quantum Elect.* **1972**, *8*, 910–911.

[55] Watanabe, A.; Saito, H.; Ishida, Y.; Nakamoto, M.; Yajima, T. "A new nozzle producing ultrathin liquid sheets for femtosecond pulse dye lasers". *Opt. Commun.* **1989**, *71*, 301–304.

[56] Lefebvre, A. H., *Atomization and sprays*; Hemisphere, New York: 1989.

[57] Makhnenko, I.; Alonzi, E. R.; Fredericks, S. A.; Colby, C. M.; Dutcher, C. S. "A review of liquid sheet breakup: perspectives from agricultural sprays". *J. Aerosol Sci.* **2021**, 105805.

[58] Ekimova, M.; Quevedo, W.; Faubel, M.; Wernet, P.; Nibbering, E. T. "A liquid flatjet system for solution phase soft-x-ray spectroscopy". *Struct. Dyn.* **2015**, *2*, 054301.

[59] Taylor, G. "Formation of thin flat sheets of water". *Proc. R. Soc. Lon. Ser.-A* **1961**, *259*, 1–17.

[60] Ha, B.; DePonte, D. P.; Santiago, J. G., et al. "Device design and flow scaling for liquid sheet jets". *Phys. Rev. Fluids* **2018**, *3*, 114202.

[61] Bush, J. W.; Hasha, A. E. "On the collision of laminar jets: fluid chains and fishbones". *J. Fluid Mech.* **2004**, *511*, 285–310.

[62] Plateau, J. A. F., *Statique expérimentale et théorique des liquides soumis aux seules forces moléculaires [Experimental and theoretical statics of liquids subjected to molecular forces alone]*; Gauthier-Villars, Paris: 1873; Vol. 2.

[63] Lord Rayleigh, "On the instability of a cylinder of viscous liquid under capillary force". *Philos. Mag. S.* **1892**, *34*, 145–154.

[64] Chandrasekhar, S., *Hydrodynamic and Hydromagnetic Stability*; Clarendon, Oxford: 1961.

[65] Eggers, J.; Villermaux, E. "Physics of liquid jets". *Rep. Prog. Phys.* **2008**, *71*, 036601.

[66] Van Hoeve, W.; Gekle, S.; Snoeijer, J. H.; Versluis, M.; Brenner, M. P.; Lohse, D. "Breakup of diminutive Rayleigh jets". *Phys. Fluids* **2010**, *22*, 122003.

[67] Sisoev, G.; Osiptsov, A.; Koroteev, A. "On the instability of a liquid sheet moving in vacuum". *Phys. Fluids* **2018**, *30*, 032106.

[68] Wine, P. H.; Nicovich, J. M. In *Encyclopedia of Radicals in Chemistry, Biology and Materials*, Chatgilialoglu, C., Studer, A., Eds.; John Wiley & Sons: 2012; Chapter "Atmospheric radical chemistry".

[69] Pernice, H.; Garcia, P.; Willner, H.; Francisco, J. S.; Mills, F. P.; Allen, M.; Yung, Y. L. "Laboratory evidence for a key intermediate in the Venus atmosphere: peroxychloroformyl radical". *P. Natl. Acad. Sci.* **2004**, *101*, 14007–14010.

[70] Hébrard, E.; Dobrijevic, M.; Bénilan, Y.; Raulin, F. "Photochemical kinetics uncertainties in modeling Titan's atmosphere: a review". *J. Photoch. Photobio. C - Photochem. Rev.* **2006**, *7*, 211–230.

[71] Summers, M. E.; Strobel, D. F. "Photochemistry and vertical transport in Io's atmosphere and ionosphere". *Icarus* **1996**, *120*, 290–316.

[72] Tielens, A. G., *The Physics and Chemistry of the Interstellar Medium*; Cambridge University Press, New York: 2005.

[73] Zhao, L.; Kaiser, R. I.; Lu, W.; Xu, B.; Ahmed, M.; Morozov, A. N.; Mebel, A. M.; Howlader, A. H.; Wnuk, S. F. "Molecular mass growth through ring expansion in polycyclic aromatic hydrocarbons via radical–radical reactions". *Nat. Commun.* **2019**, *10*, 1–7.

[74] Simmie, J. M. "Detailed chemical kinetic models for the combustion of hydrocarbon fuels". *Prog. Energ. Combust.* **2003**, *29*, 599–634.

[75] Law, C. K., *Combustion Physics*; Cambridge University Press, New York: 2010.

[76] Zádor, J.; Taatjes, C. A.; Fernandes, R. X. "Kinetics of elementary reactions in low-temperature autoignition chemistry". *Prog. Energ. Combust.* **2011**, *37*, 371–421.

[77] Zeng, J.; Cao, L.; Xu, M.; Zhu, T.; Zhang, J. Z. "Complex reaction processes in combustion unraveled by neural network-based molecular dynamics simulation". *Nat. Commun.* **2020**, *11*, 1–9.

[78] Smit, C.; Swaaij, R. v.; Hamers, E.; Sanden, M. v. d. "The role of the silyl radical in plasma deposition of microcrystalline silicon". *J. Appl. Phys.* **2004**, *96*, 4076–4083.

[79] Carrier, W.; Zheng, W.; Osamura, Y.; Kaiser, R. I. "First infrared spectroscopic characterization of digermyl (Ge_2H_5) and d5-digermyl (Ge_2D_5) radicals in low temperature germane matrices". *Chem. Phys.* **2006**, *325*, 499–508.

[80] Longenecker, J. G.; Mebel, A. M.; Kaiser, R. I. "First infrared spectroscopic detection of the monobridged diboranyl radical (B_2H_5, C_{2v}) and its D5-isotopomer in low-temperature diborane ices". *Inorg. Chem.* **2007**, *46*, 5739–5743.

[81] McLean, B.; Webber, G. B.; Page, A. J. "Boron nitride nucleation mechanism during chemical vapor deposition". *J. Phys. Chem. C* **2018**, *122*, 24341–24349.

[82] Lee, Y. T. "Molecular beam studies of elementary chemical processes (Nobel lecture)". *Angew. Chem. Int. Edit.* **1987**, *26*, 939–951.

[83] Cole-Filipiak, N. "Production and Photodissociation of Neutral Free Radicals"., Ph.D. Thesis, University of California, Berkeley, 2015.

[84] Casavecchia, P.; Leonori, F.; Balucani, N.; Petrucci, R.; Capozza, G.; Segoloni, E. "Probing the dynamics of polyatomic multichannel elementary reactions by crossed molecular beam experiments with soft electron-ionization mass spectrometric detection". *Phys. Chem. Chem. Phys.* **2009**, *11*, 46–65.

[85] Daly, N. "Scintillation type mass spectrometer ion detector". *Rev. Sci. Instrum.* **1960**, *31*, 264–267.

[86] Haefer, R. "On the pumping speed of large area cryopumps". *Vacuum* **1980**, *30*, 19–22.

[87] OPTEK, *Photologic slotted optical switch: OPB920, OPB970, OPB980, and OPB990 series.*, Carrollton, Texas: 2008.

[88] Negru, B. "Photodissociation Dynamics of Neutral Free Radicals"., Ph.D. Thesis, University of California, Berkeley, 2012.

[89] Batt, L.; Milne, R. "Pyrolysis of alkyl nitrites (RONO)". *Int. J. Chem. Kinet.* **1974**, *6*, 945–949.

[90] Scheer, A. M.; Mukarakate, C.; Robichaud, D. J.; Ellison, G. B.; Nimlos, M. R. "Radical chemistry in the thermal decomposition of anisole and deuterated anisoles: an investigation of aromatic growth". *J. Phys. Chem. A* **2010**, *114*, 9043–9056.

[91] Cole-Filipiak, N. C.; Shapero, M.; Negru, B.; Neumark, D. M. "Revisiting the photodissociation dynamics of the phenyl radical". *J. Chem. Phys.* **2014**, *141*, 104307.

[92] Welz, O.; Savee, J. D.; Osborn, D. L.; Vasu, S. S.; Percival, C. J.; Shallcross, D. E.; Taatjes, C. A. "Direct kinetic measurements of Criegee intermediate (CH_2OO) formed by reaction of CH_2I with O_2". *Science* **2012**, *335*, 204–207.

[93] Roessler, C. G.; Agarwal, R.; Allaire, M.; Alonso-Mori, R.; Andi, B.; Bachega, J. F.; Bommer, M.; Brewster, A. S.; Browne, M. C.; Chatterjee, R., et al. "Acoustic injectors for drop-on-demand serial femtosecond crystallography". *Structure* **2016**, *24*, 631–640.

[94] Vakili, M.; Vasireddi, R.; Gwozdz, P. V.; Monteiro, D. C.; Heymann, M.; Blick, R. H.; Trebbin, M. "Microfluidic polyimide gas dynamic virtual nozzles for serial crystallography". *Rev. Sci. Instrum.* **2020**, *91*, 085108.

[95] Galinis, G.; Strucka, J.; Barnard, J. C.; Braun, A.; Smith, R. A.; Marangos, J. P. "Micrometer-thickness liquid sheet jets flowing in vacuum". *Rev. Sci. Instrum.* **2017**, *88*, 083117.

[96] Nazari, R.; Zaare, S.; Alvarez, R. C.; Karpos, K.; Engelman, T.; Madsen, C.; Nelson, G.; Spence, J. C.; Weierstall, U.; Adrian, R. J., et al. "3D printing of gas-dynamic virtual nozzles and optical characterization of high-speed microjets". *Opt. Express* **2020**, *28*, 21749–21765.

[97] Koralek, J. D.; Kim, J. B.; Brůža, P.; Curry, C. B.; Chen, Z.; Bechtel, H. A.; Cordones, A. A.; Sperling, P.; Toleikis, S.; Kern, J. F., et al. "Generation and characterization of ultrathin free-flowing liquid sheets". *Nat. Commun.* **2018**, *9*, 1–8.

[98] Ventura, D. A.; Nikelly, J. G. "Pulse dampening system for high pressure liquid chromatography". *Anal. Chem.* **1978**, *50*, 1017–1018.

[99] Polino, D.; Famulari, A.; Cavallotti, C. "Analysis of the reactivity on the C_7H_6 potential energy surface". *J Phys. Chem. A* **2011**, *115*, 7928–7936.

[100] Yuan, W.; Li, Y.; Dagaut, P.; Yang, J.; Qi, F. "Investigation on the pyrolysis and oxidation of toluene over a wide range conditions. I. Flow reactor pyrolysis and jet stirred reactor oxidation". *Combust. Flame* **2015**, *162*, 3–21.

[101] Yuan, W.; Li, Y.; Dagaut, P.; Yang, J.; Qi, F. "Investigation on the pyrolysis and oxidation of toluene over a wide range conditions. II. A comprehensive kinetic modeling study". *Combust. Flame* **2015**, *162*, 22–40.

[102] Zhang, T.; Zhang, L.; Hong, X.; Zhang, K.; Qi, F.; Law, C. K.; Ye, T.; Zhao, P.; Chen, Y. "An experimental and theoretical study of toluene pyrolysis with tunable synchrotron VUV photoionization and molecular-beam mass spectrometry". *Combust. Flame* **2009**, *156*, 2071–2083.

[103] Braun-Unkhoff, M.; Frank, P.; Just, T. "High temperature reactions of benzyl radicals". *Berichte der Bunsengesellschaft* **1990**, *94*, 1417–1425.

[104] Oehlschlaeger, M. A.; Davidson, D. F.; Hanson, R. K. "High-Temperature Thermal Decomposition of Benzyl Radicals". *J Phys. Chem. A* **2006**, *110*, 6649–6653.

[105] Shapero, M.; Cole-Filipiak, N. C.; Haibach-Morris, C.; Neumark, D. M. "Benzyl radical photodissociation dynamics at 248 nm". *J Phys. Chem. A* **2015**, *119*, 12349–12356.

[106] Hedaya, E.; Kent, M. "Flash vacuum pyrolysis. VIII. 1, 2-Indandione. A source of fulvenallene and some of its isomers". *J. Am. Chem. Soc.* **1970**, *92*, 2149–2151.

[107] Schissel, P.; Kent, M.; McAdoo, D. J.; Hedaya, E. "Flash vacuum pyrolysis. VII. Fulvenallene. The ring contraction and expansion of phenylcarbene". *J. Am. Chem. Soc.* **1970**, *92*, 2147–2149.

[108] Angell, C. "The vapor-phase infrared spectrum and structure of fulvenallene". *J. Mol. Struct.* **1971**, *10*, 265–273.

[109] Sakaizumi, T.; Katoh, F.; Ohashi, O.; Yamaguchi, I. "The microwave spectra of fulvenallene and its deuterated species". *J. Mol. Spectrosc.* **1993**, *159*, 112–121.

[110] Wentrup, C.; Wentrup-Byrne, E.; Müller, P. "Automerization in vinylidenecyclopentadiene and phenylcarbene". *J. Chem. Soc., Chem. Commun.* **1977**, 210–211.

[111] Hafner, K. "Novel pentafulvenes-versatile building blocks in π-perimeter chemistry". *Pure Appl. Chem.* **1990**, *62*, 531–540.

[112] Lindner, H. J.; Hafner, K. "Solid state dimerization of a 5-vinylidene-cyclopentadiene". *Mol. Cryst. Liq. Cryst. Sci. Technol., Sect. A* **1996**, *276*, 339–348.

[113] Thapa, J.; Spencer, M.; Akhmedov, N. G.; Goulay, F. "Kinetics of the OH radical reaction with fulvenallene from 298 to 450 K". *J. Phys. Chem. Lett.* **2015**, *6*, 4997–5001.

[114] Botter, R.; Jullien, J.; Pechine, J.; Piade, J.; Solgadi, D. "Ionization potentials of unstable species: Photoelectron spectrum of fulvenallene". *J. Electron Spectrosc. Relat. Phenom.* **1978**, *13*, 141–143.

[115] Müller, C.; Schweig, A.; Thiel, W.; Grahn, W.; Bergman, R. G.; Vollhardt, K. P. C. "Theory and application of photoelectron spectroscopy. 80. Photoelectron spectra of 2, 5-dehydrotropylidene, 3, 6-dehydrooxepin, and fulvenallene". *J. Am. Chem. Soc.* **1979**, *101*, 5579–5581.

[116] Steinbauer, M.; Hemberger, P.; Fischer, I.; Bodi, A. "Photoionization of C_7H_6 and C_7H_5: observation of the fulvenallenyl radical". *ChemPhysChem* **2011**, *12*, 1795–1797.

[117] Polino, D.; Cavallotti, C. "Fulvenallene decomposition kinetics". *J Phys. Chem. A* **2011**, *115*, 10281–10289.

[118] Giegerich, J.; Fischer, I. "Photodissociation dynamics of fulvenallene, C_7H_6". *Phys. Chem. Chem. Phys.* **2013**, *15*, 13162–13168.

[119] Da Silva, G.; Bozzelli, J. W. "The C_7H_5 fulvenallenyl radical as a combustion intermediate: Potential new pathways to two-and three-ring PAHs". *J. Phys. Chem. A* **2009**, *113*, 12045–12048.

[120] Chakraborty, A.; Fulara, J.; Maier, J. P. "The electronic spectrum of the fulvenallenyl radical". *Angew. Chem., Int. Ed. Engl.* **2016**, *128*, 236–239.

[121] Da Silva, G.; Trevitt, A. J. "Chemically activated reactions on the C_7H_5 energy surface: propargyl + diacetylene, i-C_5H_3 + acetylene, and n-C_5H_3 + acetylene". *Phys. Chem. Chem. Phys.* **2011**, *13*, 8940–8952.

[122] Zwier, T. S.; Allen, M. "Metastable diacetylene reactions as routes to large hydrocarbons in Titan's atmosphere". *Icarus* **1996**, *123*, 578–583.

[123] Wong, A.-S.; Yung, Y. L.; Friedson, A. J. "Benzene and haze formation in the polar atmosphere of Jupiter". *Geophys. Res. Lett.* **2003**, *30*.

[124] Lavvas, P.; Coustenis, A.; Vardavas, I. "Coupling photochemistry with haze formation in Titan's atmosphere, Part II: Results and validation with Cassini/Huygens data". *Planet. Space Sci.* **2008**, *56*, 67–99.

[125] Meadows, V. S.; Orton, G.; Line, M.; Liang, M.-C.; Yung, Y. L.; Van Cleve, J.; Burgdorf, M. J. "First Spitzer observations of Neptune: Detection of new hydrocarbons". *Icarus* **2008**, *197*, 585–589.

[126] Maranzana, A.; Indarto, A.; Ghigo, G.; Tonachini, G. "First carbon ring closures started by the combustive radical addition of propargyl to butadiyne. A theoretical study". *Combust. Flame* **2013**, *160*, 2333–2342.

[127] Da Silva, G. "Reaction of benzene with atomic carbon: Pathways to fulvenallene and the fulvenallenyl radical in extraterrestrial atmospheres and the interstellar medium". *J. Phys. Chem. A* **2014**, *118*, 3967–3972.

[128] Zhao, L.; Yang, T.; Kaiser, R. I.; Troy, T. P.; Xu, B.; Ahmed, M.; Alarcon, J.; Belisario-Lara, D.; Mebel, A. M.; Zhang, Y., et al. "A vacuum ultraviolet photoionization study on high-temperature decomposition of JP-10 (exo-tetrahydrodicyclopentadiene)". *Phys. Chem. Chem. Phys.* **2017**, *19*, 15780–15807.

[129] Da Silva, G.; Trevitt, A. J.; Steinbauer, M.; Hemberger, P. "Pyrolysis of fulvenallene (C_7H_6) and fulvenallenyl (C_7H_5): Theoretical kinetics and experimental product detection". *Chem. Phys. Lett.* **2011**, *517*, 144–148.

[130] Da Silva, G.; Cole, J. A.; Bozzelli, J. W. "Kinetics of the cyclopentadienyl + acetylene, fulvenallene + H, and 1-ethynylcyclopentadiene + H reactions". *J. Phys. Chem. A* **2010**, *114*, 2275–2283.

[131] Derudi, M.; Polino, D.; Cavallotti, C. "Toluene and benzyl decomposition mechanisms: Elementary reactions and kinetic simulations". *Phys. Chem. Chem. Phys.* **2011**, *13*, 21308–21318.

[132] Spangler, R. J.; Kim, J. H. "The pyrolysis of homophthalic anhydride. Simple synthesis of benzocyclobutenone and fulveneallene". *Tetrahedron Lett.* **1972**, *13*, 1249–1251.

[133] Negru, B.; Goncher, S. J.; Brunsvold, A. L.; Just, G. M.; Park, D.; Neumark, D. M. "Photodissociation dynamics of the phenyl radical via photofragment translational spectroscopy". *J. Chem. Phys.* **2010**, *133*, 074302.

[134] Negru, B.; Just, G. M.; Park, D.; Neumark, D. M. "Photodissociation dynamics of the *tert*-butyl radical *via* photofragment translational spectroscopy at 248 nm". *Phys. Chem. Chem. Phys.* **2011**, *13*, 8180–8185.

[135] Kuhnke, K.; Kern, K.; David, R.; Comsa, G. "High efficiency molecular-beam ionization detector with short ionization region". *Rev. Sci. Instrum.* **1994**, *65*, 3458–3465.

[136] Harich, S. A. PHOTRAN, a program for forward convolution analysis of photodissociation, 2003.

[137] CMLAB2, version 6/93, modified by J. D. Myers. This is an interactive version built on the original cmlab2 program: Zhao, X. PhD Dissertation, University of California, 1988.

[138] Frisch, M. J.; Trucks, G. W.; Schlegel, H. B.; Scuseria, G. E.; Robb, M. A.; Cheeseman, J. R.; Scalmani, G.; Barone, V.; Mennucci, B.; Petersson, G. A.; Nakatsuji, H.; Caricato, M.; Li, X.; Hratchian, H. P.; Izmaylov, A. F.; Bloino, J.; Zheng, G.; Sonnenberg, J. L.; Hada, M.; Ehara, M.; Toyota, K.; Fukuda, R.; Hasegawa, J.; Ishida, M.; Nakajima, T.; Honda, Y.; Kitao, O.; Nakai, H.; Vreven, T.; Montgomery Jr., J. A.; Peralta, J. E.; Ogliaro, F.; Bearpark, M.; Heyd, J. J.; Brothers, E.; Kudin, K. N.; Staroverov, V. N.; Kobayashi, R.; Normand, J.; Raghavachari, K.; Rendell, A.; Burant, J. C.; Iyengar, S. S.; Tomasi, J.; Cossi, M.; Rega, N.; Millam, J. M.; Klene, M.; Knox, J. E.; Cross, J. B.; Bakken, V.; Adamo, C.; Jaramillo, J.; Gomperts, R.; Stratmann, R. E.; Yazyev, O.; Austin, A. J.; Cammi, R.; Pomelli, C.; Ochterski, J. W.; Martin, R. L.; Morokuma, K.; Zakrzewski, V. G.; Voth, G. A.; Salvador, P.; Dannenberg, J. J.; Dapprich, S.; Daniels, A. D.; ö. Farkas; Foresman, J. B.; Ortiz, J. V.; Cioslowski, J.; Fox, D. J. Gaussian 09 Revision E.01., Gaussian Inc. Wallingford CT 2009.

[139] Caricato, M.; Trucks, G. W.; Frisch, M. J.; Wiberg, K. B. "Oscillator strength: How does TDDFT compare to EOM-CCSD?" *J. Chem. Theory Comput.* **2011**, *7*, 456–466.

[140] Miura, M.; Aoki, Y.; Champagne, B. "Assessment of time-dependent density functional schemes for computing the oscillator strengths of benzene, phenol, aniline, and fluorobenzene". *J. Chem. Phys.* **2007**, *127*, 084103.

[141] Marcus, R. A.; Rice, O. "The kinetics of the recombination of methyl radicals and iodine atoms". *J. Phys. Chem.* **1951**, *55*, 894–908.

[142] Beyer, T.; Swinehart, D. F. "Algorithm 448: Number of Multiply-Restricted Partitions". *Commun. ACM* **1973**, *16*, 379.

[143] Astholz, D. C.; Troe, J.; Wieters, W. "Unimolecular processes in vibrationally highly excited cycloheptatrienes. I. Thermal isomerization in shock waves". *J. Chem. Phys.* **1979**, *70*, 5107–5116.

[144] Karas, A. J.; Gilbert, R. G.; Collins, M. A. "Rigorous derivation of reaction path degeneracy in transition state theory". *Chem. Phys. Lett.* **1992**, *193*, 181–184.

[145] Levine, R. D.; Bernstein, R. B. "Energy disposal and energy consumption in elementary chemical reactions: the information theoretic approach". *Acc. Chem. Res.* **1974**, *7*, 393–400.

[146] Fitch, W. L.; Sauter, A. D. "Calculation of relative electron impact total ionization cross sections for organic molecules". *Anal. Chem.* **1983**, *55*, 832–835.

[147] Zhou, Z.; Xue, W. "Manganese-catalyzed oxidative homo-coupling of aryl Grignard chlorides". *J. Organomet. Chem.* **2009**, *694*, 599–603.

[148] S. E. Stein, Director, NIST Mass Spec Data Center, "Mass Spectra", in *NIST Chemistry WebBook, NIST Standard Reference Database Number 69*, ed. P. J. Linstrom and W. G. Mallard, National Institute of Standards and Technology, Gaithersburg MD, http://webbook.nist.gov, p. 20899.

[149] Robinson, J. C.; Sveum, N. E.; Goncher, S. J.; Neumark, D. M. "Photofragment translational spectroscopy of allene, propyne, and propyne-d_3 at 193 nm". *Mol. Phys.* **2005**, *103*, 1765–1783.

[150] Yang, B.; Huang, C.; Wei, L.; Wang, J.; Sheng, L.; Zhang, Y.; Qi, F.; Zheng, W.; Li, W.-K. "Identification of isomeric C_5H_3 and C_5H_5 free radicals in flame with tunable synchrotron photoionization". *Chem. Phys. Lett.* **2006**, *423*, 321–326.

[151] Gu, X.; Guo, Y.; Kaiser, R. I. "Mass spectra of the 2,4-pentadiynylidyne (C_5H; $X^2\Pi$) and 2,4-pentadiynyl-1 (n-C_5H_3; X^2B_1) radicals". *Int. J. Mass Spectrom.* **2007**, *261*, 100–107.

[152] Kato, S.; Morokuma, K. "Potential energy characteristics and energy partitioning in chemical reactions: *Ab initio* MO study of four-centered elimination reaction $CH_3CH_2F \rightarrow CH_2{=}CH_2 + HF$". *J. Chem. Phys.* **1980**, *73*, 3900–3914.

[153] Hilborn, R. C. "Einstein coefficients, cross sections, f values, dipole moments, and all that". *Am. J. Phys.* **1982**, *50*, 982–986.

[154] Graedel, T. "The homogeneous chemistry of atmospheric sulfur". *Rev. Geophys.* **1977**, *15*, 421–428.

[155] Tyndall, G. S.; Ravishankara, A. "Atmospheric oxidation of reduced sulfur species". *Int. J. Chem. Kinet.* **1991**, *23*, 483–527.

[156] Andreae, M. O. "Ocean-atmosphere interactions in the global biogeochemical sulfur cycle". *Mar. Chem.* **1990**, *30*, 1–29.

[157] Stefels, J. "Physiological aspects of the production and conversion of DMSP in marine algae and higher plants". *J. Sea Res.* **2000**, *43*, 183–197.

[158] Kiene, R. P.; Linn, L. J.; Bruton, J. A. "New and important roles for DMSP in marine microbial communities". *J. Sea Res.* **2000**, *43*, 209–224.

[159] Otte, M. L.; Wilson, G.; Morris, J. T.; Moran, B. M. "Dimethylsulphoniopropionate (DMSP) and related compounds in higher plants". *J. Exp. Bot.* **2004**, *55*, 1919–1925.

[160] Schulz, S.; Dickschat, J. S. "Bacterial volatiles: The smell of small organisms". *Nat. Prod. Rep.* **2007**, *24*, 814–842.

[161] Dominé, F.; Ravishankara, A.; Howard, C. J. "Kinetics and mechanisms of the reactions of methylthio, methylsulfinyl, and methyldithio radicals with ozone at 300 K and low pressures". *J. Phys. Chem.* **1992**, *96*, 2171–2178.

[162] Berresheim, H.; Eisele, F.; Tanner, D.; McInnes, L.; Ramsey-Bell, D.; Covert, D. "Atmospheric sulfur chemistry and cloud condensation nuclei (CCN) concentrations over the northeastern Pacific coast". *J. Geophys. Res-Atmos.* **1993**, *98*, 12701–12711.

[163] Andreae, M. O.; Elbert, W.; de Mora, S. J. "Biogenic sulfur emissions and aerosols over the tropical South Atlantic: 3. Atmospheric dimethylsulfide, aerosols and cloud condensation nuclei". *J. Geophys. Res-Atmos.* **1995**, *100*, 11335–11356.

[164] Borissenko, D.; Kukui, A.; Laverdet, G.; Le Bras, G. "Experimental study of SO_2 formation in the reactions of CH_3SO radical with NO_2 and O_3 in relation with the atmospheric oxidation mechanism of dimethyl sulfide". *J. Phys. Chem. A* **2003**, *107*, 1155–1161.

[165] Barnes, I.; Hjorth, J.; Mihalopoulos, N. "Dimethyl sulfide and dimethyl sulfoxide and their oxidation in the atmosphere". *Chem. Rev.* **2006**, *106*, 940–975.

[166] Moses, J. I.; Zolotov, M. Y.; Fegley Jr, B. "Photochemistry of a volcanically driven atmosphere on Io: Sulfur and oxygen species from a Pele-type eruption". *Icarus* **2002**, *156*, 76–106.

[167] Wong, M. H.; Mahaffy, P. R.; Atreya, S. K.; Niemann, H. B.; Owen, T. C. "Updated Galileo probe mass spectrometer measurements of carbon, oxygen, nitrogen, and sulfur on Jupiter". *Icarus* **2004**, *171*, 153–170.

[168] Zhang, X.; Liang, M. C.; Mills, F. P.; Belyaev, D. A.; Yung, Y. L. "Sulfur chemistry in the middle atmosphere of Venus". *Icarus* **2012**, *217*, 714–739.

[169] Irwin, P. G.; Toledo, D.; Garland, R.; Teanby, N. A.; Fletcher, L. N.; Orton, G. A.; Bézard, B. "Detection of hydrogen sulfide above the clouds in Uranus's atmosphere". *Nature Astronomy* **2018**, *2*, 420–427.

[170] Nishikida, K.; Williams, F. "Angular dependence of proton hyperfine splittings in the electron spin resonance spectrum of the methylsulfinyl radical". *J. Am. Chem. Soc.* **1974**, *96*, 4781–4784.

[171] Howard, J. "The electron spin resonance spectrum of $(CH_3)_3{}^{13}COO$". *Can. J. Chem.* **1979**, *57*, 253–254.

[172] Sagstuen, E.; Jørgensen, J.-P.; Henriksen, T. "The structure of sulfur radicals. An ESR study of irradiated sulfur-containing purines and pyrimidines". *Radiat. Res.* **1982**, *89*, 453–467.

[173] Swarts, S. G.; Becker, D.; DeBolt, S.; Sevilla, M. D. "Electron spin resonance investigation of the structure and formation of sulfinyl radicals: reaction of peroxyl radicals with thiols". *J. Phys. Chem.* **1989**, *93*, 155–161.

[174] Wetmore, S. D.; Eriksson, L. A.; Boyd, R. J. "The calculation of accurate ^{17}O hyperfine coupling constants in the hydroxyl radical: A difficult problem for current quantum chemical methods". *J. Chem. Phys.* **1998**, *109*, 9451–9462.

[175] Aplincourt, P.; Ruiz–López, M. F.; Assfeld, X.; Bohr, F. "Structure of isolated and solvated peroxyl radicals". *J. Comput. Chem.* **1999**, *20*, 1039–1048.

[176] Bellamy, L.; Conduit, C.; Pace, R.; Williams, R. "Infra-red spectra and solvent effects. Part 5. Solvent effects on X=O dipoles and on rotational isomers". *T. Faraday Soc.* **1959**, *55*, 1677–1683.

[177] Chen, M.; Yang, R.; Ma, R.; Zhou, M. "Infrared spectra of the sulfenic ester CH_3SOCH_3 and its photodissociation products in solid argon". *J. Phys. Chem. A* **2008**, *112*, 7157–7161.

[178] Chu, L.-K.; Lee, Y.-P. "Transient infrared spectra of CH_3SOO and CH_3SO observed with a step-scan Fourier-transform spectrometer". *J. Chem. Phys.* **2010**, *133*, 184303.

[179] Reisenauer, H. P.; Romański, J.; Mlostoń, G.; Schreiner, P. R. "Matrix isolation and spectroscopic properties of the methylsulfinyl radical $CH_3(O)S^{\bullet}$". *Chem. Commun.* **2013**, *49*, 9467–9469.

[180] Estep, M. L.; Schaefer III, H. F. "The methylsulfinyl radical CH_3SO examined". *Phys. Chem. Chem. Phys.* **2016**, *18*, 22293–22299.

[181] Hung, W.-C.; Shen, M.-y.; Lee, Y.-P.; Wang, N.-S.; Cheng, B.-M. "Photoionization spectra and ionization thresholds of CH_3SO, CH_3SOH, and $CH_3SS(O)CH_3$". *J. Chem. Phys.* **1996**, *105*, 7402–7411.

[182] Cheng, B.-M.; Chew, E. P.; Hung, W.-C.; Eberhard, J.; Lee, Y.-P. "Photoionization studies of sulfur radicals and products of their reactions". *J. Synchrotron Radiat.* **1998**, *5*, 1041–1043.

[183] Dominé, F.; Murrells, T. P.; Howard, C. J. "Kinetics of the reactions of nitrogen dioxide with CH_3S, CH_3SO, CH_3SS, and CH_3SSO at 297 K and 1 Torr". *J. Phys. Chem.* **1990**, *94*, 5839–5847.

[184] Kukui, A.; Bossoutrot, V.; Laverdet, G.; Le Bras, G. "Mechanism of the reaction of CH_3SO with NO_2 in relation to atmospheric oxidation of dimethyl sulfide: experimental and theoretical study". *J. Phys. Chem. A* **2000**, *104*.

[185] Reisenauer, H. P.; Romański, J.; Mlostoń, G.; Schreiner, P. R. "Reactions of the methylsulfinyl radical [$CH_3(O)S^{\bullet}$] with oxygen ($^3O_2$) in solid argon". *Chem. Commun.* **2015**, *51*, 10022–10025.

[186] Li, X.-Y.; Meng, L.-P.; Zheng, S.-J. "Theoretical studies on reaction mechanism of CH_3SO with NO". *Chinese J. Chem.* **2007**, *25*, 1480–1485.

[187] Li, X.; Meng, L.; Sun, Z.; Zheng, S. "Computational study on the reactions of XO (X = F, Cl and Br) with CH_3SO and CH_3SO_2". *J. Mol. Struct.: THEOCHEM* **2008**, *870*, 53–60.

[188] Li, X.; Meng, L.; Zheng, S. "Theoretical studies on SO_x (x = 1–3) formation in the reaction of CH_3SO radical with O_3". *J. Mol. Struct.: THEOCHEM* **2007**, *847*, 52–58.

[189] Li, Z.; Li, H.; Liu, Y.; Shi, X.; Tang, H. "Weak interaction between CH_3SO and HOCl: hydrogen bond, chlorine bond and oxygen bond". *Chinese Sci. Bull.* **2009**, *54*, 3014–3022.

[190] Tušar, S.; Lesar, A. "H-bonded $CH_3SO/H_2SO_4/H_2O$ complexes: Quantum chemical study". *Acta Chim. Slov.* **2015**, *62*, 565–573.

[191] Li, X.; Fan, H.; Meng, L.; Zeng, Y.; Zheng, S. "Theoretical investigation on stability and isomerizations of CH_3SO isomers". *J. Phys. Chem. A* **2007**, *111*, 2343–2350.

[192] Zhao, H.-Q.; Cheung, Y.-S.; Heck, D.; Ng, C.; Tetzlaff, T.; Jenks, W. "A 193-nm-laser photofragmentation time-of-flight mass spectrometric study of dimethylsulfoxide". *J. Chem. Phys.* **1997**, *106*, 86–93.

[193] Blank, D. A.; North, S. W.; Stranges, D.; Suits, A. G.; Lee, Y. T. "Unraveling the dissociation of dimethyl sulfoxide following absorption at 193 nm". *J. Chem. Phys.* **1997**, *106*, 539–550.

[194] Rudolph, R.; North, S. W.; Hall, G. E.; Sears, T. J. "Diode laser measurements of CD_3 quantum yields and internal energy for the dissociation of dimethyl sulfoxide-d_6". *J. Chem. Phys.* **1997**, *106*, 1346–1352.

[195] Thorson, G. M.; Cheatum, C. M.; Coffey, M. J.; Fleming Crim, F. "Photofragment energy distributions and dissociation pathways in dimethyl sulfoxide". *J. Chem. Phys.* **1999**, *110*, 10843–10849.

[196] Ho, J.-W.; Chen, W.-K.; Cheng, P.-Y. "A direct observation of a concerted two-bond breaking reaction". *J. Am. Chem. Soc.* **2007**, *129*, 3784–3785.

[197] Cole-Filipiak, N. C.; Shapero, M.; Haibach-Morris, C.; Neumark, D. M. "Production and photodissociation of the methyl perthiyl radical". *J. Phys. Chem. A* **2016**, *120*, 4818–4826.

[198] Sullivan, E. N.; Nichols, B.; Neumark, D. M. "Photodissociation dynamics of the simplest alkyl peroxy radicals, CH_3OO and C_2H_5OO, at 248 nm". *J. Chem. Phys.* **2018**, *148*, 044309.

[199] Ruscic, B.; Bross, D. Active Thermochemical Tables (ATcT) values based on ver. 1.122 of the Thermochemical Network. *ATcT.anl.gov* **2016**.

[200] Chase Jr, M. W. NIST-JANAF thermochemical tables. *J. Phys. Chem. Ref. Data, Monograph* **1998**, *9*.

[201] Bise, R. T.; Choi, H.; Pedersen, H. B.; Mordaunt, D. H.; Neumark, D. M. "Photodissociation spectroscopy and dynamics of the methylthio radical (CH_3S)". *J. Chem. Phys.* **1999**, *110*, 805–816.

[202] Bouchoux, G.; Salpin, J.-Y. "Gas-phase basicity and heat of formation of sulfine CH_2SO". *J. Am. Chem. Soc.* **1996**, *118*, 6516–6517.

[203] Nagy, B.; Szakács, P.; Csontos, J.; Rolik, Z.; Tasi, G.; Kállay, M. "High-accuracy theoretical thermochemistry of atmospherically important sulfur-containing molecules". *J. Phys. Chem. A* **2011**, *115*, 7823–7833.

[204] Speth, R.; Braatz, C.; Tiemann, E. "REMPI spectroscopy of SO singlet states". *J. Mol. Spectrosc.* **1998**, *192*, 69–74.

[205] Borin, A. C.; Ornellas, F. R. "The lowest triplet and singlet electronic states of the molecule SO". *Chem. Phys.* **1999**, *247*, 351–364.

[206] Axelrod, M.; Bickart, P.; Goldstein, M. L.; Green, M. M.; Kjær, A.; Mislow, K. "Absolute configuration and optical rotatory dispersion of methyl alkyl sulfoxides". *Tetrahedron Lett.* **1968**, *9*, 3249–3252.

[207] Penn, R. E.; Block, E.; Revelle, L. K. "Flash vacuum pyrolysis studies. 5. Methanesulfenic acid". *J. Am. Chem. Soc.* **1978**, *100*, 3622–3623.

[208] Shen, H.-M.; Zhou, W.-J.; Wu, H.-K.; Yu, W.-B.; Ai, N.; Ji, H.-B.; Shi, H.-X.; She, Y.-B. "Metal-free chemoselective oxidation of sulfides to sulfoxides catalyzed by immobilized taurine and homotaurine in aqueous phase at room temperature". *Tetrahedron Lett.* **2015**, *56*, 4494–4498.

[209] Karrer, P.; Antia, N.; Schwyzer, R. "Über zwei einfache, optisch aktive Sulfoxyde" [Two simple, optically active sulfoxides]. *Helv. Chim. Acta* **1951**, *34*, 1392–1399.

[210] Curtiss, L. A.; Redfern, P. C.; Raghavachari, K. "Gaussian-4 theory using reduced order perturbation theory". *J. Chem. Phys.* **2007**, *127*, 124105.

[211] Germain, E.; Auger, J.; Ginies, C.; Siess, M.-H.; Teyssier, C. "*In vivo* metabolism of diallyl disulphide in the rat: identification of two new metabolites". *Xenobiotica* **2002**, *32*, 1127–1138.

[212] Dolejšek, Z.; Nováková, J. "A mass spectrometric study of the allyl radical interaction with oxides: MoO_3". *Collect. Czech. Chem. Commun.* **1979**, *44*, 673–683.

[213] Zhu, R.; Hsu, C.-C.; Lin, M.-C. "*Ab initio* study of the $CH_3 + O_2$ reaction: Kinetics, mechanism and product branching probabilities". *J. Chem. Phys.* **2001**, *115*, 195–203.

[214] Cheung, Y.-S.; Li, W.-K.; Ng, C.-Y. "A Gaussian-2 *ab initio* study of isomeric CH_3S_2, $CH_3S_2^+$ and $CH_3S_2^-$". *J. Mol. Struct.: THEOCHEM* **1995**, *339*, 25–38.

[215] Ruscic, B.; Berkowitz, J. "Photoionization mass spectrometric studies of the isomeric transient species mercaptomethyl (CH_2SH) and methylthio (CH_3S)". *J. Chem. Phys* **1992**, *97*, 1818–1823.

[216] Zare, R. N. "Molecular Fluorescence and Photodissociation". *PhD Thesis, Harvard University* **1964**.

[217] Busch, G. E.; Wilson, K. R. "Triatomic photofragment spectra. III. NOCl photodissociation". *J. Chem. Phys.* **1972**, *56*, 3655–3664.

[218] Davis, H.; Kim, B.; Johnston, H.; Lee, Y. "Dissociation energy and photochemistry of NO_3". *J. Phys. Chem.* **1993**, *97*.

[219] Tarnovsky, V.; Levin, A.; Deutsch, H.; Becker, K. "Electron-impact ionization of the SO free radical". *J. Chem. Phys.* **1995**, *102*, 770–773.

[220] Bursey, M. M.; Hass, J. R.; Harvan, D. J.; Parker, C. E. "Consequences of charge reversal in gaseous alkoxide ions. Oxenium ions". *J. Am. Chem. Soc.* **1979**, *101*, 5485–5489.

[221] Kosarim, A.; Smirnov, B.; Capitelli, M.; Laricchiuta, A.; Paniccia, F. "Electron impact ionization cross sections of vibrationally and electronically excited oxygen molecules". *Chem. Phys. Lett.* **2006**, *422*, 513–517.

[222] Tureček, F.; McLafferty, F. W.; Smith, B. J.; Radom, L. "Neutralization-reionization and *ab initio* study of the CH_2=CHSOH $\rightleftharpoons$ CH_3CH=S=O rearrangement. *Int. J. Mass Spectrom. Ion Proc.* **1990**, *101*, 283–300.

[223] Copan, A. V.; Schaefer III, H. F.; Agarwal, J. "Examining the ground and first excited states of methyl peroxy radical with high-level coupled-cluster theory". *Mol. Phys.* **2015**, *113*, 2992–2998.

[224] Song, M.-X.; Zhao, Z.-X.; Zhang, W.; Bai, F.-Q.; Zhang, H.-X.; Sun, C.-C. "A CASSCF/CASPT2 study on the low-lying electronic states of the CH_3SS and its cation". *Int. J. Quantum Chem.* **2012**, *112*, 1537–1546.

[225] Kapur, G.; Singh, A.; Sarpal, A. "Determination of aromatics and naphthenes in straight run gasoline by ^{1}H NMR spectroscopy. Part I". *Fuel* **2000**, *79*, 1023–1029.

[226] Hinrichs, J.; Shastry, V.; Junk, M.; Hemberger, Y.; Pitsch, H. "An experimental and computational study on multicomponent evaporation of diesel fuel droplets". *Fuel* **2020**, *275*, 117727.

[227] Atkinson, R.; Arey, J.; Aschmann, S. M. "Atmospheric chemistry of alkanes: review and recent developments". *Atmos. Environ.* **2008**, *42*, 5859–5871.

[228] Tzompa-Sosa, Z.; Henderson, B.; Keller, C.; Travis, K.; Mahieu, E.; Franco, B.; Estes, M.; Helmig, D.; Fried, A.; Richter, D., et al. "Atmospheric implications of large C_2-C_5 alkane emissions from the US oil and gas industry". *J. Geophys. Res. - Atmos.* **2019**, *124*, 1148–1169.

[229] Coustenis, A.; Salama, A.; Schulz, B.; Ott, S.; Lellouch, E.; Encrenaz, T.; Gautier, D.; Feuchtgruber, H. "Titan's atmosphere from ISO mid-infrared spectroscopy". *Icarus* **2003**, *161*, 383–403.

[230] Smith, G. P.; Nash, D. "Local sensitivity analysis for observed hydrocarbons in a Jupiter photochemistry model". *Icarus* **2006**, *182*, 181–201.

[231] Ashfold, M. N.; Ingle, R. A.; Karsili, T. N.; Zhang, J. "Photoinduced C–H bond fission in prototypical organic molecules and radicals". *Phys. Chem. Chem. Phys.* **2019**, *21*, 13880–13901.

[232] Giegerich, J.; Fischer, I. "The photodissociation dynamics of alkyl radicals". *J. Chem. Phys.* **2015**, *142*, 044304.

[233] Reisler, H.; Krylov, A. I. "Interacting Rydberg and valence states in radicals and molecules: experimental and theoretical studies". *Int. Rev. Phys. Chem.* **2009**, *28*, 267–308.

[234] Wendt, H.; Hunziker, H. "The UV spectra of primary, secondary, and tertiary alkyl radicals". *J. Chem. Phys.* **1984**, *81*, 717–723.

[235] North, S. W.; Blank, D. A.; Chu, P. M.; Lee, Y. T. "Photodissociation dynamics of the methyl radical 3s Rydberg state". *J. Chem. Phys.* **1995**, *102*, 792–798.

[236] Wu, G.; Jiang, B.; Ran, Q.; Zhang, J.; Harich, S. A.; Yang, X. "Photodissociation dynamics of the methyl radical at 212.5 nm: effect of parent internal excitation". *J. Chem. Phys.* **2004**, *120*, 2193–2198.

[237] Poullain, S. M.; Chicharro, D. V.; Zanchet, A.; González, M. G.; Rubio-Lago, L.; Senent, M. L.; García-Vela, A.; Bañares, L. "Imaging the photodissociation dynamics of the methyl radical from the 3s and $3p_z$ Rydberg states". *Phys. Chem. Chem. Phys.* **2016**, *18*, 17054–17061.

[238] Amaral, G.; Xu, K.; Zhang, J. "UV photodissociation dynamics of ethyl radical via the $\tilde{A}\ ^2A'$ (3s) state". *J. Chem. Phys.* **2001**, *114*, 5164–5169.

[239] Steinbauer, M.; Giegerich, J.; Fischer, K. H.; Fischer, I. "The photodissociation dynamics of the ethyl radical, C_2H_5, investigated by velocity map imaging". *J. Chem. Phys.* **2012**, *137*, 014303.

[240] Chicharro, D. V.; Poullain, S. M.; Zanchet, A.; Bouallagui, A.; García-Vela, A.; Senent, M. L.; Rubio-Lago, L.; Bañares, L. "Site-specific hydrogen-atom elimination in photoexcited ethyl radical". *Chem. Sci.* **2019**, *10*, 6494–6502.

[241] Poullain, S. M.; Chicharro, D. V.; Zanchet, A.; Rubio-Lago, L.; García-Vela, A.; Bañares, L. "The 3s *versus* 3p Rydberg state photodissociation dynamics of the ethyl radical". *Phys. Chem. Chem. Phys.* **2019**, *21*, 23017–23025.

[242] Knopp, G.; Beaud, P.; Radi, P.; Tulej, M.; Gerber, T. In *Femtochemistry And Femtobiology: Ultrafast Dynamics in Molecular Science*, Douhal, A., Ed.; World Scientific, Toledo, Spain: 2002; Chapter "Femtosecond photodissociation of the ethyl radical C_2H_5", pp 116–120.

[243] Song, Y.; Zheng, X.; Zhou, W.; Lucas, M.; Zhang, J. "Ultraviolet photodissociation dynamics of the *n*-propyl and *i*-propyl radicals". *J. Chem. Phys.* **2015**, *142*, 224306.

[244] Sun, G.; Zheng, X.; Song, Y.; Lucas, M.; Zhang, J. "Ultraviolet photodissociation dynamics of the *n*-butyl, *s*-butyl, and *t*-butyl radicals. *J. Chem. Phys.* **2020**, *152*, 244303.

[245] Sun, G.; Song, Y.; Zhang, J. "Ultraviolet photodissociation dynamics of 1-pentyl radical". *Chinese J. Chem. Phys.* **2018**, *31*, 439.

[246] Lucas, M. "UV photodissociation dynamics of polyatomic free radicals using high-n Rydberg atom time of flight spectroscopy"., Ph.D. Thesis, University of California, Riverside, 2016.

[247] Private communication.

[248] Sirjean, B.; Buda, F.; Hakka, H.; Glaude, P.-A.; Fournet, R.; Warth, V.; Battin-Leclerc, F.; Ruiz-Lopez, M. "The autoignition of cyclopentane and cyclohexane in a shock tube". *P. Combust. Inst.* **2007**, *31*, 277–284.

[249] Ji, C.; Dames, E.; Sirjean, B.; Wang, H.; Egolfopoulos, F. N. "An experimental and modeling study of the propagation of cyclohexane and mono-alkylated cyclohexane flames". *P. Combust. Inst.* **2011**, *33*, 971–978.

[250] Wang, Z.; Cheng, Z.; Yuan, W.; Cai, J.; Zhang, L.; Zhang, F.; Qi, F.; Wang, J. "An experimental and kinetic modeling study of cyclohexane pyrolysis at low pressure". *Combust. flame* **2012**, *159*, 2243–2253.

[251] Stein, S.; Rabinovitch, B. "Ring opening and isomerization of a series of chemically activated cycloalkyl radicals". *J. Phys. Chem.* **1975**, *79*, 191–198.

[252] Gierczak, T.; Gawłowski, J.; Niedzielski, J. "Isomerization of excited cyclohexyl, 1-hexen-6-yl and cyclopentylmethyl radicals". *J. Photoch. Photobio. A* **1990**, *55*, 25–35.

[253] Houle, F.; Beauchamp, J. "Thermal decomposition pathways of alkyl radicals by photoelectron spectroscopy. Application to cyclopentyl and cyclohexyl radicals". *J. Phys. Chem.* **1981**, *85*, 3456–3461.

[254] Matheu, D. M.; Green Jr, W. H.; Grenda, J. M. "Capturing pressure-dependence in automated mechanism generation: reactions through cycloalkyl intermediates". *Int. J. Chem. Kinet.* **2003**, *35*, 95–119.

[255] Zhang, H. R.; Huynh, L. K.; Kungwan, N.; Yang, Z.; Zhang, S. "Combustion modeling and kinetic rate calculations for a stoichiometric cyclohexane flame. 1. Major reaction pathways". *J. Phys. Chem. A* **2007**, *111*, 4102–4115.

[256] Sirjean, B.; Glaude, P.-A.; Ruiz-Lopèz, M.; Fournet, R. "Theoretical kinetic study of thermal unimolecular decomposition of cyclic alkyl radicals". *J. Phys. Chem. A* **2008**, *112*, 11598–11610.

[257] Goldsmith, C. F.; Ismail, H.; Green, W. H. "Pressure and temperature dependence of the reaction of vinyl radical with alkenes III: measured rates and predicted product distributions for vinyl + butene. *J. Phys. Chem. A* **2009**, *113*, 13357–13371.

[258] Gong, C.-M.; Li, Z.-R.; Li, X.-Y. "Theoretical kinetic study of thermal decomposition of cyclohexane". *Energ. Fuel.* **2012**, *26*, 2811–2820.

[259] Peukert, S.; Naumann, C.; Braun-Unkhoff, M.; Riedel, U. "The reaction of cyclohexane with H-atoms: A shock tube and modeling study". *Int. J. Chem. Kinet.* **2012**, *44*, 130–146.

[260] Fan, X.; Wang, G.; Li, Y.; Wang, Z.; Yuan, W.; Zhao, L. "Experimental and kinetic modeling study of 1-hexene combustion at various pressures". *Combust. Flame* **2016**, *173*, 151–160.

[261] Roberts, B. P.; Steel, A. J. "Long-range proton hyperfine splittings in the EPR spectra of cyclohexyl and alkylcyclohexyl radicals: ring inversion in the cyclohexyl radical". *J. Chem. Soc. Perk. T. 2* **1992**, 2025–2029.

[262] Pottie, R.; Harrison, A.; Lossing, F. "Free radicals by mass spectrometry. XXIV. Ionization potentials of cycloalkyl free radicals and cycloalkanes". *J. Am. Chem. Soc.* **1961**, *83*, 3204–3206.

[263] Platz, J.; Sehested, J.; Nielsen, O.; Wallington, T. "Atmospheric chemistry of cyclohexane: UV spectra of c-$C_6H_{11}^{\bullet}$ and (c-C_6H_{11})$O_2^{\bullet}$ radicals, kinetics of the reactions of (c-C_6H_{11})$O_2^{\bullet}$ radicals with NO and NO_2, and the fate of the alkoxy radical (c-C_6H_{11})$O^{\bullet}$". *J. Phys. Chem. A* **1999**, *103*, 2688–2695.

[264] Noyes, W. *n*-Butyl nitrite. *Org. Synth.* **1936**, *16*, 7–8.

[265] Chai, J.-D.; Head-Gordon, M. Long-range corrected hybrid density functionals with damped atom–atom dispersion corrections. *Phys. Chem. Chem. Phys.* **2008**, *10*, 6615–6620.

[266] Dunning Jr, T. H. "Gaussian basis sets for use in correlated molecular calculations. I. The atoms boron through neon and hydrogen". *J. Chem. Phys.* **1989**, *90*, 1007–1023.

[267] Kendall, R. A.; Dunning Jr, T. H.; Harrison, R. J. "Electron affinities of the first-row atoms revisited. Systematic basis sets and wave functions". *J. Chem. Phys.* **1992**, *96*, 6796–6806.

[268] Frisch, M. J.; Trucks, G. W.; Schlegel, H. B.; Scuseria, G. E.; Robb, M. A.; Cheeseman, J. R.; Scalmani, G.; Barone, V.; Petersson, G. A.; Nakatsuji, H.; Li, X.; Caricato, M.; Marenich, A. V.; Bloino, J.; Janesko, B. G.; Gomperts, R.; Mennucci, B.; Hratchian, H. P.; Ortiz, J. V.; Izmaylov, A. F.; Sonnenberg, J. L.; Williams-Young, D.; Ding, F.; Lipparini, F.; Egidi, F.; Goings, J.; Peng, B.; Petrone, A.; Henderson, T.; Ranasinghe, D.; Zakrzewski, V. G.; Gao, J.; Rega, N.; Zheng, G.; Liang, W.; Hada, M.; Ehara, M.; Toyota, K.; Fukuda, R.; Hasegawa, J.; Ishida, M.; Nakajima, T.; Honda, Y.; Kitao, O.; Nakai, H.; Vreven, T.; Throssell, K.; Montgomery Jr., J. A.; Peralta, J. E.; Ogliaro, F.; Bearpark, M. J.; Heyd, J. J.; Brothers, E. N.; Kudin, K. N.; Staroverov, V. N.; Keith, T. A.; Kobayashi, R.; Normand, J.; Raghavachari, K.; Rendell, A. P.; Burant, J. C.; Iyengar, S. S.; Tomasi, J.; Cossi, M.; Millam, J. M.; Klene, M.; Adamo, C.; Cammi, R.; Ochterski, J. W.; Martin, R. L.; Morokuma, K.; Farkas, O.; Foresman, J. B.; Fox, D. J. Gaussian 16 Revision A.03., Gaussian Inc. Wallingford CT, 2016.

[269] Stanton, J. F.; Bartlett, R. J. "The equation of motion coupled-cluster method. A systematic biorthogonal approach to molecular excitation energies, transition probabilities, and excited state properties". *J. Chem. Phys.* **1993**, *98*, 7029–7039.

[270] Gilbert, R. G.; Smith, S. C., *Theory of Unimolecular and Recombination Reactions*; Blackwell Scientific Publications: Oxford, UK: 1990.

[271] Das, R. C.; Koga, O.; Suzuki, S. "Chemical ionization mass spectrometry of alkyl nitrates and nitrites". *B. Chem. Soc. Japan* **1979**, *52*, 65–68.

[272] Effenhauser, C.; Felder, P.; Huber, J. R. "Photodissociation of alkyl nitrites in a molecular beam. Primary and secondary reactions". *J. Phys. Chem.* **1990**, *94*, 296–302.

[273] Heinemann-Fiedler, P.; Hoyermann, K.; Rohde, G. "The reactions of the cyclic hydrocarbon radicals c-C_3H_5, c-C_5H_9, and c-C_6H_{11} with O atoms in the gas phase. *Ber. Bunsen. Phys. Chem.* **1990**, *94*, 1400–1404.

[274] Rohrs, H. W.; Wickham-Jones, C. T.; Ellison, G. B.; Berry, D.; Argrow, B. M. "Fourier transform infrared absorption spectroscopy of jet-cooled radicals". *Rev. Sci. Instrum.* **1995**, *66*, 2430–2441.

[275] Hernandez-Castillo, A. O.; Abeysekera, C.; Stanton, J. F.; Zwier, T. S. "Structural characterization of phenoxy radical with mass-correlated broadband microwave spectroscopy. *J. Phys. Chem. Lett.* **2019**, *10*, 2919–2923.

[276] Yamashita, S. "Mass spectrometric study of the primary processes in photochemical reactions. II. Mass spectra of methyl and ethyl radicals". *B. Chem. Soc. Japan* **1974**, *47*, 1373–1374.

[277] Jiao, C.; Adams, S. "Electron ionization of cyclohexene". *J. Phys. B: At. Mol. Opt. Phys.* **2014**, *47*, 225203.

[278] Li, Y.; Klippenstein, S. J.; Zhou, C.-W.; Curran, H. J. "Theoretical kinetics analysis for $\dot{H}$ atom addition to 1,3-butadiene and related reactions on the $\dot{C}_4H_7$ potential energy surface". *J. Phys. Chem. A* **2017**, *121*, 7433–7445.

[279] Klots, C. E. "Thermochemical and kinetic information from metastable decompositions of ions". *J. Chem. Phys.* **1973**, *58*, 5364–5367.

[280] Yu, C.; Youngs, F.; Bersohn, R.; Turro, N. "Photodissociation at 193 nm of cyclooctatetraene and styrene into benzene and acetylene". *J. Phys. Chem.* **1985**, *89*, 4409–4412.

[281] Baer, T.; Hase, W. L., *Unimolecular reaction dynamics: theory and experiments*; Oxford University Press: New York, USA: 1996.

[282] Evleth, E.; Cao, H.; Kassab, E.; Sevin, A. "Computation of the direct adiabatic channel for the relaxation of electronically excited C_2H_5 radical to give H + C_2H_4". *Chem. Phys. Lett.* **1984**, *109*, 45–49.

[283] Matsika, S.; Yarkony, D. R. "Accidental conical intersections of three states of the same symmetry. I. Location and relevance". *J. Chem. Phys.* **2002**, *117*, 6907–6910.

[284] Chicharro, D. V.; Zanchet, A.; Bouallagui, A.; Rubio-Lago, L.; García-Vela, A.; Bañares, L.; Poullain, S. M. "Site-specific hydrogen-atom elimination in photoexcited alkyl radicals". *Phys. Chem. Chem. Phys.* **2021**, *23*, 2458–2468.

[285] Min, Z.; Quandt, R.; Bersohn, R. "Kinetic energies of hydrogen atoms photodissociated from alkyl radicals". *Chem. Phys. Lett.* **1998**, *296*, 372–376.

[286] Langmuir, I.; Schaefer, V. J. "Rates of evaporation of water through compressed monolayers on water". *J. Frankl. Inst.* **1943**, *235*, 119–162.

[287] Rideal, E. K. "On the influence of thin surface films on the evaporation of water". *J. Phys. Chem.* **1925**, *29*, 1585–1588.

[288] Sebba, F.; Briscoe, H. V. A. "The evaporation of water through unimolecular films". *J. Chem. Soc.* **1940**, 106–114.

[289] Hickman, K.; Trevoy, D. "Studies in high vacuum evaporation: The falling-stream tensimeter". *Ind. Eng. Chem.* **1952**, *44*, 1882–1888.

[290] Hickman, K. "Surface behavior in the pot still". *Ind. Eng. Chem.* **1952**, *44*, 1892–1902.

[291] Hickman, K. "Maximum evaporation coefficient of water". *Ind. Eng. Chem.* **1954**, *46*, 1442–1446.

[292] Eames, I.; Marr, N.; Sabir, H. "The evaporation coefficient of water: a review". *Int. J. Heat Mass Tran.* **1997**, *40*, 2963–2973.

[293] Ward, C.; Fang, G. "Expression for predicting liquid evaporation flux: Statistical rate theory approach". *Phys. Rev. E* **1999**, *59*, 429.

[294] Ward, C. "Liquid-vapour phase change rates and interfacial entropy production". *J. Non-Equil. Thermody.* **2002**, *27*, 289–303.

[295] Persad, A. H.; Ward, C. A. "Expressions for the evaporation and condensation coefficients in the Hertz-Knudsen relation". *Chem. Rev.* **2016**, *116*, 7727–7767.

[296] Johnson, A. M.; Lancaster, D. K.; Faust, J. A.; Hahn, C.; Reznickova, A.; Nathanson, G. M. "Ballistic evaporation and solvation of helium atoms at the surfaces of protic and hydrocarbon liquids". *J. Phys. Chem. Lett.* **2014**, *5*, 3914–3918.

[297] Lancaster, D. K.; Johnson, A. M.; Kappes, K.; Nathanson, G. M. "Probing gas–liquid interfacial dynamics by helium evaporation from hydrocarbon liquids and jet fuels". *J. Phys. Chem. C* **2015**, *119*, 14613–14623.

[298] Hahn, C.; Kann, Z. R.; Faust, J. A.; Skinner, J.; Nathanson, G. M. "Super-Maxwellian helium evaporation from pure and salty water". *J. Chem. Phys.* **2016**, *144*, 044707.

[299] Kann, Z.; Skinner, J. "Sub-and super-Maxwellian evaporation of simple gases from liquid water". *J. Chem. Phys.* **2016**, *144*, 154701.

[300] Lancaster, D. K. "Inert gas scattering and evaporation from jet fuel surrogates using liquid microjets"., Ph.D. Thesis, University of Wisconsin-Madison, 2014.

[301] Patel, E.-H.; Williams, M. A.; Koehler, S. P. "Kinetic energy and angular distributions of He and Ar atoms evaporating from liquid dodecane". *J. Phys. Chem. B* **2017**, *121*, 233–239.

[302] Faubel, M.; Kisters, T. "Non-equilibrium molecular evaporation of carboxylic acid dimers". *Nature* **1989**, *339*, 527–529.

[303] Maselli, O. J.; Gascooke, J. R.; Lawrance, W. D.; Buntine, M. A. "The dynamics of evaporation from a liquid surface". *Chem. Phys. Lett.* **2011**, *513*, 1–11.

[304] Ryazanov, M.; Nesbitt, D. J. "Quantum-state-resolved studies of aqueous evaporation dynamics: NO ejection from a liquid water microjet". *J. Chem. Phys.* **2019**, *150*, 044201.

[305] Davies, J. F.; Miles, R. E.; Haddrell, A. E.; Reid, J. P. "Influence of organic films on the evaporation and condensation of water in aerosol". *P. Natl. Acad. Sci.* **2013**, *110*, 8807–8812.

[306] Huisman, A. J.; Krieger, U.; Zuend, A.; Marcolli, C.; Peter, T. "Vapor pressures of substituted polycarboxylic acids are much lower than previously reported". *Atmos. Chem. Phys.* **2013**, *13*, 6647–6662.

[307] Charvat, A.; Lugovoj, E.; Faubel, M.; Abel, B. "New design for a time-of-flight mass spectrometer with a liquid beam laser desorption ion source for the analysis of biomolecules". *Rev. Sci. Instrum.* **2004**, *75*, 1209–1218.

[308] Braibanti, A.; Fisicaro, E.; Dallavalle, F.; Lamb, J.; Oscarson, J.; Rao, R. S. "Molecular thermodynamic model for the solubility of noble gases in water". *J. Phys. Chem.* **1994**, *98*, 626–634.

[309] Clever, H. L.; Battino, R.; Saylor, J.; Gross, P. "The solubility of helium, neon, argon and krypton in some hydrocarbon solvents". *J. Phys. Chem.* **1957**, *61*, 1078–1082.

[310] Lancaster, D. K.; Johnson, A. M.; Burden, D. K.; Wiens, J. P.; Nathanson, G. M. "Inert gas scattering from liquid hydrocarbon microjets". *J. Phys. Chem. Lett.* **2013**, *4*, 3045–3049.

[311] Faust, J. "Collisions and reactions with glycerol films and water microjets: exploring the chemistry of interfacial ions"., Ph.D. Thesis, University of Wisconsin-Madison, 2015.

[312] Sadtchenko, V.; Brindza, M.; Chonde, M.; Palmore, B.; Eom, R. "The vaporization rate of ice at temperatures near its melting point". *J. Chem. Phys.* **2004**, *121*, 11980–11992.

[313] Loeb, L. B., *The Kinetic Theory of Gases*; Dover, New York: 1961.

[314] Brastad, S. M.; Nathanson, G. M. "Molecular beam studies of HCl dissolution and dissociation in cold salty water". *Phys. Chem. Chem. Phys.* **2011**, *13*, 8284–8295.

[315] Snow, W.; Dowell, J.; Chevrenak, J.; Berek, H. "Molecular beam measurements of total collision cross sections of H_2O". *J. Chem. Phys.* **1973**, *58*, 2517–2520.

[316] Tesa-Serrate, M. A.; Smoll Jr, E. J.; Minton, T. K.; McKendrick, K. G. "Atomic and molecular collisions at liquid surfaces". *Ann. Rev. Phys. Chem.* **2016**, *67*, 515–540.

[317] Hurlbut, F. C.; Beck, D. *"New Studies of Molecular Scattering at the Solid Surface"*; tech. rep.; University of California, Berkeley. Institute of Engineering Research, 1959.

[318] Sinha, M.; Fenn, J. In *"Scattering of an argon beam by a liquid glycerine surface". Proc. 5th Int. Symp. Molecular Beams, Nice, France*, 1975.

[319] Edwards, D.; Fatouros, P.; Ihas, G.; Mrozinski, P.; Shen, S.; Gasparini, F.; Tam, C. "Specular reflection of ^{4}He atoms from the surface of liquid ^{4}He". *Phys. Rev. Lett.* **1975**, *34*, 1153.

[320] Edwards, D.; Fatouros, P.; Ihas, G. "Scattering of ^{3}He atoms at the surface of liquid ^{4}He". *Phys. Lett. A* **1976**, *59*, 131–132.

[321] Saecker, M. E.; Govoni, S. T.; Kowalski, D. V.; King, M. E.; Nathanson, G. M. "Molecular beam scattering from liquid surfaces". *Science* **1991**, *252*, 1421–1424.

[322] King, M. E.; Nathanson, G. M.; Hanning-Lee, M.; Minton, T. K. "Probing the microscopic corrugation of liquid surfaces with gas-liquid collisions". *Phys. Rev. Lett.* **1993**, *70*, 1026.

[323] Kenyon, A. J.; McCaffery, A. J.; Quintella, C. M.; Zidan, M. D. "Investigation of dynamical processes at liquid surfaces by molecular scattering". *J. Chem. Soc. Faraday T.* **1993**, *89*, 3877–3884.

[324] Nathanson, G. M. "Molecular beam studies of gas-liquid interfaces". *Ann. Rev. Phys. Chem.* **2004**, *55*, 231–255.

[325] Klassen, J. K.; Nathanson, G. M. "Hydrogen-bond breaking and proton exchange in collisions of gaseous formic acid with liquid sulfuric acid". *Science* **1996**, *273*, 333–335.

[326] Klassen, J. K.; Fiehrer, K. M.; Nathanson, G. M. "Collisions of organic molecules with concentrated sulfuric acid: scattering, trapping, and desorption". *J. Phys. Chem. B* **1997**, *101*, 9098–9106.

[327] Bianchini, R. H.; Tesa-Serrate, M. A.; Costen, M. L.; McKendrick, K. G. "Collision-energy dependence of the uptake of hydroxyl radicals at atmospherically relevant liquid surfaces. *J. Phys. Chem. C* **2018**, *122*, 6648–6660.

[328] Barker, J. A.; Auerbach, D. J. "Gas–surface interactions and dynamics: thermal energy atomic and molecular beam studies". *Surf. Sci. Rep.* **1984**, *4*, 1–99.

[329] Miyake, T.; Namiki, A.; Takemoto, T.; Soeki, S.; Katoh, H.; Kamba, H.; Suzaki, T.; Nakamura, T. "A molecular beam study of the trapping and desorption of oxygen from Si(100) surfaces". *Jpn. J. Appl. Phys.* **1990**, *29*, 723.

[330] Siders, J. L.; Sitz, G. O. In *P. Soc. Photo.-Opt. Ins.* 1995; Vol. 2547, pp 206–217.

[331] Bosio, S. B.; Hase, W. L. "Energy transfer in rare gas collisions with self-assembled monolayers". *J. Chem. Phys.* **1997**, *107*, 9677–9686.

[332] Irimia, D.; Dobrikov, D.; Kortekaas, R.; Voet, H.; van den Ende, D. A.; Groen, W. A.; Janssen, M. H. "A short pulse (7 μs FWHM) and high repetition rate (dc-5kHz) cantilever piezovalve for pulsed atomic and molecular beams". *Rev. Sci. Instrum.* **2009**, *80*, 113303.

[333] Even, U. "The Even-Lavie valve as a source for high intensity supersonic beam". *EPJ Techniques and Instrumentation* **2015**, *2*, 1–22.

[334] Stern, T.; Blaquiere, A.; Valat, J. "Reactivity measurement using pseudo-random source excitation". *J. Nucl. Energy AB* **1962**, *16*, 499–508.

[335] Hirschy, V.; Aldridge, J. "A cross correlation chopper for molecular beam modulation". *Rev. Sci. Instrum.* **1971**, *42*, 381–383.

[336] Comsa, G.; David, R.; Schumacher, B. "Magnetically suspended cross-correlation chopper in molecular beam-surface experiments". *Rev. Sci. Instrum.* **1981**, *52*, 789–796.

[337] Hoskovec, M.; Grygarová, D.; Cvačka, J.; Streinz, L.; Zima, J.; Verevkin, S. P.; Koutek, B. "Determining the vapour pressures of plant volatiles from gas chromatographic retention data". *J. Chromatogr. A* **2005**, *1083*, 161–172.

[338] Chuck, C. J.; Donnelly, J. "The compatibility of potential bioderived fuels with Jet A-1 aviation kerosene". *Appl. Energ.* **2014**, *118*, 83–91.

[339] Kroenlein, K.; Muzny, C.; Diky, V.; Chirico, R.; Magee, J.; Abdulagatov, I.; Frenkel, M. *NIST/TRC Web Thermo Tables (WTT) NIST Standard Reference Subscription Database 3 - Professional Edition Version 2.*, 2011.

[340] Arakawa, R.; Rabinovitch, B. "Isomerization of 1-methylcyclobutene by single collision activation at a surface. Variation of initial energy". *J. Phys. Chem.* **1982**, *86*, 4772–4776.

[341] Guenther, A.; Hewitt, C. N.; Erickson, D.; Fall, R.; Geron, C.; Graedel, T.; Harley, P.; Klinger, L.; Lerdau, M.; McKay, W., et al. "A global model of natural volatile organic compound emissions". *J. Geophys. Res-Atmos.* **1995**, *100*, 8873–8892.

[342] Gligorovski, S.; Strekowski, R.; Barbati, S.; Vione, D. "Environmental implications of hydroxyl radicals ($^{\bullet}$OH)". *Chem. Rev.* **2015**, *115*, 13051–13092.

[343] Jursic, B. S. "Density functional theory exploring the HONO potential energy surface". *Chem. Phys. Lett.* **1999**, *299*, 334–344.

[344] Bauerfeldt, G. F.; Arbilla, G.; Silva, E. C. d. "Evaluation of reaction thermochemistry using DFT calculated molecular properties: application to trans-HONO (X^1A') $\rightarrow$ HO (X^2P)+ NO (X^2P)". *J. Brazil. Chem. Soc.* **2005**, *16*, 190–196.

[345] Criegee, R.; Wenner, G. "Die Ozonisierung des 9,10-Oktalins" [The ozonization of 9,10-octalin]. *Liebigs Ann. Chem.* **1949**, *564*, 9–15.

[346] Johnson, D.; Marston, G. "The gas-phase ozonolysis of unsaturated volatile organic compounds in the troposphere". *Chem. Soc. Rev.* **2008**, *37*, 699–716.

[347] Loerting, T.; Liedl, K. R. "Toward elimination of discrepancies between theory and experiment: The rate constant of the atmospheric conversion of SO_3 to H_2SO_4. *Proc. Nat. Acad. Sci.* **2000**, *97*, 8874–8878.

[348] McNamara, J. P.; Hillier, I. H. "Structure and reactivity of dinitrogen pentoxide in small water clusters studied by electronic structure calculations". *J. Phys. Chem. A* **2000**, *104*, 5307–5319.

[349] Anglada, J. M.; Martins-Costa, M. T.; Francisco, J. S.; Ruiz-López, M. F. "Reactivity of undissociated molecular nitric acid at the air–water interface". *J. Am. Chem. Soc.* **2020**.

[350] Zhu, C.; Kumar, M.; Zhong, J.; Li, L.; Francisco, J. S.; Zeng, X. C. "New mechanistic pathways for Criegee–water chemistry at the air/water interface". *J. Am. Chem. Soc.* **2016**, *138*, 11164–11169.

[351] Tseng, C.-M.; Lee, Y. T.; Lin, M.-F.; Ni, C.-K.; Liu, S.-Y.; Lee, Y.-P.; Xu, Z.; Lin, M.-C. "Photodissociation dynamics of phenol". *J. Phys. Chem. A* **2007**, *111*, 9463–9470.

[352] Lieberman, M. A.; Lichtenberg, A. J., *Principles of Plasma Discharges and Materials Processing*; John Wiley & Sons, New York: 2005.

[353] Prasad, A.; Craggs, J. "Measurement of ionization and attachment coefficients in humid air in uniform fields and the mechanism of breakdown". *P. Phys. Soc.* **1960**, *76*, 223.

[354] Hackam, R. "Electrical breakdown of water vapour". *Phy. Lett. A* **1970**, *33*, 65–66.

[355] Hackam, R. "Breakdown potential of water vapour between plane parallel electrodes". *J. Phys. D: Appl. Phys.* **1971**, *4*, 1134.

[356] Mirza, J.; Smith, C.; Calderwood, J. "Sparking potentials of saturated hydrocarbon gases". *J. Phys. D: Appl. Phys.* **1971**, *4*, 1126.

[357] Škoro, N.; Marić, D.; Malović, G.; Graham, W.; Petrović, Z. L. "Electrical breakdown in water vapor". *Phys. Rev. E* **2011**, *84*, 055401.

[358] Sivoš, J.; Škoro, N.; Marić, D.; Malović, G.; Petrović, Z. L. "Breakdown and dc discharge in low-pressure water vapour". *J. Phys. D: Appl. Phys.* **2015**, *48*, 424011.

[359] Rumble, J. R. CRC Handbook of Chemistry and Physics, 101st Edition (Internet Version 2020).

[360] Pátek, J.; Klomfar, J. "Solid–liquid phase equilibrium in the systems of LiBr–H_2O and LiCl–H_2O". *Fluid Phase Equilibr.* **2006**, *250*, 138–149.

[361] Patil, K. R.; Tripathi, A. D.; Pathak, G.; Katti, S. S. "Thermodynamic properties of aqueous electrolyte solutions. 1. Vapor pressure of aqueous solutions of lithium chloride, lithium bromide, and lithium iodide". *J. Chem. Eng. Data* **1990**, *35*, 166–168.

[362] Pátek, J.; Klomfar, J. "A computationally effective formulation of the thermodynamic properties of LiBr–H_2O solutions from 273 to 500 K over full composition range". *Int. J. Refrig.* **2006**, *29*, 566–578.

[363] Yao, W.; Bjurström, H.; Setterwall, F. "Surface tension of lithium bromide solutions with heat-transfer additives". *J. Chem. Eng. Data* **1991**, *36*, 96–98.

[364] Sawada, I.; Yamada, M.; Fukusako, S.; Kawanami, T. "Thermophysical properties of aqueous solutions near the equilibrium freezing temperature". *Int. J. Thermophys.* **1998**, *19*, 749–759.

[365] Wimby, J. M.; Berntsson, T. S. "Viscosity and density of aqueous solutions of LiBr, LiCl, $ZnBr_2$, $CaCl_2$, and $LiNO_3$. 1. Single salt solutions". *J. Chem. Eng. Data* **1994**, *39*, 68–72.

[366] Mashovets, V.; Baron, N.; Shcherba, M. Viscosity and density of lithium chloride, lithium bromide, and lithium iodide aqueous solutions at average and low temperatures. *Zh. Prikl. Khim.* **1971**, *44*, 1981–1986.

[367] Zafar, A.; Chickos, J. "The vapor pressure and vaporization enthalpy of squalene and squalane by correlation gas chromatography". *J. Chem. Thermodyn.* **2019**, *135*, 192–197.

[368] Harris, K. R. "Temperature and pressure dependence of the viscosities of 2-ethylhexyl benzoate, bis(2-ethylhexyl) phthalate, 2,6,10,15,19,23-hexamethyltetracosane (squalane), and diisodecyl phthalate". *J. Chem. Eng. Data* **2009**, *54*, 2729–2738.

[369] Durupt, N.; Aoulmi, A.; Bouroukba, M.; Rogalski, M. "Heat capacities of liquid long-chain alkanes". *Thermochim. Acta* **1996**, *274*, 73–80.

[370] Korosi, G.; Kovats, E. S. "Density and surface tension of 83 organic liquids". *J. Chem. Eng. Data* **1981**, *26*, 323–332.

[371] Sasse, K.; Jose, J.; Merlin, J.-C. "A static apparatus for measurement of low vapor pressures. Experimental results on high molecular-weight hydrocarbons". *Fluid Phase Equilibr.* **1988**, *42*, 287–304.

[372] Khasanshin, T.; Shchamialiou, A.; Poddubskij, O. "Thermodynamic properties of heavy n-alkanes in the liquid state: n-dodecane". *Int. J. Thermophys.* **2003**, *24*, 1277–1289.

[373] Luning Prak, D. J.; Alexandre, S. M.; Cowart, J. S.; Trulove, P. C. "Density, viscosity, speed of sound, bulk modulus, surface tension, and flash point of binary mixtures of n-dodecane with 2,2,4,6,6-pentamethylheptane or 2,2,4,4,6,8,8-heptamethylnonane". *J. Chem. Eng. Data* **2014**, *59*, 1334–1346.

[374] Schmidt, R. L.; Randall, J. C.; Clever, H. L. "The surface tension and density of binary hydrocarbon mixtures: benzene-n-hexane and benzene-n-dodecane". *J. Phys. Chem.* **1966**, *70*, 3912–3916.

[375] Cuesta, S. P.-d. l.; Knopper, L.; van der Wielen, L. A.; Cuellar, M. C. "Techno-economic assessment of the use of solvents in the scale-up of microbial sesquiterpene production for fuels and fine chemicals". *Biofuel. Bioprod. Bior.* **2019**, *13*, 140–152.

[376] Štejfa, V.; Fulem, M.; Růžička, K.; Červinka, C.; Rocha, M. A.; Santos, L. M.; Schröder, B. "Thermodynamic study of selected monoterpenes". *J. Chem. Thermodyn.* **2013**, *60*, 117–125.

[377] Clará, R. A.; Marigliano, A. C. G.; Sólimo, H. N. "Density, viscosity, and refractive index in the range (283.15 to 353.15) K and vapor pressure of α-pinene, d-limonene,($\pm$)-linalool, and citral over the pressure range 1.0 kPa atmospheric pressure". *J. Chem. Eng. Data* **2009**, *54*, 1087–1090.

[378] Fujisawa, M.; Matsushita, T.; Kimura, T. "Excess molar heat capacities of ((R)-(+)-α-pinene + (S)-(-)-α-pinene) at temperatures between 293.15-308.15 K". *J. Therm. Anal. Calorim.* **2005**, *81*, 137–139.

[379] Daisey, J. M.; Hopke, P. K. "Potential for ion-induced nucleation of volatile organic compounds by radon decay in indoor environments". *Aerosol Sci. Tech.* **1993**, *19*, 80–93.

[380] Wagner, Z.; Bendová, M.; Rotrekl, J.; Orvalho, S. "Densities, vapor pressures, and surface tensions of selected terpenes". *J. Solution Chem.* **2019**, *48*, 1147–1166.

Appendix A

Publications Resulting from Graduate Work

1. C. Lee*, M. N. Pohl*, I. A. Ramphal*, and D. M. Neumark. A Liquid Flat Jet System for Molecular Beam Scattering Experiments. *Rev. Sci. Instrum.* (in preparation, **equal authorship*).

2. I. A. Ramphal, M. Shapero, and D. M. Neumark. Photodissociation Dynamics of the Cyclohexyl Radical from the 3p Rydberg State at 248 nm. *J. Phys. Chem. A*, **2021**, 125, 3900.

3. I. A. Ramphal, C. Lee, and D. M. Neumark. Photodissociation Dynamics of the Methylsulfinyl Radical at 248 nm. *Mol. Phys.*, **2019**, 117, 3043.

4. M. Shapero*, I. A. Ramphal*, and D. M. Neumark. Photodissociation of the Cyclopentadienyl Radical at 248 nm. *J. Phys. Chem. A*, **2018**, 122, 4265 (**equal authorship*).

5. I. A. Ramphal, M. Shapero, C. Haibach-Morris, and D. M. Neumark. Photodissociation Dynamics of Fulvenallene and the Fulvenallenyl Radical at 248 and 193 nm. *Phys. Chem. Chem. Phys.*, **2017**, 19, 29305.

Appendix B

Rice-Ramsperger-Kassel-Marcus Code

This appendix contains a typical version of the Python code used to perform Rice-Ramsperger-Kassel-Marcus (RRKM) calculations. The goal is to evaluate energy-dependent rate constants for unimolecular reactions, according to:

$$k(E) = \sigma \frac{W^{\ddagger}(E - E_o)}{h\rho(E)}$$

where h is Planck's constant, σ is the reaction path degeneracy, $W^{\ddagger}(E - E_o)$ is the sum of states for the transition state at energy $E - E_o$, and ρ(E) is the rovibrational density of states of the reactant at energy E.

When the function is called, it expects to be provided with the location of an input text file (.txt format). Input files should have the following structure:

v1, v2, v3, ...

B1, B2, B3, ...

s1, s2, s3, ...

d1, d2, d3, ...

1/0, 1/0, 1/0, ...

V_o1, V_o2, V_o3, ...

where v_i is the frequency (integer values in cm^{-1}) of the i^{th} vibrational mode, B_i, s_i and d_i are respectively the rotational constant (in cm^{-1}), symmetry number and rotor dimensionality of the i^{th} internal rotor mode, the value 1/0 treats the rotor as a hindered/free rotor, and $V_{o,i}$ is the torsional barrier height for hindered rotors (this should be 0 for free rotors). The program is currently set up to print out the result of each function call, but can be modified easily to output data to a file instead if many calls are to be made.

```
import sys
import math

def BeyerSwinehart(reactant,TS,E_max,E_o):

    ### Constants

    h = 6.62607004*10**-34 #J s, Planck's constant
    c = 2.99792458*10**10 # cm/s, speed of light
    N_A = 6.0221409*10**23 # particles per mole
    k_B = 1.38064852*10**-23 # J/K, Boltzmann's constant


    ### Initial conditions

    E_max = E_max #115.2880368 # kcal/mol, E_max under consideration
    E_max = E_max*4.184*1000/(N_A*h*c) # cm-1, convert E_max from kcal/mol
    to wavenumbers
    E_o = E_o # kcal/mol, E_o for the reaction
    E_o = E_o*4.184*1000/(N_A*h*c) # cm-1, convert E_o from kcal/mol to
   wavenumbers
    delta = 1 # cm^-1, energy step size


    ### Initialize vector for w, B, s, and rotor dimensionality

    w_R = []
    B_R = []
    s_R = []
    d_R = []
    w_T = []
    B_T = []
    s_T = []
    d_T = []


    ### Open desired data text files for the reactant and transition state

    dataFile = "C:\\users\\datafile.txt"
    Rdata = dataFile + str(reactant) + ".txt"
    TSdata = dataFile + str(TS) + ".txt"

    f = open(Rdata,"r") # open reactant rovibrational data file
    Rrovib_data = f.read().split('\n')
    Rvib_modes = Rrovib_data[0].split(',') # reactant vibrational
   frequencies
    Rrot_modes = Rrovib_data[1].split(',') # reactant rotation constants
    Rrot_sym = Rrovib_data[2].split(',')   # symmetry numbers of the
   rotors
    Rrot_dim = Rrovib_data[3].split(',')   # dimensionality of the rotors
```

```
    f.close()

    f = open(TSdata,"r") #open TS rovibrational data file
    TSrovib_data = f.read().split('\n')
    TSvib_modes = TSrovib_data[0].split(',') # TS vibrational frequencies
    TSrot_modes = TSrovib_data[1].split(',') # TS rotation constants
    TSrot_sym = TSrovib_data[2].split(',')   # symmetry number of the
rotors
    TSrot_dim = TSrovib_data[3].split(',')   # dimensionality of the
rotors
    f.close()


    ### Populate the w vibrational mode vectors

    for mode in Rvib_modes:
        w_R.append(round(float(mode)))

    for mode in TSvib_modes:
        w_T.append(round(float(mode)))


    ### Populate the B, s and d rotatioanl mode vectors

    u_R = 0  # initialize number of reactant 1-D rotors
    p_R = 0  # initialize number of reactant 2-D rotors
    u_T = 0  # initialize number of TS 1-D rotors
    p_T = 0  # initialize number of TS 2-D rotors









    if float(Rrot_modes[0]) > 0.0:          # reactant vectors
        i = 0
        while i < len(Rrot_modes):
            B_R.append(float(Rrot_modes[i]))
            s_R.append(int(Rrot_sym[i]))
            if float(Rrot_dim[i]) == 1.0:
                u_R += 1
                d_R.append(1)
            elif float(Rrot_dim[i]) == 2.0:
                p_R += 1
                d_R.append(2)
            i += 1
```

```
    if float(TSrot_modes[0]) > 0.0:          # TS vectors
        i = 0
        while i < len(TSrot_modes):
            B_T.append(float(TSrot_modes[i]))
            s_T.append(int(TSrot_sym[i]))
            if float(TSrot_dim[i]) == 1.0:
                u_T += 1
                d_T.append(1)
            elif float(TSrot_dim[i]) == 2.0:
                p_T += 1
                d_T.append(2)
            i += 1



    ### Set up the reactant pure rotational density of states vector

    if u_R == 0 and p_R == 0: # set up an empty rotational density of
states
        pr_R = [0]*int(E_max/delta+1)
        pr_R[0] = 1
    else:
        pr_R = [math.pi**(u_R/2)/(math.gamma(p_R+u_R/2))]*int(E_max/delta
+1)
        i = 0
        while i < len(B_R):
            if d_R[i] == 1: # multiply pr_R by the expression for 1-D
rotors
                j = 0
                while j < len(pr_R):
                    pr_R[j] = pr_R[j]/(s_R[i]*B_R[i]**0.5)
                    j += 1
            elif d_R[i] == 2: # multiply pr_R by the expression for 2-D
rotors
                j = 0
                while j < len(pr_R):
                    pr_R[j] = pr_R[j]/(s_R[i]*B_R[i])
                    j += 1
            i += 1
        i = 1
        while i <= int(E_max/delta): # multiply pr_R by its energy
dependence
            pr_R[i] = pr_R[i]*(i**(p_R+u_R/2-1))
            i += 1
        pr_R[0] = pr_R[0]*0.5*(delta/2)**(p_R+u_R/2-1) # set the first
entry to p(delta/2)


```

```
139     ### Set up the transition state pure rotational density of states
    vector
140 
141     if u_T == 0 and p_T == 0: # set up an empty rotational density of
    states
142         pr_T = [0]*int(E_max/delta+1)
143         pr_T[0] = 1
144     else:
145         pr_T = [math.pi**(u_T/2)/(math.gamma(p_T+u_T/2))]*int(E_max/delta
    +1)
146         i = 0
147         while i < len(B_T):
148             if d_T[i] == 1: # multiply pr_T by the expression for 1-D
    rotors
149                 j = 0
150                 while j < len(pr_T):
151                     pr_T[j] = pr_T[j]/(s_T[i]*B_T[i]**0.5)
152                     j += 1
153             elif d_T[i] == 2: # multiply pr_T by the expression for 2-D
    rotors
154                 j = 0
155                 while j < len(pr_T):
156                     pr_T[j] = pr_T[j]/(s_T[i]*B_T[i])
157                     j += 1
158             i += 1
159         i = 1
160         while i <= int(E_max/delta): # multiply pr_T by its energy
    dependence
161             pr_T[i] = pr_T[i]*(i**(p_T+u_T/2-1))
162             i += 1
163         pr_T[0] = pr_T[0]*0.5*(delta/2)**(p_T+u_T/2-1) # set the first
    entry to p(delta/2)
164 
165 
166 
167 
168     ### Populate the reactant rovibrational density of states vector
169 
170     j = 0
171     while j < len(w_R):
172         w_j = w_R[j]
173         i = int(w_j/delta)
174         while i <= int(E_max/delta):
175             pr_R[i] = pr_R[i] + pr_R[int(i-w_j/delta)] # populate density
    of states vector with vibrational modes
176             i += 1
177         j += 1
178 
179 
180 
```

```
181
182     ### Populate the transition state rovibrational density of states
    vector
183
184     j = 0
185     while j < len(w_T):
186         w_j = w_T[j]
187         i = int(w_j/delta)
188         while i <= int(E_max/delta):
189             pr_T[i] = pr_T[i] + pr_T[int(i-w_j/delta)] # populate density
    of states vector with vibrational modes
190             i += 1
191         j += 1
192
193
194     ### Calculate k(E) using TS sum of states and reactant pr(E_max)
195
196     k = 0 # counter for the energy index used to produce the sum of states
     W
197     W = 0 # initialize a null sum of states for the TS
198     while k < int(E_max-E_o+1/(2*delta)): # adds up the states between E =
     0 and E_max - E_o
199         W += pr_T[k]
200         k += 1
201
202     k_E = W/(pr_R[int(E_max)]/c) # calculate the RRKM microcanonical rate
    constant
203     #print(W)
204     #print(pr_R[int(E_max)]/c)
205
206     print(str(reactant), '-->', str(TS), 'with rate constant k(E) =', k_E,
     's^-1.')
```

Appendix C

High-voltage arcs during liquid jet experiments

A practical consideration when using volatile liquids is the electrical breakdown of their vapors in the vicinity of high-voltage electronics. There are two components carrying high voltage through the main scattering chamber which can be problematic: the photomultiplier tube typically operates using a 1.550 kV potential, while the doorknob is held at -30 kV. The quadrupole power supply carries 800 V, but this passes through an electrical feedthrough on top of the rotating tec-ring and directly into the ultrahigh vacuum detector and thus causes no issues.

In the course of developing the liquid jet experiment we initially achieved vacuum on the order of 10^{-3}–10^{-4} Torr. Since this was deemed too high to open the detector gate-valve, the high-voltage electronics were never energized under these conditions. Improvements in cryopumping and liquid catching eventually allowed us to achieve ∼5-10 x 10^{-5} Torr using water jets, emboldening us to turn on and open the detector. After some delay of typically 5-30 minutes, we noticed that the “Arc" warning light on the doorknob power supply was intermittently lighting up. In the aftermath of one instance of arcing we found that the front trifilter was reading an incorrect voltage, and was unresponsive to commands changing the voltage setpoint. The problem was traced back to an operational amplifier within the Merlin 5221 control unit, and the entire circuit board has to be replaced by Extrel. We have never been able to conclusively identify where this arcing happens, but it occurred on several occasions. Presumably this happens within the main chamber, since the doorknob and trifilter cables both feed into the main chamber and rest near one another when they are attached to the detector. We have not been able to observe the arc when inspecting the chamber, and determining the location is not worth damaging the ionizer assembly.

With water jets, this issue has occurred with ambient main chamber pressures at least as low as ∼5-6 x 10^{-5} Torr. We have successfully run water jets for entire days with the main chamber at ∼2-3 x 10^{-5} Torr without issue. It is recommended to achieve a vacuum better than 2 x 10^{-5} Torr before energizing the detector, and ideally the pressure would be less than 1 x 10^{-5} Torr. We regularly achieve 4-6 x 10^{-6} Torr with water flat jets, and have never

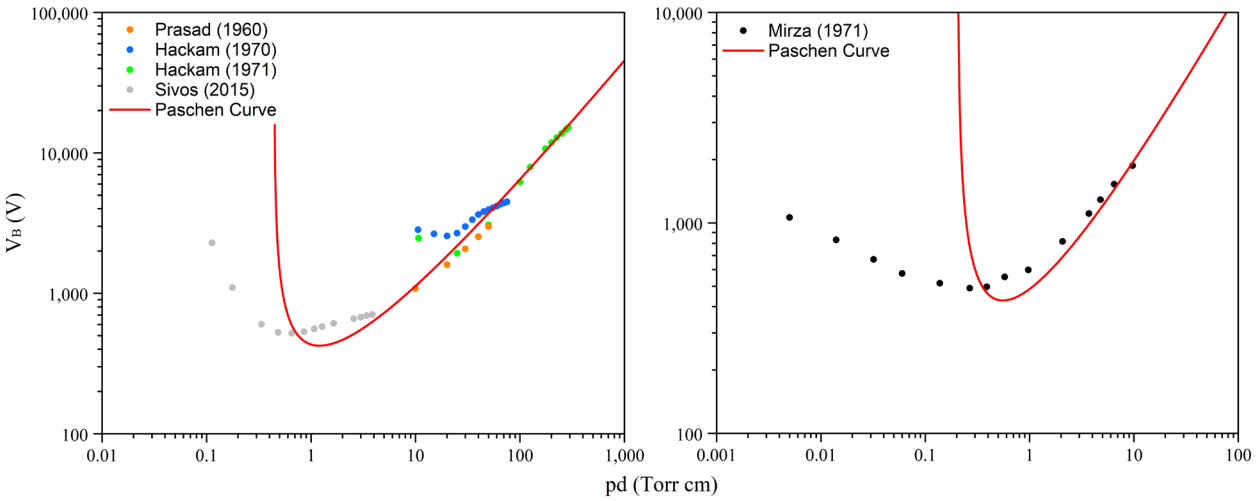

Figure C.1: Paschen curves for water (left) and dodecane (right) vapors. Data for other alkanes are nearly indistinguishable from decane.[356] Note the different scales in each plot.

experienced any problems with the detector under these pressures.

It initially seems peculiar that electrical breakdown would be occurring at all at the pressures described above. An empirical relation between the voltage V_B required to induce electrical breakdown in a gas and the pressure-distance gap, pd, is given by Paschen's Law:[352]

$$V_B = \frac{Bpd}{\ln(Apd) + \ln[\ln(1 + 1/\gamma)]} \tag{C.1}$$

where A and B are species-dependent constants and γ is the secondary-electron emission coefficient that determines how easily a discharge can propagate through the gas. Figure C.1 shows Paschen curves for water and decane vapor collected from the literature.[353–358] The resulting curves are similar to those of other gases such as N_2, O_2 and Ar. As the pd gap decreases from high pressures the voltage required to induce breakdown decreases, eventually reaching a minimum before sharply increasing. Why then do we encounter arcs for pressures as low as 5 x 10^{-5} Torr?

The liquid jets are a continuous gas source emitting a huge quantity of vapor into the vacuum chamber through evaporation. Despite the large pumping capacity present in our apparatus, the gas density must vary smoothly from the recorded value at the ion guage near the turbopump inlet (the pressure values normally given by us), to that corresponding to the vapor pressure of the liquid just above the liquid surface according to its temperature. The geometry of flat jets also means that the gas density undergoes a slower decrease with distance away from the jet surface than for cylindrical jets. In general this implies arcing is more likely to occur closer to the location of the liquid jet in the scattering chamber for a given voltage, depending on the physical gap length. As a general rule it is strongly advised to never operate the detector above about 4×10^{-5} Torr with a liquid jet in the chamber.

Appendix D

Physical Properties of Select Liquids

Physical properties relevant to liquid jet experiments are aggregated here for select liquids of potential interest. Chosen aqueous liquids are water and salty water (here taken to mean a roughly 8 molal LiBr solution – about 12 mol % LiBr); alcohols are ethanol and *i*-propanol; the cyclic monoterpene α-pinene (2,6,6-trimethylbicyclo[3.1.1]hept-2-ene); the linear sesquiterpene farnesene (3,7,11-trimethyl-1,3,6,10-dodecatetraene); and the alkanes n-dodecane and squalane (2,6,10,15,19,23-hexamethyltetracosane). Structures of these liquids are shown in Figure D.1 and Table D.1 contains their physical properties. Since both dynamic (η) and kinematic (ν) viscosities are often reported it is helpful to note their relationship through the density (ρ): $\eta = \rho\nu$. Some quantities in Table D.1 are extrapolated or derived from data in the enclosed references.

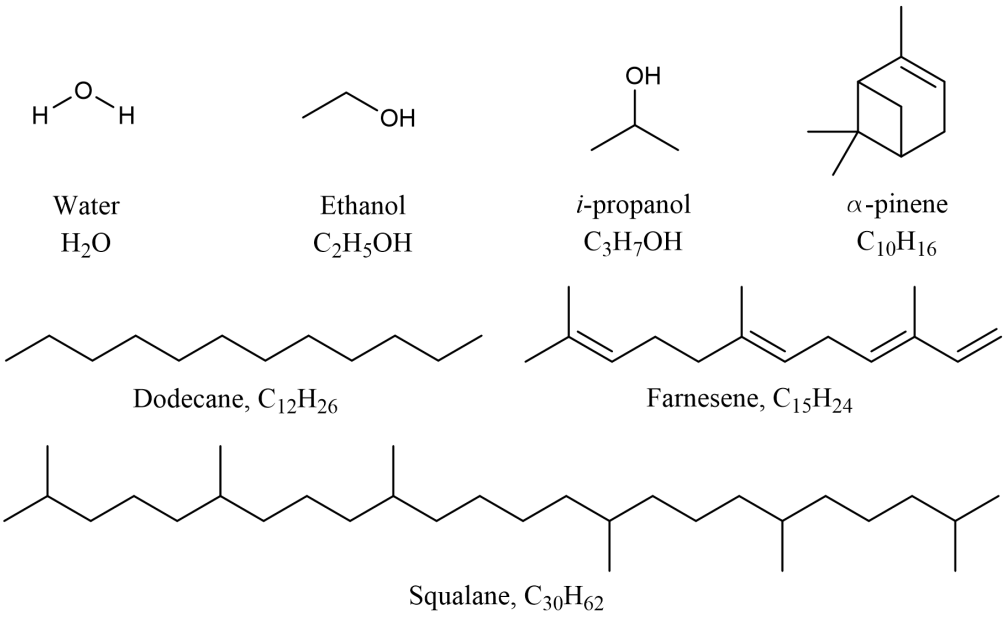

Figure D.1: Structures of the liquids considered in this Appendix as liquid jet candidates.

Table D.1: Physical properties of several liquids: freezing point (T_f), vapor pressure (P_{vap}), density (ρ), vaporization enthalpy (ΔH_{vap}), heat capacity (C_p), surface tension (γ), and kinematic viscosity (ν). For ρ, ΔH_{vap}, and C_p reference values at 298 K are given. Other quantities are given first at 298 K and then parenthetically close to their respective T_f.

Liquid	$\mathbf{T_f}$ **(K)**	$\mathbf{P_{vap}}$ **(Torr)**	ρ **(g/cm^3)**	$\mathbf{\Delta H_{vap}}$ **(kJ/mol)**	$\mathbf{C_p}$ **(J/mol K)**	γ **(mN/m)**	ν **(cSt)**
Water	273[a]	23.8 (4.6)[a]	0.997[a]	44.0[a]	75.3[a]	72 (76)[a]	0.89 (1.8)[a]
Salty water	206[b]	11.6[c] (0.005[d])	1.1[e]	45[d,e]	65.5[e]	82[f] (100[g])	2[g,h] (94[d,i])
Squalane	235[a]	1×10^{-8} (–)[j]	0.812[k]	134[j]	904[l]	29 (32)[m,n]	30 (1946)[k,n]
Dodecane	264[a]	0.14 (0.004)[o]	0.749[p]	61.5[a]	373[p]	25.3[q] (26.8[r])	1.8 (2.9)[q]
Farnesene	183[s]	0.0015 (-)[t]	0.814[s]	72.5[t]	313[n]	26 (-)[u]	3[s] (12.4[n])
α-pinene	199[a]	4.5 (3×10^{-4})[v]	0.854[w]	45.4[w]	249[x]	26[y] (34[z])	1.5[w] (24[n])
Ethanol	159[a]	59 (2×10^{-5})[a]	0.784[n]	42.8[a]	112[a]	22 (40)[n]	1.1 (38.4)[n]
Isopropanol	185[a]	45 (6×10^{-4})[a,n]	0.780[n]	45.4[n]	157[a]	21 (29)[n]	2.3 (26)[n]

[a] CRC Handbook of Chemistry and Physics[359]
[b] (Pátek & Klomfar, 2006a)[360]
[c] (Patil et al., 1990)[361]
[d] (Brastad & Nathanson, 2011)[314]
[e] (Pátek & Klomfar, 2006b)[362]
[f] (Yao et al., 1991)[363]
[g] (Sawada et al., 1998)[364]
[h] (Wimby & Berntsson, 1994)[365]
[i] (Mashovets et al., 1971)[366]
[j] (Zafar & Chickos, 2019)[367]
[k] (Harris, 2009)[368]
[l] (Durupt et al., 1996)[369]
[m] (Korosi & Kovats, 1981)[370]
[n] (NIST Thermochemical Tables)[339]
[o] (Sasse et al., 1988)[371]
[p] (Khasanshin et al., 2003)[372]
[q] (Luning et al., 2014)[373]
[r] (Schmidt et al., 1966)[374]
[s] (Chuck & Donnelly, 2014)[338]
[t] (Hoskovec et al., 2005)[337]
[u] (Cuesta et al., 2019)[375]
[v] (Štejfa et al., 2013)[376]
[w] (Clará et al., 2009)[377]
[x] (Fujisawa et al., 2005)[378]
[y] (Daisey & Hopke, 1993)[379]
[z] (Wagner et al., 1993)[380]